Physics of Atomic Nuclei, Vol. 63, No. 1, 2000, pp. 1–30. Translated from Yadernaya Fizika, Vol. 63, No. 1, 2000, pp. 5–35.

REVIEWS

Processes in the Coulomb Field of Nuclei and Electromagnetic Properties of Hadrons

L. G. Landsberg

Institute for High Energy Physics, Protvino, Moscow oblast, 142284 Russia

Received January 21, 1999

Abstract—Particle-production processes in the Coulomb field of nuclei at high energies have been considered, and the electromagnetic properties of hadrons (mesons and hyperons) have been investigated in these processes. The results of previous investigations have been summarized, and new data from the SELEX (Fermilab) and SPHINX (Institute for High Energy Physics, Protvino) facilities have been discussed. © *2000 MAIK "Nauka/Interperiodica".*

1. INTRODUCTION

This review article, which is an extended report presented by the author at the 21st Workshop on Fundamental Problems in High-Energy Physics and Field Theory [Institute for High Energy Physics (IHEP), Protvino, Russia, June 1998] and at some scientific seminars in Russia and in the United States, deals with high-energy coherent processes of particle production in the Coulomb field of nuclei,

$$h + Z \longrightarrow a + Z. \qquad (1)$$

Specifically, we consider the interaction of an incident particle h with a virtual photon of the Coulomb field of a nucleus (see diagram in Fig. 1). This virtual photon is characterized by a nonzero square q^2 of the 4-momentum [square of the 4-momentum transfer in reaction (1)]. It will be shown below that, at very high energies, the minimal value of the 4-momentum transfer squared, $q^2_{\min} = [(M_a^2 - M_h^2)/2E_h]^2$, is very close to zero—that is, a virtual photon becomes a nearly real one [here, M_h and M_a are the masses of the corresponding particles in reaction (1), while E_h is the energy of the primary particle]. Thus, an investigation of processes in the Coulomb field of a nucleus makes it possible to analyze the interaction of an incident particle with a "photon target."

For the first time, processes in the Coulomb field of nuclei (they are also known as Primakoff reactions) were considered independently by Primakoff [1] and by Pomeranchuk and Shmushkevich [2]. They are of great interest since they open the possibility for investigating rare radiative hadron decays $a \longrightarrow h\gamma$ under conditions where a heavy background from $a \longrightarrow h\pi^0$, $\pi^0 \longrightarrow 2\gamma$ hadron decays with one lost photon hinders the application of direct method for studying the above radiative processes. In the following, it will be shown that the cross section for reaction (1) has the form

$$\sigma_{\text{Coul}} = \sigma_0 \Gamma(a \longrightarrow h\gamma), \qquad (2)$$

where the coefficient σ_0 is reliably calculable by QED methods and where $\Gamma(a \longrightarrow h\gamma)$ is the partial width with respect to the relevant radiative decay. It follows that, by measuring the absolute value of the cross section for the Coulomb production process (1), we can determine the radiative width $\Gamma(a \longrightarrow h\gamma)$ even in those cases where a direct determination of this quantity is impossible.

Processes in the Coulomb field of nuclei also offer the possibilities for inquiries into photoproduction reactions or Compton scattering on unstable primary particles (such as pions, kaons, and Σ hyperons). In particular, such processes may be of considerable interest in seeking exotic hadrons [3–5]—for example, multiquark states with hidden strangeness, as is illustrated by the diagram in Fig. 2: according to the vector-dominance model, the photon is coupled rather strongly to the ϕ meson, whose wave function has the form $|\phi\rangle \simeq |s\bar{s}\rangle$; therefore, the diagram in Fig. 2 represents a natural mechanism for embedding an $s\bar{s}$ pair in a nascent hadron—that is, for producing particles with hidden strangeness.

2. DIRECT METHODS FOR STUDYING RADIATIVE DECAYS AND THEIR LIMITATIONS

Let us now consider radiative hadron decays. Radiative decays, as well as other electromagnetic hadronic processes featuring hadrons, are of great interest for

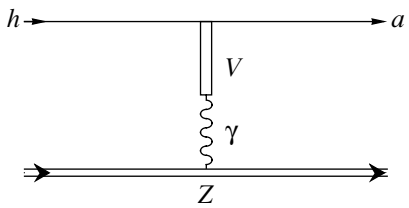

Fig. 1. Diagram describing the process $h + Z \longrightarrow a + Z$ (1) in the Coulomb field of a nucleus (here, γ is a virtual photon of the Coulomb field of a nucleus.

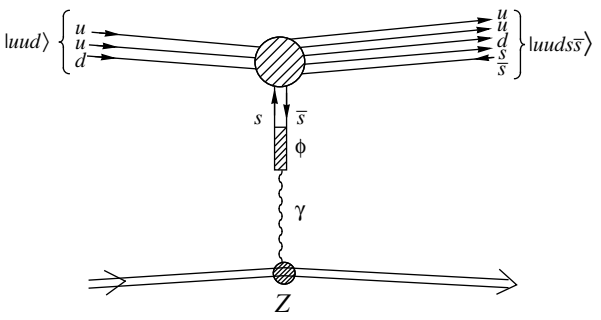

Fig. 2. Diagram describing the mechanism that can be responsible for the production of exotic baryons with hidden strangeness in the Coulomb field of a nucleus.

studying the internal structure of these particles. Such processes, which are governed by the interaction of real and virtual photons with electric charges of quark fields, make it possible to obtain unique information about the quark content of hadrons and about their phenomenological parameters like magnetic and transition moments, form factors, and polarizabilities. A theoretical analysis is simpler for electromagnetic processes than for purely hadronic processes, which are mediated by strong interactions; therefore, the former can be studied in greater detail. They are expected to play an important role as a testing ground for models describing the structure of hadrons (quark models, chiral models, and bag and string models). Although the present-day accuracy of theoretical calculations for radiative decays is not very high (this is due primarily to complications that arise in going over from a quark-level consideration to a description of hadrons), there are grounds to believe that considerable advances will be made here upon a further development of lattice QCD calculations. It should be noted, however, that we have been awaiting this progress for too long a time. Yet, there is a hope that detailed experimental information about radiative decays may be of paramount importance for pursuing further the investigation of large-distance hadronic phenomena and for solving the fundamental problem of confinement.

Let us first consider direct methods for detecting the radiative decays of hadrons. In experiments of this type, the particle a being studied is formed in well-separated hadronic reactions or in electromagnetic processes (photoproduction or resonance production in e^+e^- collisions). In order to isolate reliably rare radiative decays, such as

$$a \longrightarrow h + \gamma, \tag{3}$$

$$a \longrightarrow h_1 + h_2 + \gamma, \tag{4}$$

it is necessary, as a rule, to detect all secondaries (both charged and neutral ones), to identify them, and to reconstruct the effective masses of the states being studied. The main problem in experiments aimed at directly detecting rare radiative decays of the type (3) or (4) is associated with the need for suppressing a background from much more intense strong-interaction-induced hadronic decays with lost photons,

$$a \longrightarrow h_1 + h_2 + \pi^0, \quad \pi^0 \longrightarrow \gamma + (\gamma) \tag{5}$$

$$a \longrightarrow h + \pi^0. \quad \pi^0 \longrightarrow \gamma + (\gamma) \tag{6}$$

[Here and below, (γ) stands for a lost photon.] Such decays can mimic radiative processes of the types (3) and (4). In order to perform successfully an investigation of radiative decays, dedicated experimental settings are required that are characterized by a high sensitivity and which satisfy some specific conditions enabling a considerable reduction of the background from lost photons. These conditions are as follows:

(i) For the processes under study, the effective masses, $M(h_1h_2\gamma)$ or $M(h\gamma)$, must be reconstructed with the highest possible resolution and a minimal combinatorial background. This condition is especially important if the total width of a hadron is relatively small. In this case, a high mass resolution can reduce substantially the background from processes with lost photons because the latter do not give rise to a narrow peak at M_a: for background processes, the mass peak is smeared in width and is shifted toward smaller mass values.

(ii) The production of sought hadrons must be studied in reactions with well-fitted kinematics that permits measuring the emission angle for the hadron a independently of the reconstruction of its decay products. This makes it possible to obtain additional kinematical conditions for isolating single photons from radiative decays and for reducing background from lost photons. For example, we can require that the sum of transverse momenta with respect to the direction at which the particle a is emitted and which is determined from reaction kinematics be equal to zero, or we can apply other kinematical selections that will be considered below.

(iii) In order to suppress the background from lost photons, a special veto system that consists of counters with a low detection threshold for photons and which covers a maximally wide acceptance must be incorporated in the facility employed.

Often, all these requirements prove to be incompatible, or they reduce very strongly the sensitivity of the experiments being discussed. We will illustrate problems associated with a direct detection of radiative decays by discussing experiments aimed at searches for the rare decay

$$\omega \longrightarrow \pi^+ + \pi^- + \gamma \tag{7}$$

under the conditions of background from the main mode of ω decay, $\omega \longrightarrow \pi^+\pi^-\pi^0$. Searches for the radiative decay (7) were performed at the LEPTON-F [6] and ASTERIX [7] facilities (see Table 1).

Table 1. Searches for the radiative decay $\omega \longrightarrow \pi^+\pi^-\gamma$ [under conditions where the background is due to the main decay mode $\omega \longrightarrow \pi^+\pi^-\pi^0$, $\pi^0 \longrightarrow \gamma(\gamma)$ with one lost photon]

Experiment	Process under study	Result: upper limit on Br $[\omega \longrightarrow \pi^+\pi^-\gamma]$ at a 95% C.L.
LEPTON-F (IHEP) [6]	$\pi^-p \longrightarrow [\pi^+\pi^-\gamma]n$ $\longrightarrow \omega n$ (p_{π^-} = 32.5 GeV) $\hookrightarrow \pi^+\pi^-\gamma$ Investigation of the mass spectrum of the $\pi^+\pi^-\gamma$ system from the reaction $\pi^-p \longrightarrow [\pi^+\pi^-\gamma]n$; the use of the effective veto system to reduce the background from lost photons	4×10^{-3}
ASTERIX (CERN, LEAR) [7]	$\bar{p}p \longrightarrow \pi^+\pi^-\pi^+\pi^-\gamma$ Annihilation of stopped antiprotons $\longrightarrow \pi^+\pi^-\pi^+\pi^-\pi^0$ $\bar{p}$; kinematical fitting of events $\longrightarrow \pi^+\pi^-\omega$ Independent reconstruction of the direction of omega-meson emission in the production reaction and in the decay process; subtraction of the background from lost photons by using the results of a kinematical analysis	4×10^{-3}
	Summary result	3×10^{-3}

The LEPTON-F facility represented a wide-aperture magnetic spectrometer that was equipped with proportional chambers and which operated in conjunction with a multichannel γ spectrometer featuring lead-glass Cherenkov counters and a system of gas Cherenkov detectors for identifying charged primaries and secondaries. The facility, which was used to implement a wide program of investigations of radiative meson decays and of searches for exotic states (see [6, 8–11]), was exposed to a 32.5-GeV negative-pion beam from the 70-GeV accelerator installed at the Institute for High-Energy Physics (IHEP, Protvino).

As a source of omega mesons, experiments that sought the radiative decay (7) employed the charge-exchange reaction

$$\pi^- + p \longrightarrow \omega + n, \tag{8}$$

which makes it possible to perform radiative-decay searches under comparatively clean experimental conditions and in processes characterized by a low multiplicity and a low combinatorial background. This reaction is, however, disadvantageous in that the direction of omega-meson emission could not be reconstructed from the analysis of process (8) alone since the final-state neutron was not recorded, which gave no way to reconstruct fully the kinematics of this charge-exchange transition.

The decay process (7) was isolated by studying the reaction

$$\pi^- + p \longrightarrow [\pi^+\pi^-\gamma] + n. \tag{9}$$

Relevant criteria for selecting events with two pions and one photon in the final state and for suppressing the background were used in identifying the reaction under study. The LEPTON-F facility also included a special veto system that consisted of scintillation counters interspersed with lead converters and which reduced, at the trigger level, the background of photons missing the aperture of the γ spectrometer. The γ spectrometer itself, in which it was required to isolate one and only one photon from reaction (9), served as a part of this veto system. The well-known radiative processes $\eta \longrightarrow \pi^+\pi^-\gamma$ (under conditions of background from the decay process $\eta \longrightarrow \pi^+\pi^-\pi^0$) and $\eta' \longrightarrow \pi^+\pi^-\gamma$ were used in developing criteria for isolating the sought reactions. For this purpose, an analysis of the effective-mass spectrum $M(\pi^+\pi^-\gamma)$ was performed for reaction (9).

This spectrum, depicted in Fig. 3, shows four structures associated with the processes listed immediately below:

(a) the reaction $\pi^-p \longrightarrow \eta n$, followed by the decay $\eta \longrightarrow \pi^+\pi^-\pi^0$, $\pi^0 \longrightarrow \gamma(\gamma)$ with one lost photon;

(b) the reaction $\pi^-p \longrightarrow \eta n$, followed by the radiative decay $\eta \longrightarrow \pi^+\pi^-\gamma$;

(c) the reaction $\pi^-p \longrightarrow \omega n$, followed by the decay $\omega \longrightarrow \pi^+\pi^-\pi^0$, $\pi^0 \longrightarrow \gamma(\gamma)$ with one lost photon (possibly with a small admixture of the decay $\omega \longrightarrow \pi^+\pi^-\gamma$);

(d) the reaction $\pi^-p \longrightarrow \eta' n$, followed by the radiative decay $\eta' \longrightarrow \pi^+\pi^-\gamma$.

The ratio $R_\eta = N(\eta_{spur})/N(\eta \longrightarrow \pi^+\pi^-\gamma)$, where $N(\eta_{spur})$ is the number of spurious $\eta \longrightarrow \pi^+\pi^-\gamma$ events from the process $\eta \longrightarrow \pi^+\pi^-\pi^0$, $\pi^0 \longrightarrow \gamma(\gamma)$, while $N(\eta \longrightarrow \pi^+\pi^-\gamma)$ is the number of true events, was monitored in varying selection criteria. The choice of selection criteria was thought to be optimal if it corresponded to a minimal value of R_η at an insignificant decrease in the efficiency of the detection of the radiative-decay processes $\eta \longrightarrow \pi^+\pi^-\gamma$ and $\eta' \longrightarrow \pi^+\pi^-\gamma$. The choice of selection criteria was discussed in detail elsewhere [6]. In particular, it was shown there that the veto system

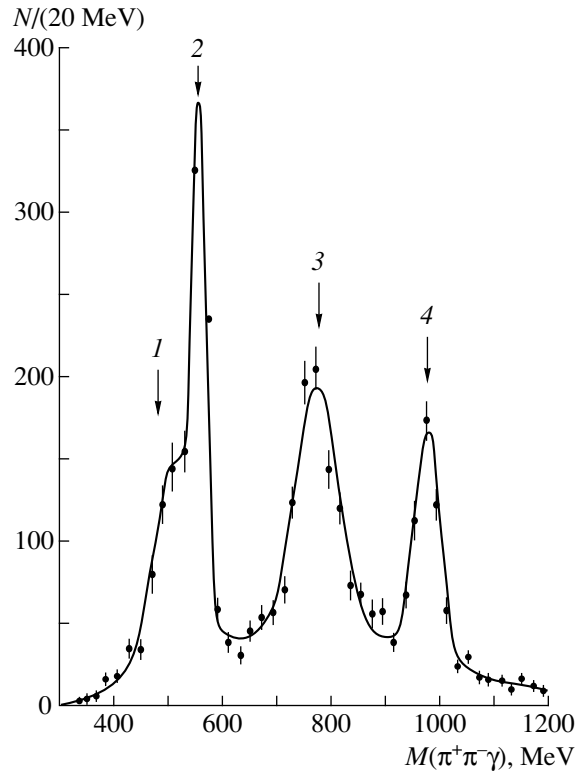

Fig. 3. Effective-mass spectrum of the $\pi^+\pi^-\gamma$ system originating from reaction (9) (data taken from [6] represent 20% of full statistics). This spectrum shows peaks from the radiative decays $\eta \longrightarrow \pi^+\pi^-\gamma$ (*2*) and $\eta' \longrightarrow \pi^+\pi^-\gamma$ (*4*) and spurious peaks from decays featuring lost photons, $\eta \longrightarrow \pi^+\pi^-\pi^0$, $\pi^0 \longrightarrow \gamma(\gamma)$ (*1*) and $\omega \longrightarrow \pi^+\pi^-\pi^0$, $\pi^0 \longrightarrow \gamma(\gamma)$ (*3*).

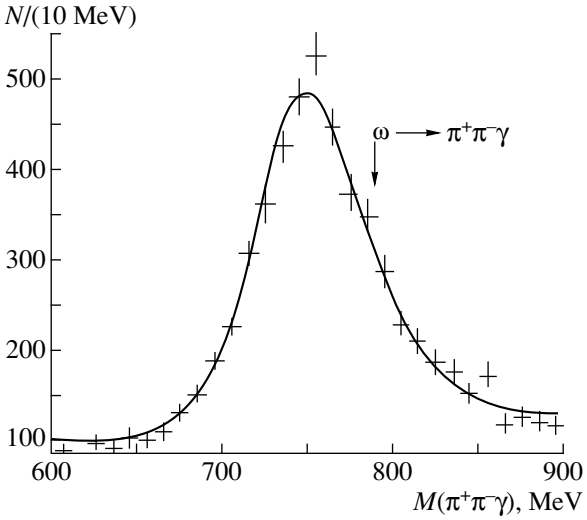

Fig. 4. Effective-mass spectrum of the $\pi^+\pi^-\gamma$ system originating from reaction (9) in the mass region of the omega-meson peak (data taken from [6] represent full statistics). The arrow indicates the mass value expected for the omega-meson peak from the decay $\omega \longrightarrow \pi^+\pi^-\gamma$.

reduced the background from lost photons by a factor of 10 to 20.

Figure 4 shows the total effective-mass spectrum of the $\pi^+\pi^-\gamma$ system in the omega-meson mass region. This spectrum was used in searches for the radiative decay (7). A Monte Carlo simulation revealed that the spurious peak from the decay process $\omega \longrightarrow \pi^+\pi^-\pi^0$, $\pi^0 \longrightarrow \gamma(\gamma)$ with one lost photon must be shifted with respect to the true omega-meson mass by about 30 MeV and have a width of 65 MeV. Experimental data comply well with this prediction.

In order to assess the possible number of events of the decay process $\omega \longrightarrow \pi^+\pi^-\gamma$ (7), the experimental distribution of $M(\pi^+\pi^-\gamma)$ was fitted to the sum of a Gaussian function (describing a spurious peak) and polynomial background. In this way, the position and width of the spurious peak and the shape of background were fixed (the normalization here remained free), and the number of events of the decay process was estimated for the resonance ω peak with preset parameters (the world-average mass value of $M_\omega = 782.6$ MeV and the instrumental width value of $\Gamma_{\text{instr}} = 43$ MeV as determined from a Monte Carlo simulation with a calibration based on $\eta' \longrightarrow \pi^+\pi^-\gamma$ data). This yielded $N(\omega \longrightarrow \pi^+\pi^-\gamma) = 30 \pm 52$ events. The total number of the decays $\omega \longrightarrow \pi^+\pi^-\pi^0$ recorded throughout the time of experiments at LEPTON-F was $N(\omega \longrightarrow \pi^+\pi^-\pi^0) = 2.64 \times 10^4$. With allowance for the apparatus efficiency, the upper limits on the product of the relevant cross section and the radiative-decay branching ratio and on the branching ratio itself are, respectively,

$$\sigma(\pi^- p \longrightarrow \omega n) \times \text{Br}(\omega \longrightarrow \pi^+\pi^-\gamma) < 17 \text{ nb} \qquad (10)$$

and

$$\text{Br}(\omega \longrightarrow \pi^+\pi^-\gamma) \qquad (11)$$
$$= \Gamma(\omega \longrightarrow \pi^+\pi^-\gamma)/\Gamma(\omega \longrightarrow \text{all channels}) < 4 \times 10^{-3}$$

These results were obtained at a 95% C.L.

In the experiments that were performed at the ASTERIX facility and which also sought the radiative decay $\omega \longrightarrow \pi^+\pi^-\gamma$ [7], a different efficient method, that which is based on the most detailed kinematical fitting of events, was used to suppress the background from lost photons. In order to implement this method, it is necessary that the direction of the emission of the decaying particle be determined independently of the detection of its decay products.

As a source of omega mesons, the ASTERIX experiments employed stopped-antiproton annihilation in the reaction

$$\begin{array}{l} \bar{p} + p \longrightarrow \omega + \pi^+ + \pi^-, \\ \qquad\qquad \hookrightarrow \pi^+\pi^-\gamma \end{array} \qquad (12)$$

where the kinematics of omega-meson emission could be fully reconstructed.

The ASTERIX facility represented a solenoidal magnetic spectrometer developing a field of 0.8 T and housing a hydrogen target surrounded by cylindrical drift and proportional chambers and endcap detectors equipped with proportional chambers. Converters in front of the last chambers (of thickness 0.9 radiation lengths) were used to record photons. The solid angle covered by the conversion system amounted to $0.75 \times 4\pi$, and the total efficiency for detecting photons with energies in excess of 150 MeV was at a level of 25 to 30%.

Measurements at ASTERIX recorded four-prong processes induced by the annihilation of antiprotons stopped in the hydrogen target. The spectrum of the missing-mass squared (MM^2) was plotted for these events on the basis of a kinematical analysis of charged particles. The four-prong events were separated into four classes:

$$\bar{p} + p \longrightarrow \pi^+\pi^-\pi^+\pi^- \quad (4C \text{ fit}), \tag{13a}$$

$$\longrightarrow \pi^+\pi^-\pi^+\pi^-\pi^0 \quad (1C \text{ fit}), \tag{13b}$$

$$\longrightarrow \pi^+\pi^-\pi^+\pi^-\gamma \quad (1C \text{ fit}), \tag{13c}$$

$$\longrightarrow \pi^+\pi^-\pi^+\pi^- \quad (MM^2) \text{ (no fitting)}. \tag{13d}$$

Here, data on photon conversion were not taken into account at the first step of data processing.

The total number of recorded four-prong events was 1.885×10^6. Of these, 3.74×10^5 events satisfied condition (13a) with a probability in excess of 1%, while 6.98×10^5 events satisfied condition (13b) or (13c) with the same probability. Events (13b) and (13c) were poorly separated because of an insufficient precision in measuring MM^2.

Events used for a further analysis were those of reactions (13b) and (13c) with one converted photon. The angle between the missing momentum (as determined on the basis of information about charged particles) and the direction of converted-photon emission was measured for such events. Figure 5 shows the experimental $\cos\vartheta^*$ distribution of events that was weighted with photon-detection efficiency. For events of reaction (13b), which features a neutral pion in the final state, it is expected that this distribution has a rectangular shape, and the experimental data confirm this on the whole. A peak in the region of large angles ($\cos\vartheta^* < -0.9$) is due to background events (misinterpretation of tracks, residues of events where the number of neutral pions is not less than two, etc.). Let us consider events for which $\cos\vartheta^* > 0.5$ (see the inset in Fig. 5); there, we can see a statistically significant peak near the value of $\cos\vartheta^* = 1$. This peak is due to events of reaction (13c) featuring single photons. Therefore, the region $\cos\vartheta^* > 0.9$ will further be used in searches for radiative meson decays.

Figure 6*a* shows the mass spectrum $M(\pi^+\pi^-\gamma)$ for events from the region $\cos\vartheta^* > 0.9$ in Fig. 5. For each

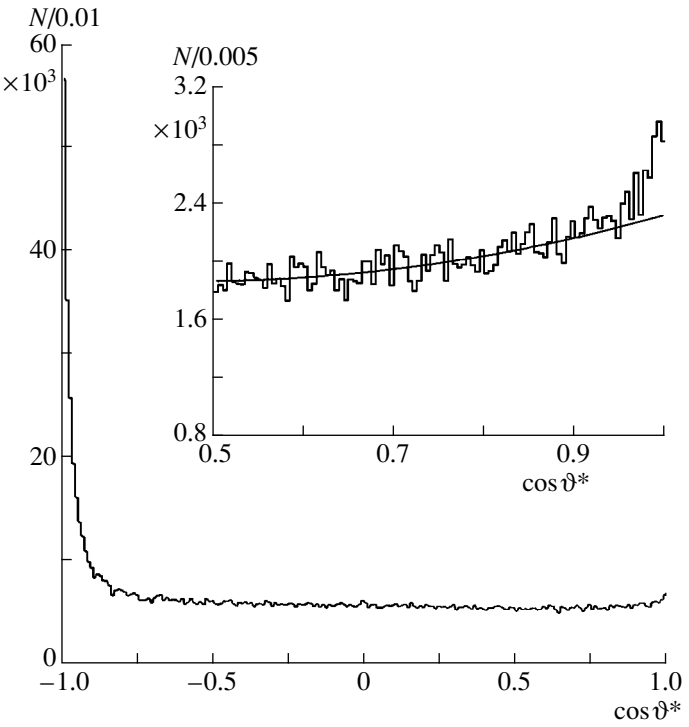

Fig. 5. $\cos\vartheta^*$ distribution of the number N of $\pi^+\pi^-\gamma$ combinations for events of reactions (13b) and (13c) with one converted photon (ϑ^* is the angle between the missing momentum as determined from data on charged particles and the direction of converted-photon emission). The inset displays this distribution for $\cos\vartheta^* > 0.5$, where we can see a statistically significant peak near the point $\cos\vartheta^* = 1$. The background from events featuring lost photons [$\pi^0 \longrightarrow \gamma(\gamma)$] is determined in the region $0.5 < \cos\vartheta^* < 0.9$.

event, the effective mass was determined from data on charged particles and from the missing momentum (which was associated with the photon). For this reason, the effective mass was independent of $\cos\vartheta^*$. Since this spectrum featured a heavy combinatorial background (four $\pi^+\pi^-\gamma$ combinations per event) and since, in addition, the conversion system had a low efficiency and could not therefore be used to suppress substantially the background from lost photons, the invariant-mass spectrum in Fig. 6*a* is formed primarily by background events. With the aid of this spectrum, it was next to impossible to study radiative decays. From data in Fig. 5, it follows that events from the region $0.5 \leq \cos\vartheta^* < 0.9$ can be used to subtract the background from lost photons in the region $\cos\vartheta^* > 0.9$. The resulting mass spectrum obtained upon background subtraction is displayed in Fig. 6*b*.

From this figure, we can see that the peak in the omega-meson mass region has now disappeared and that η and η' peaks correspond to the world-average mass values—that is, they are due to the radiative decays $\eta \longrightarrow \pi^+\pi^-\gamma$ and $\eta' \longrightarrow \pi^+\pi^-\gamma$, which are known to have large branching fractions. Data on the

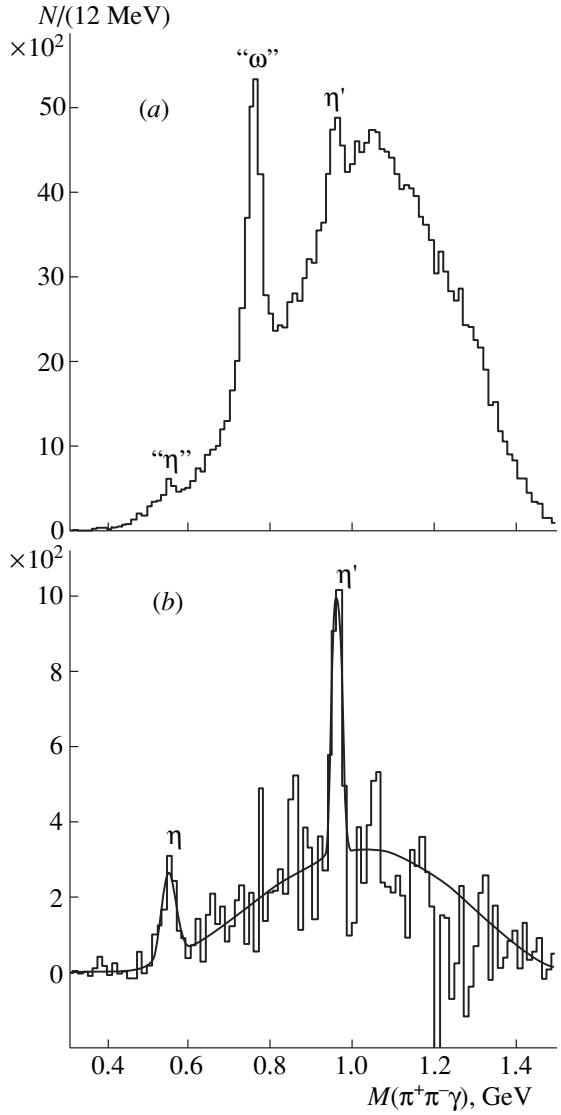

Fig. 6. (*a*) Effective-mass spectrum of the $\pi^+\pi^-\gamma$ system for events from Fig. 5 in the region $\cos\vartheta^* > 0.9$ ("ω" and "η" peaks are due to the decays $\omega \longrightarrow \pi^+\pi^-\pi^0$ and $\eta \longrightarrow \pi^+\pi^-\pi^0$ with one lost photon); (*b*) as in Fig. 6*a*, but upon the subtraction of the background that is associated with events featuring lost photons and which was determined in the region $0.5 < \cos\vartheta^* < 0.9$ (with a correct normalization). In these figures, *N* is the number of $\pi^+\pi^-\gamma$ combinations.

spectrum $M(\pi^+\pi^-\gamma)$ in Fig. 6*b* can now be used to set an upper limit on the branching fraction for the decay $\omega \longrightarrow \pi^+\pi^-\gamma$. A fit to the spectrum revealed that 155 ± 306 events (less than 767 events at a 95% C.L.) occur in the region specified by omega-meson parameters. In all, 214 500 events of the decay process $\omega \longrightarrow \pi^+\pi^-\pi^0$ were recorded throughout the experimental time. On this basis, the relevant branching ratio was constrained from above at a 95% C.L. as

$$\mathrm{Br}(\omega \longrightarrow \pi^+\pi^-\gamma) = \Gamma(\omega \longrightarrow \pi^+\pi^-\gamma)/\Gamma(\omega \longrightarrow \text{all channels}) \lesssim 4 \times 10^{-3}. \quad (14)$$

The corresponding upper limit is very close to that in (11), which was obtained from the measurements [6] at the LEPTON-F facility. The weighted upper limit (at a 95% C.L.) according to the data from the LEPTON-F and ASTERIX experiments is as follows:

$$\mathrm{Br}(\omega \longrightarrow \pi^+\pi^-\gamma) < 3 \times 10^{-3}. \quad (15)$$

The results of the experiments discussed above indicate that, in the case where the main source of background in searches for radiative decays of the type (3) or (4) are processes (5) and (6) with lost photons, the sensitivity of direct methods for radiative-decay searches can hardly be made higher than a value several times as great as the upper limits in (11) and (14). For example, the region of possible direct searches for radiative decays of the type $a \longrightarrow b_1 b_2 \gamma$ is constrained by the condition

$$\mathrm{Br}(a \longrightarrow b_1 b_2 \gamma) \gtrsim 10^{-2} \times \mathrm{Br}(a \longrightarrow b_1 b_2 \pi^0). \quad (16)$$

If, however, there is no background from reactions of types (5) and (6), the sensitivity of direct methods for radiative-decay searches can be substantially improved. This is illustrated by the results obtained at the GAMS and LEPTON facilities (see Table 2 [9, 11–13] and Figs. 7–9). But for rare radiative decays of the type $a \longrightarrow h\gamma$, which are accompanied by the background from processes with lost photons, data on radiative widths can be deduced from an analysis of processes occurring in the Coulomb field of nuclei, as was discussed in the Introduction. We will consider these processes in greater detail in the next section (see also [1, 2, 14–16]).

3. PARTICLE-PRODUCTION PROCESSES IN THE COULOMB FIELD OF NUCLEI

Figure 10 displays a generic diagram describing the production of the system of particles, *X*, with an effective mass M_X, in the interaction of primary particles *h* with virtual photons of the Coulomb field of a (*Z*, *A*) nucleus,

$$h + Z \longrightarrow X + Z. \quad (17)$$

Let us consider the kinematics of the coherent process (17). In this reaction, the square of the 4-momentum transfer is given by

$$t = (\mathcal{P}_X - \mathcal{P}_h)^2 = \mathcal{P}_X^2 + \mathcal{P}_h^2 - 2\mathcal{P}_X\mathcal{P}_h = M_X^2 + M_h^2 - 2E_X E_h + 2p_X p_h \cos\vartheta,$$

where $\mathcal{P}_X$ is the 4-momentum of the system *X*; p_X and E_X are its 3-momentum and energy, respectively; ϑ is the angle between the vectors $\mathbf{p}_X$ and $\mathbf{p}_h$; and M_X is the effective mass of the system *X*. At high energies, we have $p_X \simeq p_h - q_{||}$, where $q_{||} = (M_X^2 - M_h^2)/2p_h$ is the longitudinal momentum of the recoil nucleus in the coher-

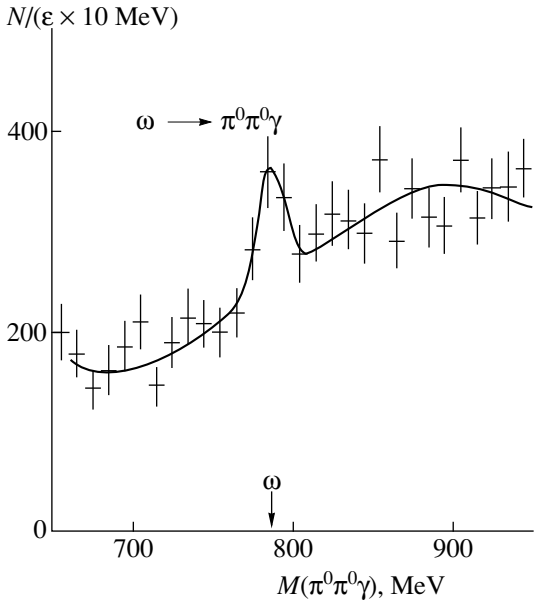

Fig. 7. Effective-mass spectrum of the $\pi^0\pi^0\gamma$ system originating from the reaction $\pi^-p \longrightarrow [\pi^0\pi^0\gamma]n$ (according to GAMS-2000 data [12]). The spectrum shows a peak from the radiative decay $\omega \longrightarrow \pi^0\pi^0\gamma$.

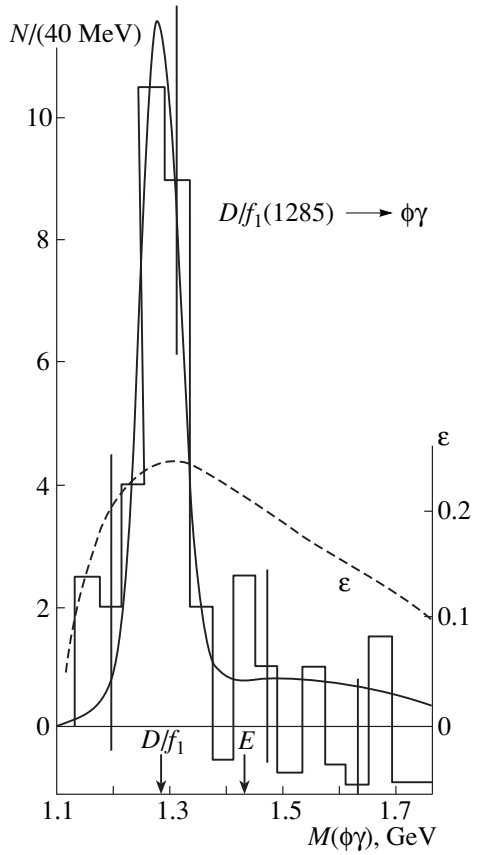

Fig. 8. Effective-mass spectrum of the $\phi\gamma$ system originating from the reaction $\pi^-p \longrightarrow [\phi\gamma]n$, $\phi \longrightarrow K^+K^-$ (according to LEPTON-F data [9]). The spectrum shows a peak from the radiative decay $D/f_1(1285) \longrightarrow \phi\gamma$. The dashed curve represent the efficiency of $\phi\gamma$ detection (right scale).

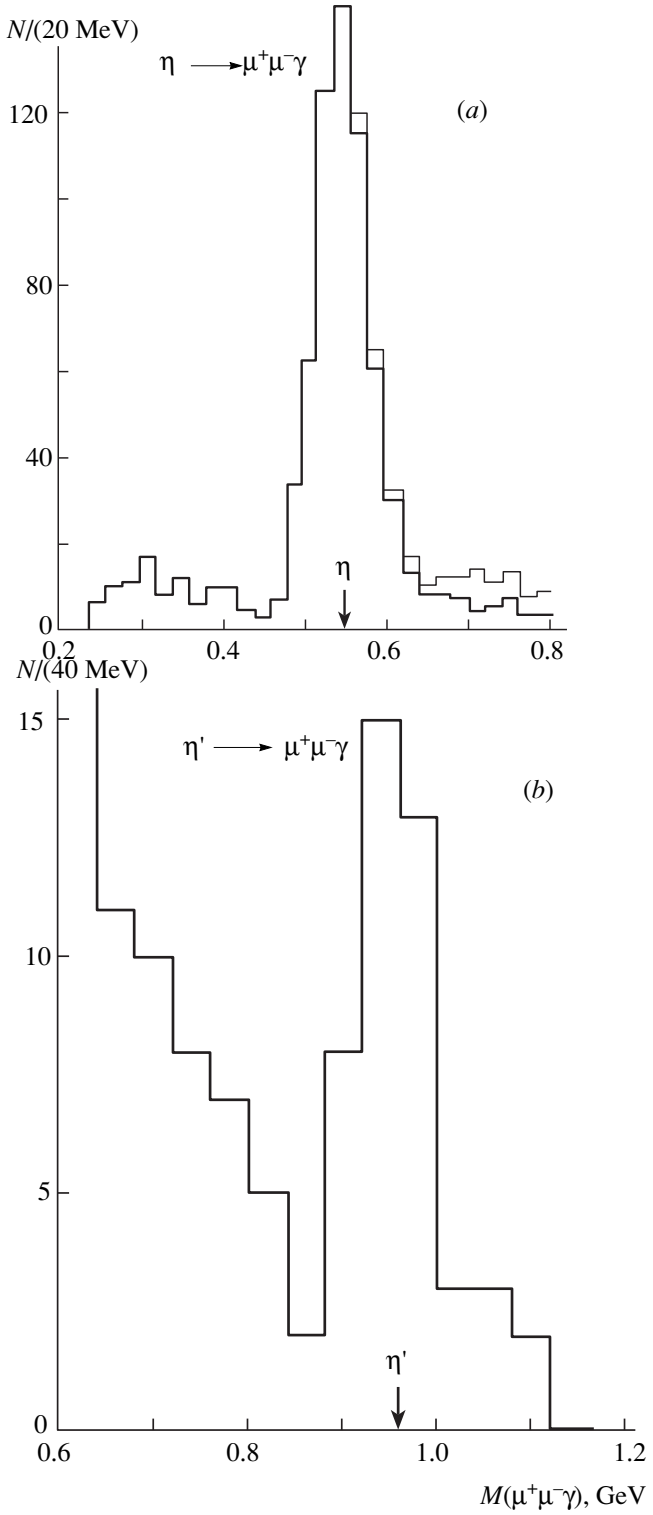

Fig. 9. Effective-mass spectra of the $\mu^+\mu^-\gamma$ system originating from the reaction $\pi^-p \longrightarrow [\mu^+\mu^-\gamma]n$ (according to LEPTON-G data [13]). The spectra show peaks corresponding to the radiative decays (*a*) $\eta \longrightarrow \mu^+\mu^-\gamma$ and (*b*) $\eta' \longrightarrow \mu^+\mu^-\gamma$. Histograms depicted by lines of different thicknesses correspond to different selection criteria.

Table 2. Discovery of some rare radiative decays of light mesons under favorable background conditions

Experiment	Process under study	Result
GAMS-2000 (IHEP) [12]	$\pi^- p \longrightarrow [\pi^0\pi^0\gamma]n$ (p_{π^-} = 38 GeV) $\longrightarrow \omega n$ $\hookrightarrow \pi^0\pi^0\gamma$	$\mathrm{Br}[\omega \longrightarrow \pi^0\pi^0\gamma] = (7.2 \pm 2.6) \times 10^{-5}$
Detection of $\omega \longrightarrow \pi^0\pi^0\gamma$	40 ± 12 events of the decay $\omega \longrightarrow \pi^0\pi^0\gamma$ have been recorded (Fig. 7)	
LEPTON-F (IHEP) [9, 11]	$\pi^- p \longrightarrow [K^+K^-\gamma]n$ (p_{π^-} = 32.5 GeV) $\longrightarrow [\phi\gamma]n$ $\hookrightarrow K^+K^-$	$\mathrm{Br}[D/f_1(1285) \longrightarrow \phi\gamma] = (0.9 \pm 0.2 \pm 0.4) \times 10^{-3}$
Detection of $D/f_1(1285) \longrightarrow \phi\gamma$	19 ± 5 events of the decay $D/f_1(1285) \longrightarrow \phi\gamma$ have been recorded (Fig. 8)	
LEPTON-G (IHEP) [13]	$\pi^- p \longrightarrow [\mu^+\mu^-\gamma]n$ $\longrightarrow (\eta, \eta')n$ $\hookrightarrow \mu^+\mu^-\gamma$	$\mathrm{Br}[\eta \longrightarrow \mu^+\mu^-\gamma] = (3.4 \pm 0.4) \times 10^{-4}$ $\mathrm{Br}[\eta' \longrightarrow \mu^+\mu^-\gamma] = (8.9 \pm 2.4) \times 10^{-5}$
Detection of $\eta \longrightarrow \mu^+\mu^-\gamma$ $\eta' \longrightarrow \mu^+\mu^-\gamma$	About 600 events of the decay $\eta \longrightarrow \mu^+\mu^-\gamma$ and 33 ± 7 events of the decay $\eta' \longrightarrow \mu^+\mu^-\gamma$ have been recorded (Fig. 9) Measurement of the electromagnetic form factors for these mesons	

ent process. We then arrive at

$$E_h \simeq p_h\left[1 + \frac{1}{2}(M_h/p_h)^2 - \frac{1}{8}(M_h/p_h)^4\right],$$

$$E_X \simeq p_X\left[1 + \frac{1}{2}(M_X/p_X)^2 - \frac{1}{8}(M_X/p_X)^4\right]$$

$$\simeq p_h(1 - q_\parallel/p_h)\left[1 + \frac{1}{2}(M_X/p_h)^2\right.$$

$$\left. + (M_X/p_h)^2(q_\parallel/p_h) - \frac{1}{8}(M_X/p_h)^4\right],$$

whence it follows that

$$2E_XE_h \simeq M_X^2 + M_h^2 + 2p_Xp_h$$

$$+ \frac{1}{4p_h^2}(M_X^4 + M_h^4 - 2M_X^2M_h^2),$$

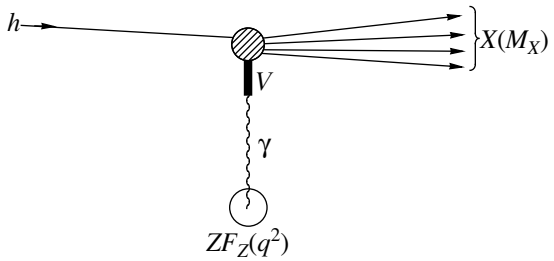

Fig. 10. Diagram representing the production of the hadron system X (with mass M_X) on virtual photons of the Coulomb field of a nucleus.

where we discarded terms of order $(M_X/p_h)^4$ and higher order terms in the mass-to-momentum ratio. The square of the momentum transfer is then given by

$$q^2 = -t = \frac{1}{4p_h^2}(M_X^2 - M_h^2)^2 + 2p_Xp_h(1 - \cos\vartheta)$$

$$\simeq \frac{1}{4p_h^2}(M_X^2 - M_h^2)^2 + (p_X\vartheta)^2 = q_{\min}^2 + p_T^2,$$

where $p_T^2 \simeq (p_X\vartheta)^2$ is the square of the transverse momentum of the system X.

Thus, it has been shown that the minimal value of the square of the 4-momentum transfer (it corresponds to $\vartheta = 0$) is

$$q_{\min}^2 = \frac{1}{4p_h^2}(M_X^2 - M_h^2)^2 \simeq \frac{1}{4E_h^2}(M_X^2 - M_h^2)^2. \quad (18a)$$

The square of the total 4-momentum transfer is

$$q^2 = q_{\min}^2 + p_T^2. \quad (18b)$$

At high primary energies E_h, the minimal value of the momentum transfer squared, $q_{\min}^2$, is very small, so that the momentum transfer squared is determined by the square of the transverse momentum of the nascent hadronic system, p_T^2. Here, the longitudinal momentum transfer is also very low.

The Coulomb production reaction (17) is characterized by the cross section

$$\left[\frac{d\sigma}{dq^2}\right]_{\text{Coul}} = \frac{\alpha Z^2}{\pi} \times \frac{\sigma(\gamma h \longrightarrow X)}{M_X^2 - M_h^2}\frac{q^2 - q_{\min}^2}{q^4}\left|F_Z(q^2)\right|^2, \quad (19)$$

where $\sigma(\gamma h \longrightarrow X)$ is the cross section for X photoproduction on the target h, $q_{\min}^2$ is the minimal value of the square of the momentum transfer in reaction (17) [see equation (18a)], and $\alpha \simeq 1/137$ is the fine-structure constant.

Expression (19) has a very simple physical meaning. It was indicated in the Introduction that, in Coulomb particle production at very high energies, virtual photons of the Coulomb field of a nucleus are characterized by very small values of q^2; therefore, they are treated as real ones in the upper vertex of the diagram in Fig. 10: to a high accuracy, the contribution of the upper vertex is parametrized by the cross section $\sigma(\gamma h \longrightarrow X)$ for photoproduction on a primary hadron. The square of the photon propagator is taken into account in calculating the cross section for the Coulomb process. The contribution of the lower vertex is described in terms of the charge of the nucleus and its electromagnetic form factor, and this leads to the factor $\alpha Z^2|F_Z(q^2)|^2$ in the Coulomb cross section. The remaining kinematical factors in (19) arise in calculating the cross section.

If a resonance state a decaying through a $a \longrightarrow bc$ channel is formed in the Coulomb production reaction, the cross section $\sigma(\gamma h \longrightarrow a)$ is described by the Breit–Wigner resonance formula for effective mass $M_X = M$ of the resonance system (see, for example, [17]); that is,

$$\sigma(\gamma h \longrightarrow a)_{\text{BW}} = \frac{2J_a + 1}{(2J_h + 1)(2S + 1)}\frac{4\pi}{K^2}|a_R|^2, \quad (20)$$

where $K = (M^2 - M_h^2)/2M$ is the momentum in the rest frame of the nascent state, while the factor $2S + 1$ is equal to two for the photonic target.

In the nonrelativistic approximation, the last factor in (20) as determined with allowance for the total resonance width Γ and the partial widths of the initial and final states has the form

$$|a_R|^2 = \frac{1}{4}\frac{\Gamma(a \longrightarrow h\gamma)\Gamma(a \longrightarrow bc)}{(M - M_a)^2 + (\Gamma/2)^2}. \quad (21)$$

The corresponding relativistic expression that takes into account corrections for the dynamical resonance width is given by

$$|a_R|^2 = \frac{M_a^2\Gamma(a \longrightarrow h\gamma)\Gamma(a \longrightarrow bc)g_\gamma(M^2)g_{bc}(M^2)}{(M^2 - M_a^2)^2 + M_a^2\Gamma^2 g^2(M^2)}, \quad (22)$$

where $g_\gamma(M^2)$, $g_{bc}(M^2)$, and $g(M^2)$ are correction factors including the dynamical resonance width and depending on resonance quantum numbers. At the resonance value of $M = M_a$, we have

$$g_\gamma(M_a^2) = g_{bc}(M_a^2) = g(M_a^2) = 1. \quad (23)$$

It can easily be verified that, in the nonrelativistic approximation, which is valid only for sufficiently narrow resonances and which corresponds to $M^2 - M_a^2 \ll M_a^2$, so that $M^2 - M_a^2 \simeq 2(M - M_a)M_a$, all the dynamical correction factors reduce to unity, and the relativistic expression (22) goes over to the nonrelativistic one as given by (21). If the decay $a \longrightarrow bc$ is dominant, we can make use of the approximation

$$g(M^2) \simeq g_{bc}(M^2). \quad (24)$$

The conventional parametrization of the dynamical factors $g_{bc}(M^2)$ have the form

$$g_{bc}(M^2) = \left(\frac{p}{p_0}\right)^{2l+1}\frac{2p_0^2}{p^2 + p_0^2}, \quad (25)$$

where l is the orbital angular momentum for the decay process $a \longrightarrow bc$, while p and p_0 are the momenta of the particle b in the X rest frame at the mass values of M and M_a, respectively.

Thus, the cross section for resonance photoproduction on a primary particle h is eventually given by

$$\sigma(\gamma h \longrightarrow M \longrightarrow bc)_{\text{BW}} = \begin{cases} \left[\frac{2J_a + 1}{2J_h + 1}\right] \times 4\pi^2\frac{M^2}{(M^2 - M_h^2)^2} \times \frac{\Gamma(a \longrightarrow h\gamma)\Gamma(a \longrightarrow bc)}{\Gamma} \\ \times \underbrace{\frac{1}{\pi}\frac{\Gamma/2}{(M - M_a)^2 + (\Gamma/2)^2}}_{=\delta(M - M_a)\ \text{for}\ \Gamma \to 0}\ (\text{nonrel. appr.}), \\ \left[\frac{2J_a + 1}{2J_h + 1}\right] \times 8\pi^2\frac{M^2 M_a}{(M^2 - M_h^2)^2} \times \frac{\Gamma(a \longrightarrow h\gamma)\Gamma(a \longrightarrow bc)}{\Gamma} \\ \times \underbrace{\frac{1}{\pi}\frac{M_a g_\gamma(M^2)g_{bc}(M^2)\Gamma}{(M^2 - M_a^2)^2 + M_a^2\Gamma^2 g_{bc}^2(M^2)}}_{=\delta(M^2 - M_a^2)\ \text{for}\ \Gamma \to 0,\quad g_\gamma = g_{bc} \to 1.}\ (\text{rel. appr.}). \end{cases} \quad (26)$$

That the replacement of the resonance expressions by a delta function is legitimate can easily be demon-

strated. It is known, for example, from [18], that we have the limiting relation

$$f(x) = \frac{m}{\pi}\frac{1}{1+(mx)^2} \xrightarrow[m\to\infty]{} \delta(x),$$

whence it follows that

$$\frac{1}{\pi}\frac{\Gamma/2}{(M-M_a)^2+(\Gamma/2)^2}$$
$$= \frac{1}{\pi}\frac{(\Gamma/2)^{-1}}{1+[(M-M_a)(\Gamma/2)^{-1}]^2}$$
$$= \frac{1}{\pi}\frac{m}{1+(mx)^2} \xrightarrow[m\to\infty]{} \delta(x) = \delta(M-M_a),$$

where $m = (\Gamma/2)^{-1}$ and $x = M - M_a$.

Similarly, we have

$$\frac{1}{\pi}\frac{M_a\Gamma g_\gamma(M^2)g_{bc}(M^2)}{(M^2-M_a^2)^2+M_a^2\Gamma^2 g_{bc}^2(M^2)}$$
$$\longrightarrow \frac{1}{\pi}\frac{M_a\Gamma}{(M^2-M_a^2)^2+M_a^2\Gamma^2}$$
$$= \frac{1}{\pi}\frac{(M_a\Gamma)^{-1}}{1+[(M^2-M_a^2)(M_a\Gamma)^{-1}]^2}$$
$$= \frac{1}{\pi}\frac{m}{1+(mx)^2} \xrightarrow[m\to\infty]{} \delta(x) = \delta(M^2-M_a^2),$$

where $m = (M_a\Gamma)^{-1}$ and $x = M^2 - M_a^2$ [since $g_\gamma(M^2) \longrightarrow g_\gamma(M_a^2) = 1$ and $g_{bc}(M^2) \longrightarrow g_{bc}(M_a^2) = 1$ for $\Gamma \longrightarrow 0$].

By using relation (26), we can obtain the transverse-momentum distribution for the Coulomb resonance-production reaction $h + Z \longrightarrow a + Z$ (1) in the approximation of a small resonance width ($\Gamma_a \longrightarrow 0$). The calculations were performed in the relativistic approximation (the nonrelativistic approximation obviously yields the same result). From relations (19) and (26), it follows that the cross section for the Coulomb process

$$h + Z \longrightarrow a + Z$$
$$\hookrightarrow b + c$$

has the form

$$\left[\frac{d\sigma}{dq^2}\right]_{\text{Coul}} = \int\left[\frac{d^2\sigma}{dq^2 dM^2}\right]_{\text{Coul}} dM^2$$
$$= \left[\frac{2J_a+1}{2J_h+1}\right]\times 8\pi\alpha Z^2\frac{\Gamma(a\longrightarrow h\gamma)\Gamma(a\longrightarrow bc)}{\Gamma}$$
$$\times\int dM^2\frac{q^2-q_{\min}^2}{q^4}\left|F_Z(q^2)\right|^2\frac{M^2M_a}{(M^2-M_h^2)^3}$$
$$\times\underbrace{\frac{1}{\pi}\frac{M_a g_\gamma(M^2)g_{bc}(M^2)\Gamma}{(M^2-M_a^2)^2+M_a^2\Gamma^2 g_{bc}^2(M^2)}}_{\simeq\,\delta(M^2-M_a^2)\text{ for }\Gamma\to 0}$$
$$= \left[\frac{2J_a+1}{2J_h+1}\right]\times 8\pi\alpha Z^2\frac{\Gamma(a\longrightarrow h\gamma)\Gamma(a\longrightarrow bc)}{\Gamma}$$
$$\times\frac{q^2-q_{\min}^2}{q^4}\left|F_Z(q^2)\right|^2\frac{M_a^3}{(M_a^2-M_h^2)^3}. \quad (27)$$

Thus, we conclude that, in the approximation of a small width of the resonance state a that is formed in the Coulomb production reaction (1) and which decays through the channel $a \longrightarrow bc$, the momentum-transfer-squared distribution of events is given by

$$\left[\frac{d\sigma}{dq^2}\right]_{\text{Coul}} = 8\pi\alpha Z^2\left[\frac{2J_a+1}{2J_h+1}\right]\Gamma(a\longrightarrow h\gamma)$$
$$\times\text{Br}(a\longrightarrow bc)\frac{M_a^3}{(M_a^2-M_h^2)^3}\frac{q^2-q_{\min}^2}{q^4}\left|F_Z(q^2)\right|^2. \quad (28)$$

In the same approximation, the total cross section for the Coulomb process (1) has the form

$$\sigma(h+Z\longrightarrow a+Z)_{\text{Coul}} = 8\pi\alpha Z^2\left[\frac{2J_a+1}{2J_h+1}\right]$$
$$\times\Gamma(a\longrightarrow h\gamma)\frac{M_a^3}{(M_a^2-M_h^2)^3}\int_{q_{\min}^2}^{q_{\max}^2}\frac{q^2-q_{\min}^2}{q^4}\left|F_Z(q^2)\right|^2 dq^2 \quad (29)$$
$$= \sigma_0\Gamma(a\longrightarrow h\gamma),$$

$$\sigma_0 = 8\pi\alpha Z^2\left[\frac{2J_a+1}{2J_h+1}\right]\frac{M_a^3}{(M_a^2-M_h^2)^3}$$
$$\times\int_{q_{\min}^2}^{q_{\max}^2}\frac{q^2-q_{\min}^2}{q^4}\left|F_Z(q^2)\right|^2 dq^2. \quad (30)$$

The quantity $q_{\max}^2$ bounds the region where Coulomb processes are dominant. In estimating the integral $I = \int_{q_{\min}^2}^{q_{\max}^2}\frac{q^2-q_{\min}^2}{q^4}\left|F_Z(q^2)\right|^2 dq^2$ with respect to momentum transfers, the nuclear form factor is parametrized in the form

$$F_Z(q^2) = \exp(-q^2/\text{b}^2). \quad (31)$$

The parameter b^2 is given by $b^2 = 6/\langle r^2\rangle$, the root-mean-square radius of the nucleus being $\langle r^2\rangle^{1/2} = 0.94A^{1/3} \times 10^{-13}$ cm (see [19]). By taking all the above into account, we obtain

$$I = \int_{q^2_{\min}}^{q^2_{\max}} \frac{q^2 - q^2_{\min}}{q^4}\left|F_Z(q^2)\right|^2 dq^2$$

$$= \int_{q^2_{\min}}^{q^2_{\max}} \frac{q^2 - q^2_{\min}}{q^4}\exp(-2q^2/b^2)dq^2 \qquad (32)$$

$$= \int_{q^2_{\min}}^{q^2_{\max}} \frac{q^2 - q^2_{\min}}{q^4}\exp(-q^2/a^2)dq^2.$$

Introducing the variable $x = q^2/a^2$ ($a^2 = b^2/2$) and assuming that $x_{\max} \le 1$ and $x_{\min} \ll x_{\max}$, we can obtain

$$I = \int_{x_{\min} = q^2_{\min}/a^2}^{x_{\max} = q^2_{\max}/a^2} \left[\frac{\exp(-x)}{x} - x_{\min}\frac{\exp(-x)}{x^2}\right]dx$$

$$= (1 + x_{\min})\left(\ln x - x + \frac{x^2}{2\times 2!} - \frac{x^3}{3\times 3!}\right. \qquad (33)$$

$$\left. + \frac{x^4}{4\times 4!}\ldots\right)_{x_{\min}}^{x_{\max}} + \frac{x_{\min}}{x_{\max}}\exp(-x_{\max}) - \exp(-x_{\min}).$$

In particular, the relevant numerical values for the lead nucleus are $\langle r^2\rangle^{1/2} = 5.56\times 10^{-13}$ cm, $b^2 = 0.0078$ GeV^2, and $a^2 = 0.0039$ GeV^2. We can evaluate the integral I for various options of $q^2_{\max}$. We have

$$I = \ln\left(\frac{q^2_{\max}}{q^2_{\min}}\right) - 1.87 \text{ for } q^2_{\max} = 5\times 10^{-3}\ \text{GeV}^2, \quad (34)$$

$$I = \ln\left(\frac{q^2_{\max}}{q^2_{\min}}\right) - 1.24 \text{ for } q^2_{\max} = 1\times 10^{-3}\ \text{GeV}^2. \quad (35)$$

Without allowance for the form factor, the result is

$$I = \ln\frac{q^2_{\max}}{q^2_{\min}} - 1. \qquad (36)$$

At sufficiently high primary energies E_h [such that $\ln(q^2_{\max}/q^2_{\min})$ is in excess of five or six], the distinctions between these estimates are rather modest.

Figure 11 shows schematically the behavior of the differential cross section $[d\sigma/dq^2]_{\text{Coul}}$ for the Coulomb particle-production process (1). The Coulomb cross section is seen to increase fast with decreasing q^2. By using expression (28), it can easily be shown that differential cross section $[d\sigma/dq^2]_{\text{Coul}}$ attains a maximum at $q_0^2 = 2q^2_{\min}$ (q_0^2 varies with the primary energy E_h in inverse proportion to its square) and that, at this point, we have $[d\sigma/dq^2]^{\max}_{\text{Coul}} \propto q^{-2}_{\min} \propto E_h^2$. With increasing primary energy, the cross section at the point of maximum grows in proportion to E_h^2, whereas the maximum itself shifts to the region of small q^2. Its width is estimated as $\Delta \simeq 6q^2_{\min} \propto E_h^{-2}$. Thus, we conclude that the total cross section for the Coulomb process is $\sigma_{\text{Coul}} \simeq [d\sigma/dq^2]^{\max}_{\text{Coul}}\Delta \propto E_h^2 E_h^{-2}$—that is, it is independent of primary energy in the first approximation. On the basis of equations (33)–(36), we can estimate this cross section more accurately. The result is $\sigma_{\text{Coul}} \propto \ln q^{-2}_{\min} \propto \ln E_h$, whence we see that, in fact, it grows logarithmically with energy.

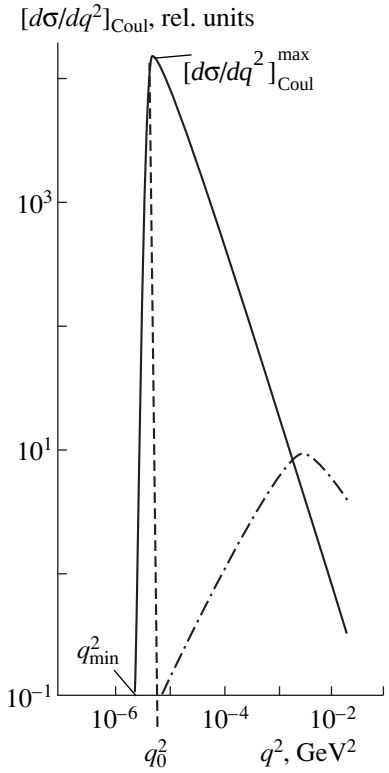

Fig. 11. Schematic behavior of the differential cross section $[d\sigma/dq^2]_{\text{Coul}}$ for the Coulomb particle-production process (1) as a function of q^2 ($q^2_{\min}$ is the minimal value of the square of the momentum transfer; $q_0^2 = 2q^2_{\min}$ is the position of the cross-section maximum; the width of the Coulomb maximum is estimated as $\Delta \simeq 6q^2_{\min} = 3q_0^2$). The dash-dotted curve represents the background from the strong-interaction-induced coherent process.

Table 3. Basic properties of processes in the Coulomb field of nuclei and of strong-interaction-induced coherent reactions

Basic properties of Coulomb processes	Basic properties of strong-interaction-induced coherent reactions	
	ω-pole exchange	Pomeron exchange (diffraction)
(a) $\sigma_{Coul} \propto \ln E_h$;	(a) $\sigma_{strong} \sim E_h^{-1}$; at high energies, this contribution dies out;	(a) σ_{strong} depends only slightly on energy (Pomeron exchange);
(b) The distribution $[d\sigma/dq^2]_{Coul}$ is concentrated in the region of small q^2 (the cross section achieves a maximum at $q_0^2 = 2q_{min}^2 = 2\left[\frac{M_a^2 - M_h^2}{2E_h}\right]^2$; that is, relevant q^2 are very small at high energies);	(b) $[d\sigma/dq^2]_{strong}$ depends on the quantum numbers of the nascent meson; in some cases, the cross section decreases at small p_T^2: $d\sigma/dq^2 \propto (q^2 - q_{min}^2)$;	(b) $[d\sigma/dq^2]_{strong\ diffr} \propto \exp[-(q^2 - q_{min}^2)b]$; $b = (8–10)A^{2/3}$ GeV^{-2};
(c) The width of the distribution is $[d\sigma/dq^2]_{Coul}$ $\Delta \simeq 6q_{min}^2$;	(c) $\sigma_{strong} \propto A^{2/3}$.	(c) $\sigma_{strong\ diffr} \propto A^{2/3}$;
(d) $\sigma_{Coul} \propto Z^2$;	At very high energies, the coherent background of this type usually does not play a significant role in the region $q^2 \leq (3–4) \times 10^{-3}$	(d) The t-channel helicity is $\lambda = 0$.
(e) In the Gottfried–Jackson frame, the helicity is $\lambda = \pm 1$ (quasireal photon); that is, the t-channel helicity is $\lambda = \pm 1$		The diffractive coherent background complicates strongly the investigation of the Coulomb processes of particle production
		Diffractive processes play a decisive role if they are allowed by the following selection rules in quantum numbers:
		(1) Flavors do not change in going over h to a.
		(2) $h(J^P) \longrightarrow a[J^P; (J+1)^{-P}; (J+2)^P]$—this is a selection rule in quantum numbers for diffractive processes (Gribov–Morrison rule)

Thus, the radiative width with respect to the decay $a \longrightarrow h\gamma$ can be determined by measuring the absolute value of the cross section for the Coulomb production process, $\sigma(h + Z \longrightarrow a + Z)_{Coul}$, because, according to (2), (29), and (30), we have

$$\sigma(h + Z \longrightarrow a + Z)_{Coul} = \sigma_0 \Gamma(a \longrightarrow h\gamma),$$

where σ_0 is a known quantity that can be calculated precisely.

The above estimates of σ_0 were obtained in the approximation where the width of the resonance a is assumed to be small. Of course, more accurate calculations based on the relativistic formula for the resonance a can also be performed. By way of example, we indicate that, in the production of $a_2(1320)^-$ mesons by 600-GeV π^- mesons, the Coulomb cross section σ_0 found on the basis of the relativistic Breit–Wigner formula (26) is 10% below the σ_0 value obtained in the narrow-resonance approximation:

$$\sigma_0[a_2(1320)^-]_{rel\ BW} \simeq 0.9\sigma_0[a_2(1320)^-]_{narrow\ width}. \quad (37)$$

Thus, we see that the more precise estimates can prove important.

It is worth discussing one more circumstance of paramount importance, which can complicate substantially the investigation of coherent particle-production processes in the Coulomb field of nuclei. The point is that strong-interaction processes can also lead to coherent reactions on nuclei. In general, we therefore have

$$\frac{d\sigma}{dq^2} = \left|A_{Coul} + A_{strong}e^{i\varphi}\right|^2, \quad (38)$$

where A_{Coul} is the Coulomb amplitude, A_{strong} is the amplitude of the coherent process caused by strong interactions, and φ is the relative phase of these two amplitudes.

In order to separate the contributions of Coulomb coherent processes and strong-interaction-induced coherent processes, it is useful to give a brief summary of their basic properties (see Table 3).

From an analysis of information presented in this table, we can conclude that, for Coulomb processes, two situations associated with the background from coherent strong-interaction-induced processes can be realized, depending of the quantum numbers of nascent particles.

(i) A coherent diffractive background is forbidden by selection rules in quantum numbers, and the background caused by strong interactions may be due to Reggeon exchanges (as a rule, omega-meson exchanges). In this case, the strong-interaction-induced coherent background dies out at high primary energies, and quite favorable conditions are realized for isolating Coulomb processes. Moreover, the above-type background decreases sometimes at low momentum transfers in proportion to q^2.

(ii) A coherent diffractive background plays a decisive role, in which case it becomes much more difficult to separate Coulomb processes. This can be done only in the case of high statistics and in the region of very low q^2 (less than 10^{-3} GeV^2).

Below, these two cases will be illustrated by experimental data.

To summarize a general consideration of particle-production processes in the Coulomb field of nuclei, it is worthwhile to make the following comments:

(a) Coulomb reactions open unique possibilities for studying rare radiative hadron decays of the type $a \longrightarrow h\gamma$ in cases where these decays cannot be separated by direct methods because of heavy backgrounds from $a \longrightarrow h\pi^0$, $\pi^0 \longrightarrow \gamma(\gamma)$ decays with lost photons or where relevant widths are too small to be measured directly, as is the case for the decay $\Sigma^0 \longrightarrow \Lambda\gamma$.

(b) Coulomb reactions also make it possible to study photoproduction and Compton scattering processes on unstable particles, such as pions, kaons, and hyperons. This opens new for performing ways exotic-hadron searches, for measuring the electromagnetic features of unstable particles (for example, polarizability), and for studying some other phenomena.

(c) In order to carry out all these investigations, it necessary to isolate reliably particle-production processes in the Coulomb field of nuclei (in particular, to separate them from the coherent background due to strong interactions) and to measure the absolute values of the cross sections for the processes being studied. All this requires precision measurements at high energies and at very low momentum transfers, but such measurements present a real challenge. This is reason why only a few experiments have been performed over the nearly 50 years that have elapsed since the first theoretical study of Primakoff on the subject [1]. The results of basic investigations of Coulomb production that were performed until recently to a comparatively high precision and furnished interesting information about the radiative decays of hadrons and about their electromagnetic properties are summarized in Table 4 [16, 20–31]. Here, we do not consider data obtained in photon beams for the radiative widths with respect to the decays $\pi^0 \longrightarrow \gamma\gamma$ and $\eta \longrightarrow \gamma\gamma$, nor do we survey experiments in hadron beams at moderate energies, where the strong-interaction-induced background could not be suppressed with the required accuracy.

In 1998, some new data on the processes of Coulomb particle production were obtained in the SELEX experiment that was performed by a large international collaboration and which employed 600-GeV beams of primary π^- mesons and Σ^- hyperons. The first results from that experiment will be discussed in the sections of this article that follow.

4. INVESTIGATION OF PARTICLE-PRODUCTION PROCESSES IN THE COULOMB FIELD OF NUCLEI IN THE SELEX EXPERIMENT

4.1. SELEX Facility

In the years 1996 and 1997, a large international collaboration that included scientists from the United States, Russia, Germany, Brazil, Israel, Italy, and other countries performed experiments at the SELEX facility that was constructed at Fermilab (Batavia, USA) and which operated in a 600-GeV beam from the Tevatron accelerator. This beam consisted primarily of Σ^- hyperons and π^- mesons in equal shares and included a very small admixture of other particles (Ξ^-, K^-, etc.). The SELEX facility [32, 33] comprised a three-stage magnetic spectrometer equipped with proportional and drift chambers, a vertex detector with microstrip silicon stations, additional microstrip detectors in the beam region, three photon spectrometers featuring lead-glass counters, a hadronic calorimeter (for neutron detection), a Cherenkov multiparticle spectrometer of the RICH type, and transition-radiation detectors for identifying charged particles. The data-acquisition system of the apparatus made it possible to record large flows of information and to develop fast trigger signals of a high level for an additional filtration of events.

Basically, the research program of experiments at the SELEX facility was aimed at studying strange–charmed baryons. However, investigations of particle-production in the Coulomb field of nuclei and in some diffractive reactions, searches for exotic hadrons that involve charmed or strange quarks or both of them, measurements of electromagnetic form factors for particles, and some other studies were performed there concurrently with the implementation of the basic program. Vast statistics of events recorded in experiments at the SELEX facility (more than 10^9 events) are being processed at present. A few first results of these investigations on particle-production processes in the Coulomb field of nuclei [34–37] are considered in the present survey.

The scope of investigation of Coulomb production processes at the SELEX facility was limited by the fact that these investigations were performed simultaneously with those of the basic program of studies in charm physics. In particular, experiments with a lead target, which are of paramount importance for inquiries into Coulomb processes, could be conducted for a very short time. For some processes, including the Coulomb production of $\Sigma^*(1385)$, the detection efficiency was

Table 4. Compendium of data on the Coulomb processes of hadron production

Experiment	Process under study	Result	References
E272 (Fermilab)	$\pi^- + (Z, A) \longrightarrow \rho(770)^- + (Z, A)$ (p_{π^-} = 156; 260 GeV) $\hookrightarrow \pi^-\pi^0$	$\Gamma[\rho(770)^- \longrightarrow \pi^-\gamma] = 71 \pm 7$ keV	[20]
	$\pi^+ + (Z, A) \longrightarrow \rho(770)^+ + (Z, A)$ (p_{π^+} = 202 GeV) $\hookrightarrow \pi^+\pi^0$	$\Gamma[\rho(770)^+ \longrightarrow \pi^+\gamma] = 59.8 \pm 4.0$ keV	[16]
	$\longrightarrow a_2(1320)^+ + (Z, A)$ $\hookrightarrow \eta\pi^+,\ K^0_S K^+$	$\Gamma[a_2(1320)^+ \longrightarrow \pi^+\gamma] = 295 \pm 60$ keV	[21]
	$\longrightarrow a_1(1260)^+ + (Z, A)$ $\hookrightarrow 3\pi$	$\Gamma[a_1(1260)^+ \longrightarrow \pi^+\gamma] = 640 \pm 246$ keV	[22]
	$\longrightarrow b_1(1235)^+ + (Z, A)$ $\hookrightarrow \omega\pi^+$	$\Gamma[b_1(1235)^+ \longrightarrow \pi^+\gamma] = 236 \pm 60$ keV	[23]
	$K^- + (Z, A) \longrightarrow K^*(890)^- + (Z, A)$ (p_{K^-} = 156 GeV) $\hookrightarrow K^0_S\pi^-$	$\Gamma[K^*(890)^- \longrightarrow K^-\gamma] = 62 \pm 12$ keV	[24]
Fermilab	$K^0_L + (Z, A) \longrightarrow K^*(896)^0 + (Z, A)$ (p_{K^0} = 60–200 GeV) $\hookrightarrow K^0_S\pi^0$	$\Gamma[K^*(896)^0 \longrightarrow K^0\gamma] = 116.5 \pm 9.9$ keV	[25]
	$\longrightarrow K^*(1430)^0 + (Z, A)$ $\hookrightarrow K^0_S\pi^0$	$\Gamma[K^*(1430)^0 \longrightarrow K^0\gamma] < 84$ keV at a 90% C.L.	[26]
CERN	$\pi^- + (Z, A) \longrightarrow \rho(770)^- + (Z, A)$ (p_{π^-} = 200 GeV) $\hookrightarrow \pi^-\pi^0$	$\Gamma[\rho(770)^- \longrightarrow \pi^-\gamma] = 81 \pm 4 \pm 4$ keV	[27]
SIGMA (IHEP)	$\pi^- + (Z, A) \longrightarrow [\pi^-\gamma] + (Z, A)$ (p_{π^-} = 40 GeV) Compton $\gamma\pi$ scattering; measurement of the magnetic and electric polarizabilities of the pion (β_π and α_π, respectively)	$\beta_\pi = (-7.1 \pm 2.8 \pm 1.8) \times 10^{-43}$ cm^3 $\alpha_\pi + \beta_\pi = (1.4 \pm 3.1 \pm 2.5) \times 10^{-43}$ cm^3	[28]
	$\pi^- + (Z, A) \longrightarrow [\pi^-\pi^0] + (Z, A)$	Investigation of the chiral anomaly $F(\gamma \longrightarrow 3\pi) = 12.9 \pm 0.9 \pm 0.5$ GeV^{-3}	[29]
CERN	$\Lambda + (Z, A) \longrightarrow \Sigma^0 + (Z, A)$ ($\langle p_\Lambda \rangle$ = 15 GeV)	$\Gamma[\Sigma^0 \longrightarrow \Lambda\gamma] = 7.6^{+2.0}_{-1.3}$ keV	[30]
Fermilab	$\Lambda + (Z, A) \longrightarrow \Sigma^0 + (Z, A)$ ($\langle p_\Lambda \rangle$ = 200 GeV)	$\Gamma[\Sigma^0 \longrightarrow \Lambda\gamma] = 8.6 \pm 0.6 \pm 0.8$ keV	[31]

Table 5. Data on the Coulomb production of the $a_2(1320)^-$ meson in the reaction $\pi^- + Z \longrightarrow a_2(1320)^- + Z$, $a_2(1320)^- \longrightarrow \rho^0\pi^- \longrightarrow \pi^+\pi^-\pi^-$ for three targets (carbon, copper, and lead)

	Target nucleus		
	C	Cu	Pb
Number of events of the coherent reaction (39)	2760523	1997972	549092
σ_0', mb/GeV [see (41)]	27.2	626	4870
Measured number of events under the resonance peak in Figs. 12*c*, 13, and 14 that corresponds to the decays $a_2(1320)^- \longrightarrow \rho^0\pi^- \longrightarrow \pi^+\pi^-\pi^-$	1587 ± 480	5170 ± 590	2945 ± 400
ε(subtr.) Monte Carlo	0.70	0.63	0.49
($L\varepsilon$), event/(mb/nucleus)	881558	149302	17831
$\Gamma[a_2(1320)^- \longrightarrow \pi^-\gamma]$, keV	304 ± 137	253 ± 49	211 ± 43

Note: The averaged value is $\Gamma[a_2(1320)^- \longrightarrow \pi^-\gamma] = 233 \pm 31(\text{stat.}) \pm 47(\text{syst.})$ keV.

severely reduced by the trigger conditions of the experiment. Despite these limitations, new results on the radiative decays of some hadrons were obtained in the SELEX experiment. We discuss these results below.

4.2. Investigation of the Coherent Reaction $\pi^- + (Z, A) \longrightarrow [\pi^-\pi^-\pi^+] + (Z, A)$

The first results on particle production in the Coulomb field of nuclei were obtained in studying the coherent three-pion-production reaction

$$\pi^- \longrightarrow (Z, A) \longrightarrow [\pi^-\pi^-\pi^+] + (Z, A) \qquad (39)$$

on carbon, copper, and lead nuclei that was induced by 600-GeV primary π^- mesons. Events selected with the aid of the so-called exclusive trigger that required the presence of three particles in the final state were used to isolate reaction (39). Obvious kinematical selection criteria—such as the requirement that the sought events be quasielastic (that is, the sum of the momenta of all three secondaries could deviate from the primary pion momentum by no more than 17.5 GeV); the identification of a primary π^- meson by means of a transition-radiation beam detector; and the isolation of the interaction vertex in the region of a carbon, a copper, or a lead target—were invoked in processing these events. Table 5 displays the statistics of events of reaction (39) that were selected according to relevant criteria.

The details of a further data processing will be described by considering the example of the coherent reaction on a copper nucleus,

$$\pi^- + \text{Cu} \longrightarrow [\pi^-\pi^-\pi^+] + \text{Cu}. \qquad (40)$$

For the 3π system, Fig. 12*a* shows the squared-transverse-momentum (p_T^2) distribution of events of reaction (40). This distribution can be fitted to two exponentials, one with the slope parameter of $b_1 = 179.4 \pm 0.6$ GeV^{-2}, which is peculiar to diffractive processes on a copper nucleus, and the other with a slope parameter $b_2 \geq 1500$ GeV^{-2}, which is in accord with the estimates for the Coulomb production reaction (with allowance for the resolution in p_T^2). In order to isolate the Coulomb production of the 3π state, it is necessary to subtract the diffractive background. Two regions of the transverse momentum squared—the region $p_T^2 < 0.001$ GeV^2 (region 1), where Coulomb production processes contribute significantly, and the region 0.002 GeV^2 $< p_T^2 <$ 0.0035 GeV^2 (region 2), which is dominated by diffractive processes—are used for this purpose.

It can be seen from Fig. 12*b* that, in either region, the effective-mass spectrum of the 3π system seems to be due to the diffractive production of a_1 mesons ($J^P = 1^+$). If, however, the diffractive background is subtracted (below, this will be considered in greater detail), the resulting mass spectrum $M(3\pi)$ will clearly show a peak at $M = 1304 \pm 5$ MeV, which has a width of $\Gamma = 121 \pm 20$ MeV and which is associated with the Coulomb production of $a_2(1320)^-$ mesons (Fig. 12*c*). It should be noted that the diffractive production of the $a_2(1320)^-$ meson, which has a spin–parity of $J^P = 2^+$, is forbidden by the selection rule in quantum numbers for diffractive processes (Gribov–Morrison rule, according to which a primary π^- meson with a spin–parity of $J^P = 0^-$ can diffractively produce $J^P = 0^-, 1^+, 2^-$, etc., states). The Coulomb production of the $a_2(1320)^-$ meson was confirmed by data from a dedicated processing that involved partitioning the transverse-momentum region 1 ($p_T^2 < 0.001$ GeV^2) into five equal subregions, with a diffractive-background subtraction being performed independently in each. What was thus obtained for the p_T^2 dependence of $a_2(1320)^-$ production complies well

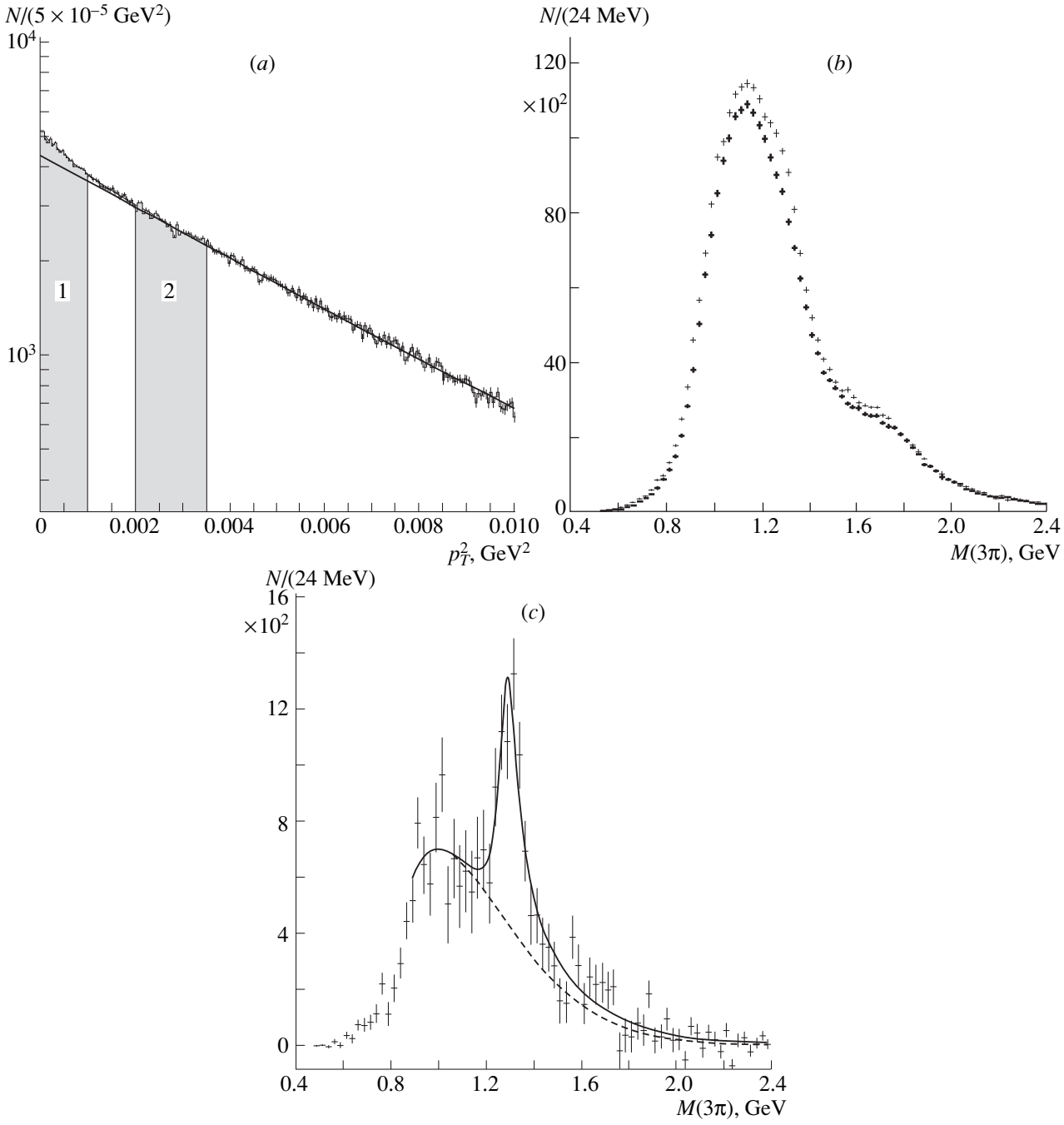

Fig. 12. SELEX data on the reaction $\pi^- + \mathrm{Cu} \longrightarrow [\pi^-\pi^-\pi^+] + \mathrm{Cu}$ at $E_{\pi^-} \simeq 600$ GeV: (*a*) p_T^2 distribution of events of this reaction (histogram) and diffractive coherent peak due to Pomeron exchange (solid curve) [region 1 ($p_T^2 < 0.001$ GeV^2) and region 2 (0.002 GeV$^2 < p_T^2 < 0.0035$ GeV^2) shown in the figure are used, respectively, to isolate the Coulomb process and to subtract the diffractive background; see main body of the text]; (*b*) effective-mass spectrum of the 3π system from this reaction for (light symbols) region 1 and (heavy symbols) region 2; and (*c*) effective-mass spectrum of the 3π system as obtained upon performing the subtraction $M(3\pi)_1 - aM(3\pi)_2$ with the normalization factor a chosen in such a way that the numbers of diffraction events in regions 1 and 2 coincide [this spectrum clearly demonstrates the Coulomb production of the $a_2(1320)^-$ meson].

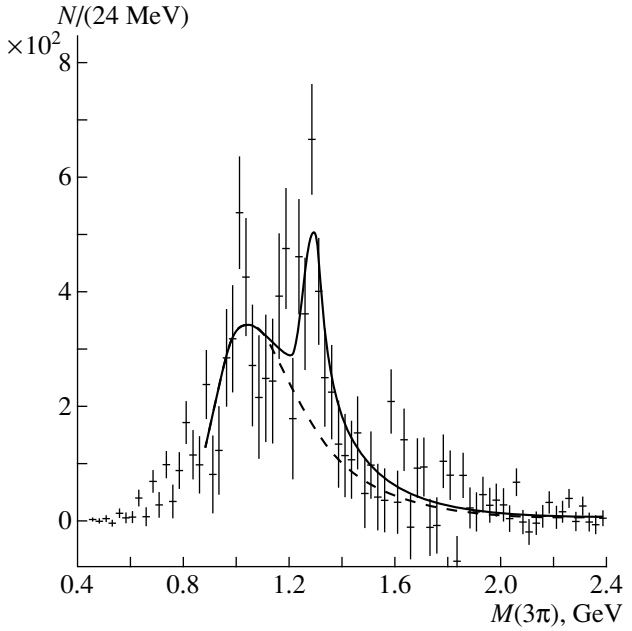

Fig. 13. Effective-mass spectrum of the three-pion system originating from the Coulomb reaction $\pi^- + C \longrightarrow [\pi^-\pi^-\pi^+] + C$ (the diffractive background has been subtracted). This spectrum clearly shows the Coulomb production of the $a_2(1320)^-$ meson.

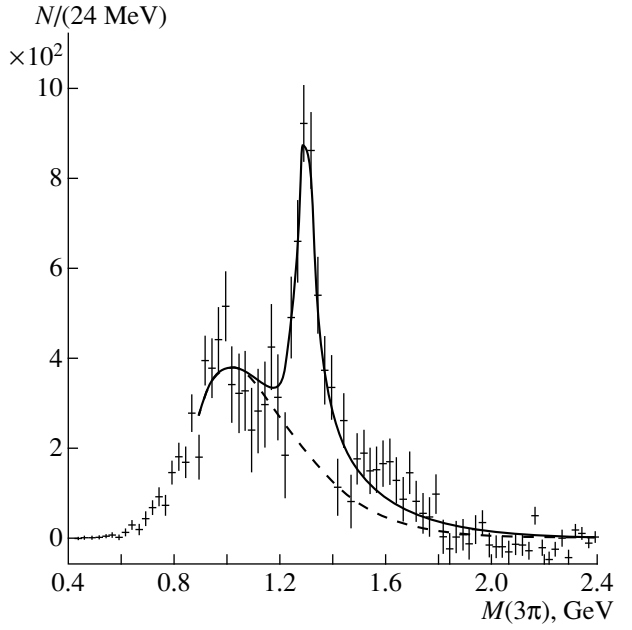

Fig. 14. As in Fig. 13, but for the Coulomb reaction π^- + Pb $\longrightarrow [\pi^-\pi^-\pi^+]$ + Pb.

with estimates for the Coulomb process (with allowance for the experimental resolution in p_T^2). Similar data were obtained for the coherent reaction (39) on carbon and lead nuclei, in which cases the Coulomb production of $a_2(1320)^-$ mesons was also recorded [see Figs. 13 and 14, which display only the mass spectra $M(3\pi)$ as obtained upon the subtraction of the diffractive background—these spectra are similar to those in Fig. 12*c*].

In order to determine the width with respect to the radiative decay $a_2(1320)^- \longrightarrow \pi^-\gamma$, it is necessary to measure the absolute value of the cross section for the Coulomb production of this meson,

$$\int\limits_{q^2_{\min}}^{0.001\ \mathrm{GeV}^2} [d\sigma(\pi^- + Z \longrightarrow a_2(1320)^- + Z)/dq^2]_{\mathrm{Coul}} dq^2,$$

and to compare it with the theoretical expression (29), which can be recast into the form

$$\int\limits_{q^2_{\min}}^{0.001\ \mathrm{GeV}^2} [d\sigma(\pi^- + Z \longrightarrow a_2(1320)^- + Z)/dq^2]_{\mathrm{Coul}} dq^2 \tag{41}$$

$$= \sigma_0' \Gamma[a_2(1320)^- \longrightarrow \pi^-\gamma].$$

For the coherent production of an a_2 meson at a primary pion energy of 600 GeV, the minimal value of the square of the momentum transfer is $q^2_{\min} = [(M^2_{a_2} - M^2_\pi)/2E_\pi]^2 \simeq 2 \times 10^{-6}$ GeV^2. In order to determine the quantity σ_0', we make use of the expression for the Coulomb production cross section [see equation (27) prior to going over to the small-width approximation $\Gamma \longrightarrow 0$. For the production of $a_2(1320)^-$ mesons, this expression can be represented as

$$\frac{d^2\sigma}{dq^2 dM^2} = 8\pi\alpha Z^2 (2J_{a_2} + 1)$$

$$\times \Gamma[a_2(1320)^- \longrightarrow \pi^-\gamma] \frac{M^2 M_{a_2}}{[M^2 - M^2_\pi]^3} \frac{q^2 - q^2_{\min}}{q^4}$$

$$\times \left|F_Z(q^2)\right|^2 \frac{1}{\pi} \frac{M_{a_2}\Gamma_{a_2} g_\gamma(M^2) g_{\rho\pi}(M^2)}{(M^2 - M^2_{a_2})^2 + M^2_{a_2}\Gamma^2_{a_2} g^2_{a_2}(M^2)} \tag{42}$$

$$= R(M, q^2)\Gamma[a_2(1320)^- \longrightarrow \pi^-\gamma]$$

with the dynamical factors

$$g_\gamma(M^2) = \left(\frac{k}{k_0}\right)^3 \frac{2k_0^2}{k^2 + k_0^2},$$

$$g_{\rho\pi}(M^2) = \left(\frac{p}{p_0}\right)^5 \frac{2p_0^2}{p^2 + p_0^2}. \tag{43}$$

Here, k and p are the γ and ρ momenta in the c.m. frame of the $\pi\gamma$ and $\rho\pi$ systems with mass M; k_0 and p_0 are the analogous momenta at the resonance point $M = M_{a_2}$; and $g_\gamma(M^2_{a_2}) = g_{\rho\pi}(M^2_{a_2}) = g_{a_2}(M^2_{a_2}) = 1$. We make use of

the approximation $g_{a_2}(M^2) = g_{\rho\pi}(M^2)$, since the process $a_2(1320) \longrightarrow \rho\pi$ represents the main channel of a_2 decay [Br($a_2 \longrightarrow \rho\pi$) = 0.70].

In the momentum-transfer region $q^2 < 0.001$ GeV^2, the effect of the nuclear form factors $F_Z(q^2)$ is very small. The corresponding corrections amount to 3% for copper nuclei and to 5% for lead nuclei. The values of σ_0' for the three nuclei under discussion (C, Cu, Pb) were determined by means of a numerical integration with respect to q^2 (from $q^2_{\min}$ to 0.001 GeV^2) and with respect to M over the mass region under study ($M <$ 2 GeV). The resulting values are presented in Table 5.

In order to obtain the absolute value of the cross section for the Coulomb production of an $a_2(1320)^-$ meson according to (41),

$$\int\limits_{q^2_{\min}}^{0.001\ \text{GeV}^2} [d\sigma(\pi^- + Z \longrightarrow a_2(1320)^- + Z)/dq^2]_{\text{Coul}} dq^2$$
$$= \int\limits_{0}^{0.001\ \text{GeV}^2} [d\sigma(\pi^- + Z \longrightarrow a_2(1320)^- + Z)/dp_T^2]_{\text{Coul}} dp_T^2,$$

the following steps of analysis must be implemented.[1)]

These steps include (i) a determination of the measured number of events at the resonance peak of the $a_2(1320)^-$ meson, $N'(a_2)$, in Figs. 12*c*, 13, and 14 [a fit of the experimental distribution of events with respect to the mass M to the relativistic formula (42) is used to do this; the corresponding values of $N'(a_2)$ are displayed in Table 5 for three mass spectra]; (ii) a determination of the efficiency associated with the subtraction of the diffractive background and with the p_T^2-resolution-induced reduction of the number of events in the p_T^2 interval under study [this efficiency, ε(subtr.) is found from a Monte Carlo simulation and is then used to determine the true number of events as $N(a_2) = N'(a_2)/\varepsilon(\text{subtr.})$]; and (iii) the absolute normalization of relevant cross sections.

Let us consider steps (ii) and (iii) in some detail. Figure 15 depicts schematically the p_T^2 distribution of events of reaction (39) and introduces the required notation.

Everywhere, the true number of events in a given p_T^2 interval and its apparent value biased because of p_T^2 resolution are denoted by N_i and N_i', respectively. We have

$$N_1 = \int\limits_0^{0.001} \left[\frac{dN}{dp_T^2}\right] dp_T^2 = N_{1\,\text{Coul}} + N_{1\,\text{diffr}},$$
$$N_1' = \int\limits_0^{0.001} \left[\frac{dN'}{dp_T^2}\right] dp_T^2 = N_{1\,\text{Coul}}' + N_{1\,\text{diffr}}', \qquad (44)$$
$$N_2' = \int\limits_{0.002}^{0.0035} \left[\frac{dN'}{dp_T^2}\right] dp_T^2 = N_{2\,\text{Coul}}' + N_{2\,\text{diffr}}',$$

where $N_{i\,\text{Coul}}'$ is the measured number of Coulomb events in the ith p_T^2 interval, while $N_{i\,\text{diffr}}'$ is the measured number of diffractive events in this interval. The interference of the Coulomb and diffraction amplitudes is ignored in this analysis: this interference is small because the former amplitude is real, whereas the latter is nearly a pure imaginary quantity. The limits of integration in p_T^2 are indicated in GeV^2.

The procedure for background subtraction employed a weight factor a determined by the parameters of momentum regions being considered and by the slope b_{diffr} of the coherent-diffraction cone in such a way as to ensure fulfillment of the condition $N_{1\,\text{diffr}}' - aN_{2\,\text{diffr}}' = 0$. We then have

$$N' = N_1' - aN_2' = (N_{1\,\text{Coul}}' - aN_{2\,\text{Coul}}') + \underbrace{(N_{1\,\text{diffr}}' - aN_{2\,\text{diffr}}')}_{=0} = N_{1\,\text{Coul}}' - aN_{2\,\text{Coul}}'. \qquad (45)$$

In order to find the true number of Coulomb events in region 1, it is necessary to determine the efficiency of the background-subtraction procedure, ε(subtr.) (this efficiency also takes into account the smearing of events because a finite resolution in p_T^2). We then have

$$N_{1\,\text{Coul}} = \frac{N_{1\,\text{Coul}}' - aN_{2\,\text{Coul}}'}{\varepsilon(\text{subtr.})}. \qquad (46)$$

The efficiency ε(subtr.) was determined via a Monte Carlo simulation, whose results are illustrated in Fig. 16. Here, we use the same notation as in Fig. 15, but the measured numbers of events, N and N', are replaced by the numbers of Monte Carlo–generated events, m and m'. From data in Fig. 16, the quantity ε(subtr.) is then determined as

$$\varepsilon(\text{subtr.}) = \frac{m_{1\,\text{Coul}}' - am_{2\,\text{Coul}}'}{m_{1\,\text{Coul}}}. \qquad (47)$$

For all three target-nucleus species being considered, the resulting values of ε(subtr.) are also presented in Table 5.

[1)] Recall that, according to (18b), we have $q^2 = p_T^2 + q^2_{\min} \simeq p_T^2$.

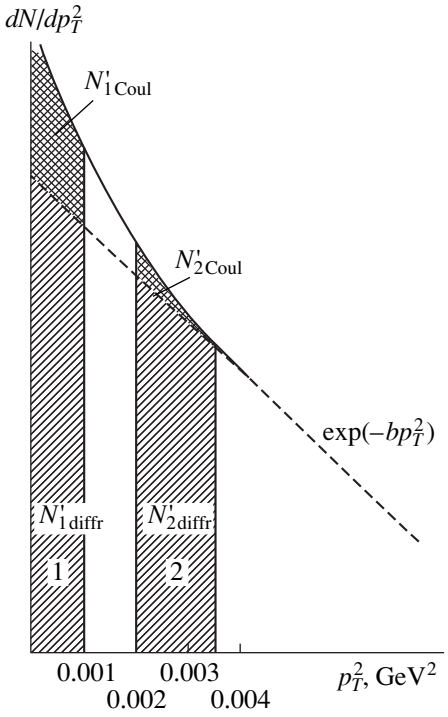

Fig. 15. Schematic p_T^2 distribution of events of reaction (39) and basic notation for the procedure of a diffractive-background subtraction (see main body of the text).

In order to determine the absolute values of the cross sections for the Coulomb reactions

$$\begin{aligned}\pi^- + Z &\longrightarrow a_2(1320)^- + Z,\\ &\hookrightarrow \rho^0\pi^- \longrightarrow \pi^+\pi^-\pi^-\end{aligned} \tag{48}$$

a normalization was performed by using the cross sections for the diffractive production of the 3π system in an $M(3\pi)$ region lying closely to the mass of the $a_2(1320)^-$ meson. Here, E272 data on the cross sections for the diffractive production of the 3π system at an incident-pion energy of 200 GeV [38] were used for an absolute normalization. Calculations within the simplest Reggeon model that were performed with allowance for Pomeron exchange revealed that the cross sections for diffractive processes occurring at 200 and 600 GeV may differ only slightly in magnitude. Eventually, we obtain

$$\begin{aligned}&\Gamma[a_2(1320)^- \longrightarrow \pi^-\gamma]\\ &= \frac{N_1[a_2(1320)^-]_{\mathrm{Coul}}}{\sigma'_0(L\varepsilon)\mathrm{Br}[a_2(1320)^- \longrightarrow \rho^0\pi^-]\varepsilon(\mathrm{subtr.})},\end{aligned} \tag{49}$$

where $(L\varepsilon)$ is the integrated luminosity of the experiment.

For the various target-nucleus species, the measured radiative widths are presented in Table 1 and Fig. 17.

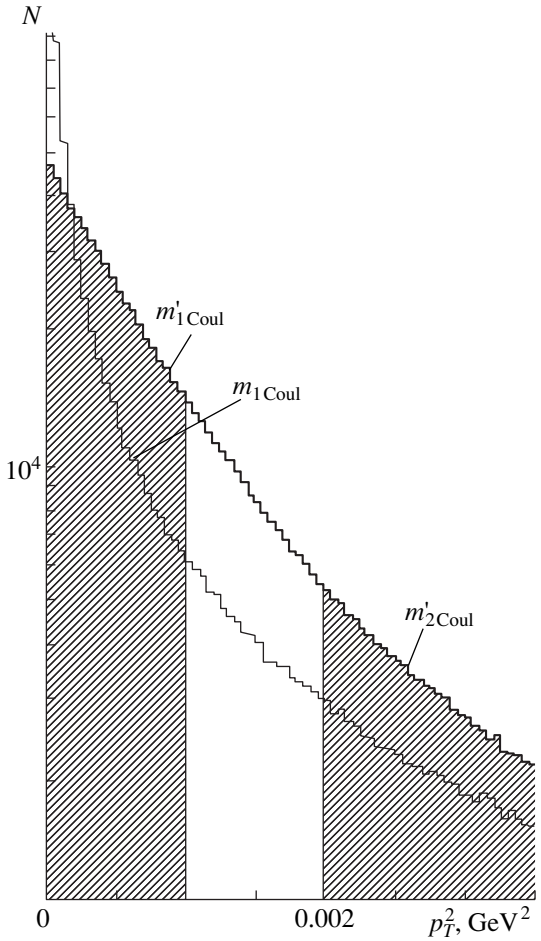

Fig. 16. Results of a Monte Carlo simulation for the Coulomb production of mesons in reaction (40) and notation for the procedure for determining ε(subtr.) (47).

The averaged value of this width according to the data for the three target-nucleus species is

$$\begin{aligned}&\Gamma[a_2(1320)^- \longrightarrow \pi^-\gamma]\\ &= 233 \pm 31(\mathrm{stat.}) \pm 47(\mathrm{syst.})\ \mathrm{keV}.\end{aligned} \tag{50}$$

This is a preliminary result [34], which is characterized by a comparatively large systematic error stemming primarily from the normalization procedure used. In a further analysis of data from the SELEX experiments, an attempt will be made to determine independently the cross sections for the diffractive processes at 600 MeV and to reduce substantially the systematic error.

The value in (50), which was obtained experimentally for the radiative width of the $a_2(1320)^-$ meson can be compared with the theoretical estimates from [39, 40], which are quoted in Table 6. At present, theoretical calculations of radiative decays are insufficiently accurate, but there is still the hope that the situation will be improved with a further development of lattice QCD.

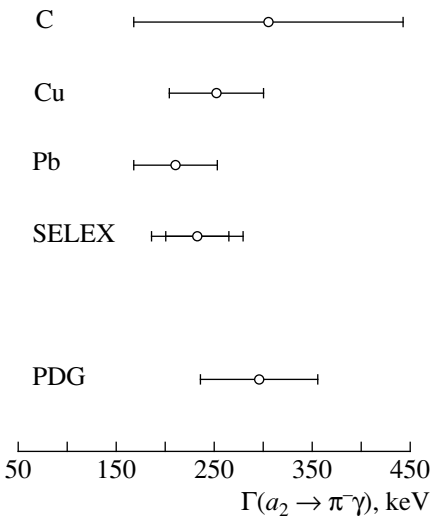

Fig. 17. SELEX results for the radiative width $\Gamma[a_2(1320)^- \longrightarrow \pi^-\gamma]$ of the $a_2(1320)^-$ meson along with previous results (see PDG [17] and Table 4). Both statistical and systematic errors are presented for the total SELEX result.

4.3. Data on the Coherent Reactions $\pi^- + (Z, A) \longrightarrow [\pi^+\pi^-\pi^-\pi^0] + (Z, A)$ *and* $\pi^- + (Z, A) \longrightarrow [\pi^+\pi^-\pi^-\eta] + (Z, A)$

Experiments at the SELEX facility also studied coherent reactions resulting in the production of three charged pions and involving additional photons in the final state ($\pi^0 \longrightarrow \gamma\gamma$, $\eta \longrightarrow \gamma\gamma$):

$$\pi^- + (Z, A) \longrightarrow [\pi^+\pi^-\pi^-\pi^0] + (Z, A), \quad \pi^0 \longrightarrow \gamma\gamma \tag{51}$$

$$\longrightarrow [\omega\pi^-] + (Z, A), \quad \omega \longrightarrow \pi^+\pi^-\pi^0 \tag{52}$$

$$\longrightarrow b_1(1235)^- + (Z, A), \quad b_1(1235)^- \longrightarrow \omega\pi^- \tag{53}$$

$$\longrightarrow [\eta\pi^-] + (Z, A), \quad \eta \longrightarrow \pi^+\pi^-\pi^0 \tag{54}$$

$$\longrightarrow a_2(1320)^- + (Z, A), \quad a_2(1320)^- \longrightarrow \eta\pi^- \tag{55}$$

$$\pi^- + (Z, A) \longrightarrow [\pi^+\pi^-\pi^-\eta] + (Z, A), \quad \eta \longrightarrow \gamma\gamma \tag{56}$$

$$\longrightarrow [f_1(1285)\pi^-] + (Z, A), \quad f_1(1285) \longrightarrow \pi^+\pi^-\eta \tag{57}$$

$$\longrightarrow [\eta'\pi^-] + (Z, A). \quad \eta' \longrightarrow \pi^+\pi^-\eta \tag{58}$$

Relevant data were also deduced from an analysis of events selected with the aid of the exclusive trigger. However, events with two photons recorded in the γ spectrometers of the apparatus were singled out in a further analysis. In addition, the quasielasticity condition was modified: it was required that the sum of the energies of the charged secondaries and two photons not differ from the primary energy by more than 50 GeV.

The results illustrating the isolation of reactions (51)–(58) are presented in Figs. 18–20.

The squared-transverse-momentum distributions of the 4π and $3\pi\eta$ systems were investigated for reactions (53) and (55). The spectra for these systems showed very distinct peaks due to the Coulomb production of $b_1(1235)^-$ and $a_2(1320)^-$ mesons (see Figs. 19 and 20). In the case of reactions (53) and (55), the background from strong-interaction-induced coherent processes is due to omega-meson exchanges since the diffractive production of these mesons is forbidden by selection rules in the quantum numbers J^P or in G parity. In view of this, the coherent background from strong interactions dies out fast with increasing energy. At 600 GeV, it is rather modest, and the Coulomb processes of meson production can be separated much more easily than in reaction (39), where we had to deal with a heavy diffractive background. The quality of data obtained for the Coulomb production of $a_2(1320)$ and $b_1(1235)$ mesons and accumulated statistics are higher than in the E272 experiment, which was performed at a lower energy [21, 23]. Presently, the data from SELEX are being further processed with the aim of performing an absolute normalization of the cross sections for the Coulomb reactions (53) and (55). These cross sections will be used to determine the radiative width $\Gamma[a_2(1320)^- \longrightarrow \pi^-\gamma])$ and $\Gamma[b_2(1235)^- \longrightarrow \pi^-\gamma])$. This determination would be of great interest, since the results of the E272 experiment deviate strongly from theoretical predictions (see the note under Table 6).

5. RADIATIVE DECAYS OF HYPERON RESONANCES AND INVESTIGATION OF HYPERON REACTIONS IN THE COULOMB FIELD OF NUCLEI

A detailed survey of data on hyperon decays was presented in [41]. In this section, we will briefly consider ${}^4[\underline{10}]_{SU(3)} \longrightarrow {}^2[\underline{8}]_{SU(3)} + \gamma$ radiative transitions for baryons belonging to the lowest $SU(3)$ decouplet and the lowest $SU(3)$ octet of baryons and present the first results obtained by studying the Coulomb production of hyperons in experiments at the SELEX facility. Let us consider some implications of $SU(3)$ symmetry for radiative decays of hyperons. Here, it is convenient to make use of the U-spin classification of particles, since the U-spin multiplets correspond to particles with identical electric charges, the U spin of the photon being equal to zero. Therefore, $B^* \longrightarrow B\gamma$ radiative baryon decays are allowed within $SU(3)$ symmetry only if B^*

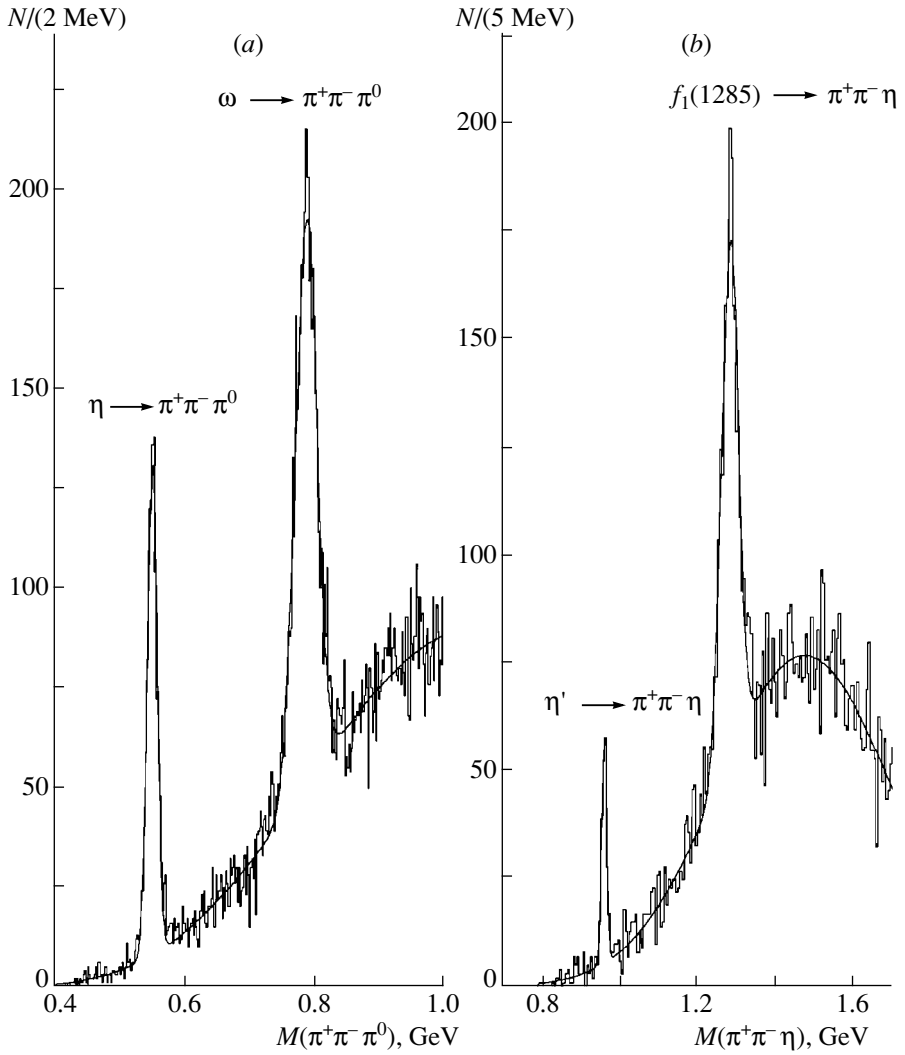

Fig. 18. Effective-mass spectrum of the $\pi^+\pi^-\pi^0$ system originating from reaction (51) [this spectrum shows manifestations of reactions (52) and (54) involving ω and η mesons]; (*b*) effective-mass spectrum of the $\pi^+\pi^-\eta$ system originating from reaction (56) (this spectrum shows manifestations of reactions (57) and (58) featuring $f_1(1285)$ and η' mesons). All spectra are presented for interactions in a copper target, and *N* represents the number of $\pi^+\pi^-\pi^0$ or $\pi^+\pi^-\eta$ combinations.

and *B* have identical *U*-spin values. Decays that do not meet this requirement are suppressed because they cannot occur without *SU*(3) violation.

Figure 21 displays the diagrams of the octet and of the decouplet for the ground baryon states belonging to the lowest *SU*(6) supermultiplet of baryons, $|\underline{56}, 0^+\rangle_{N=0}$. Also shown is the system of *U*-spin multiplets in which these baryons are grouped. It should be borne in mind that, in the baryon octet, there are two neutral baryons, Λ and Σ^0, that are not pure *U*-spin states. The *U*-spin multiplets contain their orthogonal superpositions

$$|u_0\rangle = \frac{1}{2}[\sqrt{3}|\Sigma^0\rangle - |\Lambda\rangle] \quad (59)$$

(a superposition representing the *U* singlet with zero *U* spin) and

Table 6. Theoretical predictions for $\Gamma[a_2(1320)^- \longrightarrow \pi^-\gamma]$

References	$\Gamma[a_2(1320)^- \longrightarrow \pi^-\gamma]$, keV	Comments
Babcock, Rosner [39]	348	The result is based on the vector-dominance model and on the width $\Gamma[a_2 \longrightarrow \rho\pi]$
Ishida, Yamada, Oda [40]*	235	The result is based on the covariant oscillator quark model

* The model presented in [40] satisfactorily describes available experimental data, with the exception of those on the decay $b_1(1235)^- \longrightarrow \pi^-\gamma$.

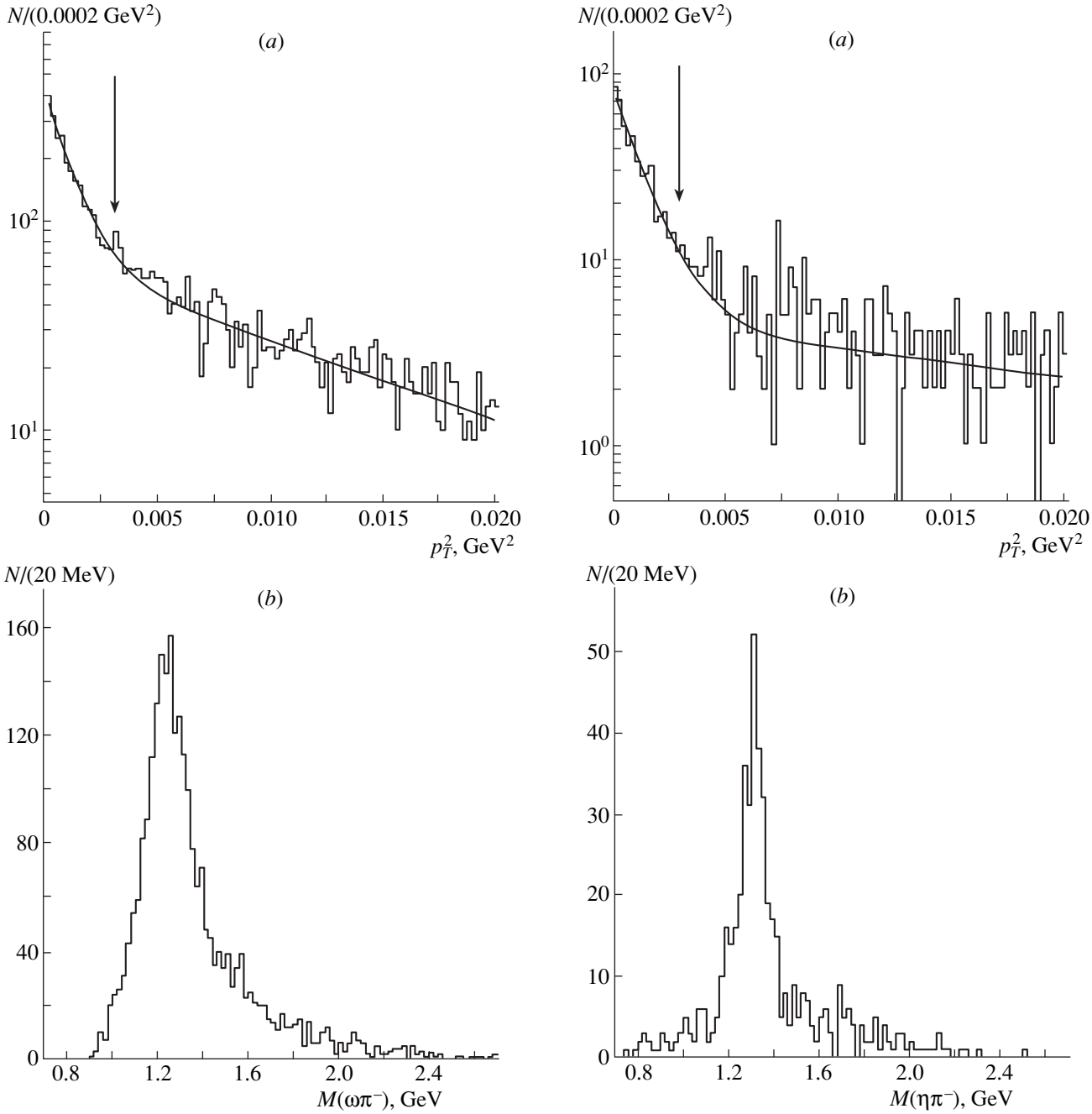

Fig. 19. SELEX data for the coherent reaction π^- + $(Z, A) \longrightarrow [\omega\pi^-] + (Z, A)$ at $E_{\pi^-} = 600$ GeV [summary data for all three targets (C, Cu, Pb)]: (*a*) p_T^2 distribution of events of reaction (52) (this distribution is dominated by the Coulomb production process; the background from the strong-interaction-induced coherent reaction due to omega-meson exchange is small; the arrow indicates the region used to isolate the Coulomb process) and (*b*) effective-mass spectrum of the $\omega\pi^-$ system for the Coulomb region $p_T^2 < 0.003$ GeV^2 [the Coulomb production process $b_1(1235)^- \longrightarrow \omega\pi^-$ is clearly seen in this spectrum].

Fig. 20. SELEX data for the coherent reaction π^- + $(Z, A) \longrightarrow [\eta\pi^-] + (Z, A)$ at $E_{\pi^-} = 600$ GeV [summary data for all three targets (C, Cu, Pb)]: (*a*) p_T^2 distribution of events of reaction (54) (this distribution is dominated by the Coulomb production process; the background from the strong-interaction-induced coherent reaction due to omega-meson exchange is small; the arrow indicates the region used to isolate the Coulomb process) and (*b*) effective-mass spectrum of the $\eta\pi^-$ system for the Coulomb region $p_T^2 < 0.003$ GeV^2 [the Coulomb production process $a_2(1320)^- \longrightarrow \eta\pi^-$ is clearly seen in this spectrum].

$$|u_1\rangle = \frac{1}{2}[|\Sigma^0\rangle + \sqrt{3}|\Lambda\rangle] \quad (60)$$

(a superposition belonging to the U triplet and corresponding to $U = 1$ and $U_z = 0$).

It can be seen from Fig. 21 that, among radiative baryon decays of the ${}^4[\underline{10}]_{SU(3)} \longrightarrow {}^2[\underline{8}]_{SU(3)} + \gamma$ type, the allowed processes are

$$\text{(a)} \quad (U = 1/2) \longrightarrow (U = 1/2) + \gamma$$
$$= \begin{cases} \Delta^+ \longrightarrow p + \gamma, \\ \Sigma^{*+} \longrightarrow \Sigma^+ + \gamma, \end{cases}$$

$$\text{(b)} \quad (U = 1) \longrightarrow (U = 1) + \gamma$$
$$= \begin{cases} \Delta^0 \longrightarrow n + \gamma \\ \Xi^{*0} \longrightarrow \Xi^0 + \gamma \\ \Sigma^{*0} \longrightarrow \frac{1}{2}[|\Sigma^0\rangle + \sqrt{3}|\Lambda\rangle] + \gamma. \end{cases}$$

At the same time, transitions violating the U spin are forbidden within $SU(3)$ symmetry:

$$(U = 3/2) \not\longrightarrow (U = 1/2) + \gamma = \begin{cases} \Sigma^{*-} \not\longrightarrow \Sigma^- + \gamma \\ \Xi^{*-} \not\longrightarrow \Xi^- + \gamma. \end{cases}$$

Radiative transitions of the type $B^*(J^P = 3/2^+) \longrightarrow B(J^P = 1/2^+) + \gamma$, which were considered above, are accompanied by the flip of the spin of one of the quarks and by the emission of a magnetic dipole ($M1$) or an electric quadrupole ($E2$) photon. Magnetic dipole transitions are dominant, the contribution of $E2$ amplitudes being very small [42–44]. The probability of a $B^* \longrightarrow B\gamma$ radiative decay (radiative width) is determined by the transition magnetic moment $\mu(B^*B)$ and is given by [44]

$$\Gamma(B^* \longrightarrow B\gamma) = \frac{1}{2}\underbrace{\left|\frac{\mu(B^*B)}{\mu_N}\right|^2 \frac{\alpha}{M_p^2}}_{\text{squared amplitude}} \times \underbrace{(P_\gamma)^3}_{\text{kinematical factor}}. \quad (61)$$

In the approximation of $SU(3)$ symmetry, the transition magnetic moments for ${}^4[\underline{10}]_{SU(3)} \longrightarrow {}^2[\underline{8}]_{SU(3)} + \gamma$ decays can be estimated as [45] (see also [41, 44])

$$\mu(\Delta^+ p) = \mu(\Delta^0 n) = -\mu(\Sigma^{*+}\Sigma^+)$$
$$= -\mu(\Xi^{*0}\Xi^0) = -2\mu(\Xi^{*0}\Sigma^0) = -\frac{2}{\sqrt{3}}\mu(\Xi^{*0}\Lambda), \quad (62a)$$

$$\mu(\Xi^{*-}\Sigma^-) = \mu(\Xi^{*-}\Xi^-) = 0. \quad (62b)$$

Let us now consider radiative decays that are forbidden within $SU(3)$ symmetry by the conservation of the U spin and discuss the mechanism of $SU(3)$ violation in these processes [42–44] by comparing the transitions

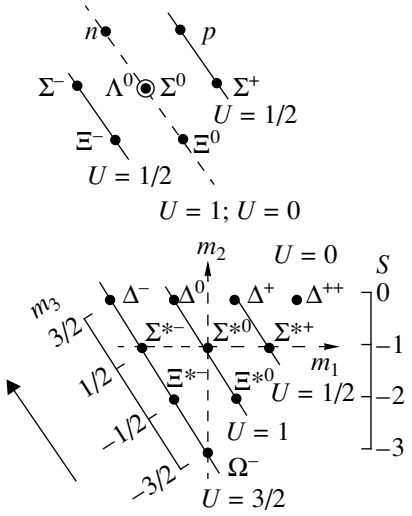

Fig. 21. Diagram of the $SU(3)$ octet and the $SU(3)$ decouplet of baryons and structure of the U-spin baryon multiplets. The following notation is used here: S is the strangeness, $m_1 = I_3$ is the third component of the isospin, $m_2 = Y = B + S$, B is the baryon charge, and $m_3 = U_3$ is the third component of the isospin. The octet of baryons includes the states $|u_0\rangle = |U = 0\rangle = \frac{1}{2}[\sqrt{3}|\Sigma^0\rangle - |\Lambda\rangle]$ and $|u_1\rangle = |U = 1,\ U_3 = 0\rangle = \frac{1}{2}[|\Sigma^0\rangle + \sqrt{3}|\Lambda\rangle]$.

$$\Sigma^*(1385)^+ \longrightarrow \Sigma^+ + \gamma, \quad (63)$$

$$\Xi^*(1530)^0 \longrightarrow \Xi^0 + \gamma \quad (64)$$

(allowed processes) and

$$\Sigma^*(1385)^- \longrightarrow \Sigma^- + \gamma, \quad (65)$$

$$\Xi^*(1530)^- \longrightarrow \Xi^- + \gamma \quad (66)$$

(processes forbidden by U-spin conservation).

Physically, the fact that processes (65) and (66) are forbidden by the above selection rule can be explained as follows. Let us first consider the decay processes (63) and (64). As was discussed above, these are magnetic dipole ($M2$) transitions proceeding via the flip of the spin of one of the quarks. For the $\Sigma^*(1385)^+$ and $\Xi^*(1530)^0$ hyperons, which consist of quarks of different charges and magnetic moments ($|uus\rangle$ and $|uss\rangle$), the photon magnetic field acting on the u and s quarks involved rotates them in opposite directions and may cause the flip of the spin of one of the quarks with respect to the total spin of the two others, whereby $SU(3)$-allowed radiative decays (63) and (64) will indeed occur. At the same time, $\Sigma^*(1385)^-$ and $\Xi^*(1530)^-$ hyperons are constituted by quarks of iden-

tical charges ($|dds\rangle$ and $|dss\rangle$). The magnetic field rotates their magnetic moments and spins in the same direction. If $\mu_d = \mu_s$ [exact $SU(3)$ symmetry], the s-quark (d-quark) spin is not flipped with respect to the total d-quark (s-quark) spin, so that the radiative decays (65) and (66) prove to be forbidden. If $SU(3)$ symmetry is violated because of the mass difference between the s and d quarks, their magnetic moments also become different ($\mu_d = -0.972\mu_N$ and $\mu_s = -0.613\mu_N$, see [17]). Therefore, spin-rotation angles in the photon magnetic field are different for these quarks, so that spin-flip radiation transitions may occur. Thus, we can see that, because of broken $SU(3)$ symmetry, the decay processes (65) and (66) are not strictly forbidden. However, the corresponding branching ratio (radiative width) are suppressed in relation to those for the allowed decays (63) and (64).

In [43, 44], the following estimates were obtained for this mechanism of $SU(3)$ violation:

$$P(\Sigma^-) = \left|\frac{\mu[\Sigma^*(1385)^-\Sigma^-]}{\mu[\Sigma^*(1385)^+\Sigma^+]}\right|^2 = \left|\frac{\mu[\Sigma^*(1385)^-\Sigma^-]}{\mu[\Delta(1232)^+ p]}\right|^2 = \frac{1}{9}\left(1-\frac{\mu_s}{\mu_d}\right)^2 = 0.015, \quad (67)$$

$$P(\Xi^-) = \left|\frac{\mu[\Xi^*(1530)^-\Xi^-]}{\mu[\Xi^*(1530)^0\Xi^0]}\right|^2 = \left|\frac{\mu[\Xi^*(1530)^-\Xi^-]}{\mu[\Delta(1232)^+ p]}\right|^2 = \frac{1}{9}\left(1-\frac{\mu_s}{\mu_d}\right)^2 = 0.015. \quad (68)$$

Measurements of the radiative widths with respect to decays (65) and (63) will make it possible to obtain very clean data on the properties of the $SU(3)$ symmetry of strong interactions and on the degree of its violation. Theoretical predictions for these radiative widths within various versions of quark models (for an overview, see [41]) and those that emerged from new calculations based on chiral QCD models [46–48] show a wide scatter. These predictions vary between 1 and 10 keV for the width with respect to the $SU(3)$-forbidden decay (65), but they constitute 100–300 keV for the $SU(3)$-allowed decay (63). In view of this, an experimental determination of the above widths from the investigation of the Coulomb reactions

$$\Sigma^- + Z \longrightarrow \Sigma^*(1385)^- + Z, \quad \Sigma^*(1385)^- \longrightarrow \Lambda\pi^- \quad (69)$$

$$\Sigma^+ + Z \longrightarrow \Sigma^*(1385)^+ + Z. \quad \Sigma^*(1385)^+ \longrightarrow \Lambda\pi^+ \quad (70)$$

is of great interest. The first preliminary data on the process (69) were obtained from experiments at the SELEX facility. Reaction (70) is still being studied.

Unfortunately, the experiments that studied the Coulomb production of $\Sigma^*(1385)$ hyperons had to be conducted concurrently with those that were performed within the main experimental program (see above); therefore, the scope of those measurements was severely limited. They could be carried out only with a lead target, because only downstream of that target was the decay gap available for recording the transition $\Lambda \longrightarrow p\pi^-$ in reactions (69) and (70). The length of the decay gap was only 50 cm, which corresponded to a 1.4% mean probability of Λ decay within this gap. The duration of the dedicated exposure of the lead target in a Σ^- beam did not exceed a few days.

The reaction

$$\Sigma^- + \mathrm{Pb} \longrightarrow [\Lambda\pi^-] + \mathrm{Pb}, \quad [\Lambda\pi^-] \longrightarrow p\pi^- \quad (71)$$

was studied to isolate the Coulomb process (69) on a lead target.

Events of reaction (71) were recorded with the aid of an exclusive trigger and were selected via a further kinematical analysis of events involving three charged particle in the final state, the positive particle being identified with the aid of a RICH SELEX detector as a proton. Moreover, it was required that a primary particle be identified as Σ^- hyperon in the transition-radiation beam detector, that the primary interaction occur in the lead-target region, and that a secondary proton and one of the negative pions satisfy the condition of isolation of $\Lambda \longrightarrow p\pi^-$ with the decay vertex occurring within the decay gap. Three charged secondaries were required to satisfy the quasielasticity condition (the sum of their momenta was allowed to deviate from the primary momentum by no more than 15.5 GeV).

The squared-transverse-momentum distribution of events where the $\Lambda\pi^-$ system is produced in reaction (71) shows a peak that is characterized by a slope parameter b not less than 800 GeV^{-2} and which suggests a significant contribution of the Coulomb production mechanism. As before, the region $0 < p_T^2 < 0.001$ GeV^2 was used to isolate the Coulomb process.

For this region, Fig. 22 shows the effective-mass spectrum $M(\Lambda\pi^-)$ for reaction (71). This spectrum exhibits a distinct peak at $M = 1.322$ GeV, which corresponds to the decays of Ξ^- hyperons of the primary beam in the lead-target region. Events of the decay $\Xi^- \longrightarrow \Lambda\pi^-$ were used to calibrate the apparatus and to determine its transverse-momentum and mass resolutions. After that, an analysis was performed for the region $M(\Lambda\pi^-) > 1.35$ GeV, which was fitted in terms of an expression of the type (27) for Coulomb particle production with allowance for the possible contribution of the resonance peak that is due to the decay $\Sigma^*(1385)^- \longrightarrow \Lambda\pi^-$.

On this basis, the number of events under the peak was determined to be

$$N[\Sigma^*(1385)^- \longrightarrow \Lambda\pi^-] = 26 \pm 20,$$
$$\hookrightarrow p\pi^-$$

or, more precisely,

$$N(\Sigma^{*-}) = N[\Sigma^*(1385)^- \longrightarrow \Lambda\pi^-] < 66 \quad (72)$$
$$\hookrightarrow p\pi^-$$

(at a 95% C.L.).

These data were used to set an upper limit on the cross section for the Coulomb production of $\Sigma^*(1385)^-$ hyperons in reaction (69). With the aid of (2) and (29), the result can be represented as

$$\sigma_0\Gamma[\Sigma^*(1385)^- \longrightarrow \Sigma^-\gamma] = \frac{N(\Sigma^{*-})}{(L\varepsilon)\cdot \mathrm{Br}((\Sigma^{*-} \longrightarrow \Lambda\pi^-)\times \mathrm{Br}(\Lambda \longrightarrow p\pi^-))}, \quad (73)$$

where σ_0 is a theoretical factor [see equations (2), (29), and (30)], and L is the luminosity of a given experiment—as before, it was determined from a normalization to the cross section for the diffractive process $\pi^- + \mathrm{Pb} \longrightarrow [3\pi]^- + \mathrm{Pb}$ by using E272 data from [38] and by taking into account the ratio of $\Sigma^-/\pi^- = 1.0$ in a beam.[2)] The efficiency is $\varepsilon = \varepsilon(\Lambda \text{ decay}) \times \varepsilon(p_T^2 < 0.001\ \mathrm{GeV}^2) \times \varepsilon(\text{additional selections}) = 0.014 \times 0.68 \times 0.93 = 0.0089$.

Eventually, the radiative width with respect to the $SU(3)$-forbidden decay (65) can be constrained from above as

$$\Gamma[\Sigma^*(1385)^- \longrightarrow \Sigma^-\gamma] < 7 \text{ GeV (at a 95\% C.L.)}. \quad (74)$$

Here, we have taken into account a systematic uncertainty of 15%, which is associated primarily with the procedure of absolute normalization. It is reasonable to compare this result with theoretical predictions lying between 2 and 10 keV (see compendium of these predictions in [48]) and with the experimental bound $\Gamma(\Sigma^{*-} \longrightarrow \Sigma^-\gamma) < 24$ keV obtained in [49] at a 95% C.L.

Data have also been obtained for the coherent reaction $\Sigma^- + \mathrm{Pb} \longrightarrow [\Lambda\pi^-] + \mathrm{Pb}$ in the region $M(\Lambda\pi^-) > 1.35$ GeV. These data yield

$$\sigma[\Sigma^- + \mathrm{Pb} \longrightarrow [\Lambda\pi^-] + \mathrm{Pb}]_{\mathrm{Coul}} = 4.0 \pm 0.5 \text{ mb/(Pb nucleus)},$$
$$\sigma[\Sigma^- + \mathrm{Pb} \longrightarrow [\Lambda\pi^-] + \mathrm{Pb}]_{\text{coh. strong}} = 20.0 \pm 0.6 \text{ mb/(Pb nucleus)}. \quad (75)$$

[2)]The luminosity L also includes the efficiency of the trigger used; that is, it is an effective luminosity.

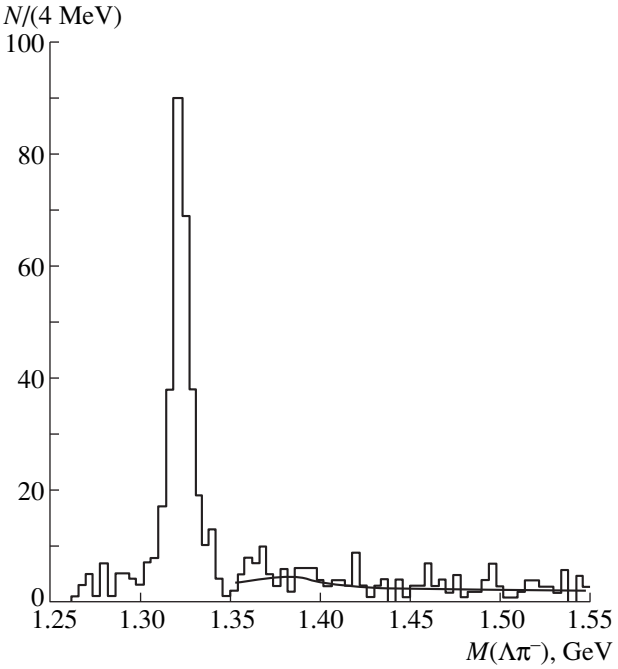

Fig. 22. Effective-mass spectrum of the $\Lambda\pi^-$ system originating from the reaction $\Sigma^- + \mathrm{Pb} \longrightarrow [\Lambda\pi^-] + \mathrm{Pb}$ (71) in the region $p_T^2 < 0.001\ \mathrm{GeV}^2$. The peak at $M = 1.322$ GeV corresponds to the decay $\Xi^- \longrightarrow \Lambda\pi^-$ in the hyperon beam within the lead target. This peak is used for the calibration of the apparatus. The curve represents an estimated upper limit on the Coulomb production of the $\Sigma^*(1385)^-$ hyperon. The number of events under the $\Sigma^*(1385)^-$ peak is 26 ± 20 (at a 95% C.L., this corresponds to $N[\Sigma^*(1385)^- \longrightarrow \Lambda\pi^-] <$ 66 events).

The ratio of these cross sections is 0.20 ± 0.03.

6. DIFFRACTIVE AND ELECTROMAGNETIC MECHANISMS OF BARYON PRODUCTION IN COHERENT HADRON REACTIONS ON NUCLEI AND SEARCHES FOR EXOTIC HADRONS

Coherent processes on nuclei open new possibilities for seeking exotic hadrons and, in particular, pentaquark baryons with hidden strangeness. The possible role of the Coulomb mechanism for these processes was discussed in the Introduction (see also [3–5]). At the same time, it was repeatedly indicated in the literature (see the review articles [50, 51] and references therein) that, at high energies, reactions of diffractive particle production are very promising for seeking this new type of hadronic matter. This is due to the multigluon structure of Pomeron exchange and to some phenomenological features of diffractive reactions. Owing to the fact that single-particle and multiparticle objects are absorbed differently in nuclei (see, for example, [50–52]), coherent processes provide a very efficient

tool for isolating resonances against the multiparticle nonresonance background.

Investigations of some diffractive processes in a 70-GeV proton beam from the IHEP accelerator are being presently performed at the SPHINX facility, which represents a wide-aperture spectrometer equipped with proportional and drift chambers and with scintillator hodoscopes. The apparatus also includes a multichannel γ spectrometer with shower Cherenkov counters made of lead glass. Charged secondaries are identified a in RICH-type Cherenkov spectrometer, the rings of Cherenkov light being recorded in a photomatrix of small phototubes, and in two multichannel gas threshold Cherenkov counters. The structure of the SPHINX facility and the procedures for measurements, for data analysis, and for the isolation of diffractive processes were described elsewhere [53–57].

Experiments at the SPHINX facility were aimed at separating coherent processes that proceed on carbon nuclei and which are characterized by a large slope of the diffraction cone in the transverse-momentum-square distribution of events [$dN/dp_T^2 \simeq \text{const} \times \exp(-bp_T^2)$, where $b \sim 10A^{2/3} \geq 50$ GeV^{-2} for the carbon nucleus]. A lenient or a stringent cut on p_T^2 ($p_T^2 < 0.075$–0.1 GeV^2 or $p_T^2 < 0.02$ GeV^2, respectively) was imposed.

In the former case, the noncoherent background in the mass spectrum of the system being studied may amount to 30–40% of all events.

In the latter case, the noncoherent background in the mass spectrum is within 8–10%, but the number of coherent events is somewhat reduced.

The most interesting results were obtained in studying the coherent reactions [53, 55–57]

$$p + \mathrm{C} \longrightarrow [\Sigma(1385)^0 K^+] + \mathrm{C}, \quad \Sigma(1385)^0 \hookrightarrow \Lambda\pi^0 \tag{76}$$

$$p + \mathrm{C} \longrightarrow [\Sigma^0 K^+] + \mathrm{C}. \quad \Sigma^0 \hookrightarrow \Lambda\gamma \tag{77}$$

Let us consider in greater detail the data on reaction (77).

Figure 23 shows the total effective-mass spectrum $M(\Sigma^0 K^+)$ isolated for this coherent reaction by the lenient cut on the transverse momenta ($p_T^2 < 0.1$ GeV^2). This spectrum was obtained by analyzing data both from old exposures at the SPHINX facility and from a new exposure that was performed with a partly upgraded apparatus, which made it possible to separate more efficiently processes featuring Λ and Σ^0 hyperons [56, 57]. The total spectrum in question shows a structure at $M \sim 1800$ MeV and a distinct peak $X(2000)$ with the parameters

$$M = 1996 \pm 7 \text{ MeV}, \quad \Gamma = 99 \pm 21 \text{ MeV}. \tag{78}$$

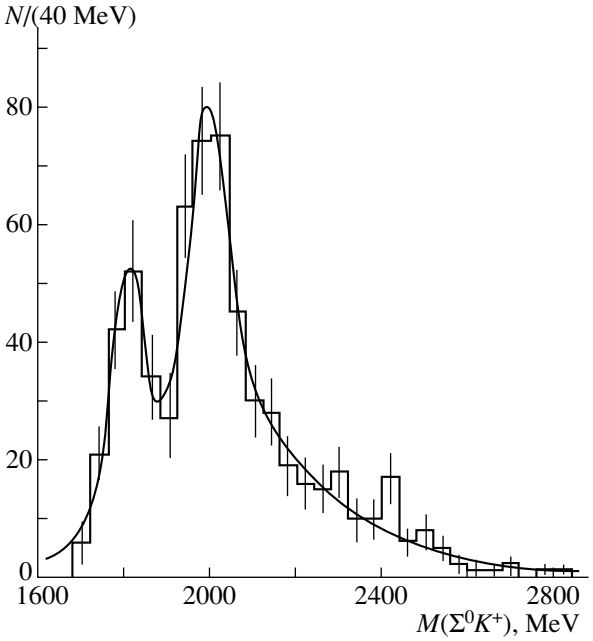

Fig. 23. Summary effective-mass spectrum of the $\Sigma^0 K^+$ system originating from the reaction $p + \mathrm{C} \longrightarrow [\Sigma^0 K^+] + \mathrm{C}$ (77) ($p_T^2 < 0.1$ GeV^2) as obtained in the first exposure with the SPHINX facility [55] and in the exposure with a partially upgraded facility [56].

It should be emphasized that data from old exposures comply well with data from the new exposure, although SPHINX was modified quite significantly as the result of its upgrade [56]. As was shown in [55], the $X(2000)$ state decays predominantly through channels involving the emission of strange particles and appears to be a serious candidate for a exotic baryon with hidden strangeness.

The results from the new exposure [56] made it possible to study the effect of the more stringent transverse-momentum cut on the mass spectrum $M(\Sigma^0 K^+)$ in greater detail. As was shown previously, the use of the more stringent p_T^2 cut affects the parameters of the $X(2000)$ peak only slightly. This peak is highly distinct even without any cuts on p_T^2. Quite surprisingly, it was found that p_T^2 cuts have a profound effect on the near-threshold structure at $M \sim 1800$ MeV. As can be seen from Fig. 24, this structure is observed only for $p_T^2 < 0.01$–0.02 GeV^2, where it shows up clearly and has the parameters

$$M = 1812 \pm 7 \text{ MeV}, \quad \Gamma = 56 \pm 16 \text{ MeV}. \tag{79}$$

Such unusual properties of the $X(1810)$ state have yet to be understood conclusively; it seems that a fur-

ther study on the basis of vaster data sets and under various experimental conditions is required.

Data suggesting the production of an unusual baryon structure at very low transverse momenta ($p_T^2 < 0.02$ GeV^2) were also obtained for the coherent reaction (76), where the mass spectrum $M(\Sigma(1385)^0K^+)$ shows a narrow state $X(2050) \longrightarrow \Sigma(1385)^0K^+$, which decays predominantly, in just the same way as $X(2000)$ does, via the emission of strange particles and which also appears to be candidate for an exotic baryon with hidden strangeness [55]. It should be noted, however, that evidence for the existence of $X(2050)$ has been obtained so far only in the old exposures of the SPHINX facility. New data on reaction (76) from experiments at the upgraded apparatus are now being processed.

It was indicated above that, because of a significant coupling between photons and ϕ mesons (vector-meson dominance), Coulomb particle production may provide a natural mechanism for the excitation of hadronic states featuring an additional quark–antiquark $s\bar{s}$ pair (that is, of cryptoexotic hadrons with hidden strangeness). Moreover, baryons with isospins $T = 1/2$ and $3/2$ can be generated in Coulomb processes induced by primary protons; at the same time, only $T = 1/2$ baryons are formed in diffractive processes. Thus, conditions for the observation of some exotic states may be especially favorable in Coulomb processes. In view of this, the hypothesis was put forth that the $X(1810)$ and $X(2050)$ states, which are separated only by the stringent transverse-momentum cut ($p_T^2 < 0.02$ GeV^2), are produced in Coulomb excitation processes [5] rather than in diffractive reactions. Of course, measurements with a carbon target, which has a modest value of Z, cannot provide the best conditions for the isolation of Coulomb reactions. Nonetheless, calculations presented below reveal that the explanation of data from the SPHINX experiment in these terms is quite feasible.

In order to estimate the expected cross section for the Coulomb production of $X(1810)^+$ baryons in the coherent reaction,

$$p + \mathrm{C} \longrightarrow X(1810)^+ + \mathrm{C}, \tag{80}$$

we make use of the expressions describing the cross sections for the Coulomb processes (29) and (30). The resulting estimate in the region $p_T^2 < 0.01$ GeV^2 is

$$\begin{aligned}\sigma[p + \mathrm{C} \longrightarrow X(1810)^+ + \mathrm{C}]_{\mathrm{Coul}} &= (2J_X + 1)\\ \times\Gamma[X(1810)^+ \longrightarrow p\gamma] &\times 1.2 \times 10^{-30}\ \mathrm{cm}^2/(\mathrm{C\ nucleus})\\ \geq \Gamma[X(1810)^+ \longrightarrow p\gamma] &\times 2.4 \times 10^{-30}\ \mathrm{cm}^2/(\mathrm{C\ nucleus}),\end{aligned} \tag{81}$$

where $J_X \geq 1/2$ is the spin of the $X(1810)$ baryon and where the width $\Gamma[X(1810)^+ \longrightarrow p\gamma]$ is measured in MeV (for more details, see [5]).

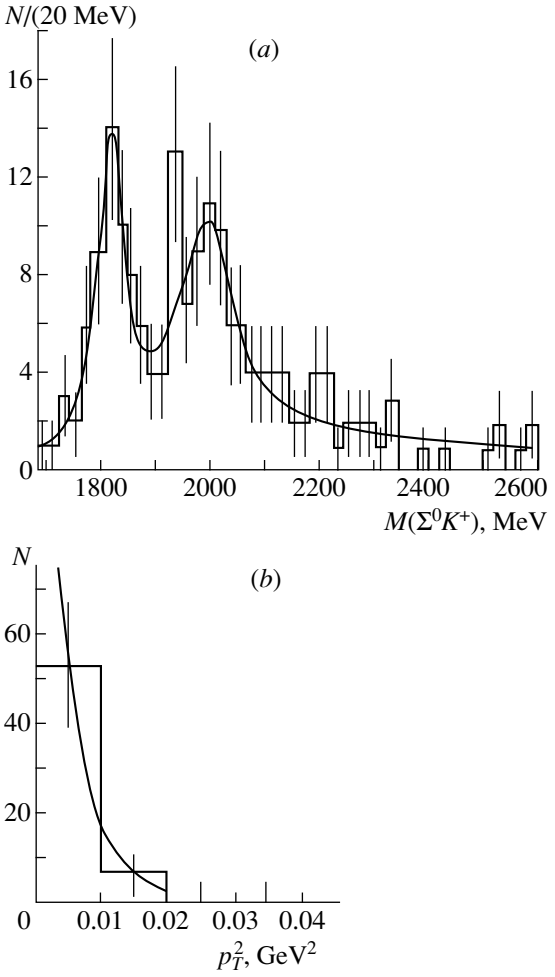

Fig. 24. Investigation of the $X(1810)$ structure in the effective-mass spectrum of the Σ^0K^+ system originating from the reaction $p + \mathrm{C} \longrightarrow [\Sigma^0K^+] + \mathrm{C}$ (77): (*a*) effective-mass spectrum for $p_T^2 < 0.01$ GeV^2 and (*b*) p_T^2 dependence for the formation of the $X(1810)^+$ structure.

In the region of low p_T^2, the experimental value of the total cross section for the Coulomb process (80) is

$$\begin{aligned}\sigma[p + \mathrm{C} \longrightarrow X(1810)^+ + \mathrm{C}]_{p_T^2 < 0.01\ \mathrm{GeV}^2}&\\ \times \mathrm{Br}[X(1810)^+ \longrightarrow \Sigma^0K^+]&\\ = (2.1 \pm 0.4) \times 10^{-31}&\mathrm{cm}^2/(\mathrm{C\ nucleus}).\end{aligned} \tag{82}$$

Since $\mathrm{Br}[X(I = 1/2)^+ \longrightarrow \Sigma^0K^+] = \frac{1}{3}\mathrm{Br}[X(I = 1/2)^+ \longrightarrow (\Sigma K)^+]$, we have, even if $X(1810) \longrightarrow \Sigma K$ decays are dominant,

$$\begin{aligned}\sigma[p + \mathrm{C} \longrightarrow X(1810)^+ + \mathrm{C}]_{p_T^2 < 0.01\ \mathrm{GeV}^2}&\\ \geq (6.3 \pm 1.3) \times 10^{-31}\ &\mathrm{cm}^2/(\mathrm{C\ nucleus}),\end{aligned} \tag{83}$$

whence it follows that, if the radiative width of $X(1810)$ is about 0.1–0.3 MeV, the cross-section estimate in (81) is in reasonable agreement with the experimental result displayed in (82). The above radiative width with respect to the decay $X(1810)^+ \longrightarrow p\gamma$ seems quite feasible. For the sake of comparison, we note that the radiative width of the Δ^+ isobar is $\Gamma(\Delta^+ \longrightarrow p\gamma) = 0.7$ MeV. The radiative width is determined by the decay amplitude A and by the kinematical factor; that is, $\Gamma = |A|^2 P_\gamma^{2l+1}$, where P_γ is the photon energy in the rest frame of the decaying baryon and l is the orbital angular momentum. The kinematical factor for the $X(1810)$ state can exceed that for Δ^+ (because of the larger mass) by more than an order of magnitude. At the same time, it should be recalled that, for states with hidden strangeness, the radiative-transition amplitude due to the process $(qqqs\bar{s}) \longrightarrow (qqq) + \phi_{\text{virt}} \longrightarrow (qqq) + \gamma(\text{VDM})$ can be sizable. Thus, SPHINX data on the new state $X(1810)$ are compatible with the assumption that the production of this hadron is due to the Coulomb mechanism. A similar conclusion can be drawn for the possible state $X(2050)$.

It is interesting to compare these data with the results obtained by directly studying the photoproduction reaction $\gamma + N \longrightarrow Y + K$, which are still rather scanty. Nonetheless, it can be stated that $X(1810)$ has not been observed so far in photoproduction reactions, although there is possibly a peak shifted toward greater values of mass by 20–40 MeV [58]. There is some evidence for a possible manifestation of $X(2050)$ in photoproduction reactions [59]. Of course, new detailed investigations of hyperon and kaon photoproduction are required here; these are expected to be performed in the near future at the CEBAF accelerator (see [59]).

7. SEARCHES FOR THE COULOMB PRODUCTION OF THE $\Delta(1232)^+$ ISOBAR IN EXPERIMENTS AT THE SPHINX FACILITY

We attempted to obtain additional information about the possibility of isolating the Coulomb production of baryons in pC interactions at the SPHINX facility by performing a search for $\Delta(1232)^+$ production in the coherent reaction

$$p + \text{C} \longrightarrow \Delta(1232)^+ + \text{C}, \quad \Delta(1232)^+ \longrightarrow p\pi^0 \tag{84}$$

Since the isospin of the $\Delta(1232)^+$ isobar is $T = 3/2$, reaction (84) cannot proceed diffractively, but it is allowed for the Coulomb mechanism.

By estimating the expected cross section for the Coulomb production of $\Delta(1232)^+$ in reaction (84) with the aid of relations (29) and (30), we obtain

$$\sigma[p + \text{C} \longrightarrow \Delta(1232)^+ + \text{C}]_{\text{Coul}} \simeq 130\ \mu\text{b/(C nucleus)}. \tag{85}$$

Since there is only one charged particle in the final state of reaction (84) and since the trigger condition in the measurements with the SPHINX facility required three charged particles in the final state, the first step of data analysis consisted in selecting events of the type $p + N \longrightarrow p + e^+ + e^- + \gamma + N$. These events were then used to identify the reaction

$$p + N \longrightarrow [p\pi^0] + N, \quad \pi^0 \longrightarrow \gamma\gamma, \quad \gamma \longrightarrow e^+e^- \tag{86}$$

which involves the conversion of one of the photons from the decay $\pi^0 \longrightarrow \gamma\gamma$ into an electron–positron pair in a target material. The second photon was recorded in the γ spectrometer of the apparatus.

Experimental data and criteria for selecting events of reaction (84) were discussed in detail elsewhere [5]. For this reason, we present here only the eventual results of these investigations.

Figure 25*a* shows the effective-mass spectrum $M(p\pi^0)$ for all events of the type (86)—that is, without any cut on p_T^2. As might have been expected, this spectrum is dominated by the contribution of diffractive processes, so that we cannot see here the production of the $\Delta(1232)^+$ isobar with isospin $T = 3/2$.

In order to isolate the Coulomb production of the $p\pi^0$ system in events of reaction (86), we imposed the cut $p_T^2 < 0.01$ GeV and subtracted the diffractive background, which was determined by considering our data in the range $0.02\ \text{GeV}^2 < p_T^2 < 0.03\ \text{GeV}^2$ (here, we introduced a correction factor that takes into account the slope of the diffraction peak). In order to suppress the diffractive background further, we introduced a selection in terms of the π^0-meson emission angle in the Gottfried–Jackson frame ($|\cos\theta_\pi| < 0.7$).

The eventual effective-mass spectrum $M(p\pi^0)$ as obtained upon applying all the above procedures for selecting the Coulomb process is depicted in Fig. 25*b*. This spectrum shows distinctly the Coulomb production of the $\Delta(1232)^+$ isobar. Estimates of the cross section for the process being studied are in reasonable agreement with the theoretical results presented in (85). An accurate experimental determination of this cross section is hindered by uncertainties in taking into account the probability of conversion of one of the photons and the efficiency of all selections used.

In summary, the present analysis of the SPHINX data does indeed make it possible to separate the Coulomb production of $\Delta(1232)^+$ isobars in coherent pC interactions induced by 70-GeV protons.

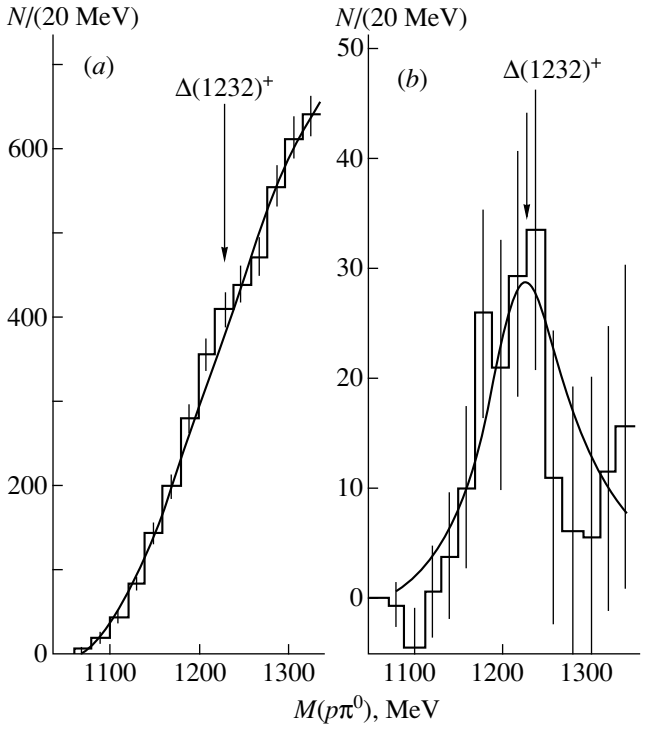

Fig. 25. Investigation of the formation of the $\Delta(1232)^+$ isobar in reaction (86): (*a*) effective-mass spectrum of the $p\pi^0$ system for all events and (*b*) effective-mass spectrum of the $p\pi^0$ system for events selected by applying the cut $p_T^2 < 0.01$ GeV^2. The latter spectrum obtained upon a diffractive-background subtraction and plotted for events passing selection in the neutral-pion emission angle in the Gottfried–Jackson frame shows a peak with parameters $M = 1232 \pm 10$ MeV and $\Gamma = 119 \pm 20$ MeV, which corresponds to the Coulomb production of the $\Delta(1232)^+$ isobar.

8. CONCLUSION

The latest results on particle production in the Coulomb field of nuclei, as discussed in this review article, have revealed that these electromagnetic processes furnish important information about the properties of hadrons and open new possibilities for exotic-state searches. The first results from the SELEX facility, which have been presented in Sections 4 and 5 are still of a preliminary character. The processing of data from this experiment is presently under way. Only the first stage of measurements has been performed at the SPHINX facility. By now, the apparatus has been completely upgraded, and its potential for separating various processes has been considerably improved; concurrently, the luminosity of the apparatus and the data-acquisition rate have been considerably increased. New measurements at this setup are being continued, and many new results are expected to appear in the next few years.

ACKNOWLEDGMENTS

I am grateful to all participants of the E781 collaboration (SELEX) and the SPHINX collaboration with whom the measurements discussed above have been performed. Special thanks are due to D.V. Vavilov, V.P. Kubarovsky, V.F. Kurshetsov, and V.V. Molchanov for collaboration and numerous stimulating discussions.

I am indebted to the organizers of the 21st Workshop on High-Energy Physics and Field Theory (IHEP, Protvino, June 1998) and of the Scientific Seminars at Rutgers University (USA) and at the Institute of Theoretical and Experimental Physics (ITEP, Moscow) for the possibility of presenting the above results at those meetings.

This work was supported in part by the Russian Foundation for Basic Research (project no. 96-02-16759a) and by the Fundamental Nuclear Physics program of the Ministry for Science and Technology of the Russian Federation.

REFERENCES

1. H. Primakoff, Phys. Rev. **81**, 119 (1951).
2. I. Ya. Pomeranchuk and I. M. Shmushkevich, Nucl. Phys. B **23**, 452 (1961).
3. M. Zielinski *et al.*, Z. Phys. C **31**, 545 (1986); **34**, 255 (1986).
4. L. G. Landsberg, Yad. Fiz. **52**, 192 (1990) [Sov. J. Nucl. Phys. **52**, 121 (1990)]; Nucl. Phys. B (Proc. Suppl.) **21**, 179 (1991).
5. D. V. Vavilov *et al.*, Yad. Fiz. **62**, 501 (1999) [Phys. At. Nucl. **62**, 459 (1999)].
6. S. I. Bityukov *et al.*, Yad. Fiz. **47**, 1258 (1988) [Sov. J. Nucl. Phys. **47**, 800 (1988)].
7. P. Weidenauer *et al.*, Z. Phys. C **47**, 353 (1990).
8. S. I. Bityukov *et al.*, Phys. Lett. B **188**, 383 (1987).
9. S. I. Bityukov *et al.*, Phys. Lett. B **203**, 327 (1988).
10. S. I. Bityukov *et al.*, Z. Phys. C **50**, 451 (1991).
11. L. G. Landsberg, Fiz. Élem. Chastits At. Yadra **21**, 1054 (1990) [Sov. J. Part. Nucl. **21**, 446 (1990)].
12. D. Alde *et al.*, Phys Lett. B **340**, 122 (1994).
13. L. G. Landsberg, Phys. Rep. **128**, 301 (1985).
14. A. Halpern *et al.*, Phys. Rev. **152**, 1295 (1966); J. Dreitlein and H. Primakoff, Phys. Rev. **125**, 591 (1962).
15. G. Berlad *et al.*, Ann. Phys. (N.Y.) **75**, 461 (1973).
16. T. Jensen *et al.*, Phys. Rev. D **27**, 26 (1983).
17. Particle Data Group (C. Caso *et al.*), Eur. Phys. J. C **3**, 1 (1998).
18. Ya. B. Zel'dovich and A. D. Myshkis, *Elements of Applied Mathematics* [in Russian] (Nauka, Moscow, 1972), p. 183.
19. H. Frauenfelder and E. M. Henley, *Subatomic Physics* (Prentice-Hall, Englewood Cliffs, 1974; Mir, Moscow, 1979).
20. J. Huston *et al.*, Phys. Rev. D **33**, 3199 (1986).
21. S. Cihangir *et al.*, Phys. Lett. B **117**, 119 (1982).
22. M. Zielinski *et al.*, Phys. Rev. Lett. **52**, 1195 (1984).

23. B. Collick *et al.*, Phys. Rev. Lett. **53**, 2374 (1984).
24. D. Berg *et al.*, Phys. Lett. B **98**, 119 (1981).
25. D. Carismith *et al.*, Phys. Rev. Lett. **56**, 18 (1986).
26. D. Carismith *et al.*, Phys. Rev. D **36**, 3502 (1987).
27. L. Capraro *et al.*, Nucl. Phys. B **288**, 659 (1987).
28. Yu. M. Antipov *et al.*, Phys. Lett. B **121**, 445 (1983).
29. Yu. M. Antipov *et al.*, Phys. Rev. D **36**, 21 (1987).
30. F. Dydak *et al.*, Nucl. Phys. B **118**, 1 (1977); T. Devlin *et al.*, Phys. Rev. D **34**, 1626 (1986).
31. P. C. Peterson *et al.*, Phys. Rev. Lett. **57**, 949 (1986).
32. R. Edelstein *et al.*, Fermilab Proposal E781, Batavia, 1987 (revised 1993); J. S. Russ, Nucl. Phys. A **585**, 39 (1995).
33. V. J. Smith, in *Proceedings of Seventh Internal Conference on Hadron Spectroscopy (Hadron-97)* (Upton, 1997), Ed. by S.-U. Chung and H. J.Willutzki, p. 627.
34. V. P. Kubarowsky, Report at ICHEP-98 (Vancouver, 1998).
35. V. F. Kyrshetsov, presented at the Conference of the Nuclear Physics Department, Russian Academy of Sciences on Fundamental Interactions of Elementary Particles, ITEP, Moscow, 1998.
36. V. P. Kubarowsky, presented at the Conference of the Nuclear Physics Department, Russian Academy of Sciences on Fundamental Interactions of Elementary Particles, ITEP, Moscow, 1998.
37. L. G. Landsberg, Plenary Talk at 21st International Conference on High-Energy Physics and Field Theory, IHEP, Protvino, 1998.
38. M. Zielinski *et al.*, Z. Phys. C **16**, 197 (1983).
39. J. Babcock and J. L. Rosner, Phys. Rev. D **14**, 1286 (1976).
40. S. Ishida *et al.*, Phys. Rev. D **40**, 1497 (1989).
41. L. G. Landsberg, Yad. Fiz. **59**, 2161 (1996) [Phys. At. Nucl. **59**, 2080 (1996)].
42. M. V. Hynes, LAMPF II Workshop Report (1982).
43. H. J. Lipkin, Phys. Rev. D **17**, 946 (1973); H. J. Lipkin and M. A. Moinester, Phys. Lett. B **287**, 179 (1992).
44. A. V. Vanyashin *et al.*, Yad. Fiz. **34**, 158 (1981) [Sov. J. Nucl. Phys. **34**, 90 (1981)].
45. M. A. Beg *et al.*, Phys. Rev. Lett. **13**, 514 (1964).
46. M. N. Butler *et al.*, Nucl Phys. B **339**, 69 (1993); Phys. Lett. B **304**, 353 (1993).
47. M. Napsuciale and J. L. Lucio, Nucl. Phys. B **494**, 260 (1997).
48. L. G. Landsberg and V. V. Molchanov, Preprint No. IHEP 97-42 (Protvino, 1997).
49. E. Arik *et al.*, Phys. Rev. Lett. **38**, 1000 (1977).
50. L. G. Landsberg, Yad. Fiz. **57**, 47 (1994) [Phys. At. Nucl. **57**, 42 (1994)].
51. L. G. Landsberg, Usp. Fiz. Nauk **164**, 1129 (1994) [Phys.–Usp. **37**, 1043 (1994)].
52. G. Bellini, Nuovo Cimento A **79**, 282 (1984).
53. SPHINX Collab. (D. V. Vavilov *et al.*), Yad. Fiz. **57**, 241, 253 (1994) [Phys. At. Nucl. **57**, 227, 238 (1994)].
54. SPHINX Collab. (M. Ya. Balatz *et al.*), Z. Phys. C **61**, 220, 339 (1994).
55. SPHINX Collab. (S. V. Golovkin *et al.*), Z. Phys. C **68**, 585 (1994).
56. SPHINX Collab. (A. V. Bezzubov *et al.*), Yad. Fiz. **59**, 2199 (1996) [Phys. At. Nucl. **59**, 2117 (1996)].
57. L. G. Landsberg, Yad. Fiz. **60**, 1541 (1997) [Phys. At. Nucl. **60**, 1397 (1997)]; in *Proceedings of Seventh Internal Conference on Hadron Spectroscopy (Hadron-97)* (Upton, 1997), Ed. by S.-U. Chung and H. J.Willutzki, p. 725.
58. M. Bockhorst *et al.*, Z. Phys. C **63**, 37 (1994).
59. R. A. Schumacher, Preprint CMU MEG-96-007 (Pittsburgh, 1996).

Translated by A. Isaakyan

Physics of Atomic Nuclei, Vol. 63, No. 1, 2000, pp. 109–119. Translated from Yadernaya Fizika, Vol. 63, No. 1, 2000, pp. 121–131.

ELEMENTARY PARTICLES AND FIELDS
Theory

Relationship between the Cross Section for Deep-Inelastic Scattering and the Cross Section for Inclusive Annihilation

V. A. Petrov* and R. A. Ryutin, *****

Institute for High Energy Physics, Protvino, Moscow oblast, 142284 Russia

Received September 15, 1998; in final form, January 26, 1999

Abstract—Arguments have been presented that suggest that available experimental data on the structure functions for the processes $ep \longrightarrow eX$ and $e^+e^- \longrightarrow p(\bar{p})X$ do not confirm the so-called reciprocity relation, which was obtained in the leading-logarithm approximation of perturbation theory. It has also been shown that the asymptotic relationship between the above processes that was obtained on the basis of more general considerations is compatible with existing data. © *2000 MAIK "Nauka/Interperiodica".*

1. INTRODUCTION

A vast body of experimental data on the deep-inelastic scattering $ep \longrightarrow eX$ and on the inclusive annihilation $e^+e^- \longrightarrow p(\bar{p})X$ has been accumulated at present. A great number of studies (see, for example, [1]) were devoted to substantiating the importance of analyzing these processes for obtaining deeper insight into fundamental phenomena like confinement and for testing various models (such as QCD, bag model, and string model) and basic principles of quantum field theory (locality, causality, etc.).

Investigation of the analytic properties and of the asymptotic behavior of the cross sections (structure functions) for deep-inelastic scattering is of great importance in this connection. Some relations between the above processes have been obtained along these lines. Among these, the most prominent ones are, first, the relation implementing an analytic continuation from the deep-inelastic-scattering channel to the inclusive-annihilation channel (crossing symmetry) and following from basic principles of quantum field theory [2–5] and, second, the reciprocity relation [6, 7], which was derived in the leading-logarithm approximation for many models, including QCD [8, 9]. There have been many fewer studies devoted to the subject in recent years than in the early 1980s, and they have been, as a rule, purely theoretical analyses not giving proper attention to experimental data (see, however, [10]).

The present article deals not only with theoretical aspects of the problem; it also attempts at establishing relationship between the results obtained and experimental data. We employ data presented by the collaborations ARGUS ($\sqrt{Q^2}$ = 9.8 GeV) [11], TASSO ($\sqrt{Q^2}$ = 14, 22, 34 GeV) [12], TPC [13], HRS ($\sqrt{Q^2}$ = 29 GeV) [14], TOPAZ ($\sqrt{Q^2}$ = 58 GeV) [15], OPAL [16], and DELPHI ($\sqrt{Q^2}$ = 91.2 GeV) [17] for inclusive annihilation and by the collaborations NMC [18], BCDMS [19], ZEUS [20], H1 [21], EMC [22], E665 [23], and SLAC [24] for deep-inelastic scattering; we also invoked the MRS parametrization [25] for relevant structure functions. Our thorough analysis revealed that, in fact, some of previous predictions are not confirmed by experimental data. At the same time, new relations between cross sections for deep-inelastic scattering and cross sections for inclusive annihilation have been obtained and contrasted against experimental data.

* e-mail: petrov@mx.ihep.su
** e-mail: ryutin@@th1.ihep.su
*** e-mail: asp9801@mx.ihep.su

2. RELATIONSHIP BETWEEN DEEP-INELASTIC SCATTERING AND INCLUSIVE ANNIHILATION

2.1. Analytic Continuation

The relation that implements an analytic continuation from the deep-inelastic-scattering channel to the inclusive-approximation channel was considered in many studies, which employed different approaches to the problem. In this connection, we only note some articles that treated the crossing-symmetry problem.

The earliest approach relied on an expansion of the chronological product of currents near the light cone and assumed that the structure functions F_i and $\bar{F}_i$ are independent of $Q^2 = |q^2|$ (q^2 is the photon virtuality). The latter implies scaling at sufficiently high Q^2. Analytic properties resulting from perturbation theory are illustrated in Fig. 1. It was shown in [4] that there exist two possibilities:

(i) $F_i(x)$ admits an analytic continuation into $\bar{F}_i(x)$.

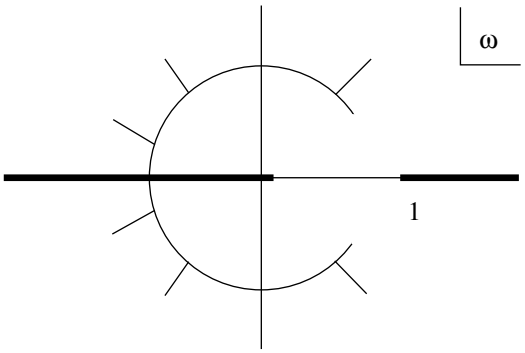

Fig. 1. Region of analyticity in ω according to perturbation theory with allowance for anomalous thresholds ($\omega = -q^2/(s - q^2)$, where s is the invariant mass of undetected hadrons in both processes, and $x = \omega$ for $\omega > 0$).

(ii) Nontrivial scaling is fulfilled for any process separately, and there is no relation of the analytic-continuation type.

In the first case, we have crossing symmetry in the form of the relation

$$\bar{F}(x) = -\operatorname{Re} F(x) + \rho(x), \tag{1}$$

where $\rho(x)$ is expressed in terms of the spectral function $F(x)$ in the annihilation region ($x > 1$) (see Fig. 1). There are two types of analytic continuation that are determined by the presence or by the absence of a cut along the real axis. Trivial crossing symmetry [2] is fulfilled under the condition $\rho \equiv 0$, in which case we have

$$\bar{F}(x) = -F(x), \quad x > 1. \tag{2}$$

Another type of crossing symmetry is determined by the same relation (1) with $\rho \neq 0$. For this case, it was indicated in [4] that, even if $F(x)$ does not have a cut for $x > 1$—that is, $\operatorname{Im} F(x) = 0$—the function $\rho(x)$ is not bound to be zero. Hence, a somewhat different relation may hold:

$$\bar{F}(x) = -F(x) + \rho(x), \quad x > 1. \tag{3}$$

At the same time, we cannot rule out the possibility that the processes being discussed have nothing to do with an analytic continuation of this type [case (ii)].

The second approach seems more correct in the sense that, by and large, it relies on the causality principle and the spectral property, not invoking the expansion of chronological products near the light cone. This approach was used in [3]—it consists in determining structure functions from the amplitude of nonforward Compton scattering—that is, from that for $t \neq 0$. By selecting important diagrams that contribute to the structure functions for deep-inelastic scattering and inclusive annihilation at $t = 0$ and comparing relevant analytic expressions, we arrive at a relation of so-called generalized crossing symmetry. This relation has the form

$$\begin{aligned}\bar{W}_2(s, q^2) &= -\operatorname{Re} W_2(s, q^2) - \epsilon(s + M^2 - q^2) \\ &\times \theta(s - s_0)\theta(q^2 - q_t^2) g(q^2, q^2, s, 0),\end{aligned} \tag{4}$$

where $g(q^2, q'^2, s, t)$ is the triple-spectral function of the Compton amplitude for $t \neq 0$ with respect to q^2, q'^2, and s ($q^2 = q'^2$ at $t = 0$). For this amplitude, we have the relation

$$g(q^2, q'^2, s, t) = g(q'^2, q^2, s, t). \tag{5}$$

For deep-inelastic scattering, the structure functions are introduced in a conventional way [2, 5, 6]: $F_2(x, q^2) = \nu W_2(x, q^2) = xW(x, q^2)$, where $x = Q^2/2pq$ and $\nu = pq/M$, p and M being the proton momentum and mass, respectively; it is also assumed that the Callan–Gross relation $F_2(x, q^2) = 2xF_1(x, q^2)$ [26] holds. The structure functions for annihilation are introduced in a similar way. In the region of annihilation, the variable $z = 1/x < 1$ is often used instead of x. We note that, in the approach being discussed, each of the structure functions $\bar{W}$ and W is expressed in terms of the single structure function g; that is, we can say that there is a single analytic function whose boundary values appear to be equal to the structure functions in question. We then obtain a relation between the structure functions without the assumption of scaling—that is, without any assumption on their behavior versus Q^2. This means that relation (4) must hold for any Q^2.

In [27], the question of whether there exists a unified function of two complex variables with boundary values equal to the structure functions for deep-inelastic scattering and inclusive annihilation was discussed in a different context. Specifically, that article addressed the question of what implications this will have if the amplitudes of the processes satisfy rather general assumptions on their behavior for $q^2 \longrightarrow \pm\infty$ at fixed s; in addition, a relation similar to the so-called reciprocity relation (see below) was obtained there in the form

$$\lim_{q^2 \to \infty} \frac{W(-q^2, s)}{\bar{W}(q^2, s)} = 1. \tag{6}$$

For the case being considered and s being fixed, relation (6) can be recast into the form

$$\lim_{x \to 1} \frac{W(x, s)}{\bar{W}(x, s)} = 1. \tag{7}$$

An advantage of the last relation over crossing symmetry is that either structure function is taken in its physical domain. Owing to this, relations (6) and (7) admit a direct experimental test with some qualifications (see below). There is also an advantage over the reciprocity relation, which was obtained within perturbation theory.

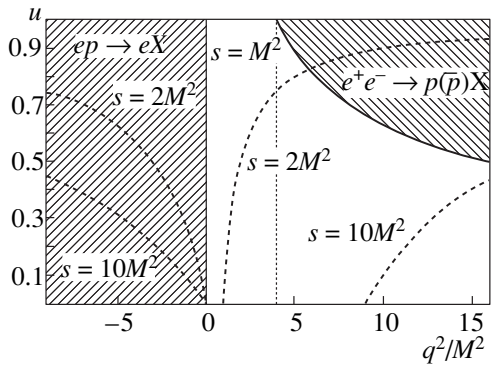

Fig. 2. Physical regions in terms of the variables q^2 and u, where $u = x$ for deep-inelastic scattering and $u = z$ for inclusive annihilation. Dashed curves correspond to s = const. At $s = M^2$, we obtain the line $u \equiv 1$. The dotted line corresponds to $q^2 = 4M^2$.

2.2. Reciprocity Relation

A connection between deep-inelastic scattering and inclusive annihilation in their physical domains (see Fig. 2) was first established by Gribov and Lipatov [6], who relied on a summation of ladder diagrams in perturbation theory (leading-logarithm approximation) for the vector and the pseudoscalar theory of interaction. This connection, which was also comprehensively discussed in [7], is manifested in the reciprocity relation

$$\overline{W}\left(\frac{1}{x}, q^2\right) = xW(x, q^2), \tag{8}$$

where $\overline{W}$ and W are the structure functions that were defined above and which are obtained from the amplitude for the Compton scattering of a virtual photon on

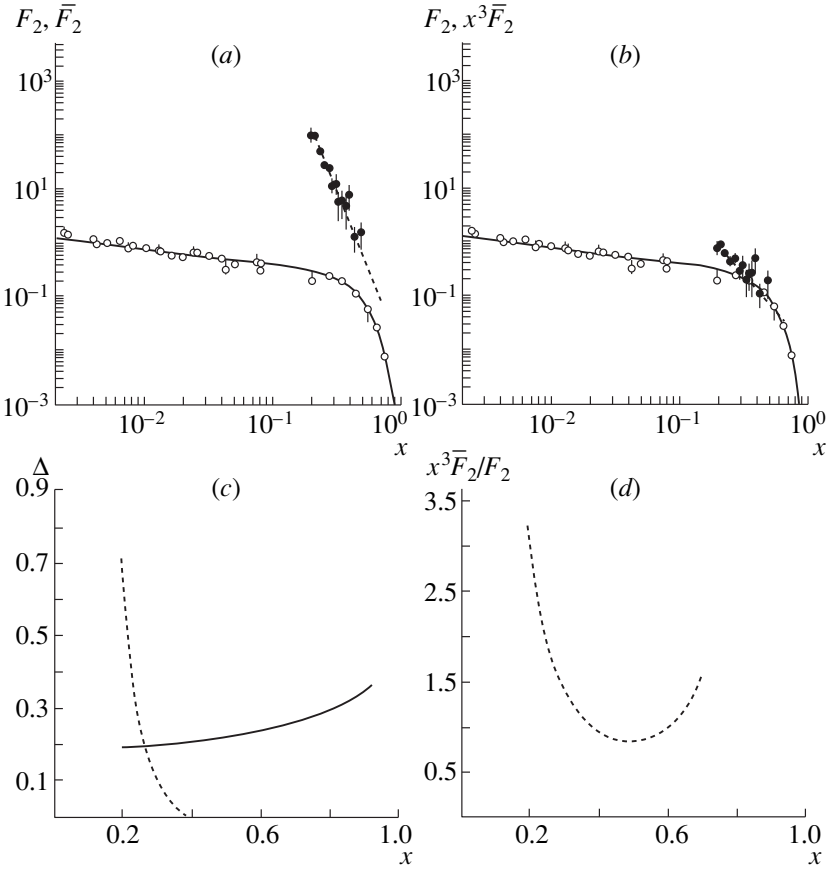

Fig. 3. Experimental points and interpolation curves at $\sqrt{Q^2} = 9.8$ GeV versus x ($x = Q^2/2pq$ for deep-inelastic scattering and $x = 2pq/Q^2$ for inclusive annihilation). In Fig. 3*a*, the solid and dashed curves represent the structure functions F_2 (the corresponding experimental data are shown by open circles) and $\bar{F}_2$ (the corresponding experimental data are shown by closed circles), respectively. In Fig. 3*b*, the solid and dashed curves represent the structure functions F_2 (the corresponding experimental data are shown by open circles) and $x^3\bar{F}_2$ (the corresponding experimental data are shown by closed circles), respectively, which appear in the reciprocity relation (13). Figure 3*c* shows the difference $\Delta = x^3\bar{F}_2 - F_2$ as calculated within QCD (solid curve) and as obtained from a data analysis (dashed curve). Figure 3*d* displays the ratio $x^3\frac{\bar{F}_2}{F_2}$, which is to be compared with unity.

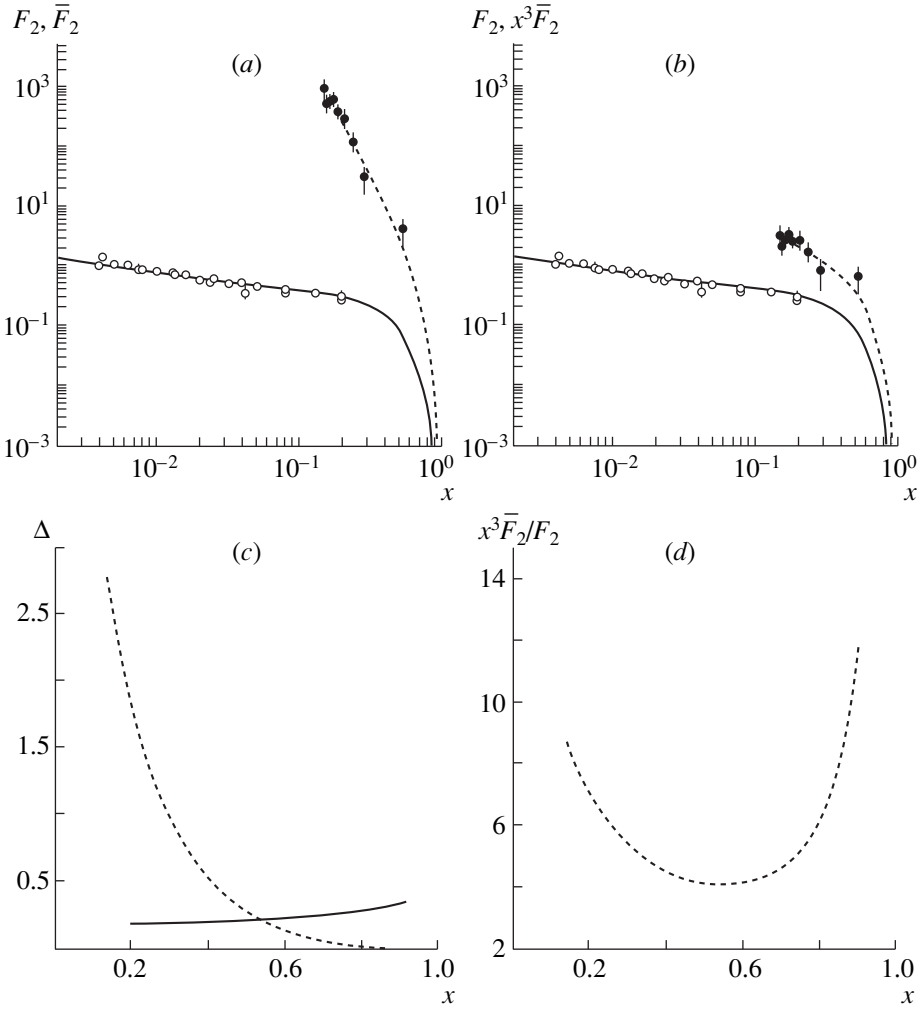

Fig. 4. As in Fig. 3, but the experimental data were taken at $\sqrt{Q^2}$ = 14 GeV.

a spinor particle. It was also indicated that, in the case of scattering on a virtual particle, relation (8) is applicable in the region $Q^2 \longrightarrow \infty$, corrections to it being $o(M^2/Q^2)$ quantities. Within QCD, a similar relation was obtained in [8, 9].

Since the appearance of the study by Gribov and Lipatov [6], the reciprocity relation has been the subject of much controversy [28–34]. The majority of the authors who discussed this issue relied on an analysis of various diagrams of perturbation theory. By way of example, we indicate that, in [28], it was shown that relation (8) is violated in the limit $x \longrightarrow 0$ because of distinctions between the mechanisms governing deep-inelastic-scattering and inclusive-annihilation reactions. Arguments were presented in [29] that are based on considering some ladder diagrams and which suggest that the reciprocity relations are valid only in the vicinity of the point $x \sim 1$, provided that $W(x) \sim (1-x)^n$ for $x \longrightarrow 1$. It is worth noting that, in [33, 34], there were no higher logarithmic corrections of perturbation theory.

The effect of taking into account nonleading logarithms was analyzed in the review articles of Curci *et al.* [30] and Floratos *et al.* [32]. The impact of nonperturbative phenomena on the reciprocity relation was considered in [33]. According to those three studies, relation (8) can be invalid everywhere. Therefore, all the results being discussed call for an experimental verification.

3. ANALYSIS OF EXPERIMENTAL DATA

3.1. Structure Functions and Cross Sections

For the sake of convenience, we represent the reciprocity relation in terms of quantities measurable directly. Specifically, we express relation (8) in terms of the functions F_2 and $\bar{F}_2$. These functions are directly related to differential cross sections for deep-inelastic-

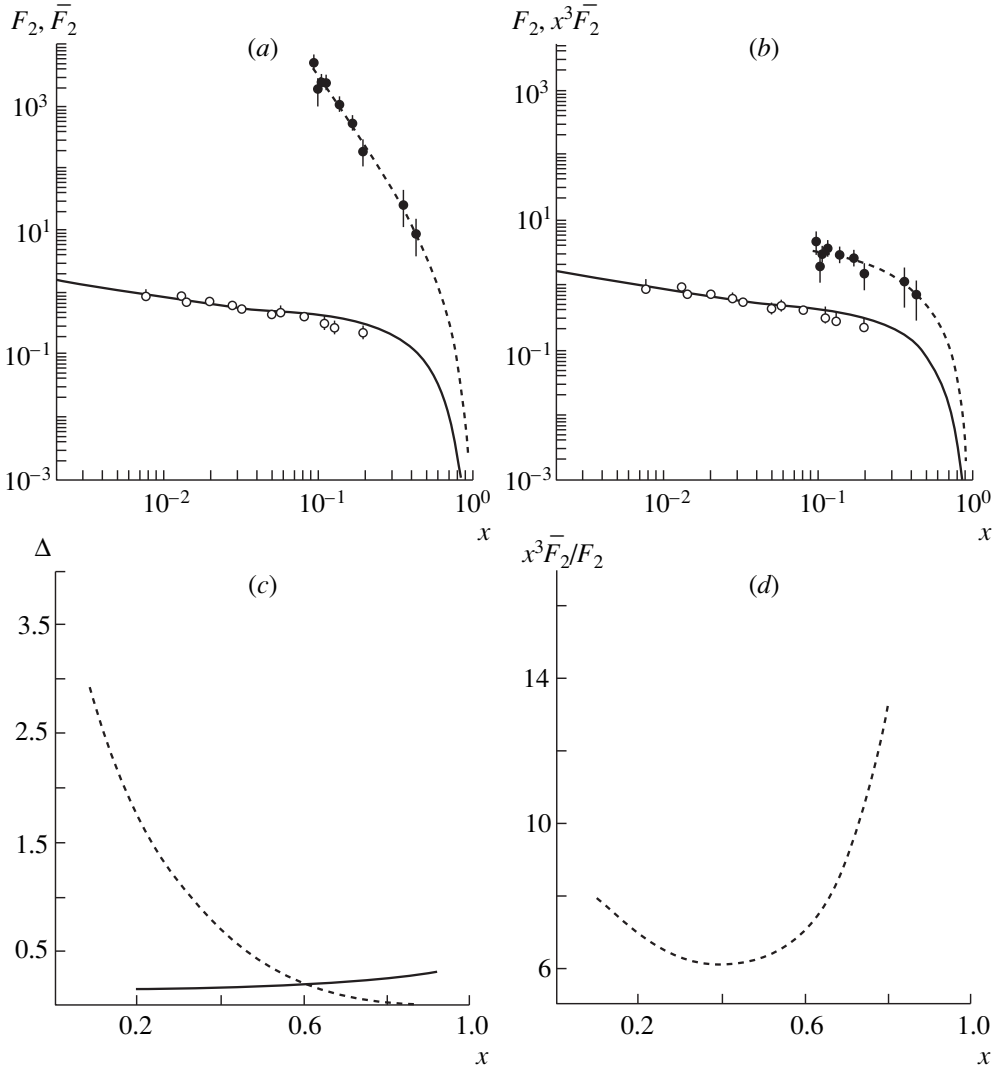

Fig. 5. As in Fig. 3, but the experimental data were taken at $\sqrt{Q^2}$ = 22 GeV.

scattering and inclusive-annihilation processes. From the experimental study reported in [18], it is known that

$$\frac{d^2\sigma(x, Q^2, E)}{dxdQ^2} = \frac{4\pi\alpha^3}{Q^4}\frac{F_2(x, Q^2)}{x} \times\left\{1 - y - \frac{Q^2}{4E^2} + \left(1 - \frac{2m^2}{Q^2}\right)\frac{y^2 + Q^2/E^2}{2(1 + R(x, Q^2))}\right\}, \quad (9)$$

where α is the fine-structure constant, E is the laboratory energy of the incident lepton (μ or e), m is its mass, $y = \nu/E$, and $R = \sigma_L/\sigma_T$ is a ratio measuring the degree of violation of the Callan–Gross relation [35]. By using equation (9), the function F_2 can be expressed in terms of an experimentally measurable quantity. For the case of annihilation, a similar formula can be obtained from the expression presented in [2] for the relevant cross section. Specifically, we have

$$\bar{F}_2(z, q^2) = \left[\frac{1}{\beta\sigma_h}\frac{d\sigma^{e^+e^- \to p + X}}{dz}\right]\frac{2\mathcal{R}}{(3 - \beta^2)z^2} = \frac{1}{z}\bar{W}(z, q^2), \quad (10)$$

$$\mathcal{R} = \frac{\sigma_h}{\sigma_0}, \quad (11)$$

$$\sigma_0 = \sigma_0(e^+e^- \longrightarrow \mu^+\mu^-) = \frac{4\pi\alpha^2}{3q^2}, \quad (12)$$

where σ_h is the cross section for the process $e^+e^- \longrightarrow$ *hadrons*, while $z = 1/x = 2pq/|q|^2$. Relation (8) can then be represented in the form

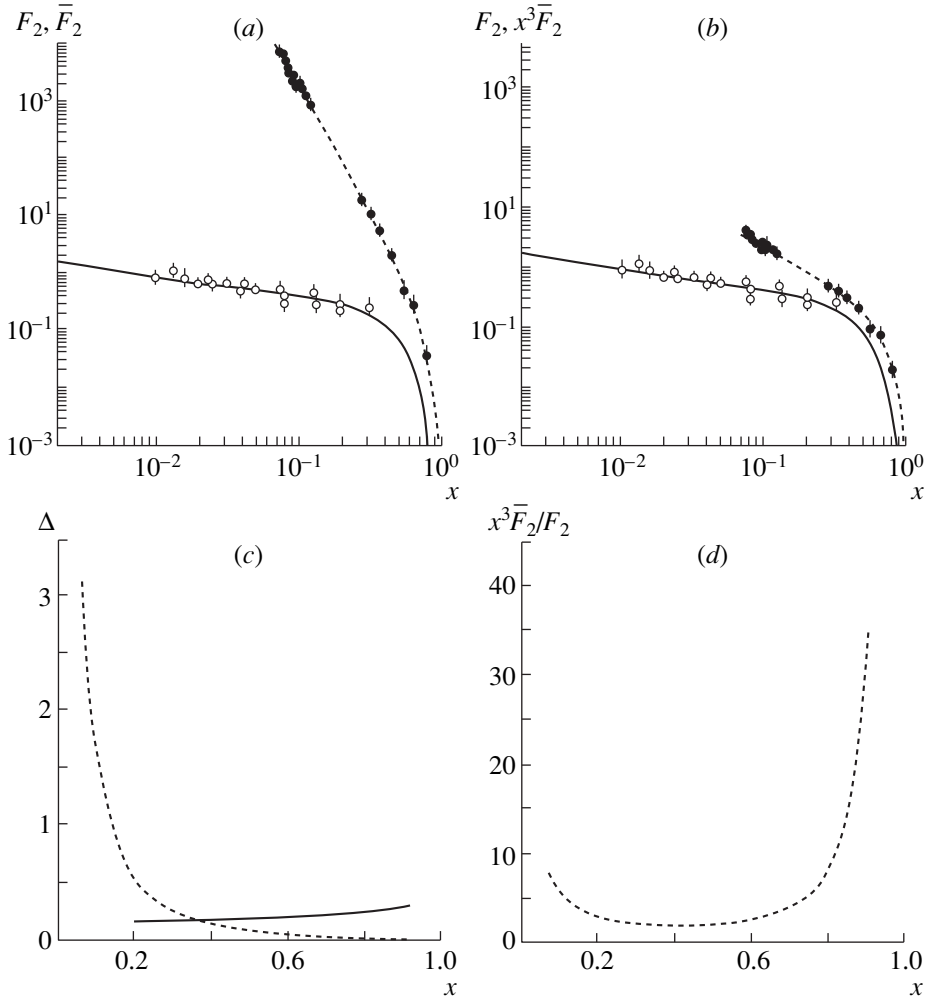

Fig. 6. As in Fig. 3, but the experimental data were taken at $\sqrt{Q^2}$ = 29 GeV.

$$F_2(x, q^2) = \frac{2z\mathcal{R}}{3-\beta}\left[\frac{1}{\beta\sigma_h}\frac{d\sigma^{e^+e^-\to p+X}}{dz}\right] = z^3\bar{F}_2(z, q^2). \quad (13)$$

The function β is retained in this expression in order that other measurable quantities could be reduced to the form (13), although this function is usually set to unity.

Prior to proceeding to analyze experimental results, it should be recalled that data on inclusive annihilation exist only for several discrete values of Q^2; this is because the energy of colliding beams is fixed, so that we had to borrow such data from experiments at different accelerators. Moreover, it is often difficult to find identical values of Q^2 for deep-inelastic scattering and inclusive annihilation; in view of this, we employ averaged values below.

In order to achieve a clearer presentation and to reveal various trends, we will make use of interpolation functions. For the structure function $F_2(x, Q^2)$, we choose the parametrization of Martin, Roberts, and Stirling [25]. For the annihilation process, we take the popular parametrization

$$\bar{F}_2(z, q^2) = Nz^a(1-z)^b(1+cz^d), \quad (14)$$

where the parameters N, a, b, c, and d, which depend on q^2, are extracted from experimental data by means of a numerical analysis.

3.2. Violation of the Reciprocity Relation

Let us proceed to analyze experimental data. Figures 3*a*–9*a* show the structure functions F_2 and $\bar{F}_2$ for deep-inelastic-scattering and inclusive-annihilation processes, while Figs. 3*b*–9*b* illustrate functions that characterize the reciprocity relation and which must be directly compared [see equation (13)]. The same figures display interpolation curves. For the sake of comparison, the difference $\Delta_{\text{exp}} = x^3\bar{F}_2 - F_2$ of the corre-

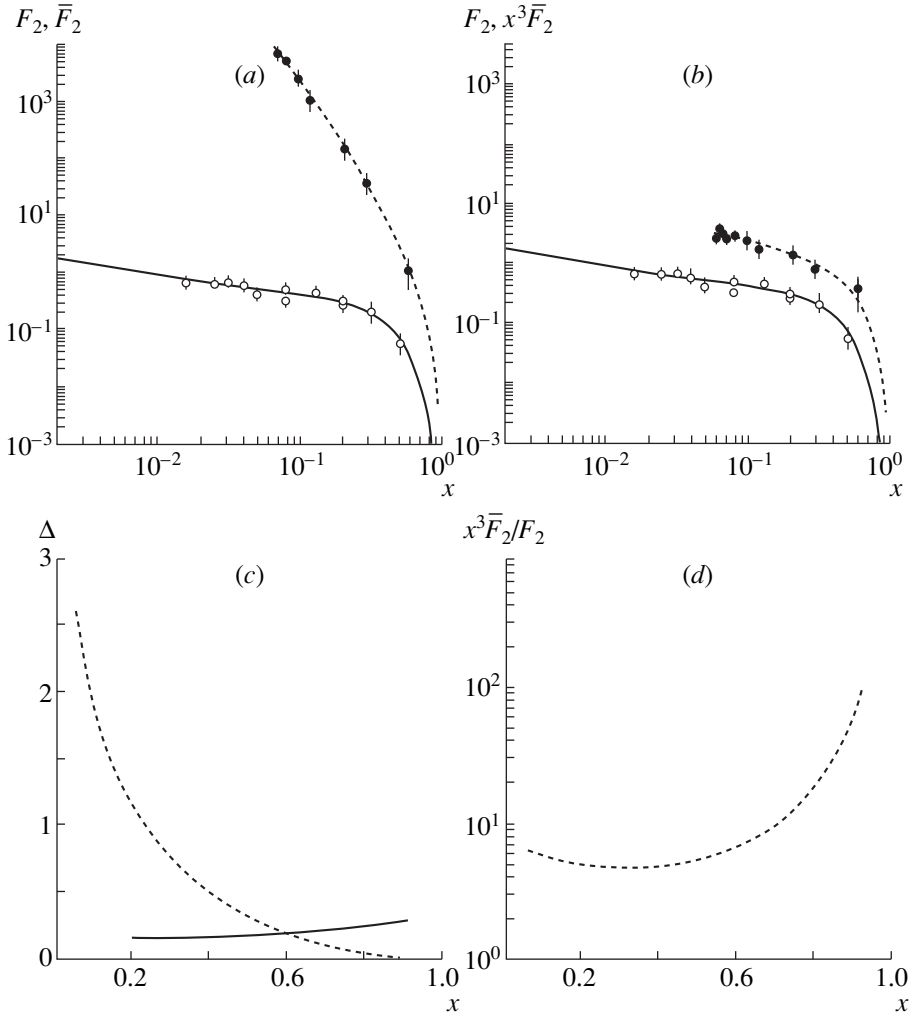

Fig. 7. As in Fig. 3, but the experimental data were taken at $\sqrt{Q^2}$ = 34 GeV.

sponding interpolation curves is presented in Figs. 3*c*–9*c* along with the correction of the next-to-leading logarithmic approximation of perturbative QCD for the nonsinglet part of the structure functions. This correction can easily be calculated with the aid of the evolution equation

$$Q^2\frac{\partial}{\partial Q^2}F_{\mathrm{NS}}(x, Q^2) = K_{\mathrm{NS}}(x, \alpha_s) \otimes F_{\mathrm{NS}}(x, Q^2), \quad (15)$$

where $F_{\mathrm{NS}} = F_{2,\mathrm{NS}}$, $\bar{F}_{2,\mathrm{NS}}$ (the kernel K_{NS} is defined in a similar way), while the notation on the right-hand side is spelled out as

$$f(x) \otimes g(x) = \int_x^1 \frac{dy}{y} f\left(\frac{x}{y}\right) g(y).$$

The correction to the kernel K_{NS} of equation (15) is given by (see [32])

$$\Delta K_{\mathrm{NS},2}(x) \equiv K_{\mathrm{NS},2}(x) - x\bar{K}_{\mathrm{NS},2}\left(\frac{1}{x}\right)$$

$$= \left(\frac{\alpha_s}{4\pi}\right)^2\left\{-4C_F^2\left[\left(-5 - x + \frac{6}{1-x}\right)\ln x \right.\right. \quad (16)$$

$$\left. + \left(3 + 3x - \frac{4}{1-x}\right)\ln^2 x + 4\frac{1+x^2}{1-x}\ln x \ln|1-x|\right]$$

$$\left. + b_0 C_F\left[-6\frac{1+x^2}{1-x}\ln x + 7(1+x) - 2\pi^2\delta(1-x)\right]\right\},$$

where C_F = 4/3 and b_0 = 23/3. Figures 3*d*–9*d* display the ratio of the functions appearing in the reciprocity relation. In addition, we note that data at $\sqrt{Q^2}$ values less than 10 GeV can be found in [10].

Figure 3 displays data at $\sqrt{Q^2}$ = 9.8 GeV. It should be emphasized that the uncertainties in the case of annihilation exceed considerably those in the case of deep-inelastic scattering; therefore, we have no specific confirmation of the reciprocity relation. Moreover, the

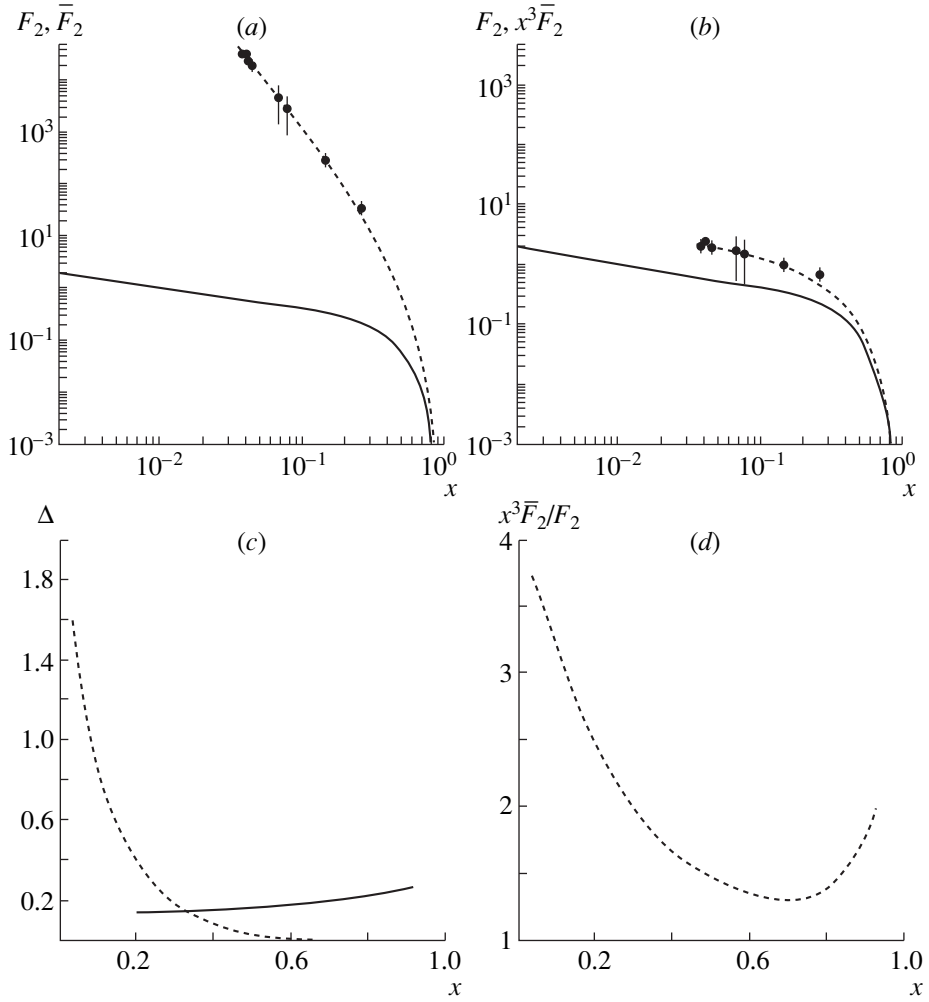

Fig. 8. As in Fig. 3, but the experimental data were taken at $\sqrt{Q^2}$ = 58 GeV.

interpolation curve shows a tendency to ascend at large x (see Fig. 3*d*). The same can be said about Figs. 4, 5, 7, and 8, where the violation of this relation is more obvious. In addition, the QCD correction is close to the interpolation curve for the above difference only in the bounded region of x. Figure 6, where we can also clearly see discrepancies between the predictions and experimental data, is more informative in what is concerned with uncertainties and with the number of points. For deep-inelastic scattering, Fig. 8 shows only the interpolation curve corresponding to $\sqrt{Q^2}$ = 58 GeV. We know, however, that the dependence of F_2 on Q^2 is rather weak; therefore, we do not expect that the uncertainties will be very large, at least at low x. Of great interest are recent data from LEP at $\sqrt{Q^2}$ = 91.2 GeV (see Fig. 9). They give sufficient ground to state that relation (8) does not hold for all x.

The authors of some studies (see, for example, [34]) attempted to clarify the reasons behind the violation of this relation and to obtain simultaneously an improved relation. In particular, it was shown in [34] that, because of the distinction between the mechanisms governing deep-inelastic-scattering and inclusive-annihilation reactions (in the case of deep-inelastic scattering, the process proceeds entirely in a bounded domain—in a so-called bag—whereas, in the case of annihilation, this bag originates from the parton jet), the right-hand side of relation (13) (that is, the interpolated values in Figs. 3*d*–9*d*) must be divided by a factor of 2 to 4. In this connection, it was concluded that the functions measured in actual experiments may differ from those appearing in the original reciprocity relation. This statement seems reasonable, but no substantial improvements are obtained in the region of small x upon introducing the above correction coefficient in the experimental data. As to the region of x close to unity, some

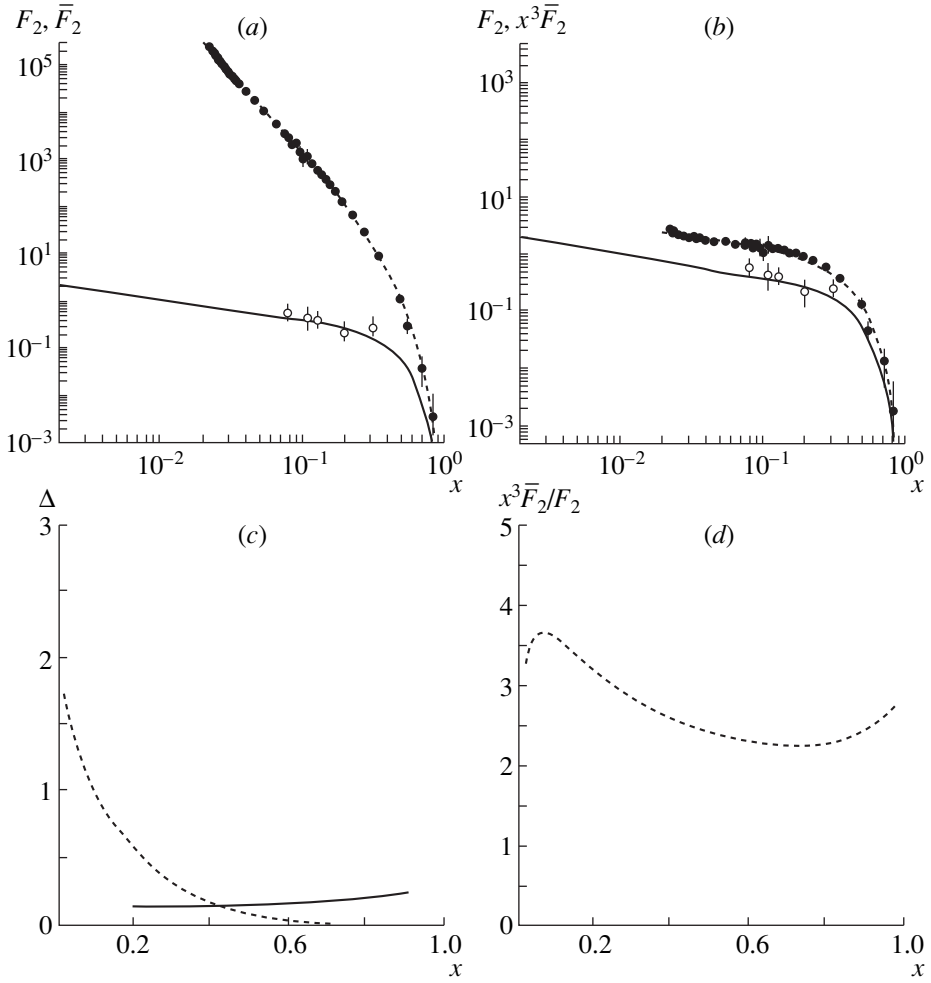

Fig. 9. As in Fig. 3, but the experimental data were taken at $\sqrt{Q^2}$ = 91.2 GeV.

kind of agreement can be observed at $\sqrt{Q^2}$ = 91.2 GeV, but no definitive conclusion can be drawn on this basis.

Thus, the experimental data discussed here indicate that the reciprocity relation does not hold at all values of x and that there is a hope that this relation holds for $x \longrightarrow 1$, provided that a correction factor of about 2 to 4 has been introduced, but this approach is not quite correct.

In the next section, it will be shown how relation (8) can be modified on the basis of the general principles of quantum field theory and how this modified version can be tested experimentally.

4. ANALYSIS OF THE MODIFIED RELATION

As was indicated above, a relation that has the form (6) or (7) and which holds at a fixed s value was obtained in [27]. Here, it is necessary to specify quantities that we eventually compare. For this purpose, we will make use of the parton model. From equation (9) and the representation

$$\frac{d^2\sigma}{dxdQ^2} = \frac{4\pi\alpha^2}{Q^4} \times \left[\sum_{i=1}^{N_f} e_{q_i}^2 (f_{q_i}(x, Q^2) + f_{\bar{q}_i}(x, Q^2))\right]\left\{1 - y + \frac{y^2}{2}\right\}, \quad (17)$$

we obtain

$$\frac{F_2}{x} = \sum_{i=1}^{N_f} e_{q_i}^2 (f_{q_i}(x, Q^2) + f_{\bar{q}_i}(x, Q^2)). \quad (18)$$

Comparing the last expression with the analogous expression for the fragmentation function in the parton model [36, 37] (N_c = 3),

$$2z\bar{F}_1 \equiv z^2\bar{F}_2 = N_c \sum_{i=1}^{N_f} e_{q_i}^2 [\bar{D}_{q_i}^h(z) + \bar{D}_{\bar{q}_i}^h(z)], \quad (19)$$

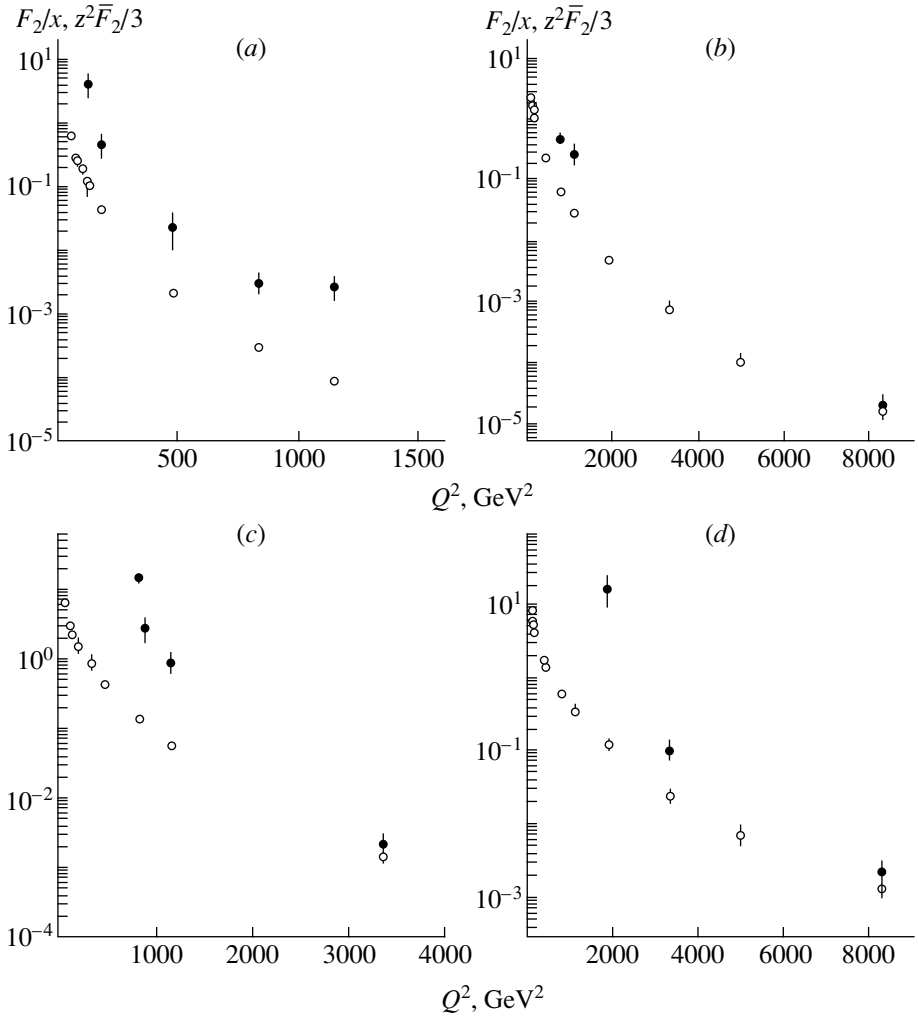

Fig. 10. Experimental Q^2 dependences of the functions (○) F^2/x and (●) $z^2\bar{F}_2/3$ [which appear in the modified reciprocity relation (20)] at s = (*a*) 110, (*b*) 580, (*c*) 780, and (*d*) 1800 GeV.

and using the asymptotic relation in the form (6) or (7), we can see that, at fixed s, we can use the constraint

$$\lim_{Q^2\to\infty} \frac{x^3(s, Q^2)\bar{F}_2(s, Q^2)}{3F_2(s, Q^2)} = 1; \qquad (20)$$

that is, we can compare the functions F_2/x and $x^2\bar{F}_2/3$ for $0 < x < 1$. It is the constraint in (20) that we propose to test experimentally.

The main difficulty in experimentally testing relation (20) is that, in the existing array of data for various Q^2 and x, it is necessary to single out points where s takes a specific fixed value (curves s = const in Fig. 2). This requirement reduces drastically the number of appropriate points. Nonetheless, the available data set proved sufficient for performing some tests with aid of interpolation curves. In this case, the data were subjected to the following simple selection criteria: $s - M^2 = Q^2(1/x - 1)$ = const for deep-inelastic scattering and $s - M^2 = Q^2(1 - z)$ = const for inclusive annihilation.

The results that we obtained are illustrated in Fig. 10, which shows that relation (20) is consistent with data at sufficiently large values of Q^2. Only the last point in Fig. 10*a* is markedly above the expected value; however, Q^2 is not sufficiently large here—if, instead of this point, we use the corresponding value from the interpolation curve, the result will be lower by a factor of about 1.5, which is quite understandable on the basis of simple considerations on the decrease at infinity. From our results, we can draw the conclusion that experimental data are compatible with the modified reciprocity relation. This may serve as a further check upon basic principles of quantum field theory.

5. CONCLUSIONS

To summarize the results of this study, we would like to note the following.

(i) The reciprocity relation derived in the leading-logarithm approximation of perturbation theory is at odds with experimental data for $\sqrt{Q^2} < 91.2$ GeV. As to its fulfillment for $\sqrt{Q^2} \geq 91.2$ GeV with allowance for the correction factor of about 2 to 4, this is no more than a phenomenological estimate, which is valid only under some assumptions.

(ii) By testing a modified constraint deduced from the basic principles of quantum field theory, it has been found that this constraint can be realized at sufficiently large Q^2. In order to prove this conclusively, it is necessary to analyze data in this region to a higher precision.

REFERENCES

1. N. B. Skachkov, Preprint No. E2-90-301, JINR (Dubna, 1997).
2. S. D. Drell, D. Levy, and T. M. Yan, Phys. Rev. **187**, 2159 (1969); Phys. Rev. D **1**, 1035, 1617, 2402 (1970).
3. H. D. Dahmen and F. Steiner, Preprint TH-1595, CERN (Geneva, 1972).
4. R. Gatto and G. Preparata, Nucl. Phys. B **47**, 313 (1972).
5. J. D. Bjorken, Phys. Rev. **179**, 1547 (1969).
6. V. N. Gribov and L. N. Lipatov, Yad. Fiz., **15**, 781, 1218 (1972) [Sov. J. Nucl. Phys. **15**, 438, 675 (1972)].
7. A. P. Bukhvostov, L. N. Lipatov, and N. P. Popov, Yad. Fiz. **20**, 532 (1974) [Sov. J. Nucl. Phys. **20**, 287 (1975)].
8. Yu. L. Dokshitzer, Zh. Éksp. Teor. Fiz. **73**, 1216 (1977) [Sov. Phys. JETP **46**, 641 (1977)].
9. D. J. Pritchard, Z. Phys. C **2**, 205 (1979); Preprint No. DAMTP-78/20.
10. V. F. Konoplyanikov and N. B. Skachkov, Preprint No. E2-93-294, JINR (Dubna, 1993).
11. H. Albrecht *et al.*, Z. Phys. C **44**, 547 (1989).
12. M. Althoff *et al.*, Z. Phys. C **17**, 5 (1983).
13. H. Aihara *et al.*, Phys. Rev. Lett. **52**, 577 (1984); **61**, 1263 (1988).
14. M. Derrick *et al.*, Phys. Rev. D **35**, 2639 (1987).
15. R. Itoh *et al.*, Phys. Lett. B **345**, 335 (1995).
16. R. Akers *et al.*, Z. Phys. C **63**, 181 (1994).
17. P. Abreu *et al.*, Nucl. Phys. B **444**, 3 (1995).
18. M. Arneodo *et al.*, Phys. Lett. B **364**, 107 (1995); Preprint No. CERN-PPE/95-138, CERN (Geneva, 1995).
19. A. C. Benvenuti *et al.*, Phys. Lett. B **223**, 485 (1989).
20. M. Derrick *et al.*, Z. Phys. C **72**, 399 (1996); **65**, 379 (1995); **69**, 607 (1995).
21. S. Aid *et al.*, Nucl. Phys. B **470**, 3 (1996); T. Ahmed *et al.*, Nucl. Phys. B **439**, 471 (1995).
22. J. J. Aubert *et al.*, Nucl. Phys. B **259**, 189 (1985).
23. M. R. Adams *et al.*, Phys. Rev. D **54**, 3006 (1996).
24. L. W. Whitlow *et al.*, Preprint No. SLAC-357 (Stanford, 1990).
25. A. D. Martin, R. G. Roberts, and W. J. Stirling, Phys. Rev. D **50**, 6734 (1994); **51**, 4756 (1995).
26. C. Callan and D. J. Gross, Phys. Rev. Lett. **22**, 156 (1969); **21**, 311 (1968).
27. V. A. Petrov, Teor. Mat. Fiz. **33**, 280 (1977).
28. Yu. L. Dokshitzer and M. T. Ryskin, Pis'ma Zh. Éksp. Teor. Fiz. **33**, 288 (1981) [JETP Lett. **33**, 272 (1981)].
29. R. Gatto, P. Menotti, and I. Vendramin, Phys. Rev. D **7**, 2524 (1973).
30. G. Curci, W. Furmanski, and R. Petronzio, Nucl. Phys. B **175**, 27 (1980).
31. L. Baulieu, E. G. Floratos, and C. Kounnas, Phys. Lett. B **89**, 84 (1979).
32. E. G. Floratos, C. Kounnas, and R. Lacaze, Nucl. Phys. B **192**, 417 (1981).
33. A. V. Belitsky, Phys. Lett. B **405**, 312 (1997).
34. T. Kawabe, Prog. Theor. Phys. **65**, 1973 (1981).
35. A. Gonzales-Arroyo, Phys. Lett. B **98**, 288 (1981); Preprint No. CPT-80/PE-1221.
36. G. Altarelli, R. K. Ellis, and G. Martinelli, Nucl. Phys. B **160**, 301 (1979).
37. G. Altarelli, Phys. Rep. **81**, 1 (1982).

Translated by A. Isaakyan

Physics of Atomic Nuclei, Vol. 63, No. 1, 2000, pp. 120–138. Translated from Yadernaya Fizika, Vol. 63, No. 1, 2000, pp. 132–151.

ELEMENTARY PARTICLES AND FIELDS
Theory

Nonrenormalizable Superpotential in Four-Dimensional String Models

G. G. Volkov, A. A. Maslikov, H. D. Dahmen[1)], and T. Stroh[1)]

Institute for High Energy Physics, Protvino, Moscow oblast, 142284 Russia

Received May 7, 1998; in final form, December 17, 1998

Abstract—A construction of an effective nonrenormalizable superpotential has been discussed within the approach of a four-dimensional heterotic superstring with free fermions on the world sheet. On the basis of $N = 2$ superconformal theory, useful selection rules that take into account all global symmetries have been obtained within the formalism of covariant vertices and the ghost-picture-changing operation. The results have been applied to the model featuring the effective observable gauge group $U(5) \times U(3)_{\mathrm{H}}$, which includes the non-Abelian horizontal group and which describes (3 + 1) generation. The full superpotential of the model up to sixth order inclusive has been obtained, and its coupling constants have been calculated. The quark–lepton mass spectrum of the model has been discussed with allowance for contributions from nonrenormalizable terms. © *2000 MAIK "Nauka/Interperiodica".*

1. INTRODUCTION

Within the fundamental idea that all known interactions of elementary particles, including gravitational interaction, have a common origin, superstring models—and in particular, a heterotic string [1, 2]—are generally recognized candidates for an adequate underlying theory capable of describing physical reality. In recent years, there have been considerable advances in the nonperturbative approach to string theory. Nonetheless, the work along these lines is far from being completed, and perturbative methods and estimates remain a powerful tool for creating and studying string models. Constructing the effective low-energy (in relation to the Planck scale) action induced by a string is the most important step in this approach.

Since string Grand Unified Theories include supergravity, it is necessary to take into account effects caused by nonrenormalizable terms. To illustrate this, we note that, in string models, quark and lepton mass matrices receive contributions not only from Yukawa trilinear interactions but also from nonrenormalizable higher order interactions. In order to estimate these contributions, it is necessary to be able to calculate the full superpotential of the model. This reduces to evaluating amplitudes within a topological expansion on the basis of (super)conformal field theory. String theories constructed in terms of free fermions on the world sheet [3, 4] admit an exact calculation of amplitudes [5], whereby the predictive power of the relevant models is considerably enhanced. Moreover, it follows from the nonrenormalizability theorem [6] that, in such superstring models, the tree superpotential is not subjected to renormalization and that it does not receive contributions in all orders of perturbation theory.

The requirement that the model possess spacetime supersymmetry implies the existence of at least (2, 0) supersymmetry on the string world sheet [7]. Some useful selection rules could be obtained [8] from amplitudes corresponding to the superpotential by thoroughly analyzing them within $N = 2$ superconformal theory with allowance for all global symmetries.

The present article is organized as follows.

In Section 2, we give a brief account of the covariant formalism for (super)strings, construct vertex operators and string scattering amplitudes associated with them, and describe the ghost-changing-picture operation [9].

In Section 3, we discuss special features of procedures for constructing realistic string Grand Unified Theories in four dimensions and present our own model formulated within the approach of free fermions. In the model describing (3 + 1) generation, we make use of the breakdown of gauge group $G \times G$ to a diagonal subgroup including non-Abelian horizontal symmetry.

In Section 4, we briefly describe the technique of vertex operators in four-dimensional models that is based on $N = 2$ superconformal theory and introduce conventions and terms used in the ensuing exposition.

In Section 5, we discuss renormalizable terms of the superpotential and calculate the full trilinear superpotential of our model.

In Section 6, we investigate nonrenormalizable four-, five-, and six-point terms; obtain useful selection rules for string amplitudes; and apply the results to our model. There, we also determine the full superpotential of the model up to the sixth order inclusive.

In Section 7, we discuss the quark–lepton mass spectrum of the model with allowance for the contribu-

[1)] Department of Physics, Siegen University, D-57068 Siegen, Germany.

tions from nonrenormalizable terms. We also consider a mechanism suppressing the $U(1)$ anomaly.

The Appendix contains operator-product expansions used in this study.

2. VERTEX OPERATORS AND AMPLITUDES IN SUPERSTRING THEORY

A superstring is described by a string field (coordinate) X_μ and its superpartner, a fermion field ψ_μ. The action functional on a two-dimensional string world sheet describes well-known two-dimensional supergravity [10]. If we choose the so-called superconformal gauge appearing to be an extension of the well-known conformal gauge,

$$h^{\alpha\beta} = e^{\varphi}\eta^{\alpha\beta}, \quad \chi_\alpha = \gamma_\alpha\zeta, \tag{1}$$

where $h^{\alpha\beta}$ is a two-dimensional metric, $\eta^{\alpha\beta}$ is a flat metric, and χ_α is a two-dimensional gravitino, the fields φ and ζ decouple by virtue of super-Weyl invariance. Upon going over to two-dimensional Euclidean space (complex plane),

$$t = +i\tau, \quad z = \exp(t + i\sigma), \tag{2}$$

we obtain the action functional for free fields in the form

$$S_E = \frac{1}{2\pi}\int d\bar{z}dz(\partial_{\bar{z}}X^\mu\partial_z X_\mu - \psi^\mu\partial_{\bar{z}}\psi_\mu - \bar{\psi}^\mu\partial_z\bar{\psi}_\mu),$$
$$Z \sim \int DXe^{-S_E}. \tag{3}$$

Now, an expansion into left- and right-handed fields becomes an expansion into analytic and antianalytic fields on a two-dimensional Euclidean surface; that is, ψ^μ is an analytic field, while $\bar{\psi}^\mu$ is an antianalytic field. The stress–energy tensor of the supermultiplet (X^μ, ψ^μ) is

$$T_B = -\frac{1}{2}(\partial_z X^\mu)^2 + \frac{1}{2}\psi^\mu\partial_z\psi_\mu. \tag{4}$$

Here, it is assumed that the operator products involved are normally ordered. The superpartner of (4) (supercurrent),

$$T_F = -\frac{1}{2}\psi^\mu\partial_z X_\mu, \tag{5}$$

is the generator of local supersymmetric transformations.

The points at 0 and ∞ correspond to in- and outstates. The lines of constant time are mapped into circles on the z plane. The shift in time, $t \longrightarrow t + a$, represents a dilatation, and we must associate the generator of dilatation with the Hamiltonian of original string theory.

The propagators of analytic fields (Green's functions in the two-dimensional case) are given by

$$\langle X_\mu(z_1)X_\nu(z_2)\rangle = -\eta_{\mu\nu}\ln(z_1 - z_2),$$
$$\langle \psi_\mu(z_1)\psi_\nu(z_2)\rangle = \frac{-\eta_{\mu\nu}}{z_1 - z_2}. \tag{6}$$

The stress–energy tensor determines an infinitesimal conformal transformation via the generator

$$T_\epsilon = \oint\frac{dz}{2\pi i}\epsilon(z)T(z). \tag{7}$$

A priori, the integral in (7) is taken over the constant-time surface $|z| = \text{const}$, but we can deform the contour since the integrand is an analytic function.

With the aid of expressions similar to (6) and (4), we can calculate the commutator of the generator in (7) with some local field operator. Here, we are interested only in the vacuum expectation values of commutators. Recall that a path integral with a weight of $\exp(-S)$ specifies an operator product, chronologically ordering operators (in the case being considered, the ordering occurs in radius). For one-time commutators, we then have

$$\langle [T_\epsilon, \phi(z)]\rangle = \frac{1}{Z}\int DXe^{-S}\oint_z dz'T(z')\phi(z'). \tag{8}$$

This means that expressions for commutators—recall that these expressions specify the transformation properties of the fields involved—are encoded in the conventional formula of the operator-product expansion.

The expansions of operator products containing the stress-energy tensor T and primary fields [that is, operators transformed under reparametrizations as tensors of conformal dimension h: $\phi(z) \longrightarrow \left(\frac{dz'}{dz}\right)^h \phi(z')$] are of particular interest for conformal theory. As a matter of fact, the operator of a free boson field like X_μ has no definite conformal dimension, since such a field has a logarithmic branch point [see (6)]. Among operators having definite conformal dimensions, we can indicate the operator $\partial_z X$ (dim = 1), the exponential operator $e^{ikX(z)}$ (dim = $k^2/2$), and a fermion field ψ (dim = 1/2).

The operator-product expansions for $T_B(z)$ and $T_F(z)$ form an $N = 1$, (1, 0) superconformal algebra:

$$T_B(w)T_B(z) \sim \frac{3\hat{c}/4}{(w-z)^4} + \frac{2}{(w-z)^2}T_B(z) + \frac{1}{w-z}\partial_z T_B(z),$$
$$T_B(w)T_F(z) \sim \frac{3/2}{(w-z)^2}T_F + \frac{1}{w-z}\partial_z T_F(z), \tag{9}$$

$$T_F(w)T_F(z) \sim \frac{\hat{c}/4}{(w-z)^3} + \frac{1/2}{w-z}T_B(z).$$

Here, $\hat{c} = (2/3)c = 6$, c being the central charge of the Virasoro algebra (conformal anomaly).

The two-dimensional metric $h^{\alpha\beta}$ and the gravitino χ_α transform nontrivially under reparametrizations and supersymmetry transformations. Therefore, the fixing of gauge according to (1) leads to nontrivial Jacobians for these transformations. According to the standard technique due to Faddeev and Popov, these determinants can be expressed in terms of path integrals of exponential functions of the action functionals for ghost–antighost systems. A ghost (c or γ) has quantum numbers of the gauge parameter (it transforms according to the representation that is dual to the adjoint representation), while an antighost (b or β) transforms according to the adjoint representation of the gauge algebra, either obeying statistics opposite to the statistics of gauge generators. It follows that, in our case, the additional contribution to the generating functional in the superconformal gauge is given by

$$\int DbDcD\beta D\gamma \times \exp\left[-\frac{1}{\pi}\int dz d\bar{z}(b_{zz}\nabla_{\bar{z}}c^z + \beta_z\nabla_{\bar{z}}\gamma + \text{c.c.})\right]. \quad (10)$$

The fields c and b (γ and β) anticommute (commute) and have conformal dimensions of –1 and +2 (–1/2 and +3/2), respectively.

Recasting expression (10) into a form that is appropriate for a curved space, we can evaluate the relevant stress–energy tensors T_{bc} and $T_{\beta\gamma}$ or reconstruct them from the requirement that the operator products with ghost fields have a correct structure. Further, an analysis of the operator-product expansions for $T_{bc}(z_1) \times T_{bc}(z_2)$ and $T_{\beta\gamma}(z_1) \times T_{\beta\gamma}(z_2)$ makes it possible to calculate the contributions of our antighost–ghost systems with the conformal dimensions j and $(1-j)$ to the central charge of the Virasoro algebra [see the first equation in (9)]. The result is

$$c = \pm(1-3k^2), \quad (11)$$

where $k = 2j - 1$ and a minus sign corresponds to commuting ghosts. Eventually, we have the following contributions:

$$c_X = D, \quad c_{bc} = -26, \quad c_\psi = D/2, \quad c_{\beta\gamma} = +11. \quad (12)$$

This corresponds to the absence of a conformal anomaly in spacetime of dimensionality $D = 26$ for a bosonic string and in spacetime of dimensionality $D = 10$ for a superstring.

For the ghost systems being considered, the anomalous current of the ghost number (that which is conserved on a flat world sheet) can be defined as

$$J_z^{bc} = c^z b_{zz}, \quad J_z^{\beta\gamma} = \beta_z\gamma, \quad \partial_{\bar{z}}J_z = (1/8)k\sqrt{h}R^{(2)},$$

where $k = 3$ and 2, respectively, while $R^{(2)}$ is the intrinsic curvature of the world sheet that is specified by the metric $h_{\alpha\beta}$. Further, we can associate a boson field with each current, requiring that all operator-product expansions of the theory remain unchanged, for example,

$$J_z^{bc} = J_z^\varphi = \partial_z\varphi, \quad T_\varphi = +\frac{1}{2}(\partial_z\varphi\partial_z\varphi + 3\partial_z^2\varphi), \quad \langle\varphi(z_1)\varphi(z_2)\rangle = \ln(z_1 - z_2). \quad (13)$$

This stress–energy tensor corresponds to the theory of a free boson field with an incorrect sign of the kinetic term and with a nonzero (–3) vacuum charge at infinity: $\langle 0|e^{+3\varphi}|0\rangle = 1$. In this theory, the conformal dimension of exponential operators is given by $\dim(:e^{\alpha\varphi}:) = (1/2)\alpha(\alpha - 3)$, and ghosts can be identified with exponentials:

$$b_{zz} \sim :e^{-\varphi}:, \quad \dim = 2; \quad c^z \sim :e^{\varphi}:, \quad \dim = -1. \quad (14)$$

Finally, it can be shown that the exponentials of free boson fields are anticommuting operators.

A similar procedure for β–γ ghosts (bosonization of bosons) is more complicated, but it is very useful. We have

$$J_z = -\partial_z c,$$
$$T_{zz}^{(c)} = -\frac{1}{2}(\partial_z c\partial_z c - 2\partial_z^2 c) = -\frac{1}{2}(J_z J_z - 2\partial_z J_z). \quad (15)$$

(The boson c should not be confused with the anticommuting ghost c^z.) We use opposite signs for the kinetic terms in performing a bosonization of the b–c and β–γ systems, because the operator-product expansions $J^{(bc)}J^{(bc)}$ and $J^{(\beta\gamma)}J^{(\beta\gamma)}$ feature anomalous terms of opposite signs. For the systems with tensor (15), the conformal dimension of exponential operators is given by

$$\dim(e^{\alpha c}) = -\frac{1}{2}\alpha(\alpha + k)\Big|_{k=2} = -\frac{\alpha^2}{2} - \alpha. \quad (16)$$

However, the process of bosonization has not yet been completed at this stage because

(i) the contribution of the tensor in (15) to the central charge is $c_c = 1 \oplus 3k^2|_{k=2} = +13$ and not 11 (the correct sign of the kinetic term was operative here);

(ii) $\dim(e^{+c}) = -3/2$ and $\dim(e^{-c}) = +1/2$, but $\dim(\beta) = +3/2$ and $\dim(\gamma) = -1/2$ (opposite signs);

(iii) the exponentials are anticommuting operators, while the ghosts β and γ commute.

All these problems are solved by introducing the system of fermions ξ and η with conformal dimensions of 0 and 1 and with the stress–energy tensor

$$T^{(\xi\eta)} = \partial_z\xi \times \eta. \quad (17)$$

This system has a central charge of –2; thus, this is precisely the value that must be added to the charge of c

fields in order to obtain 11. Eventually, the combinations

$$\beta \sim \partial_z \xi e^{-c} \sim e^{-c+\chi}\partial_z \chi, \quad \gamma \sim \eta e^{+c} \sim e^{c-\chi},$$
$$\langle \chi(z_1)\chi(z_2)\rangle = -\langle c(z_1)c(z_2)\rangle = \ln(z_1 - z_2) \tag{18}$$

have correct dimensions and correct operator products.

We note that the system with stress–energy tensor (15) and $k = 2$ corresponds to a free massless boson field c with a vacuum charge of +2 at infinity. Thus, only the correlation functions for operators with a total charge of –2 are nonzero for this system. The boson field c will play a key role in calculating string scattering amplitudes.

A scattering amplitude must be a sum of path integrals for two-dimensional quantum field theory with insertions of vertex operators in Riemann surfaces of relevant genus (string world sheets). By a vertex operator for a given physical state, we mean the set of two-dimensional conformal fields representing the state quantum numbers with respect to all symmetries of the model.

For the state with a set Λ of quantum numbers and a momentum K^μ, the integrated vertex operator has the form

$$V_\Lambda(K) = \int d^2z \sqrt{h} W_\Lambda(z, \bar{z}) e^{(i/2)KX} e^{(i/2)K\bar{X}}. \tag{19}$$

Integration is necessary here since the vertex can be placed at any point on the world sheet. For the operator $V_\Lambda(K)$ to be invariant under reparametrizations, it is necessary that the operator $W_\Lambda(z, \bar{z}) e^{(i/2)KX} e^{(i/2)K\bar{X}}$ be a primary field of dimension (1, 1).

As soon as the gauge is fixed according to (1), the string action functional develops ghost corrections. A sphere corresponds to a tree amplitude, and an N-point amplitude can be represented as

$$A(\Lambda_1, K_1; \ldots; \Lambda_N, K_N)$$
$$= g^{(N-2)} \int DXD\psi D\phi_{\text{int}} DbDcD\beta D\gamma$$
$$\times \exp\{-[S_{\text{str}}(X_\mu, \psi_\mu, \phi_{\text{int}}) + S_{\text{gh}}(b, c, \beta, \gamma)]\} \prod_{i=1}^{N} V_{\Lambda_i}(K_i), \tag{20}$$

where g is the triple constant of string interaction, while the fields ϕ_{int} describe the internal degrees of freedom of a string (they can manifest themselves in noncritical dimensions). The same amplitude can be represented in other equivalent forms if the bosonization procedure is used.

We can now write an N-point amplitude in the form of an amplitude of free theory in two-dimensional flat space. We have

$$A(\Lambda_1, K_1; \ldots; \Lambda_N, K_N) = g^{(N-2)}$$
$$\times \int \prod_{i=1}^{N} d^2 z_i \left\langle \prod_{j=1}^{N} e^{(i/2)K_j X} W_\Lambda(z_j, \bar{z}_j) e^{(i/2)K_j \bar{X}} \right\rangle. \tag{21}$$

We note that expression (21) is not yet well defined because the fixing of gauge according to (1) did not remove completely reparametrization invariance. The residual symmetry group is the open three-parameter group of linear fractional transformations with complex coefficients [$SL(2, C)$],

$$z \longrightarrow \frac{az + b}{cz + d}, \tag{22}$$

where $ad - bc = 1$.

A natural means to avoid this problem is to divide expression (21) by the $SL(2, C)$ group volume. By using infinitesimal transformations of the $SL(2, C)$ transformations (22) in the form

$$\delta z = \lambda_{-1} + \lambda_0 z + \lambda_1 z^2,$$

we can find the Jacobian of the transition from any three complex z_i to three complex parameters λ_i. We have

$$\left| \frac{\partial(z_i, z_j, z_k)}{\partial(\lambda_{-1}, \lambda_0, \lambda_1)} \right|^2 = |z_i - z_j|^2 |z_i - z_k|^2 |z_j - z_k|^2. \tag{23}$$

We can now remove integration with respect to group parameters and fix arbitrarily the values of three z_i. The standard choice is $z_i \longrightarrow \infty$, $z_j = 1$, and $z_k = 0$.

For a boson string, the form of vertex operators is completely determined by the conditions requiring that the conformal dimension be correct and that the quantum numbers of a given state exist with respect to all symmetries of the model.

For superstrings (the critical dimension is $D = 10$), the situation is more complicated. In this case, the ghost degrees of freedom—in particular, c ghosts [see (16)], bosonized bosonic ghosts—become operative; in addition; the spectrum of the theory contains spacetime fermionic states with quite a nontrivial construction of vertex operators.

It is well known that, in superstrings, spacetime bosonic states correspond to the Neveu–Schwarz sector with antiperiodic boundary conditions for fermionic fields on the world sheet [$\psi^\mu(\tau, \sigma + 2\pi) = -\psi^\mu(\tau, \sigma)$], whereas spacetime fermionic states correspond to the Ramond sector with periodic boundary conditions [$\psi^\mu(\tau, \sigma + 2\pi) = \psi^\mu(\tau, \sigma)$].

Making the change of variable $z = e^w = \exp(t + i\sigma)$ (2) and performing this conformal transformation for the tensor ψ_μ of dimension 1/2, we obtain

$$\psi_\mu(w) \longrightarrow \psi'_\mu(z) = \left(\frac{dz}{dw}\right)^{1/2} \psi_\mu[z(w)]$$
$$= e^{w/2} \psi_\mu[z(w)] = \sqrt{z}\psi_\mu(z). \tag{24}$$

It follows that, upon one circumvention around a string, $w \longrightarrow w + 2i\pi$, we obtain the factor of $e^{i\pi} = -1$ on the right-hand side of (24). Hence, periodic (Ramond) fields are two-valued on the z plane. Thus, the analytic

function $\psi^\mu(z)$ has a square-root branch point at z_0 (the point to which the asymptotic state of the string is mapped). The vertex operator generating Ramond states (so-called spin operators) must be operators that lead to this structure of ramification.

In order to construct the required operator, we replace fermions on the world sheet, ψ^μ, by fermion pairs and bosonize them:

$$\frac{1}{\sqrt{2}}(\psi^1 \pm i\psi^2) = \psi^{1\pm i2} \sim e^{\pm i\phi_{12}}, \text{ etc.} \tag{25}$$

(We note that, in terms of the fields $\psi^{1\pm i2}$, the fermionic action functional takes the form $\int d^2z\, \psi^{1+i2}\partial_+\psi^{1-i2}$ + c.c., which is similar to that of the ghost action functional.) If we now construct the (spin) operator

$$S_\beta = \prod_{(k,l)=(1,2)}^{(9,10)} e^{(\pm i/2)\phi_{kl}} = e^{i\alpha_\beta\phi}, \tag{26}$$

we will obtain a ramification for $\psi^\mu(z)$. Here, the index β determines the choice of the signs $\pm$ for all (five for $D = 10$) exponentials. Thus, we have $2^5 = 32$ components of the spin operator, but $32 = 16 + \overline{16}$ is the dimension of the spinor representation of the $SO(10)$ group. Moreover, the coefficients in the exponentials determine the weights of the vectors of the spinor representation, $\alpha_\beta = (\pm 1/2, \pm 1/2, \ldots, \pm 1/2)$, and we can construct the $SO(2N)$ generators in the bosonized form.

However, the operator $S_\beta(z)$ has the dimension of $|\alpha_\beta|^2/2 = N/8$; in the case of superstrings, $D = 10$, and we obtain 5/8, but the vertex operator must have the dimension equal to unity.

The problem can be solved by taking into account superconformal ghost degrees of freedom. Indeed, the transformation of supersymmetry for the string coordinate has the form $\delta X^\mu = i\varepsilon\psi^\mu$, and the ghost γ has quantum numbers of the parameter ε. Thus, we see that, if the Ramond vertex operator generates a ramification for the field ψ^μ, the ghosts γ and β must also have a square-root branch point. As a result, the spin field for commuting spinor fields, $e^{(-1/2)c(z)}$, with a conformal dimension of 3/8 [see equation (16)] must be added to the spinor operator S_β. Thus, the first version of the covariant fermion vertex is

$$V^f_{(-1/2)} \sim e^{(-1/2)c(z)} S_\beta(z) e^{iKX(z)}. \tag{27}$$

This is, however, insufficient for describing fermion scattering, because $V^f_{(-1/2)}$ has a fermion ghost charge of –1/2, so that only a four-fermion amplitude can cancel out the ghost background charge of +2. Therefore, we need the second version of the fermion vertex, $V^f_{(+1/2)}$, with a positive ghost charge.

In the Becchi–Rouet–Stora–Tyutin (BRST) formulation, physical states are constructed as those that are invariant under the BRST transformation:

$$Q_{\text{BRST}}|\text{phys}\rangle = 0, \quad Q^2_{\text{BRST}} = 0.$$

Owing to the last condition, states of the form $|\text{null}\rangle = Q_{\text{BRST}}|\psi\rangle$ satisfy the first condition; however, such states have zero norm. Thus, attention should be given only to operators with a nontrivial BRST cohomology, and we can choose states that are characteristic representatives of cohomology classes.

In the case of superstrings, we have

$$Q_{\text{BRST}} = \oint \frac{dz}{2i\pi}\left\{[cT_B(X, \psi; \beta, \gamma) - bc\partial c] + \frac{1}{2}\gamma\psi^\mu\partial X_\mu + \frac{1}{4}\gamma^2 b\right\}, \tag{28}$$

where $T_B(X, \psi; \beta, \gamma)$ is the full strength tensor for all the above fields. As a matter of fact, the only operators that commute with Q_{BRST} (those that correspond to BRST invariant states) and which have a positive ghost charge can be written as $[Q_{\text{BRST}}, V]$. All of these are null vectors (spurions), with the exception of

$$V'_{\text{phys}} = [Q_{\text{BRST}}, \xi V_{\text{phys}}]. \tag{29}$$

This comes as no surprise since ξ is not a part of the irreducible algebra of the fermionic ghosts β and γ; this is because a representation of the irreducible current algebra includes bosons c and fermions η and $\partial\xi$, but not ξ themselves [see equations (18)].

It follows that, by setting $V_{\text{phys}} = V^f_{(-1/2)}$, we obtain a second version of the fermion vertex operator with a ghost number of 1/2 [9] (this version is referred to as +1/2 picture):

$$V^f_{(+1/2)} \sim \left\{e^{c/2}\left[\partial X_\mu + \frac{i}{4}(K\times\psi)\psi_\mu\right]\gamma^\mu_{\alpha\beta}S^\beta + \frac{1}{2}e^{(3/2)c}\eta b S_\alpha\right\}e^{iKX}. \tag{30}$$

The second term in (30) does not contribute to the expectation value because of ghost-charge nonconservation, and the entire contribution comes from the component $j_{\text{BRST}} \sim (1/2)(e^c e^{-\chi})\psi^\mu\partial X_\mu \sim (1/2)\gamma T_F$ [see equation (5)]. Since $e^{-\chi}(z_1)\xi(z_2) \sim 1/(z_1 - z_2)$, we can recast relation (29) into the form

$$V_{q+1} = :e^c T_F V_q:. \tag{31}$$

As a matter of fact, there are an infinite number of pictures (this is so for bosonic vertex operators as well). This is because the β–γ system of commuting ghosts is described by the first-order action functional (10). For a free β–γ system, there exist an infinite number of equivalent linearly independent vacua (pictures) featur-

ing different ghost charges, and there are no transitions between these vacua [9].

The relation in (29) or (31) describes the picture-changing operation that leads to a change in the ghost charge by unity.

3. GRAND UNIFICATION MODELS ON THE BASIS OF A FOUR-DIMENSIONAL HETEROTIC STRING

In order that a heterotic string defined in ten-dimensional space could describe a real world, six dimensions must be unobservable—for example, they may be compactified into a six-dimensional object of Planck scale. More generally, we can consider a four-dimensional heterotic string equipped with an intrinsic conformal model $\mathcal{M}_{c_L;\,c_R}$ that contributes to the central charges of the left-hand and right-hand Virasoro algebras, $c_L = 15 - 4 \times 3/2 = 9$ and $c_R = 26 - 4 = 22$, respectively, whereby the cancellation of conformal anomalies is ensured.

Thus, we can see that, in the formulation of a four-dimensional heterotic string with free fermions on the world sheet [3, 4], there are, in addition to two transverse bosonic coordinates X_μ and $\bar{X}_\mu$ and their left-handed superpartners ψ_μ, 44 right-handed and 18 left-handed real fermions in the intrinsic sector (each real fermion contributes $c_f = 1/2$ to the corresponding central charge). Hence, a model can be specified by a set of admissible boundary conditions that correspond to a circumvention around a closed string for all fermions: $f \longrightarrow -\exp(i\pi\alpha(f))f$, $\alpha(f) \in [-1, 1]$. The value of $\alpha = 1$ corresponds to the periodic (R) boundary condition, while the value of $\alpha = 0$ corresponds to the antiperiodic (NS) boundary condition; if fermions can be paired and transformed into a complex fermion, rational values are admissible for α. In the light-cone gauge, each set of fermionic boundary conditions is described by a $(20_L; 44_R)$-dimensional α vector, the fact that the field ψ_μ has two degrees of freedom being taken into account here.

There always exists a diagonal basis in which the set Ξ of admissible fermionic boundary conditions is described by a set of basis α vectors b_i and their combinations $\sum_i m_i b_i$ ($m_i = 0, 1, \ldots, N_i$) referred to as sectors. The integers N_i specify the additive group of basis vectors, $Z(b_i)$. Here, the set of basis vectors must satisfy the well-known conditions that follow from the requirement of modular invariance of the generating functional [3, 4].

It would be useful to obtain a four-dimensional construction by performing a fermionization of extra bosonic coordinates of a heterotic string of critical dimension. This implies that real boson and fermion fields are identified as $\partial\phi \sim \chi_i\chi_{i+1}$. With allowance for all the above, the supercurrent in (5) for a fermionic heterotic string can be represented as

$$T_F \sim \psi^\mu \partial X_\mu + f_{ijk}\chi^i\chi^j\chi^k, \tag{32}$$

where f_{ijk} are the structure constants of a semisimple Lie group G of dimension $3(10 - 4) = 18$. For the model to possess $N = 1$ spacetime supersymmetry, it is necessary that this group be $G = SU(2)^6$ [11]. In this case, the fermions on the world sheet, χ, are broken down into the triplets (χ_i, y_i, ω_i), $i = 1, \ldots, 6$, with admissible boundary conditions of the type (1, 1, 1), (1, 0, 0) or (0, 0, 0), (0, 1, 1), depending on the conditions for the fermions ψ^μ (R or NS).

The number of quasirealistic string Grand Unified Theories that describe correctly the observable sector of the Standard Model (SM) is not so great. They are well known and are based on the following gauge groups [12–14]: the SM group; the Pati–Salam group $SU(4)^c \times SU(2)_L \times SU(2)_R$; the flip gauge group $SU(5) \times U(1)$; and the $SO(10)$ group, which includes the flip group. Attempts have also been made to construct string Grand Unified Theories on the basis of the $SU(5) \times U(1)$ and $SO(10)$ groups at level 2 of the current algebra and at level 3 with three effective generations [16]. A different method for constructing a string Grand Unified Theory on the basis of gauge groups of the type $G \times G$ was proposed in [17].

We deem it interesting to study a string Grand Unified Theory including a rank-16 gauge group of the form $G \times G \subset E_8 \times E_8$, where the group G contains, as subgroups, not only the SM group but also a non-Abelian horizontal group like $SU(3)_H$ or $SU(3)_H \times U(1)_H$. Such a subgroup describes three observable fermion generations in a natural way, explaining their nature [$SU(3)_H$ triplets], and leads to interesting low-energy physics compatible with up-to-date experimental data [18]. In addition, we note that, when the gauge group is broken down in this construction to a diagonal subgroup, there arise higher representations that are peculiar to level 2 and which are necessary for a further chain of gauge-symmetry breaking.

The model discussed in the present article is constructed in terms of six basis vectors [17]. These vectors (see Table 1) generate the additive group $Z_2^4 \times Z_4 \times Z_8$. Here, the boundary conditions for 20 left-handed fermions (ψ, χ, y, ω) and 12 right-handed fermions $(\bar{\varphi})$ are given in the real notation. The remaining 32 right-handed fermions are represented as (8 + 8) complex quantities Ψ and Φ. As a matter of fact, the left-handed fermions also admit pairing for the above choice of basis. We will make use of this circumstance, numbering them from 1 to 10.

In the model being considered, the rank-22 affine current algebra of level 1 is generated originally in the right-handed sector: $SO(2)^3_{1,2,3} \times SO(6)_4 \times [U(5) \times U(3)_H]^2$. The corresponding gauge superfields arise in

Table 1. Basis of boundary conditions for two-dimensional fermions

Vector	$\psi_{1,2}$	$\chi_i y_j y_k$	$y_i \chi_j \omega_k$	$\omega_i \omega_j \chi_k$	$\bar{\varphi}_{1,\ldots,12}$	$\Psi_{1,\ldots,8}$	$\Phi_{1,\ldots,8}$
b_1	11	111111	111111	111111	1^{12}	1^8	1^8
b_2	11	111111	000000	000000	0^{12}	$(1/2)^8$	0^8
b_3	11	111100	000011	000000	$0^4 1^8$	0^8	1^8
$b_4 = S$	11	110000	001100	000011	0^{12}	0^8	0^8
b_5	11	001100	000000	110011	1^{12}	$(1/4)^5 - (3/4)^3$	$-(1/4)^5\,(3/4)^3$
b_6	11	110000	000011	001100	$1^2 0^4 1^6$	1^8	0^8

the 0 and $S = b_4$ sectors. What is enclosed in brackets can be considered as the result of a breakdown of the fundamental string group $E_8 \times E_8$, whereas the remaining part can be treated as a hidden group originating from compactification.

A full list of model massless states at the Plank scale, together with all quantum numbers (excitation of left-handed fermions, representations, and hypercharges according to gauge groups), is given in Table 2. In particular, it presents all fermionic states of the sectors with positive (left-hand) helicity (third column). Their superpartners arise in the sectors with the $S = b_4$ component changed by unity. The first two columns quote the excitations of left-handed χ, y, and ω fermions for scalar superpartners, in terms of which we will define all vertex operators (see Section 4). The first column contains the number of a row (for the sake of convenience), the symbol corresponding to a given set of superfields, and (everywhere, with the exception of the first row) the numbers of two fermions χ with nonzero $U(1)_R$ charges (+1/2). Row no. 1 (Φ) describes vectorlike supermultiplets (there are superfields in antirepresentations as well), which can be Higgs fields. In terms of quantities used in Section 4, these fields are described by NS-type vertex operators, for which the number of a fermion χ with a nonzero charge (+1) is indicated in the second column. All the remaining fields are described by R-type vertex operators, for which excitations of the fermions y and ω are indicated in the second column. The symbol $\pm_k$ stands for the charge of $\pm 1/2$ corresponding to the kth fermion. The lower signs in the fifth and sixth rows corresponds to sectors whose components are indicated in parentheses. The helicity according to the hidden group $SO(2)^3_{1,2,3} \times SO(6)_4$ is indicated as $\pm_1$, $\pm_2$, $\pm_3$, and $\pm_4$ (fourth column).

The sector of model no. 2 (Ψ fields) describes 3 + 1 generations [triplet and singlet according to the horizontal group $SU(3)_H$] including the right-handed neutrino.

In the model being considered, the original gauge group $(U(5) \times U(3))^I \times (U(5) \times U(3))^{II}$ can be broken down, via the Higgs mechanism, to the diagonal subgroup: $G \times G \longrightarrow G$. As a result, the effective level of the current algebra increases to 2, and there arise higher representations of the group G^{diag}. In this construction, it is reasonable to consider both the flip and the nonflip embedding of the matter fields Ψ (no. 2) in the $SU(5)$ group [19]. By way of example, we indicate that, in [19], the consistency of the evolution of coupling constants [20] is discussed within various versions of unification with allowance for various possible corrections, including those from massive string states [21]. In the flip version, the electromagnetic charge can be constructed as

$$Q_{em} = Q^{II} - Q^{I} = (T_5^{II} - T_5^{I}) + \frac{2}{5}(\tilde{Y}_5^{II} - \tilde{Y}_5^{I}) = \bar{T}_5 + \frac{2}{5}\bar{Y}_5,$$

where $T_5 = \mathrm{diag}(1/15, 1/15, 1/15, 2/5, -3/5)$.

It is interesting to note that the model being discussed can be constructed in terms of different basis vectors with a different additive group. For example, the spectrum of the model is completely reproduced by the basis vectors from Table 3 with additive group $Z_2 \times Z_6 \times Z_{12} \times Z_2 \times Z_2 \times Z_2$ [22].

4. GLOBAL $U(1)_R$ SYMMETRIES IN A STRING AMPLITUDE

The possibility of obtaining a realistic description of the fermion masses and mixing angles is a decisive criterion for choosing a string-unification model. Within our approach, it is therefore necessary to write down all renormalizable and appropriate nonrenormalizable contributions to the superpotential W and to study their implications for the fermion mass matrix for various ways of horizontal-symmetry breaking.

In superstring models, an acceptable superpotential is determined both by gauge invariance and by a two-dimensional superconformal model on the world sheet. This imposes additional severe constraints on the superpotential. In particular, each term in the superpotential must correspond to a nonzero correlation of vertex operators on the world sheet.

Conformal invariance makes it possible to construct vertex operators in different pictures corresponding to different ghost numbers. A canonical vertex operator for spacetime boson (fermion) is constructed in –1 (–1/2)

Table 2. Quantum numbers of massless states of the model considered in this article

No., χ	y, ω	$b_1, b_2, b_3, b_4, b_5, b_6$	SO_{hid}	$U(5)^{\text{I}}$	$U(3)^{\text{I}}$	$U(5)^{\text{II}}$	$U(3)^{\text{II}}$	$\tilde{Y}_5^{\text{I}}$	$\tilde{Y}_3^{\text{I}}$	$\tilde{Y}_5^{\text{II}}$	$\tilde{Y}_3^{\text{II}}$
1	2	*NS*		5	$\bar{3}$	1	1	-1	-1	0	0
	2			1	1	5	$\bar{3}$	0	0	-1	-1
	6	0 2 0 1 2(6) 0		5	1	5	1	-1	0	-1	0
$\hat{\underline{\Phi}}$	6			1	3	1	3	0	1	0	1
	10			5	1	1	3	-1	0	0	1
	10			1	3	5	1	0	1	-1	0
2	$+_3+_4$	0 1 0 0 0 0		1	3	1	1	$\frac{5}{2}$	$-\frac{1}{2}$	0	0
	$+_3+_4$			$\bar{5}$	3	1	1	$-\frac{3}{2}$	$-\frac{1}{2}$	0	0
	$+_3+_4$			10	1	1	1	$\frac{1}{2}$	$\frac{3}{2}$	0	0
$\hat{\underline{\Psi}}$	$-_3-_4$	0 3 0 0 0 0		1	1	1	1	$\frac{5}{2}$	$\frac{3}{2}$	0	0
6, 10	$-_3-_4$			$\bar{5}$	1	1	1	$-\frac{3}{2}$	$\frac{3}{2}$	0	0
	$-_3-_4$			10	3	1	1	$\frac{1}{2}$	$-\frac{1}{2}$	0	0
3	$+_7\mp_8$	0 0 1 1 3 0	$-_1\pm_2$	1	1	1	3	0	$-\frac{3}{2}$	0	$-\frac{1}{2}$
	$+_7\mp_8$	0 0 1 1 7 0	$-_1\pm_2$	1	$\bar{3}$	1	1	0	$\frac{1}{2}$	0	$\frac{3}{2}$
$\hat{\underline{\Psi}}^{\text{H}}$	$-_7\mp_8$	0 2 1 1 3 0	$+_1\pm_2$	1	$\bar{3}$	1	3	0	$\frac{1}{2}$	0	$-\frac{1}{2}$
2,10	$-_7\mp_8$	0 2 1 1 7 0	$+_1\pm_2$	1	1	1	1	0	$-\frac{3}{2}$	0	$\frac{3}{2}$
4	$\mp_5\mp_7$	1 1 1 0 1 1	$\mp_1\pm_3$	1	1	1	$\bar{3}$	0	$-\frac{3}{2}$	0	$\frac{1}{2}$
	$\mp_5\mp_7$	1 1 1 0 5 1	$\mp_1\pm_3$	1	$\bar{3}$	1	1	0	$\frac{1}{2}$	0	$-\frac{3}{2}$
$\hat{\underline{\Phi}}^{\text{H}}$	$\mp_5\pm_7$	1 3 1 0 1 1	$\pm_1\pm_3$	1	$\bar{3}$	1	$\bar{3}$	0	$\frac{1}{2}$	0	$\frac{1}{2}$
2,10	$\mp_5\pm_7$	1 3 1 0 5 1	$\pm_1\pm_3$	1	1	1	1	0	$-\frac{3}{2}$	0	$-\frac{3}{2}$
5	$\mp_4+_9$	0 1(3) 1 0 2(6) 1	$-_1\pm_3$	1	$3(\bar{3})$	1	1	$\pm\frac{5}{4}$	$\pm\frac{1}{4}$	$\pm\frac{5}{4}$	$\mp\frac{3}{4}$
	$\mp_4-_9$		$+_1\pm_3$	$5(\bar{5})$	1	1	1	$\pm\frac{1}{4}$	$\mp\frac{3}{4}$	$\pm\frac{5}{4}$	$\mp\frac{3}{4}$
$\hat{\underline{\phi}}$	$\pm_4-_9$	0 1(3) 1 0 4 1	$-_1\pm_3$	1	1	1	$3(\bar{3})$	$\pm\frac{5}{4}$	$\mp\frac{3}{4}$	$\pm\frac{5}{4}$	$\pm\frac{3}{4}$
6,10	$\pm_4+_9$		$+_1\pm_3$	1	1	$5(\bar{5})$	1	$\pm\frac{5}{4}$	$\mp\frac{3}{4}$	$\pm\frac{1}{4}$	$\mp\frac{3}{4}$
2,10	$+_4\pm_5$	1 2 0 0 3(5) 1	$\pm_1-_4$	1	1	1	1	$\pm\frac{5}{4}$	$\pm\frac{3}{4}$	$\mp\frac{5}{4}$	$\mp\frac{3}{4}$
$\hat{\underline{\sigma}}$ 2, 6	$+_3\mp_5$	1 1(3) 0 1 5(3) 1	$+_1\mp_4$	1	1	1	1	$\pm\frac{5}{4}$	$\pm\frac{3}{4}$	$\pm\frac{5}{4}$	$\pm\frac{3}{4}$
6,10	$+_7\pm_3$	0 0 1 0 2(6) 0	$\mp_3+_4$	1	1	1	1	$\pm\frac{5}{4}$	$\mp\frac{3}{4}$	$\pm\frac{5}{4}$	$\mp\frac{3}{4}$

Table 3. Different set of basis vectors for the model considered in this article

Vector	$\psi_{1,2}$	$\chi_i y_j y_k$	$y_i \chi_j \omega_k$	$\omega_i \omega_j \chi_k$	$\bar{\varphi}_{1,\ldots,12}$	$\Psi_{1,\ldots,8}$	$\Phi_{1,\ldots,8}$
b_1	11	111111	111111	111111	1^{12}	1^8	1^8
b_2	11	111111	000000	000000	0^{12}	$1^5\ 1/3^3$	0^8
b_3	11	110011	000000	001100	$0^8 1^4$	$1/2^5\ 1/6^3$	$-1/2^5\ 1/6^3$
$b_4 = S$	11	110000	001100	000011	0^{12}	0^8	0^8
b_5	11	000000	110000	001111	$1^6 0^2 1^2 0^2$	$1^5\ 0^3$	$0^5\ 1^3$
b_6	11	110000	000011	001100	$1^6 0^4 1^2$	0^8	1^8

pattern. The conformal fields that represent the ghost charge q can be written as e^{qc} with conformal dimension $(-1/2q^2 - q, 0)$.

A modular-invariant theory featuring $N = 1$ spacetime supersymmetry also contains a hidden global $N = 2$ superconformal symmetry of the world sheet [7], the latter distinguishing three components of the $N = 1$ supercurrent, T_F^+, T_F^-, and T_F^0, having the charges of +1, –1, and 0 with respect to the $U_J(1)$ group. The conserved current J of the $N = 2$ world-sheet algebra can play a key role in constructing a realistic phenomenology. In terms of operator products, the $N = 2$ algebra has the form

$$T_F^+(w)T_F^-(z) \sim \frac{\hat{c}}{(w-z)^3} + \frac{2\partial J}{(w-z)^2} + \frac{2T + \partial J}{w-z},$$
$$J(w)T_F^+(z) \sim \pm\frac{T_F^+}{w-z}, \quad J(w)J(z) \sim \frac{\hat{c}/2}{(w-z)^2}. \tag{33}$$

Thus, all vertex operators have a definite $U(1)$ charge. In our description of a four-dimensional heterotic superstring with free fermions, $J(z)$ is given by

$$J(z) = i\partial_z(H_{\chi 12} + H_{\chi 34} + H_{\chi 56}), \tag{34}$$

where $H_{\chi ij}$ stands for the bosonized components of the supersymmetry generator (which corresponds to the basis vector S with the Ramond conditions for fermions χ) [8].

For the bosonic and fermionic components of the chiral superfields, the general expressions for the vertex operator are given, respectively, by

$$V^b_{(-1)}(z) = e^{-c}e^{i\alpha H_{\chi 12}}e^{i\beta H_{\chi 34}}e^{i\gamma H_{\chi 56}}Ge^{(i/2)KX}e^{(i/2)K\bar{X}} \tag{35}$$

and by

$$V^f_{\alpha(-1/2)}(z) = e^{-c/2}S_\alpha e^{i(\alpha-1/2)H_{\chi 12}} \times e^{i(\beta-1/2)H_{\chi 34}}e^{i(\gamma-1/2)H_{\chi 56}}Ge^{(i/2)KX}e^{(i/2)K\bar{X}}, \tag{36}$$

where $\alpha, \beta, \gamma = 0, \pm 1/2, \pm 1$. The conformal fields for the left-handed fermions χ (excitations of the basis vector $S = b_4$ generating supersymmetry) are written explicitly, whereas G contains the remaining left- and right-handed conformal fields. In relation to (26), there emerged additional factors because, in four dimensions, ψ^μ is now broken down into (4 + 6) fermions (six enter into the intrinsic conformal model) and because the spacetime spinor S_α then has a conformal dimension of (1/4, 0).

For bosonic (fermionic) vertex operators in the canonical –1 (–1/2) picture, the $U_J(1)$ charge is $\alpha + \beta + \gamma = 1$ $(\alpha + \beta + \gamma - 3/2 = -1/2)$. This condition and the requirement that a vertex operator have a correct conformal dimension of (1, 1) $(\alpha^2 + \beta^2 + \gamma^2 \le 1)$ lead to a unique solution in the form of permutations

$$(1, 0, 0)\ (\mathrm{NS}) \text{ and } (1/2, 1/2, 0)\ (\mathrm{R}). \tag{37}$$

These are α, β, and γ charges for a canonical bosonic vertex.

Since we consider supersymmetric theories, we can make use of a canonical bosonic vertex (–1 picture), which determines the remaining vertices in different pictures [see, for example, equation (36)]. We define a vertex as an R (NS) vertex if it contains (does not contain) $H_{\chi ij}$ fields (for fermions χ) with charges α, β, and $\gamma = \pm 1/2$ in a canonical boson picture. This means that, for the NS sector, the left-hand component is equal to zero and that all the remaining sectors are R sectors (for massless states).

Owing to spacetime symmetry, only N-point functions with two fermionic vertices are necessary for reconstructing the superpotential. The tree string amplitude has the form

$$A_N = \frac{g^{(N-2)}}{(2\pi)^{(N-3)}}\sqrt{2} \times \int\prod_{i=1}^{N-3} d^2 z_i \langle V^f_{1(-1/2)}V^f_{2(-1/2)}V^b_{3(-1)}V^b_{4(0)}\ldots V^b_{N(0)}\rangle. \tag{38}$$

The choice of picture is determined by the requirement that the total ghost charge be –2.

It goes without saying that, for a nonzero amplitude, the total charge must be equal to zero (upon performing the picture-changing operation) not only for $U_J(1)$ global symmetry but also for any global left-hand $U_R(1)_i$ symmetry. In particular, the requirement of conservation of three left-hand $U(1)_{\alpha,\beta,\gamma}$ R symmetries leads to

useful selection rules for nonzero amplitudes (see below).

5. RENORMALIZED THREE-POINT AMPLITUDES

Prior to performing calculations, we would like to formulate some selection rules that follow from the conservation of $U(1)_{\alpha,\beta,\gamma}$. According to expression (38) for the renormalized case (three-point amplitude), we have two canonical fermionic vertices and one canonical bosonic vertex. From (36), it follows that, upon going over from one bosonic vertex to a fermionic vertex, each of the α, β, and γ charges decreases by 1/2. At the same time, we know the admissible values of the charges in the canonical bosonic vertex [see (37)]. In this way, we obtain the following possible combinations of charges for the canonical bosonic vertices:

	$(NS)^3$			$R^2 \times (NS)$			R^3		
α	1	0	0	1/2	1/2	0	1/2	1/2	0
β	0	1	0	1/2	1/2	0	1/2	0	1/2
γ	0	0	1	0	0	1	0	1/2	1/2

The $R \times (NS)^2$ case is forbidden. In order to realize this fact, we transform two vertices (R and NS) from the bosonic into the fermionic ones (36) and sum their charges. Here, two of the three charges prove to be half-integers, and the remaining canonical bosonic NS vertex cannot compensate them, nor can the bosonic NS vertices in the zero picture do this. In general, this argument applies to all operators of the form $R \times (NS)^k$. Therefore, such operators are forbidden in the superpotential.

We now proceed to calculate the renormalized superpotential of our model. By way of example, we take the $R^2 \times (NS)$ contribution to the three-point fermion–fermion–boson function. We have

$$\Psi^1_{(1,3)}\Psi^2_{(\bar{5},1)}\Phi^3_{(5,\bar{3})},$$

where the 1 and 2 fields belong to the R sector, while the 3 field is from the NS sector. The α, β, and γ charges correspond to the positions 2, 6, and 10 (see b_4 in Table 1). In the bosonic sector, the left-handed Ramond fermions in $\Psi^1_{(1,3)}$ and $\Psi^2_{(\bar{5},1)}$ occupy positions 3, 4, 6, and 10. In the field $\Phi^3_{(5,\bar{3})}$ from the NS sector, there is an excitation no. 2 of a fermion on the world sheet. Nonzero $U(1)_R$ charges of these three vertex operators are $\beta_1 = \gamma_1 = \beta_2 = \gamma_2 = 1/2$ and $\alpha_3 = 1$. For the corresponding vertices, we therefore have

$$V^f_{1(-1/2)} = e^{-c/2}S_\alpha e^{(-i/2)H_2}\Sigma^+_3\Sigma^+_4 e^{(i/2)K_1X}\bar{G}_1 e^{(i/2)K_1\bar{X}}, \quad (39)$$

$$V^f_{2(-1/2)} = e^{-c/2}S_\alpha e^{(-i/2)H_2}\Sigma^-_3\Sigma^-_4 e^{(i/2)K_2X}\bar{G}_2 e^{(i/2)K_2\bar{X}}, \quad (40)$$

$$V^b_{3(-1)} = e^{-c}e^{iH_2}e^{(i/2)K_3X}\bar{G}_3 e^{(i/2)K_3\bar{X}}, \quad (41)$$

where $\Sigma^\pm_k \equiv e^{(\pm i/2)H_k}$ (H_k is the boson that corresponds to the left-handed complex kth fermion). The right-handed operator $\bar{G}_j = \prod_i e^{iW^1_i J_i}(j)$ corresponds to gauge degrees of freedom.

We can see that the correlation of these vertex operators is nonzero. Thus, we can easily obtain the superpotential W_1 (Higgs matter) with the corresponding coefficient $g\sqrt{2}$. We have

$$W_1 = g\sqrt{2}[\hat{\Psi}_{(1,3)}\hat{\Psi}_{(\bar{5},1)}\hat{\Phi}_{(5,\bar{3})} + \hat{\Psi}_{(1,1)}\hat{\Psi}_{(\bar{5},3)}\hat{\Phi}_{(5,\bar{3})} + \hat{\Psi}_{(10,3)}\hat{\Psi}_{(\bar{5},3)}\hat{\Phi}_{(\bar{5},3)} + \hat{\Psi}_{(10,3)}\hat{\Psi}_{(10,1)}\hat{\Phi}_{(5,\bar{3})}]. \quad (42)$$

From the above form of the Yukawa coupling, it follows that two (chiral) generations must be light (in relation to the M_W scale).

The $SU(3)_H$ anomalies of the matter fields (Table 2, second row) are canceled in a natural way by the chiral horizontal superfields forming the sets $\hat{\Psi}^H_{(1,N;1,N)}$ and $\hat{\Phi}^H_{(1,N;1,N)}$, where $N = \underline{1}$ and $\underline{3}$ (with both $SO(2)$ helicities; see Table 2, nos. 3 and 4, respectively). The superpotential W_2 includes the following $R^2 \times (NS)$ terms and two R^3 terms:

$$\begin{aligned} W_2 = g\sqrt{2}\{&[\hat{\Phi}^H_{(1,1;1,\bar{3})}\hat{\Phi}^H_{(1,\bar{3};1,1)}\hat{\Phi}_{(1,3;1,3)} \\ &+ \hat{\Phi}^H_{(1,1;1,1)}\hat{\Phi}^H_{(1,\bar{3};1,\bar{3})}\hat{\Phi}_{(1,3;1,3)} \\ &+ \hat{\Phi}^H_{(1,\bar{3};1,\bar{3})}\hat{\Phi}^H_{(1,\bar{3};1,\bar{3})}\hat{\Phi}_{(1,\bar{3};1,\bar{3})} \\ &+ \hat{\Psi}^H_{(1,\bar{3};1,1)}\hat{\Psi}^H_{(1,\bar{3};1,3)}\hat{\Phi}_{(1,\bar{3};1,\bar{3})} \\ &+ \hat{\Psi}^H_{(1,1;1,3)}\hat{\Psi}^H_{(1,\bar{3};1,3)}\hat{\Phi}_{(1,3;1,3)}] \\ &+ [\hat{\Phi}_{(5,\bar{3};1,1)}\hat{\phi}_{(-_1+_3)(1,3;1,1)}\hat{\phi}_{(+_1-_3)(\bar{5},1;1,1)} \\ &+ \hat{\Phi}_{(1,1;5,\bar{3})}\hat{\phi}_{(-_1+_3)(1,1;1,3)}\hat{\phi}_{(+_1-_3)(1,1;\bar{5},1)} \\ &+ \text{conjugate representations}] \\ &+ \hat{\sigma}^1_{(-_1-_4)}\hat{\sigma}^2_{(+_1+_4)}\hat{\Psi}_{(1,1;1,1)} + \hat{\sigma}^2_{(+_1-_4)}\hat{\sigma}^3_{(+_3+_4)}\hat{\Phi}^H_{(-_1-_3)}\}. \end{aligned} \quad (43)$$

From (43), it follows that some horizontal fields in sectors 3 and 4 remain massless in the tree approximation and that the horizontal fields are sterile—that is, they interact with ordinary chiral matter only through the $U(1)_H$ and $SU(3)_H$ gauge bosons. Thus, this sterile matter is of interest from the viewpoint of experimental searches at accelerators and in astrophysics.

The $(NS)^3$ contributions of the Higgs fields to the renormalized superpotential are given by

$$W_3 = g\sqrt{2}\{\hat{\Phi}_{(5,1;1,3)}\hat{\Phi}_{(\bar{5},1;\bar{5},1)}\hat{\Phi}_{(1,1;5,\bar{3})}$$

$$+\hat{\Phi}_{(5,1;1,3)}\hat{\Phi}_{(1,\bar{3};1,\bar{3})}\hat{\Phi}_{(\bar{5},3;1,1)}$$
$$+\hat{\Phi}_{(1,3;5,1)}\hat{\Phi}_{(\bar{5},1;\bar{5},1)}\hat{\Phi}_{(5,\bar{3};1,1)} \quad (44)$$
$$+\hat{\Phi}_{(1,3;5,1)}\hat{\Phi}_{(1,\bar{3};1,\bar{3})}\hat{\Phi}_{(1,1;\bar{5},3)}$$
$$+ \text{conjugate representations}\}$$

Thus, the sum $W_1 + W_2 + W_3$ represents the total renormalizable superpotential, which includes all nonzero three-point expectation values (of the F type) of the vertex operators for the corresponding two-dimensional conformal model.

6. NONRENORMALIZABLE FOUR-, FIVE-, AND SIX-POINT CONTRIBUTIONS TO THE SUPERPOTENTIAL

From equation (38), it follows that vertices, from the fourth one, must be written in a noncanonical form (in the zero picture). The formula implementing a transition from one picture (q) to another ($q + 1$) has the form [8]

$$V_{q+1}(z) = \lim_{w\to z} e^{c}(w)T_F(w)V_q(z). \quad (45)$$

However, the sum of $U(1)_J$ charges for the first three vertices in (38) is zero, and the $U(1)_J$ charge of a canonical (–1 picture) bosonic vertex is +1. Therefore, the effective contribution [in the sense of its subsequent use in equation (38)] to expression (45) comes only from T_F^{-1}. For the complex case, this contribution is given by

$$T_F^{-1} = \frac{i}{2\sqrt{2}}\sum_k e^{-iH_k}[(1-i)e^{iH_{k'}}e^{iH_{\bar{k}'}}$$
$$+(1+i)e^{iH_{k'}}e^{-iH_{\bar{k}'}} \quad (46)$$
$$+(1+i)e^{-iH_{k'}}e^{iH_{\bar{k}'}}+(1-i)e^{-iH_{k'}}e^{-iH_{\bar{k}'}}].$$

We assume that, for complex fermions on the world sheet, $\hat{\chi}^{(*)}_{n,n+1} = \frac{1}{\sqrt{2}}(\chi_n \pm i\chi_{n+1}) = e^{\pm iH_{(n+1)/2}}$ and that $H_{k'}$ and $H_{\bar{k}'}$ are analogous bosonizations for y_n and ω_n. We write explicitly the exponentials for χ and denote by Σ the spin fields for y (ω). In the case of complex fermions, we have $\Sigma^{\pm}_{\bar{k}'} \equiv e^{(\pm i/2)Hk'}$ (or $\bar{k}'$). In our model, the complex triplets $(\hat{\chi}_k, \hat{y}_{k'}, \hat{\omega}_{\bar{k}'})$ correspond to complex fermions with numbers (2, 5, 8), (6, 3, 9), and (10, 4, 7).

The general expression for T_F^{-1}, which is also applicable in the case of noncomplexifiable fermions, has the form

$$T_F^{-1} = e^{-iH_{\chi 12}}\tau_{12} + e^{-iH_{\chi 34}}\tau_{34} + e^{-iH_{\chi 56}}\tau_{56}, \quad (47)$$

where

$$\tau_{mn} = \frac{i}{\sqrt{2}}(y_m\omega_m + iy_n\omega_n).$$

Gauge invariance admits a large number of contributions to four-, five-, and six-point terms (see comments to W_4 and W_5). It is important that, by virtue of the global symmetries of the left-hand superstring sector, some of these terms vanish.

Let us first consider four-point contributions to the superpotential. Here, all nonzero four-point operators belong to the class of R^4 amplitudes [8]. Indeed, operators of the $(NS)^n$ vanish because, by virtue of (38), they are proportional to $\langle \tau_{m_4, m_4+1}(z_4)\ldots\tau_{m_n, m_n+1}(z_n)\rangle \equiv 0$ (here, $m_i = 1, 3, 5$). Further, we note that, if there is at least one NS operator among four vertex operators, we can rewrite it in the zero picture; that is,

$$V^{b(NS)}_{4(0)} = \tau_{m,m+1}e^{(i/2)KX}\bar{G}_R e^{(i/2)K\bar{X}}. \quad (48)$$

For its correlation with $\tau_{m,m+1}$ to be nonzero, it is necessary that it involve four spin fields Σ originating from one complex triple $(\hat{\chi}_k, \hat{y}_{k'}, \hat{\omega}_{\bar{k}'})$ corresponding to (m, $m + 1$) pairing. Spin fields Σ enter into R vertex operators (two in each), but they belong to different triples. Hence, the remaining three operators are insufficient for the correlation with $\tau_{m,m+1}$ from the fourth NS operator to be nonzero [8].

Let us now consider the only remaining four-point case, that of R^4. We begin this consideration by analyzing $U(1)^3_R$ constraints. It is well known that, for the first and second vertices in (38), each canonical charge decreases by 1/2 (a total change is –1) and that the third canonical vertex remains unchanged; for the remaining canonical bosonic vertices, one of the three charges decreases by unity (owing to the quantity T_F^{-1}, which consists of three parts, each carrying a charge of –1).

The following few comments, which below will reduce the sampling of admissible arrangements of charges, are in order here.

(i) It is important that, if one of the charges α, β, and γ is equal to zero in the canonical vertex V^b_{-1}, this charge for the vertex V^b_0 in the zero picture is also equal to zero, because the only nontrivial operator product in (45) for the term being discussed is $e^c(w)e^{-c}(z) \sim (w - z) \longrightarrow 0$.

(ii) In an NS operator, which originally has one charge of +1 in the canonical picture, all charges vanish upon going over to the zero picture (48).

(iii) By virtue of the above two circumstances, we need not consider the arrangement of charges where one of the rows (α, β, or γ) consists only of unities and zeros with the number of zeros greater than two. In order to demonstrate this, we note that, in this case, we can take two R operators (as was indicated above, this is their minimal admissible number) in the –1/2 canonical fermionic picture with the result that there is then a charge of –1 instead of two zeros. If there is a third zero, the corresponding operator is taken in the –1

canonical bosonic picture, it can be seen that, because the remaining vertex operators appear in the zero picture, it is impossible to compensate the above charge of –1 [see item (ii)]. It follows that the combinations being discussed are forbidden by the charge-conservation law.

(iv) For more delicate reasons, arrangements featuring a row where there are two zeros and where the remaining numbers are unities also disappear. We will now prove this. By choosing, in just the same way as in item (iii), the –1/2 patterns for two operators with zeros and by going over to the –1 picture for one more vertex operator (with unity), a nonzero correlation function will be obtained for three conformal fields corresponding to the charge being considered (α, β, or γ). However, the full correlation function is proportional to $\langle(\tau_{m,m+1})^{(n-3)}\rangle = 0$ owing to the presence of the product of the remaining $(n-3)$ vertex operators in the zero picture. This vanishing is due to the fact that the operator product of the τ fields is always nonsingular.

(v) On the basis of items (iii) and (iv), we can state that amplitudes of the $R^2 \times (NS)^n$ type disappear. Indeed, two charges of 1/2 must be paired in each of the R operators in order that the charges be integral. Hence, the third charge row features two zeros, the remaining numbers being unities and zeros.

(vi) Charge combinations including charge rows of the (1/2, 1/2, 1, …, 1 or 0) type (or of the type formed by any permutations of these numbers) are not allowed. Let us demonstrate this explicitly. By choosing the (–1/2, –1/2, –1, 0, …, 0) picture arrangement and using the statements proven in items (i) and (ii), we find that the total charge corresponding to the row being considered is +1, which is inconsistent with the requirement of charge conservation. It follows, among other things, that terms of the $R^3 \times (NS)^n$ type are forbidden, which generalizes the conclusions drawn in [8] for such amplitudes.

In view of the above, there is the only admissible combination of charges for R^4 (for canonical bosonic vertices), that which is presented in the first part of Table 4. (Needless to say, all permutations of four vertices and the permutations of the α, β, and γ charges are also admissible.) Other combinations with total charges of (0, 2, 2)), (1, 3/2, 3/2), and (1/2, 3/2, 2) (and their permutations) are forbidden by $U(1)_R^3$ conservation.

We can now consider the fourth-order superpotential. It is necessary to calculate the correlation function $\langle V^f_{1(-1/2)} V^f_{2(-1/2)} V^b_{3(-1)} V^b_{4(0)}\rangle$. In the *R* case, it is necessary to go over from the –1 picture to the zero picture for the vertex operator V^b_R. With the aid of (45), it can be shown that the operator obtained in the zero picture from the vertex operator

$$V^b_{R(-1)} = e^{-c} e^{(i/2)H_k} e^{(i/2)H_l} \Sigma^{\pm}_{k'} \Sigma^{\pm}_{l'} e^{(i/2)KX} \overline{G}_R e^{(i/2)K\bar{X}}$$

has the form

$$V^b_{R(0)} = \frac{i}{2\sqrt{2}} \{ e^{(-i/2)H_k} e^{(i/2)H_l} \times (\Sigma^{\mp}_{k'}[(1 \pm i)e^{iH_{\tilde{k}}} + (1 \mp i)e^{-iH_{\tilde{k}}}])\Sigma^{\pm}_{l'} + e^{(i/2)H_k} \times e^{(-i/2)H_l} \Sigma^{\pm}_{k'} (\Sigma^{\mp}_{l'}[(1 \pm i)e^{iH_{\tilde{l}}} + (1 \mp i)e^{-iH_{\tilde{l}}}]) \} \times e^{(i/2)KX} \overline{G}_R e^{(i/2)K\bar{X}}. \quad (49)$$

Thus, the *R* operator in the zero picture appears to be a superposition of four vertex operators.

In the model being considered, 50 R^4 terms are allowed by gauge invariance. Of these, only nine correspond to the total-charge combination (2, 1, 1). The remaining terms correspond to the combination (0, 2, 2); therefore, they vanish. By way of example, we consider one of the admissible terms. The vertex operators involve

$$(1, 3, 1, 1)_{mat} \sim e^{-c/2} e^{(-i/2)H_2} \Sigma^+_3 \Sigma^+_4 \quad \left(f, -\frac{1}{2}\right),$$

$$(+_1, -_3)(1, \bar{3}, 1, 1)_{no.\,4} \sim e^{-c/2} e^{(-i/2)H_6} \Sigma^+_5 \Sigma^+_7 \quad \left(f, -\frac{1}{2}\right),$$

$$(-_1, -_4)_{no.\,6} \sim e^{-c} e^{(i/2)H_2} e^{(i/2)H_{10}} \Sigma^+_4 \Sigma^+_5 \quad (b, -1),$$

$$(+_3, +_4)_{no.\,6} \sim \frac{i\sqrt{2}}{4} \Big\{ e^{(-i/2)H_6} e^{(i/2)H_{10}} \Sigma^+_3 \Sigma^+_7 \times [(1-i)e^{iH_9} + (1+i)e^{-iH_9}] + \underline{e^{(i/2)H_6} e^{(-i/2)H_{10}} \Sigma^-_3 \Sigma^-_7} \times [(1+i)e^{iH_4} + \underline{(1-i)e^{-iH_4}}] \Big\} (b, 0).$$

Here, we have omitted the factor $e^{(i/2)K_iX} \overline{G}_R e^{(i/2)K_i\bar{X}}$. The correlation of the product of the underlined terms with the first three vertices is nonzero. Here, we present the calculations in greater detail. We have

$$A_4 = \frac{g^2\sqrt{2}}{2\pi} \int d^2z \langle \text{left part} \rangle \times \langle \overline{G}_1 \overline{G}_2 \overline{G}_3 \overline{G}_4 \rangle \left\langle \prod_i e^{(i/2)K_iX} e^{(i/2)K_i\bar{X}} \right\rangle, \quad (50)$$

where

$$\langle \text{left part} \rangle = \frac{1+i}{2\sqrt{2}} z_{12}^{-3/4} z_{13}^{-1/2} z_{14}^{-3/4} z_{23}^{-3/4} z_{24}^{-1/2} z_{34}^{-3/4},$$

and where the right part is given by

$$\langle \overline{G}_1 \overline{G}_2 \overline{G}_3 \overline{G}_4 \rangle$$

$$= \prod_i \left\langle e^{iW_i^1 J_i}(1) e^{iW_i^2 J_i}(2) e^{iW_i^3 J_i}(3) e^{iW_i^4 J_i}(4) \right\rangle$$

$$= \prod_{k<l} (\bar{z}_{kl})^{\sum_i W_i^k W_i^l} \prod_i C_i^{1234}. \qquad (51)$$

Here, C_i^{1234} ensures gauge invariance. From conformal invariance, we obtain the constraint $\frac{1}{2}\sum_i (W_i^l)^2 = 1 \; \forall \, l$; from gauge invariance, it follows that $\sum_l W_i^l = 0 \; \forall \, i$, where $i = 1, \ldots, 22$ and $l = 1, \ldots, N$. Thus, we can find that $\sum_{k<l} \sum_i W_i^k W_i^l = -N$.

For some representatives of gauge multiplets, we now write down, in tabular form, the weight (charge) W^l vectors for the vertices being considered.

	$U(1)^3$			$SO(6)$			$U(5)$	$U(3)$			$U(5)$	$U(3)$
W^1		0^3			0^3		$1/4^5$	1/4	1/4	5/4	0^5	0^3
W^2	1/2	0	−1/2		0^3		$-1/8^5$	3/8	3/8	−5/8	$3/8^5$	$-1/8^3$
W^3	−1/2	0	0	−1/2	1/2	1/2	$1/8^5$		$-3/8^3$		$-1/8^5$	$3/8^3$
W^4	0	0	1/2	1/2	−1/2	−1/2	$-1/4^5$		$-1/4^3$		$-1/4^5$	$-1/4^3$

From equations (50) and (51), it follows that the amplitude A_4 features the factor

$$|z_{12}|^{-3/2} |z_{13}|^{-1} |z_{14}|^{-3/2} |z_{23}|^{-3/2} |z_{24}|^{-1} |z_{34}|^{-3/2}.$$

If we fix the gauge by setting $z_1 = \infty$, $z_2 = z$, $z_3 = 1$, and $z_4 = 0$ and take into account the Faddeev–Popov minideterminant (23), we can arrive at the integral

$$I_4 = \int d^2 z |z|^{-1} |z-1|^{-3/2}$$

$$= 8\pi \sum_{k=0}^{\infty} \frac{1}{1+4k} \left[\frac{(2k-1)!!}{(2k)!!} \right]^2 = \frac{128}{\pi} \Gamma^4(5/4) = 27.50.$$

Further, we must make use of the amplitude at zero momentum and take into account the dimensional factor $(2\sqrt{8\pi}/gM_{\mathrm{Pl}})$. For the remaining terms, the calculations are analogous.

Thus, we conclude that, in the model being considered, the full nonzero nonrenormalizable four-point superpotential $W_4 = \mathrm{R}^4$ includes the following nine terms (see also the tables in [22]):

$$W_4 = \frac{2gI_4}{\sqrt{\pi} M_{\mathrm{Pl}}}$$

$$\times \{ \hat{\Psi}_{(1,3;1,1)} \hat{\Phi}^{\mathrm{H}}_{(+_1,-_3)(1,\bar{3};1,1)} \hat{\sigma}_{1(-_1,-_4)} \hat{\sigma}_{3(+_3,+_4)}$$

$$+ [\hat{\phi}_{1(-_1,+_3)(1,3;1,1)} \hat{\phi}_{1(-_1,-_3)(1,\bar{3};1,1)}$$

$$+ \hat{\phi}_{3(-_1,+_3)(1,1;3,1)} \hat{\phi}_{3(-_1,-_3)(1,1;\bar{3},1)}] \hat{\sigma}_{2(+_1,-_4)} \hat{\sigma}_{2(+_1,+_4)}$$

$$+ \hat{\phi}_{1(-_1,-_3)(1,\bar{3};1,1)} \hat{\phi}_{3(-_1,+_3)(1,1;1,3)}$$

$$\times [\hat{\Phi}^{\mathrm{H}}_{2(+_1,-_3)(1,\bar{3};1,1)} \hat{\Phi}^{\mathrm{H}}_{3(+_1,+_3)(1,\bar{3};1,\bar{3})} \qquad (52)$$

$$+ \hat{\Psi}^{\mathrm{H}}_{3(+_1,+_2)(1,\bar{3};1,3)} \hat{\Psi}^{\mathrm{H}}_{3(+_1,-_2)(1,\bar{3};1,3)}]$$

$$+ \hat{\sigma}_{1(+_1,-_4)} \hat{\sigma}_{1(-_1,-_4)} \hat{\sigma}_{3(-_3,+_4)} \hat{\sigma}_{3(+_3,+_4)}$$

$$+ \hat{\phi}_{1(-_1,+_3)(1,3;1,1)} \hat{\phi}_{3(-_1,-_3)(1,1;1,\bar{3})} [\hat{\Psi}^{\mathrm{H}}_{3(+_1,-_2)(1,\bar{3};1,3)} \hat{\Psi}^{\mathrm{H}}_{4(+_1,+_2)}$$

$$+ \hat{\Psi}^{\mathrm{H}}_{3(+_1,+_2)(1,\bar{3};1,3)} \hat{\Psi}^{\mathrm{H}}_{4(+_1,-_2)}$$

$$+ \hat{\Phi}^{\mathrm{H}}_{1(+_1,-_3)(1,1;1,\bar{3})} \hat{\Phi}^{\mathrm{H}}_{3(+_1,+_3)(1,\bar{3};1,\bar{3})}] \}.$$

Let us now consider the five-point contribution to the superpotential. We already know that $\mathrm{R} \times (\mathrm{NS})^4$, $(\mathrm{NS})^5$, $\mathrm{R}^2 \times (\mathrm{NS})^3$, and $\mathrm{R}^3 \times (\mathrm{NS})^2$ operators vanish (see Sections 5 and 6).

Thus, nonzero contributions to the five-order superpotential come from $\mathrm{R}^4 \times (\mathrm{NS})$ and R^5 operators.

Let us first consider $\mathrm{R}^4 \times (\mathrm{NS})$ operators. Only the combination of $U(1)^3_{\mathrm{R}}$ charges of canonical bosonic vertices that is presented in the second part of Table 4 (plus permutations of rows and columns) is admissible; otherwise, we would either obtain half-integer total charges or arrive at the cases described at the beginning of this section.

In our model, full gauge invariance admits 51 different terms of the $\mathrm{R}^4 \times (\mathrm{NS})$ type; however, only 43 of these survive an analysis according to N = 2 intrinsic superconformal theory.

The nonzero nonrenormalizable five-point $\mathrm{R}^4 \times (\mathrm{NS})$ superpotential has the form (see also the tables from [22])

$$W_5 = \frac{2\sqrt{2}gI_5}{\pi M_{\mathrm{Pl}}^2} \{ \hat{\Phi}_{5(5,1;1,3)} [\hat{\Psi}_{(10,3;1,1)} \hat{\Psi}_{(10,1;1,1)}$$

$$+ \hat{\Psi}_{(1,3;1,1)} \hat{\Psi}_{(\bar{5},1;1,1)} + \hat{\Psi}_{(\bar{5},3;1,1)} \hat{\Psi}_{(1,1;1,1)}$$

$$+ \hat{\phi}_{1(1,3;1,1)} \hat{\phi}_{2(1,\bar{5};1,1)}] [\hat{\Psi}^{\mathrm{H}}_{1(1,1;1,3)} \hat{\Psi}^{\mathrm{H}}_{3(1,\bar{3};1,3)}$$

Table 4. Admissible charge combinations in the four- and five-point terms of the superpotential

	R^4				Total charge	$R^4 \times (NS)$					Total charge	R^5					Total charge
α	0	1/2	1/2	0	1	1/2	1/2	1/2	1/2	1	3	1/2	1/2	1/2	1/2	0	2
β	1/2	0	0	1/2	1	1/2	1/2	0	0	0	1	1/2	1/2	1/2	0	1/2	2
γ	1/2	1/2	1/2	1/2	2	0	0	1/2	1/2	0	1	0	0	0	1/2	1/2	1

$$
\begin{aligned}
&+\hat{\Phi}^{H}_{1(1,1;1,\bar{3})}\hat{\Phi}^{H}_{2(1,\bar{3};1,1)}+\hat{\Phi}^{H}_{3(1,\bar{3};1,\bar{3})}\hat{\Phi}^{H}_{4(1,1;1,1)}]\\
&+\hat{\Phi}_{5(\bar{5},1;1,\bar{3})}[\hat{\Psi}_{(10,3;1,1)}\hat{\Psi}_{(\bar{5},3;1,1)}\\
&+\hat{\phi}_{1(1,\bar{3};1,1)}\hat{\phi}_{2(1,5;1,1)}][\hat{\Psi}^{H}_{2(1,\bar{3};1,1)}\hat{\Psi}^{H}_{3(1,\bar{3};1,3)}\\
&+\hat{\Phi}^{H}_{3(1,\bar{3};1,\bar{3})}\hat{\Phi}^{H}_{3(1,\bar{3};1,\bar{3})}]\\
&+\hat{\Phi}_{6(1,3;5,1)}\hat{\phi}_{3(1,1;1,3)}\hat{\phi}_{4(1,1;\bar{5},1)} \qquad (53)\\
&\times[\hat{\Psi}^{H}_{1(1,1;1,3)}\hat{\Psi}^{H}_{3(1,\bar{3};1,3)}+\hat{\Phi}^{H}_{1(1,1;1,\bar{3})}\hat{\Phi}^{H}_{2(1,\bar{3};1,1)}\\
&+\hat{\Phi}^{H}_{3(1,\bar{3};1,\bar{3})}\hat{\Phi}^{H}_{4(1,1;1,1)}]\\
&+\hat{\Phi}_{6(1,\bar{3};\bar{5},1)}\hat{\phi}_{3(1,1;1,\bar{3})}\hat{\phi}_{4(1,1;5,1)}\\
&\times[\hat{\Psi}^{H}_{2(1,\bar{3};1,1)}\hat{\Psi}^{H}_{3(1,\bar{3};1,3)}+\hat{\Phi}^{H}_{3(1,\bar{3};1,\bar{3})}\hat{\Phi}^{H}_{3(1,\bar{3};1,\bar{3})}\\
&+\hat{\Phi}_{5(5,1;1,3)}\hat{\Psi}_{(\bar{5},1;1,1)}\hat{\Phi}^{H}_{1(1,1;1,\bar{3})}\hat{\sigma}_1\hat{\sigma}_3\\
&+\hat{\Phi}_{5(\bar{5},1;1,\bar{3})}\hat{\Psi}_{(\bar{5},1;1,1)}\hat{\Psi}_{(10,1;1,1)}\\
&\times[\hat{\Psi}^{H}_{1(1,1;1,3)}\hat{\Psi}^{H}_{4(1,1;1,1)}+\hat{\Phi}^{H}_{1(1,1;1,\bar{3})}\hat{\Phi}^{H}_{1(1,1;1,\bar{3})}]\},
\end{aligned}
$$

where the parameter I_5 takes different values for the different terms. Here, we have not indicated explicitly the field quantum numbers according to hidden gauge groups. Therefore, several terms are in fact encoded in each term from (53), but these can easily be recovered by using the table of states.

By way of illustration, we present the results of the calculations for the last term explicitly. We have

$$V^{f}_{1\ R(-1/2)} \sim e^{-c/2}S_{\alpha}e^{(-i/2)H_2}\Sigma^{-}_{3}\Sigma^{-}_{4} \qquad (54)$$

for $(\bar{5}, 1, 1, 1)_{\mathrm{mat}}$,

$$V^{f}_{2\ R(-1/2)} \sim e^{-c/2}S_{\beta}e^{(-i/2)H_2}\Sigma^{+}_{3}\Sigma^{+}_{4} \qquad (55)$$

for $(10, 1, 1, 1)_{\mathrm{mat}}$, and

$$V^{b}_{5\ NS(-1)} \sim e^{-c}e^{iH_{10}} \qquad (56)$$

for $(\bar{5}, 1, 1, \bar{3})_{\mathrm{Higgs}}$.

The remaining two boson fields must be written in the noncanonical zero picture. We first write them in the canonical form and then go over to the zero picture. For the $(+_1, -_3)$ $(1, 1, 1, \bar{3})_{\mathrm{no.\ 4}}$ field, the required expression in the canonical picture has the form

$$V^{b}_{R(-1)} \sim e^{-c}e^{(i/2)H_2}e^{(i/2)H_{10}}\Sigma^{+}_{5}\Sigma^{+}_{7}.$$

Upon going over to the zero picture, we arrive at

$$
\begin{aligned}
V^{b}_{3\ R(0)} &\sim e^{(-i/2)H_2}e^{(i/2)H_{10}}\\
&\times\{\Sigma^{-}_{5}[(1+i)e^{iH_8}+(1-i)e^{-iH_8}]\}\Sigma^{+}_{7} \qquad (57)\\
&+e^{(i/2)H_2}e^{(-i/2)H_{10}}\Sigma^{+}_{5}\{\Sigma^{-}_{7}[\underline{(1+i)e^{iH_4}}-\underline{\underline{(1-i)e^{-iH_4}}}]\}.
\end{aligned}
$$

For the $(-_1, +_3)$ $(1, 1, 1, \bar{3})_{\mathrm{no.\ 4}}$ field, the canonical form is similar to that in the preceding case, and it is sufficient to change only the sign of Σ. Eventually, this yields

$$
\begin{aligned}
V^{b}_{4\ R(0)} &\sim e^{(-i/2)H_2}e^{(i/2)H_{10}}\\
&\times\{\Sigma^{+}_{5}[(1-i)e^{iH_8}+(1+i)e^{-iH_8}]\}\Sigma^{-}_{7} \qquad (58)\\
&+e^{(i/2)H_2}e^{(-i/2)H_{10}}\Sigma^{-}_{5}\Sigma^{+}_{7}\{[\underline{\underline{(1-i)e^{iH_4}}}+\underline{(1+i)e^{-iH_4}}]\}.
\end{aligned}
$$

Further, it is necessary to calculate the correlation of the product of all five vertex operators presented immediately above. The expression

$$
\begin{aligned}
&(1+i)^2\left\langle e^{(-i/2)H_4}(1)e^{(i/2)H_4}(2)e^{iH_4}(3)e^{-iH_4}(4)\right\rangle\\
&+(1-i)^2\left\langle e^{(-i/2)H_4}(1)e^{(i/2)H_4}(2)e^{-iH_4}(3)e^{iH_4}(4)\right\rangle \qquad (59)\\
&\quad=2iz_{12}^{-1/4}z_{34}^{-1}\frac{z_{14}z_{23}-z_{13}z_{24}}{(z_{13}z_{24}z_{14}z_{23})^{1/2}}
\end{aligned}
$$

appears to be the most nontrivial factor in these calculations. The full left-hand part of the amplitude being considered has the form

$$
\begin{aligned}
&2iz_{12}^{-1}z_{13}^{-3/4}z_{14}^{-3/4}z_{15}^{-1/2}z_{23}^{-3/4}z_{24}^{-3/4}z_{25}^{-1/2}\\
&\times z_{34}^{-1}z_{35}^{-1/2}z_{45}^{-1/2}(z_{14}z_{23}-z_{13}z_{24}). \qquad (60)
\end{aligned}
$$

Upon taking into account the right-hand part, we obtain

$$
\begin{aligned}
&2i|z_{13}|^{-3/2}|z_{14}|^{-3/2}|z_{15}|^{-1}|z_{23}|^{-3/2}|z_{24}|^{-3/2}\\
&\times|z_{25}|^{-1}|z_{35}|^{-1}|z_{45}|^{-1}\left(\frac{z_{14}z_{23}-z_{13}z_{24}}{z_{12}z_{34}}\right). \qquad (61)
\end{aligned}
$$

Table 5. Admissible charge combinations in the six-point terms of the superpotential

	R^6						Total charge	R^6						Total charge	$R^5 \times (NS)$						Total charge	$R^4 \times (NS)^2$						Total charge
α	1/2	1/2	1/2	1/2	1/2	1/2	3	1/2	1/2	1/2	1/2	0	0	2	1/2	1/2	0	1/2	1/2	1	3	1/2	1/2	1/2	1/2	1	1	4
β	1/2	1/2	0	0	1/2	1/2	2	1/2	1/2	0	0	1/2	1/2	2	1/2	0	1/2	1/2	1/2	0	2	1/2	1/2	0	0	0	0	1
γ	0	0	1/2	1/2	0	0	1	0	0	1/2	1/2	1/2	1/2	2	0	1/2	1/2	0	0	0	1	0	0	1/2	1/2	0	0	1

In order to simplify the calculations, we go over to the limit $z_5 \longrightarrow \infty$. If we permute the vertices as ($1 \rightleftarrows 5$, $2 \rightleftarrows 4$) and fix the time-ordered gauge as $z_1 \longrightarrow \infty$, $z_4 = 1$, and $z_5 = 0$, the parenthetical term assumes the value of –1. Upon taking into account the Jacobian in (23), we eventually arrive at the integral

$$I_5 = \iint d^2z_2 d^2z_3 |z_2|^{-3/2} |z_3|^{-3/2} \times |z_2 - 1|^{-3/2} |z_3 - 1|^{-3/2} = I_4^2 = (27.50)^2.$$

Let us consider R^5 terms. Obviously, there is only one admissible combination of $U(1)_R^3$ charges of canonical bosonic vertex operators (and their permutations) that is presented in the third part of Table 4 (in any other case, we would obtain half-integer total charges). In particular, it follows that R^5 terms must include simultaneously R vertices of all three possible types [three permutations of (1/2, 1/2, 0)]. For the model considered here, this means that the superfield $\hat{\sigma}_2$ (from sector no. 6) must participate in R^5 interactions, because this is the only field with Ramond fermions of the world sheet with numbers 6 and 2 (fermions χ). We were unable to find such gauge-invariant terms.

In conclusion, we consider nonrenormalizable six-point contributions to the superpotential. From the discussions in Section 5 and at the beginning of this section, it follows that only six-point amplitudes of the R^6, $R^5 \times (NS)$, and $R^4 \times (NS)^2$ types are allowed. For these cases, the admissible arrangements of $U(1)_R$ charges are presented in Table 5.

In the present model, the R^6 terms of the superpotential play an important role in constructing the mass matrix of the matter field. Table 6 displays the full list of R^6 terms that make nonzero contributions in calculating relevant amplitudes in $N = 2$ superconformal theory. [There are also three trivial terms that correspond to the first part of Table 5 and which are obtained by multiplying the last two singlet R^3 combinations from the superpotential W_2—see equation (43).] In front of each of these terms, we must of course take into account a dimensional coefficient of the form $\left(\frac{4g}{\pi^{3/2} M_{Pl}^3}\right) I_6$, where the integral I_6 must be calculated individually for each term according to superconformal theory. By way of example, we indicate that, for three rows of the penultimate (sixth) part of Table 6, we have

$$I_6 = \int d^2z_1 d^2z_2 d^2z_3 [(z_3 - 1)\bar{z}_3][|z_1|^{1/2} |z_2|^{1/2} |z_1 - 1|^{3/2} \times |z_1 - z_3|^{3/2} |z_2 - 1|^{3/2} |z_2 - z_3|^{3/2} |z_3|^{3/2}]^{-1} = 20800 \pm 200.$$

For the first, third, and sixth rows of the fifth part of this table, we obtained a rough estimate of $I_6 = 1400 \pm 400$.

7. FERMION MASS MATRIX

If we restrict our consideration to the renormalized superpotential, an analysis of the mass matrices of matter fields shows that two generations remain massless, but that the remaining two generations have degenerate masses. However, mass degeneracy can be avoided by taking into account the last term W_5, which is characterized by a large vacuum expectation value of the three-field condensate. In particular, the masses of the *b* and *b*' quarks are different.

With allowance for the contributions from the five-point and six-point terms (W_5 and W_6, respectively), the fermion mass matrices are given by

$$\left\langle \Phi^{1,2,3}_{(5;\,\bar{3});\,4} \right\rangle = H^{1,2,3}, \quad \left\langle \Phi^{1,2,3}_{(\bar{5};\,3);\,4} \right\rangle = \bar{H}^{1,2,3}. \qquad (62)$$

Here and below, the superscripts 1, 2, 3 represent the horizontal generation indices.

The mass matrices for (*e*, *d*) and *u* (in the flip case) are, respectively,

$$\begin{pmatrix} h_1^{11} & h_1^{12} & h_1^{13} & H^1 + \bar{H}_5^1 \\ h_1^{21} & h_1^{22} & h_1^{23} & H^2 + \bar{H}_5^2 \\ h_1^{31} & h_1^{32} & h_1^{33} & H^3 + \bar{H}_5^3 \\ H^1 + \bar{H}_5^1 & H^2 + \bar{H}_5^2 & H^3 + \bar{H}_5^3 & h_3 \end{pmatrix}$$

Table 6. Six-point R^6 terms in the superpotential that satisfy the requirements of full gauge invariance and all intrinsic global symmetries

$\Psi_1(1, 3, 1, 1)$	$\Psi_2(\bar{5}, 3, 1, 1)$	$\Psi_2^H(1, \bar{3}, 1, 1)_{-1,+2}$	$\Psi_4(1, 1, 1, 1)$	$\Psi_5(\bar{5}, 1, 1, 1)$	$\Psi_4^H(1, 1, 1, 1)_{+1,+2}$
$\Psi_3^H(1, \bar{3}, 1, 3)_{+1,-2}$	$\phi_2(5, 1, 1, 1)_{+1,+3}$	$\phi_3(1, 1, 1, \bar{3})_{-1,-3}$	$\Psi_1^H(1, 1, 1, 3)_{-1,-2}$	$\phi_2(5, 1, 1, 1)_{+1,+3}$	$\phi_3(1, 1, 1, \bar{3})_{-1,-3}$
$\Psi_1(1, 3, 1, 1)$	$\Psi_2(\bar{5}, 3, 1, 1)$	$\Psi_3^H(1, \bar{3}, 1, 3)_{+1,+2}$	$\Psi_4(1, 1, 1, 1)$	$\Psi_5(\bar{5}, 1, 1, 1)$	$\Phi_1^H(1, 1, 1, \bar{3})_{-1,+3}$
$\Psi_2^H(1, \bar{3}, 1, 1)_{-1,-2}$	$\phi_2(5, 1, 1, 1)_{+1,+3}$	$\phi_3(1, 1, 1, \bar{3})_{-1,-3}$	$\Phi_1^H(1, 1, 1, \bar{3})_{+1,-3}$	$\phi_2(5, 1, 1, 1)_{+1,+3}$	$\phi_3(1, 1, 1, \bar{3})_{-1,-3}$
$\Psi_1(1, 3, 1, 1)$	$\Psi_2(\bar{5}, 3, 1, 1)$	$\Phi_3^H(1, \bar{3}, 1, \bar{3})_{+1,+3}$	$\Psi_5(\bar{5}, 1, 1, 1)$	$\Psi_6(10, 3, 1, 1)$	$\Psi_1^H(1, 1, 1, 3)_{-1,+2}$
$\Psi_3^H(1, \bar{3}, 1, \bar{3})_{-1,-3}$	$\phi_2(5, 1, 1, 1)_{+1,+3}$	$\phi_3(1, 1, 1, \bar{3})_{-1,-3}$	$\Psi_3^H(1, \bar{3}, 1, 3)_{+1,-2}$	$\phi_3(1, 1, 1, 3)_{-1,+3}$	$\phi_2(\bar{5}, 1, 1, 1)_{+1,-3}$
$\Psi_2(\bar{5}, 3, 1, 1)$	$\Psi_3(10, 1, 1, 1)$	$\Psi_1^H(1, 1, 1, 3)_{-1,+2}$	$\Psi_5(\bar{5}, 1, 1, 1)$	$\Psi_6(10, 3, 1, 1)$	$\Psi_3^H(1, \bar{3}, 1, 3)_{+1,+2}$
$\Psi_3^H(1, \bar{3}, 1, 3)_{+1,-2}$	$\phi_3(1, 1, 1, 3)_{-1,+3}$	$\phi_2(\bar{5}, 1, 1, 1)_{+1,-3}$	$\Psi_1^H(1, 1, 1, 3)_{-1,-2}$	$\phi_3(1, 1, 1, 3)_{-1,+3}$	$\phi_2(\bar{5}, 1, 1, 1)_{+1,-3}$
$\Psi_2(\bar{5}, 3, 1, 1)$	$\Psi_3(10, 1, 1, 1)$	$\Psi_3^H(1, \bar{3}, 1, 3)_{+1,+2}$	$\Psi_5(\bar{5}, 1, 1, 1)$	$\Psi_6(10, 3, 1, 1)$	$\Phi_1^H(1, 1, 1, \bar{3})_{-1,+3}$
$\Psi_1^H(1, 1, 1, 3)_{-1,-2}$	$\phi_3(1, 1, 1, 3)_{-1,+3}$	$\phi_2(\bar{5}, 1, 1, 1)_{+1,-3}$	$\Phi_2^H(1, \bar{3}, 1, 1)_{+1,-3}$	$\phi_3(1, 1, 1, 3)_{-1,+3}$	$\phi_2(\bar{5}, 1, 1, 1)_{+1,-3}$
$\Psi_2(\bar{5}, 3, 1, 1)$	$\Psi_3(10, 1, 1, 1)$	$\Phi_1^H(1, 1, 1, \bar{3})_{-1,+3}$	$\Psi_5(\bar{5}, 1, 1, 1)$	$\Psi_6(10, 3, 1, 1)$	$\Phi_2^H(1, \bar{3}, 1, 1)_{-1,+3}$
$\Phi_2^H(1, \bar{3}, 1, 1)_{+1,-3}$	$\phi_3(1, 1, 1, 3)_{-1,+3}$	$\phi_2(\bar{5}, 1, 1, 1)_{+1,-3}$	$\Phi_1^H(1, 1, 1, \bar{3})_{+1,-3}$	$\phi_3(1, 1, 1, 3)_{-1,+3}$	$\phi_2(\bar{5}, 1, 1, 1)_{+1,-3}$
$\Psi_2(\bar{5}, 3, 1, 1)$	$\Psi_3(10, 1, 1, 1)$	$\Phi_2^H(1, \bar{3}, 1, 1)_{-1,+3}$	$\Psi_5(\bar{5}, 1, 1, 1)$	$\Psi_6(10, 3, 1, 1)$	$\Phi_3^H(1, \bar{3}, 1, \bar{3})_{+1,+3}$
$\Phi_1^H(1, 1, 1, \bar{3})_{+1,-3}$	$\phi_3(1, 1, 1, 3)_{-1,+3}$	$\phi_2(\bar{5}, 1, 1, 1)_{+1,-3}$	$\Phi_4^H(1, 1, 1, 1)_{-1,-3}$	$\phi_3(1, 1, 1, 3)_{-1,+3}$	$\phi_2(\bar{5}, 1, 1, 1)_{+1,-3}$
$\Psi_2(\bar{5}, 3, 1, 1)$	$\Psi_3(10, 1, 1, 1)$	$\Phi_3^H(1, \bar{3}, 1, \bar{3})_{+1,+3}$	$\Psi_5(\bar{5}, 1, 1, 1)$	$\Psi_6(10, 3, 1, 1)$	$\Phi_4^H(1, 1, 1, 1)_{+1,+3}$
$\Phi_4^H(1, 1, 1, 1)_{-1,-3}$	$\phi_3(1, 1, 1, 3)_{-1,+3}$	$\phi_2(\bar{5}, 1, 1, 1)_{+1,-3}$	$\Phi_3^H(1, \bar{3}, 1, \bar{3})_{-1,-3}$	$\phi_3(1, 1, 1, 3)_{-1,+3}$	$\phi_2(\bar{5}, 1, 1, 1)_{+1,-3}$
$\Psi_2(\bar{5}, 3, 1, 1)$	$\Psi_3(10, 1, 1, 1)$	$\Phi_4^H(1, 1, 1, 1)_{+1,+3}$	$\Psi_6(10, 3, 1, 1)$	$\Psi_6(10, 3, 1, 1)$	$\Psi_2^H(1, \bar{3}, 1, 1)_{-1,+2}$
$\Phi_3^H(1, \bar{3}, 1, \bar{3})_{-1,-3}$	$\phi_3(1, 1, 1, 3)_{-1,+3}$	$\phi_2(\bar{5}, 1, 1, 1)_{+1,-3}$	$\Psi_3^H(1, \bar{3}, 1, 3)_{+1,-2}$	$\phi_2(5, 1, 1, 1)_{+1,+3}$	$\phi_3(1, 1, 1, \bar{3})_{-1,-3}$
$\Psi_3(10, 1, 1, 1)$	$\Psi_3(10, 1, 1, 1)$	$\Psi_1^H(1, 1, 1, 3)_{-1,+2}$	$\Psi_6(10, 3, 1, 1)$	$\Psi_6(10, 3, 1, 1)$	$\Psi_3^H(1, \bar{3}, 1, 3)_{+1,+2}$
$\Psi_4^H(1, 1, 1, 1)_{+1,-2}$	$\phi_2(5, 1, 1, 1)_{+1,+3}$	$\phi_3(1, 1, 1, \bar{3})_{-1,-3}$	$\Psi_2^H(1, \bar{3}, 1, 1)_{-1,-2}$	$\phi_2(5, 1, 1, 1)_{+1,+3}$	$\phi_3(1, 1, 1, \bar{3})_{-1,-3}$
$\Psi_3(10, 1, 1, 1)$	$\Psi_3(10, 1, 1, 1)$	$\Psi_4^H(1, 1, 1, 1)_{+1,+2}$	$\Psi_6(10, 3, 1, 1)$	$\Psi_6(10, 3, 1, 1)$	$\Phi_3^H(1, \bar{3}, 1, \bar{3})_{+1,+3}$
$\Psi_1^H(1, 1, 1, 3)_{-1,-2}$	$\phi_2(5, 1, 1, 1)_{+1,+3}$	$\phi_3(1, 1, 1, \bar{3})_{-1,-3}$	$\Phi_3^H(1, \bar{3}, 1, \bar{3})_{-1,-3}$	$\phi_2(5, 1, 1, 1)_{+1,+3}$	$\phi_3(1, 1, 1, \bar{3})_{-1,-3}$
$\Psi_3(10, 1, 1, 1)$	$\Psi_3(10, 1, 1, 1)$	$\Phi_1^H(1, 1, 1, \bar{3})_{-1,+3}$	$\Psi_4(1, 1, 1, 1)$	$\Phi_4^H(1, 1, 1, 1)_{-1,-3}$	$\phi_2(5, 1, 1, 1)_{+1,+3}$
$\Phi_1^H(1, 1, 1, \bar{3})_{+1,-3}$	$\phi_2(5, 1, 1, 1)_{+1,+3}$	$\phi_3(1, 1, 1, \bar{3})_{-1,-3}$	$\phi_2(\bar{5}, 1, 1, 1)_{+1,-3}$	$\sigma_1(1, 1, 1, 1)_{-1,-4}$	$\sigma_3(1, 1, 1, 1)_{+3,+4}$
$\Psi_4(1, 1, 1, 1)$	$\Psi_5(\bar{5}, 1, 1, 1)$	$\Psi_1^H(1, 1, 1, 3)_{-1,+2}$	$\Psi_4(1, 1, 1, 1)$	$\Phi_4^H(1, 1, 1, 1)_{-1,-3}$	$\phi_4(1, 1, 5, 1)_{+1,+3}$
$\Psi_4^H(1, 1, 1, 1)_{+1,-2}$	$\phi_2(5, 1, 1, 1)_{+1,+3}$	$\phi_3(1, 1, 1, \bar{3})_{-1,-3}$	$\phi_4(1, 1, \bar{5}, 1)_{+1,-3}$	$\sigma_1(1, 1, 1, 1)_{-1,-4}$	$\sigma_3(1, 1, 1, 1)_{+3,+4}$

and

$$\begin{pmatrix} H_5^{11} & \bar{H}^3 + H_5^{12} & -\bar{H}^2 + H_5^{13} & h_2^1 \\ -\bar{H}^3 + H_5^{21} & H_5^{22} & \bar{H}^1 + H_5^{23} & h_2^2 \\ \bar{H}^2 + H_5^{31} & -\bar{H}^1 + H_5^{32} & H_5^{33} & h_2^3 \\ h_2^1 & h_2^2 & h_2^3 & H_5 \end{pmatrix},$$

where the quantities H, H_5, and $h_{1,2,3}$ carrying the generation superscripts represent the contributions to the fermion mass matrix from the renormalizable five- and six-point terms of the superpotential. We have

$$\bar{H}_5^i = A^i \langle \hat{\Phi}_{5(5,1;1,3)} \rangle_0, \quad H_5^{ij} = A^{ij} \langle \hat{\Phi}_{5(\bar{5},1;1,\bar{3})} \rangle_0,$$

$$H_5 = A \langle \hat{\Phi}_{5(\bar{5},1;1,\bar{3})} \rangle_0,$$

$$h_1^{ij} = A^{ij} \langle \phi_{2(5,1,1,1)} \rangle_0 \langle \phi_{3(1,1,1,\bar{3})} \rangle_0,$$

$$h_2^i = A^i \langle \phi_{3(1,1,1,3)} \rangle_0 \langle \phi_{2(\bar{5},1,1,1)} \rangle_0,$$

$$h_3 = A \langle \phi_{2(5,1,1,1)} \rangle_0 \langle \phi_{3(1,1,1,\bar{3})} \rangle_0,$$

where

$$A^i = \langle \hat{\Psi}^{\mathrm{H}}_{1(1,1;1,3)} \rangle_0 \langle \hat{\Psi}^{\mathrm{H}\,i}_{3(1,\bar{3};1,3)} \rangle_0 + \langle \hat{\Phi}^{\mathrm{H}}_{1(1,1;1,\bar{3})} \rangle_0 \langle \hat{\Phi}^{\mathrm{H}\,i}_{2(1,\bar{3};1,1)} \rangle_0 + \langle \hat{\Phi}^{\mathrm{H}\,i}_{3(1,\bar{3};1,\bar{3})} \rangle_0 \langle \hat{\Phi}^{\mathrm{H}}_{4(1,1;1,1)} \rangle_0,$$

$$A^{ij} = \langle \hat{\Psi}^{\mathrm{H}\,i}_{2(1,\bar{3};1,1)} \rangle_0 \langle \hat{\Psi}^{\mathrm{H}\,j}_{3(1,\bar{3};1,3)} \rangle_0 + \langle \hat{\Phi}^{\mathrm{H}\,i}_{3(1,\bar{3};1,\bar{3})} \rangle_0 \langle \hat{\Phi}^{\mathrm{H}\,j}_{3(1,\bar{3};1,\bar{3})} \rangle_0,$$

$$A = \langle \hat{\Psi}^{\mathrm{H}}_{1(1,1;1,3)} \rangle_0 \langle \hat{\Psi}^{\mathrm{H}}_{4(1,1;1,1)} \rangle_0 + \langle \hat{\Phi}^{\mathrm{H}}_{1(1,1;1,\bar{3})} \rangle_0 \langle \hat{\Phi}^{\mathrm{H}}_{1(1,1;1,\bar{3})} \rangle_0.$$

We again omitted the quantum numbers corresponding to hidden gauge groups. These quantum numbers can be recovered easily by using the table of states of the model. We use here a condensed notation for the product of superfields. In particular, each product of the form $\Psi_k^{\mathrm{H}} \Psi_l^{\mathrm{H}}$ or $\Phi_k^{\mathrm{H}} \Phi_l^{\mathrm{H}}$ with $k \neq l$ stands for two terms with opposite hidden quantum numbers. The contributions to the mass matrices come from all R^6 terms of the superpotential from Table 6, with the exception of the last two and three trivial ones not indicated in this table.

The result for the nonflip case is obtained by means of the substitution $u \rightleftharpoons d, e$.

We can try to use some of the horizontal fields Ψ_i^{H}, Φ_i^{H}, and ϕ_i (see the spectrum of the model) to violate partly the horizontal symmetry $U(3)_{\mathrm{H}}^{\mathrm{I}} \times U(3)_{\mathrm{H}}^{\mathrm{II}}$ at the scale of Grand Unification, preserving $N = 1$ spacetime supersymmetry. In this case, the contribution of nonrenormalizable five- and six-point terms can be important for constructing a realistic fermion mass matrix. It is worth noting that the form of ansatz for the mass matrix will depend on the way in which the original gauge symmetry $U(3)_{\mathrm{H}}^{\mathrm{I}} \times U(3)_{\mathrm{H}}^{\mathrm{II}}$ is broken at the scale M_{GUT}.

Below, we present an example in which horizontal symmetry is broken at a high-energy scale of about M_{GUT}, but $N = 1$ supersymmetry is preserved. In this example, we will consider the possibility of large expectation values of about M_{GUT} only for the following scalar fields: $\Psi_{1,2,4}^{\mathrm{H}}$, $\Phi_{1,2,4}^{\mathrm{H}}$, ϕ_1, ϕ_3, and all σ.

In order to preserve supersymmetry, we must ensure fulfillment of all equalities $D_p^a = F_j = 0$, including all broken groups, and take into account all vacuum expectation values of the scalar fields $\Phi_{1,2,4}^{\mathrm{H}}$, $\Psi_{1,2,4}^{\mathrm{H}}$, ϕ_1, ϕ_3, σ_1, σ_2, and σ_3 (the vacuum expectation value of the field σ_1 is admissible only in the nonflip version of the model because, otherwise, this field would carry an electromagnetic charge).

From the list of states of the model, we can draw the conclusion that, in this model, the hidden group $U(1)_1$ is anomalous: $\mathrm{tr}U(1)_1 = 12$. This means that, in the one-loop approximation of the string, there exists the Fayet–Iliopoulos D term, which is determined by the vacuum expectation value of the dilaton,

$$\xi = \frac{\mathrm{tr}U(1)_1}{16\pi} \frac{g_{\mathrm{GUT}}^2 M_{\mathrm{Pl}}^2}{192\pi^2}.$$

In principle, this term can violate supersymmetry at a high-energy scale and destabilize the vacuum [23]. This can be avoided if the potential has a D-flat direction with respect to $U(1)_1$ charged fields that have vacuum expectation values violating the anomalous group (and possibly some other groups), compensating the D term, and restoring supersymmetry. In order that supersymmetry not be violated through the corresponding D terms, such fields must have appropriate charges with respect to the remaining groups.

Let us write explicitly the equations $D_p^a = 0$ for the example being considered. In doing this, we will assume that the vacuum expectation values for the $SU(3)_{\mathrm{H}}^{\mathrm{I,II}}$ triplets have the form $(0, 0, V)$ and that those for the $SU(4)_{\mathrm{hid}}$ quadruplets have the form $(0, 0, 0, V)$. We redefine $|\Phi_i^{\mathrm{H}}|^2 \pm |\bar{\Phi}_i^{\mathrm{H}}|^2 \longrightarrow \Phi_i, \bar{\Phi}_i$; $|\Psi_i^{\mathrm{H}}|^2 \pm |\bar{\Psi}_i^{\mathrm{H}}|^2 \longrightarrow \Psi_i, \bar{\Psi}_i$; etc., where the overbars label fields with "bottom" quantum numbers from the table of states. Obviously, all new variables must obey the inequalities $0 \leq f_i$ and $-f_i \leq \bar{f}_i \leq f_i$. Thus, we have

(i) $D_{SU(3)_{\mathrm{I}}}^8$

$$-\Psi_2 - \Phi_2 + \bar{\phi}_1 = 0,$$

(ii) $D^8_{SU(3)_{II}}$

$$\Psi_1 - \Phi_1 + \bar{\phi}_3 = 0,$$

(iii, iv) $D^{I}_{Y_5} \pm D^{II}_{Y_5}$

$$\bar{\phi}_1 + \bar{\phi}_3 + \bar{\sigma}_2 + \bar{\sigma}_3 = 0, \quad \bar{\sigma}_1 = 0,$$

(v) $D^{II}_{Y_3} - D^{I}_{Y_3}$

$$\Psi_1 + \Psi_2 + 3\Psi_4 + 2\Phi_1 - 2\Phi_2 - \bar{\phi}_1 + \bar{\phi}_3 = 0,$$

(vi) $D^{II}_{Y_3}$

$$-2\Psi_1 + 6\Psi_2 + 6\Psi_4 + 2\Phi_1 - 6\Phi_2$$
$$-6\Phi_4 - 3\bar{\phi}_1 + \bar{\phi}_3 + 3\bar{\sigma}_2 - 3\bar{\sigma}_3 = 0,$$

(vii) D^{hid}_2

$$\bar{\Psi}_1 + \bar{\Psi}_2 + \bar{\Psi}_4 = 0,$$

(viii) D^{hid}_3

$$\bar{\Phi}_1 + \bar{\Phi}_2 + \bar{\Phi}_4 + \bar{\phi}_1 + \bar{\phi}_3 - \bar{\sigma}_3 = 0,$$

(xi) $D^{hid}_{SU(4)}$

$$-\sigma_1 - \bar{\sigma}_2 - \sigma_3 = 0,$$

(x) D^{hid}_1

$$-\Psi_1 - \Psi_2 + \Psi_4 - \bar{\Phi}_1 + \bar{\Phi}_2 + \bar{\Phi}_4$$
$$-\phi_1 - \phi_3 + \sigma_2 = -2\xi.$$

It should be noted from the outset that the variables ϕ_1, ϕ_3, and σ_2 appear only in the last equation, which involves the anomalous term ξ. Therefore, this set of equations admits a solution in which only ϕ_1, ϕ_3, and σ_2 take nonzero values. However, the superpotential [see expression (52) for W_4] features a hazardous term of the type $(\phi_1^2 + \phi_3^2)\sigma_2^2$, which will then lead to the breakdown of supersymmetry (the condition $F_j = \partial W/\partial\Phi_j = 0$ is not satisfied). Hence, we must set $\sigma_2 = 0$ and, for example, $\phi_1 = \phi_3 = \xi = g^2_{GUT}M^2_{Pl}/256\pi^3$. In this case, the horizontal group is broken down as $U(3)^2_H \longrightarrow SU(2)^2_H \times U(1)_H$, and we also have the violation $U(1)^2_5 \longrightarrow U(1)$. In the hidden group, only the anomalous subgroup $U(1)_1$ is broken.

In the nonflip version, we can consider nonzero $\sigma_1 = \sigma_3$ as well, in which case the condition $\bar{\sigma}_2 = \sigma_2 = 0$ removes the possibility of supersymmetry breaking due to the last two terms in the superpotential W_2 (43). This is accompanied by the breakdown of the hidden non-Abelian group $SU(4)^{hid}_4 \longrightarrow SU(3)^{hid}$; of seven Abelian gauge groups, only two remain unbroken in the model being considered: these are $U(1)^{hid}_2$ and the linear combination $Y' \sim 15Y^{hid}_3 - 3(Y^I_5 + Y^{II}_5) - 10(Y^I_3 + Y^{II}_3)$.

From the form of the $\hat{\sigma}$-dependent contribution to the superpotential W_2 (43), it follows that the fourth-generation field $\hat{\Psi}_{(1,1;1,1)}$ (the fourth neutrino in the nonflip case) acquires a considerable mass. Owing to the first term in expression (52) for W_4, the right-handed neutrinos from the superfield $\hat{\Psi}_{(1,3;1,1)}$ also develop large masses. A detailed consideration of the neutrino mass matrix will be given elsewhere.

APPENDIX

Useful Operator-Product Expansions

We have

$$e^{qc}(z_1)e^{pc}(z_2) \sim \frac{e^{(p+q)c}(z_2)}{z_{12}^{pq}}$$

for ghost fields,

$$S_\alpha(z_1)S_\beta(z_2) \sim \frac{C_{\alpha\beta}}{z_{12}^{1/2}}$$

for spin fields in four dimensions,

$$f(z_1)f(z_2) \sim \frac{1}{z_{12}}, \quad \sigma_\pm(z_1)f(z_2) \sim \frac{1}{\sqrt{2}}\ \frac{1}{z_{12}^{1/2}}\sigma_\mp(z_2),$$

$$\sigma_\pm(z_1)\sigma_\pm(z_2) \sim \frac{1}{|z_{12}|^{1/4}} + \ldots$$

for real fermions (Ising model), and

$$e^{i\alpha H}(z_1)e^{i\beta H}(z_2) \sim \frac{e^{i(\alpha+\beta)H}(z_2)}{z_{12}^{-\alpha\beta}},$$

$$\left\langle \prod_j e^{i\alpha_j H}(z_j) \right\rangle = \prod_{j<k} z_{jk}^{\alpha_j\alpha_k}$$

for exponentials.

REFERENCES

1. M. B. Green and J. H. Schwarz, Phys. Lett. B **149**, 117 (1984).
2. D. J. Gross, J. A. Harvey, E. Martinec, *et al.*, Nucl. Phys. B **256**, 253 (1985).
3. H. Kawai, D. Lewellen, and S.-H. H. Tye, Phys. Rev. Lett. **57**, 1832 (1986); Nucl. Phys. B **288**, 1 (1987).
4. I. Antoniadis, C. Bachas, and C. Kounnas, Nucl. Phys. B **289**, 87 (1987); I. Antoniadis and C. Bachas, Nucl. Phys. B **298**, 586 (1988).
5. S. Kalara, J. López, and D. V. Nanopoulos, Phys. Lett. B **245**, 421 (1990).
6. M. Dine and N. Seiberg, Phys. Rev. Lett. **57**, 2625 (1986).

7. C. M. Hull and E. Witten, Phys. Lett. B **160**, 398 (1985); T. Banks, L. J. Dixon, D. Friedan, *et al.*, Nucl. Phys. B **299**, 613 (1988).
8. S. Kalara, J. L. López, and D. V. Nanopoulos, Nucl. Phys. B **353**, 650 (1991).
9. D. Friedan, E. Martinec, and S. Shenker, Phys. Lett. B **160**, 55 (1985); Nucl. Phys. B **271**, 93 (1986).
10. S. Deser and B. Zumino, Phys. Lett. B **65**, 369 (1976); L. Brink, P. Divecchia, and P. Howe, *ibid.*, **65**, 471 (1976).
11. H. Dreiner, J. L. López, D.V. Nanopoulos, *et al*., Nucl. Phys. B **320**, 401 (1989).
12. I. Antoniadis, J. Ellis, J. S. Hagelin, *et al*., Phys. Lett. B **194**, 231 (1987); **208**, 209 (1988); J. Ellis, J. L. López, and D. V. Nanopoulos, Phys. Lett. B **245**, 375 (1990); J. L. López, D. V. Nanopoulos, and A. Zichichi, CERN-TH-6934/93 (Geneva, 1993); G. Antoniadis, G. Leontaris, and J. Rizos, Phys. Lett. B **245**, 1611 (1990); J. Ellis, G. K. Leontaris, S. Lola, *et al.*, Phys. Lett. B **425**, 86 (1998); hep-ph/9711476.
13. B. C. Allanach, S. F. King, G. K. Leontaris, *et al*., Phys. Lett. B **407**, 275 (1997).
14. I. Antoniadis, J. Ellis, J. S. Hagelin, *et al*., Phys. Lett B **231**, 65 (1989); J. López, D. Nanopoulos, and K. Yuan, Nucl. Phys. B **399**, 654 (1993); A. Faraggi, Phys. Lett. B **274**, 47 (1992); **278**, 131 (1992); **302**, 202 (1993); **236**, 62 (1994); A. Faraggi, D. Nanopoulos, and K. Yuan, Nucl. Phys. B **335**, 347 (1990).
15. D. C. Lewellen, Nucl. Phys. B **337**, 61 (1990); S. Chaudhuri, S. Chung, and J. D. Lykken in *Yukawa Couplings and the Origins of Mass*, Ed. by P. Ramond (International Press, 1995); hep-ph/9405374; S. Chaudhuri, G. Hockney, and J. Lykken, Nucl. Phys. B **469**, 357 (1996); K. R. Dienes and J. March-Russel, Nucl. Phys. B **479**, 113 (1996).
16. Z. Kakushadze, G. Shiu, S.-H. H. Tye, *et al.*, Phys. Lett. B **408**, 173 (1997); hep-th/9710149; Int. J. Mod. Phys. A **13**, 2551 (1998) and references therein; Z. Kakushadze, G. Shiu, and S.-H. H. Tye, Nucl. Phys. B **501**, 547 (1997).
17. S. M. Sergeev and G. G. Volkov, Preprint DFPD/TH/51, INFN, Sezione di Padova (1992); G. G. Volkov and S. M. Sergeev, Yad. Fiz. **57**, 168 (1994) [Phys. At. Nucl. **57**, 158 (1994)]; A. A. Maslikov, S. M. Sergeev, and G. G. Volkov, Phys. Lett. B **328**, 319 (1994); Phys. Rev. D **50**, 7440 (1994); A. A. Maslikov, I. A. Naumov, and G. G. Volkov, Int. J. Mod. Phys. A **11**, 1117 (1996); http://www-theory.fnal.gov/superstrings/Models/four-dim/volkov.myo
18. A. N. Amaglobeli, A. R. Kereselidze, and A. G. Liparteliani, Phys. Lett. B **237**, 417 (1990); A. A. Maslikov and G. G. Volkov, *Towards a Low Energy Quark-Lepton Family with Non-Abelian Gauge Symmetry*, ENSLAPP-A-382/92 (1992); V. A. Monich, B. V. Struminsky, and G. G. Volkov, Phys. Lett. B **104**, 382 (1981); A. G. Liparteliani, V. A. Monich, Yu. P. Nikitin, *et al.*, in *Proceedings of the International Conference Neutrino-77, Baksan Valley, USSR* (Nauka, Moscow, 1978), Vol. 2, p. 541; Yad. Fiz. **27**, 1395 (1978) [Sov. J. Nucl. Phys. **27**, 735 (1978)]; A. A. Maslikov, I. A. Naumov, and G. G. Volkov, Nuovo Cimento A **108**, 1285 (1995); A. N. Amaglobeli *et al.*, Yad. Fiz. **59**, 330 (1996) [Phys. At. Nucl. **59**, 310 (1996)].
19. A. A. Maslikov, I. A. Naumov, and G. G. Volkov, Phys. Lett. B **409**, 160 (1997).
20. S. Kalara, J. L. López, and D. V. Nanopoulos, Phys. Lett. B **269**, 84 (1991); K. R. Dienes, Phys. Rep. **287**, 447 (1997); hep-th/9602045.
21. V. S. Kaplunovsky, Nucl. Phys. B **307**, 145 (1988); **382**, 436 (1992) (Erratum); L. J. Dixon, V. S. Kaplunovsky, and J. Lois, Nucl. Phys. B **355**, 649 (1991); V. S. Kaplunovsky and J. Lois, Nucl. Phys. B **444**, 191 (1995); I. Antoniadis, J. Ellis, R. Lacaze, *et al.*, Phys. Lett. B **268**, 188 (1991).
22. H. D. Dahmen, A. A. Maslikov, I. A. Naumov, *et al.*, hep-th/9711192.
23. M. Dine, N. Seiberg, and E. Witten, Nucl. Phys. B **289**, 585 (1987).

Translated by A. Isaakyan

Physics of Atomic Nuclei, Vol. 63, No. 1, 2000, pp. 139–143. From Yadernaya Fizika, Vol. 63, No. 1, 2000, pp. 152–157.

ELEMENTARY PARTICLES AND FIELDS
Theory

Renormalization Group and Relations between Scattering Amplitudes in a Theory with Different Mass Scales*

A. V. Gulov and V. V. Skalozub**
Dniepropetrovsk State University, pr. Gagarina 72, Dniepropetrovsk, 320625 Ukraine
Received November 12, 1998

Abstract—In the Yukawa model with two different mass scales, the renormalization group equation is used to obtain relations between scattering amplitudes at low energies. By considering fermion–fermion scattering as an example, a basic one-loop renormalization group relation is derived which gives the possibility to reduce the problem to the scattering of light particles in the "external field" substituting a heavy virtual state. Applications of the results to problems of searches for new physics beyond the Standard Model are discussed. *© 2000 MAIK "Nauka/Interperiodica".*

1. INTRODUCTION

An important problem of current high-energy physics is searching for deviation from the Standard Model (SM) of elementary particles which may appear due to heavy virtual states entering the extended models and having masses much greater than the W-boson mass m_W [1]. One of the approaches for the description of such phenomena is the construction of the effective Lagrangians that arise owing to the decoupling of heavy particles. In principle, it is possible to write down a lot of different effective Lagrangians describing effects of new physics beyond the SM. In [2], the effective Lagrangians generated at a tree level in a general renormalizable gauge theory have been derived. These objects by construction contain a great number of arbitrary parameters responsible for specific processes. But it is well known that a renormalizable theory includes a small number of independent constants due to relations between them. The renormalizability of the theory results in the renormalization group (RG) equations for scattering amplitudes [3]. In [4], it has been proven that RG equation can be used to obtain a set of relations between the parameters of the effective Lagrangians. Two main observations were used. First, it has been shown that a heavy virtual state may be considered as an external field scattering SM light particles. Second, the renormalization of the vertices, describing scattering on the external field, can be determined by the β and γ functions calculated with light particles, only. Hence, the relations mentioned above follow. As an example, the SM with the heavy Higgs scalar has been investigated. In the decoupling region, the RG equations for scattering amplitudes have been reduced to the ones for vertices describing the scattering of light particles on the external field substituting the corresponding virtual heavy field. In [4], the only scalar field of the theory was taken as the heavy particle, and no mixing between the heavy and the light fields at the one-loop level has been considered. Here, we are going to investigate the Yukawa model with a heavy scalar field χ and a light scalar field φ. The purposes of our investigation are twofold: to derive the one-loop RG relation for the four-fermion scattering amplitude in the decoupling region and to find out the possibility of reducing this relation in the equation for the vertex describing the scattering of light particles on the external field when the mixing between heavy and light virtual states takes place. In [4], the specific algebraic identities originated from the RG equation for scattering amplitude have been derived. When the explicit couplings in effective Lagrangians are unknown and represented by arbitrary parameters, one may treat the identities as the equations dependent on the parameters and appropriate β and γ functions. If due to a symmetry the number of β and γ functions is less than the number of RG relations, one can obtain a nontrivial system of equations for the parameters mentioned. This was shown for the gauge couplings [4]. In the present paper, we derive RG relations for the effective Lagrangian parameters in the model including one-loop mixing of heavy and light fields.

2. RENORMALIZATION GROUP RELATION FOR THE AMPLITUDE

The Lagrangian of the model reads

$$\mathcal{L} = \frac{1}{2}(\partial_\mu\varphi)^2 - \frac{m^2}{2}\varphi^2 - \lambda\varphi^4 + \frac{1}{2}(\partial_\mu\chi)^2 - \frac{\Lambda^2}{2}\chi^2 - \xi\chi^4 + \rho\varphi^2\chi^2 + \bar{\psi}(i\partial_\mu\gamma_\mu - M - G_\varphi\varphi - G_\chi\chi)\psi, \quad (1)$$

where ψ is the Dirac spinor field. The S-matrix element for the four-fermion scattering at the one-loop level is

* This article was submitted by the authors in English.
** e-mail: skalozub@ff.dsu.dp.ua

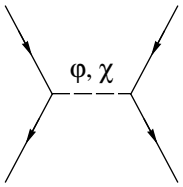

Fig. 1. Tree-level contribution to the four-fermion amplitude.

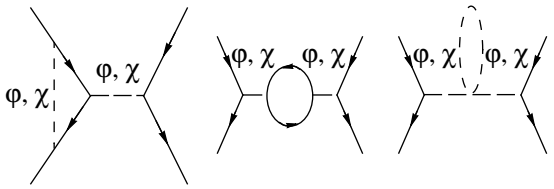

Fig. 2. One-loop level contribution to the one-particle reducible four-fermion amplitude.

given by

$$\hat{S} = -\frac{i}{2}\int \frac{dp_1}{(2\pi)^4}\dots\frac{dp_4}{(2\pi)^4}(2\pi)^4 \times \delta(p_1 + \dots + p_4)\mathcal{N}[S_{1PR} + S_{box}],$$

$$S_{1PR} = \sum_{\phi_1,\phi_2=\varphi,\chi} G_{\phi_1}G_{\phi_2} \times\left(\frac{\delta_{\phi_1\phi_2}}{s-m_{\phi_1}} + \frac{1}{s-m_{\phi_1}}\Pi_{\phi_1\phi_2}(s)\frac{1}{s-m_{\phi_2}}\right) \times\bar{\psi}(p_1)[1 + 2\Gamma(p_2, -p_1-p_2)]\psi((p_2)\bar{\psi}(p_4))\psi(p_3), \quad (2)$$

where $s = (p_1 + p_2)^2$, S_{1PR} is the contribution from the one-particle reducible diagrams shown in Figs. 1 and 2, and S_{box} is the contribution from the box diagram. The one-loop polarization operator of scalar fields $\Pi_{\phi_1\phi_2}$ and the one-loop vertex function Γ are usually defined through the Green's functions

$$D_{\phi_1\phi_2}(s) = \frac{\delta_{\phi_1\phi_2}}{s-m_{\phi_1}} + \frac{1}{s-m_{\phi_1}}\Pi_{\phi_1\phi_2}(s)\frac{1}{s-m_{\phi_2}},$$

$$G_{\phi\phi\psi}(p,q) = -\sum_{\phi_1} G_{\phi_1}D_{\phi_1\phi}(q^2)S_\psi(p) \times[1 + \Gamma(p,q)]S_\psi(-p-q), \quad (3)$$

where S_ψ is the spinor propagator in the momentum representation. The renormalized fields, masses, and charges are defined as follows:

$$\psi = Z_\psi^{-1/2}\psi_0, \quad \begin{pmatrix}\varphi\\ \chi\end{pmatrix} = Z_\phi^{-1/2}\begin{pmatrix}\varphi_0\\ \chi_0\end{pmatrix},$$

$$\begin{pmatrix}G_\varphi\\ G_\chi\end{pmatrix} = Z_G^{-1}\begin{pmatrix}G_{\varphi_0}\\ G_{\chi_0}\end{pmatrix}, \quad (4)$$

$$M^2 = M_0^2 - \delta M^2, \quad m^2 = m_0^2 - \delta m^2, \quad \Lambda^2 = \Lambda_0^2 - \delta\Lambda^2.$$

Using the dimensional regularization (the dimension of the momentum space is $D = 4 - \varepsilon$) and the $\overline{MS}$ renormalization scheme [5], one can compute the renormalization constants

$$Z_\psi = 1 - \frac{1}{16\pi^2\varepsilon}(G_\varphi^2 + G_\chi^2),$$

$$\delta M^2 = \frac{3}{8\pi^2\varepsilon}(G_\varphi^2 + G_\chi^2)M^2,$$

$$Z_\phi^{1/2} = 1 - \frac{1}{8\pi^2\varepsilon} \times\begin{pmatrix} G_\varphi^2 & 2G_\varphi G_\chi\dfrac{\Lambda^2-6M^2}{\Lambda^2-m^2}\\ -2G_\varphi G_\chi\dfrac{m^2-6M^2}{\Lambda^2-m^2} & G_\chi^2\end{pmatrix}, \quad (5)$$

$$\delta m^2 = \frac{1}{4\pi^2\varepsilon}[(G_\varphi^2 + 6\lambda)m^2 - 6G_\varphi^2M^2 - \rho\Lambda^2],$$

$$\delta\Lambda^2 = \frac{1}{4\pi^2\varepsilon}[(G_\chi^2 + 6\xi)\Lambda^2 - 6G_\chi^2M^2 - \rho m^2],$$

$$Z_G^{-1} = \left[1 - \frac{3}{16\pi^2\varepsilon}(G_\varphi^2 + G_\chi^2)\right](Z_\phi^{1/2})^T.$$

From equation (5), we obtain the appropriate β and γ functions [5] at the one-loop level:

$$\beta_\varphi = \frac{dG_\varphi}{d\ln\kappa} = \frac{1}{16\pi^2}\left(5G_\varphi^3 + 3G_\varphi G_\chi^2 - 4\frac{m^2-6M^2}{\Lambda^2-m^2}G_\varphi G_\chi^2\right),$$

$$\beta_\chi = \frac{dG_\chi}{d\ln\kappa} = \frac{1}{16\pi^2}\left(5G_\chi^3 + 3G_\chi G_\varphi^2 + 4\frac{\Lambda^2-6M^2}{\Lambda^2-m^2}G_\chi G_\varphi^2\right), \quad (6)$$

$$\gamma_m = -\frac{d\ln m^2}{d\ln\kappa} = -\frac{1}{4\pi^2}\left(G_\varphi^2\frac{m^2-6M^2}{m^2} + 6\lambda - \rho\frac{\Lambda^2}{m^2}\right),$$

$$\gamma_\Lambda = -\frac{d\ln\Lambda^2}{d\ln\kappa} = -\frac{1}{4\pi^2}\left(G_\chi^2\left(1-6\frac{M^2}{\Lambda^2}\right)+6\xi-\rho\frac{m^2}{\Lambda^2}\right),$$

$$\gamma_\psi = -\frac{d\ln\psi}{d\ln\kappa} = \frac{1}{32\pi^2}(G_\varphi^2+G_\chi^2).$$

Then, the S-matrix element can be expressed in terms of the renormalized quantities (4). The contribution from the one-particle reducible diagrams becomes

$$S_{1PR} = \sum_{\phi_1,\phi_2} G_{\phi_1}G_{\phi_2}\left(\frac{\delta_{\phi_1\phi_2}}{s-m_{\phi_1}}+\frac{1}{s-m_{\phi_1}}\right.$$
$$\left.\times\Pi^{fin}_{\phi_1\phi_2}(s)\frac{1}{s-m_{\phi_2}}\right)\bar\psi(p_1)[1+2\Gamma^{fin}(p_2,-p_1-p_2)] \quad (7)$$
$$\times\psi(p_2)\bar\psi(p_4)\psi(p_3),$$

where the functions $\Pi^{fin}_{\phi_1\phi_2}$ and Γ^{fin} are the expressions for $\Pi_{\phi_1\phi_2}$ and Γ without the terms proportional to $1/\varepsilon$. Since the quantity S_{box} is finite, the renormalization procedure leaves it without changes. Introducing the RG operator at the one-loop level [6]

$$\mathcal{D} = \frac{d}{d\ln\kappa} = \frac{\partial}{\partial\ln\kappa}+\mathcal{D}^{(1)} = \frac{\partial}{\partial\ln\kappa}$$
$$+\sum_\phi\beta_\phi\frac{\partial}{\partial G_\phi}-\gamma_m\frac{\partial}{\partial\ln m^2}-\gamma_\Lambda\frac{\partial}{\partial\ln\Lambda^2}-\gamma_\psi\frac{\partial}{\partial\ln\psi}, \quad (8)$$

we find that the following relation holds for the S-matrix element:

$$\mathcal{D}(S_{1PR}+S_{box}) = \frac{\partial S^{(1)}_{1PR}}{\partial\ln\kappa}+\mathcal{D}^{(1)}S^{(0)}_{1PR} = 0. \quad (9)$$

Here, $S^{(0)}_{1PR}$ and the $S^{(1)}_{1PR}$ are the contributions to the S_{1PR} at the tree level and at the one-loop level, respectively:

$$S^{(0)}_{1PR} = \left(\frac{G_\varphi^2}{s-m^2}+\frac{G_\chi^2}{s-\Lambda^2}\right)\bar\psi\psi\times\bar\psi\psi, \quad (10)$$

$$\frac{\partial S^{(1)}_{1PR}}{\partial\ln\kappa} = \frac{\bar\psi\psi\times\bar\psi\psi}{4\pi^2}\left(-(G_\varphi^2+G_\chi^2)\left(\frac{G_\varphi^2}{s-m^2}+\frac{G_\chi^2}{s-\Lambda^2}\right)\right.$$
$$+\frac{G_\varphi^2[\rho\Lambda^2-6\lambda m^2+G_\varphi^2(6M^2-s)]}{(s-m^2)^2} \quad (11)$$
$$\left.+\frac{2G_\varphi^2G_\chi^2(6M^2-s)}{(s-m^2)(s-\Lambda^2)}+\frac{G_\chi^2[\rho m^2-6\xi\Lambda^2+G_\chi^2(6M^2-s)]}{(s-\Lambda^2)^2}\right).$$

The first term in equation (11) originates from the one-loop correction to the fermion-scalar vertex. The remaining terms are connected with the polarization operator of scalars. The third term describes the one-loop mixing between the scalar fields. It is compensated in the RG relation (9) by the mass-dependent terms in the β functions produced by the nondiagonal elements in Z_ϕ. Equation (9) is the consequence of the renormalizability of the model. It insures the leading logarithm terms of the one-loop S-matrix element to reproduce the appropriate tree-level structure. In contrast to the familiar treatment, we are not going to improve scattering amplitudes by solving equation (9). We will use it as an algebraic identity implemented in the renormalizable theory. Naturally, if one knows the explicit couplings expressed in terms of the basic set of parameters of the model, this RG relation is trivially fulfilled. But the situation changes when the couplings are represented by unknown arbitrary parameters, as occurs in the effective Lagrangian approach [1, 2]. In this case, the RG relations are the algebraic equations dependent on these parameters and appropriate β and γ functions. In the presence of a symmetry, the number of β and γ functions is less than the number of RG relations. So, one has a nontrivial system of equations relating the parameters of effective Lagrangians. Such a scenario is realized for the gauge coupling, as has been demonstrated in [4]. Although the considered simple model has no gauge couplings and no relation between the effective Lagrangian parameters occurs, we are able to demonstrate the general procedure of deriving the RG relations for effective Lagrangians parameters in the theory with one-loop mixing. This point is essential for dealing with the effective Lagrangians describing deviations from the SM. At energies $s \ll \Lambda^2$, the heavy scalar field χ is decoupled. So, the four-fermion scattering amplitude consists of the contribution of the model with no heavy field χ plus terms of order s/Λ^2. The expansion of the heavy scalar propagator,

$$\frac{1}{s-\Lambda^2} \longrightarrow -\frac{1}{\Lambda^2}\left(1+O\left(\frac{s}{\Lambda^2}\right)\right), \quad (12)$$

in equation (10) results in the effective contact four-fermion interaction

$$\mathcal{L}_{eff} = -\alpha\bar\psi\psi\times\bar\psi\psi, \quad \alpha = \frac{G_\chi^2}{\Lambda^2}, \quad (13)$$

and the tree-level contribution to the amplitude becomes

$$S^{(0)}_{1PR} = \left(\frac{G_\varphi^2}{s-m^2}-\alpha+O\left(\frac{s}{\Lambda^4}\right)\right)\bar\psi\psi\times\bar\psi\psi. \quad (14)$$

In the decoupling region, the lowest order effects of the heavy scalar are described by the parameter α, only. The method of constructing the RG equation in terms of the low-energy quantities G_φ, λ, m, M, and α was proposed in [6]. As has been demonstrated in [6], the redefinition of the parameters of the model allows one to remove all the heavy-particle loop contributions to

equation (11). Let us define a new set of fields, charges, and masses $\tilde{\psi}$, $\tilde{G}_\varphi$, $\tilde{G}_\chi$, $\tilde{\Lambda}$, $\tilde{m}$, and $\tilde{M}$,

$$G_\varphi^2 = \tilde{G}_\varphi^2\left(1 + \frac{3\tilde{G}_\chi^2}{16\pi^2}\ln\frac{\kappa^2}{\tilde{\Lambda}^2}\right),$$

$$G_\chi^2 = \tilde{G}_\chi^2\left(1 + \frac{3\tilde{G}_\chi^2}{16\pi^2}\ln\frac{\kappa^2}{\tilde{\Lambda}^2}\right),$$

$$m^2 = \tilde{m}^2\left(1 - \frac{\tilde{\rho}}{8\pi^2}\frac{\tilde{\Lambda}^2}{\tilde{m}^2}\ln\frac{\kappa^2}{\tilde{\Lambda}^2}\right), \qquad (15)$$

$$\Lambda^2 = \tilde{\Lambda}^2\left(1 + \frac{3\tilde{\xi}}{4\pi^2}\ln\frac{\kappa^2}{\tilde{\Lambda}^2}\right),$$

$$\psi = \tilde{\psi}\left(1 - \frac{\tilde{G}_\chi^2}{64\pi^2}\ln\frac{\kappa^2}{\tilde{\Lambda}^2}\right).$$

One can rewrite the differential operator (8) in terms of these new low-energy parameters as

$$\mathcal{D} = \frac{\partial}{\partial\ln\kappa} + \tilde{\mathcal{D}}^{(1)} = \frac{\partial}{\partial\ln\kappa} + \sum_\phi \tilde{\beta}_\phi\frac{\partial}{\partial\tilde{G}_\phi} - \tilde{\gamma}_m\frac{\partial}{\partial\ln\tilde{m}^2} - \tilde{\gamma}_\Lambda\frac{\partial}{\partial\ln\tilde{\Lambda}^2} - \tilde{\gamma}_\psi\frac{\partial}{\partial\ln\tilde{\psi}}, \qquad (16)$$

where $\tilde{\beta}$ and $\tilde{\gamma}$ functions are obtained from the one-loop relations (6) and (15):

$$\tilde{\beta}_\varphi = \frac{1}{16\pi^2}\left(5\tilde{G}_\varphi^3 - 4\frac{\tilde{m}^2 - 6\tilde{M}^2}{\tilde{\Lambda}^2 - \tilde{m}^2}\tilde{G}_\varphi\tilde{G}_\chi^2\right),$$

$$\tilde{\beta}_\chi = \frac{1}{16\pi^2}\left(2\tilde{G}_\chi^3 + \left(3 + 4\frac{\tilde{\Lambda}^2 - 6\tilde{M}^2}{\tilde{\Lambda}^2 - \tilde{m}^2}\right)\tilde{G}_\chi\tilde{G}_\varphi^2\right),$$

$$\tilde{\gamma}_m = -\frac{1}{4\pi^2}\left(\tilde{G}_\varphi^2\frac{\tilde{m}^2 - 6\tilde{M}^2}{\tilde{m}^2} + 6\tilde{\lambda}\right), \qquad (17)$$

$$\tilde{\gamma}_\Lambda = -\frac{1}{4\pi^2}\left(\tilde{G}_\chi^2\left(1 - 6\frac{\tilde{M}^2}{\tilde{\Lambda}^2}\right) - \tilde{\rho}\frac{\tilde{m}^2}{\tilde{\Lambda}^2}\right),$$

$$\tilde{\gamma}_\varphi = \frac{1}{32\pi^2}\tilde{G}_\varphi^2.$$

Hence, one immediately notices that $\tilde{\beta}$ and $\tilde{\gamma}$ functions contain only the light-particle loop contributions, and all the heavy-particle loop terms are completely removed from them. The *S*-matrix element expressed in terms of new parameters satisfies the following RG relation:

$$\mathcal{D}(S_{1PR} + S_{box}) = \frac{\partial\tilde{S}_{1PR}^{(1)}}{\partial\ln\kappa} + \tilde{\mathcal{D}}^{(1)}\tilde{S}_{1PR}^{(0)} = 0, \qquad (18)$$

$$\tilde{S}_{1PR}^{(0)} = \left(\frac{\tilde{G}_\varphi^2}{s - \tilde{m}^2} - \tilde{\alpha} + O\left(\frac{s^2}{\tilde{\Lambda}^4}\right)\right)\bar{\tilde{\psi}}\tilde{\psi}\times\bar{\tilde{\psi}}\tilde{\psi}, \qquad (19)$$

$$\frac{\partial\tilde{S}_{1PR}^{(1)}}{\partial\ln\kappa} = \frac{\bar{\tilde{\psi}}\tilde{\psi}\times\bar{\tilde{\psi}}\tilde{\psi}}{4\pi^2}\left(-\frac{\tilde{G}_\varphi^4}{s - \tilde{m}^2} + \frac{\tilde{G}_\varphi^2[-6\tilde{\lambda}\tilde{m}^2 + \tilde{G}_\varphi^2(6\tilde{M}^2 - s)]}{(s - \tilde{m}^2)^2} + \tilde{\alpha}\tilde{G}_\varphi^2 - \frac{2\tilde{G}_\varphi^2\tilde{\alpha}(6\tilde{M}^2 - s)}{s - m^2} + O\left(\frac{s^2}{\tilde{\Lambda}^4}\right)\right), \qquad (20)$$

where $\tilde{\alpha} = \tilde{G}_\chi^2/\tilde{\Lambda}^2$ is the redefined effective four-fermion coupling. As one can see, equation (20) includes all the terms of equation (11) except for the heavy-particle loop contributions. It depends on the low-energy quantities $\tilde{\psi}$, $\tilde{G}_\varphi$, $\tilde{\alpha}$, $\tilde{\lambda}$, $\tilde{m}$, and $\tilde{M}$. The first and second terms in equation (20) are just the one-loop amplitude calculated within the model with no heavy particles. The third and fourth terms describe the light-particle loop correction to the effective four-fermion coupling and the mixing of heavy and light virtual fields.

3. ELIMINATION OF ONE-LOOP SCALAR FIELD MIXING

Due to the mixing term, it is impossible to split the RG relation (18) for the *S*-matrix element into those for vertices. Hence, we are not able to consider equation (18) in the framework of the scattering of light particles on an external field induced by the heavy virtual scalar, as has been done in [4]. But this is an important step in deriving the RG relation for effective Lagrangian parameters. Fortunately, there is a simple procedure allowing one to avoid the mixing in equation (20). The way is to diagonalize the leading logarithm terms of the scalar polarization operator in the redefinition of $\tilde{\varphi}$, $\tilde{\chi}$, $\tilde{G}_\varphi$, and $\tilde{G}_\chi$:

$$\begin{pmatrix}\varphi\\ \chi\end{pmatrix} = \zeta^{1/2}\begin{pmatrix}\tilde{\varphi}\\ \tilde{\chi}\end{pmatrix},$$

$$\begin{pmatrix}G_\varphi\\ G_\chi\end{pmatrix} = \left[1 + \frac{3\tilde{G}_\chi^2}{32\pi^2}\ln\frac{\kappa^2}{\tilde{\Lambda}^2}\right](\zeta^{-1/2})^T\begin{pmatrix}\tilde{G}_\varphi\\ \tilde{G}_\chi\end{pmatrix}, \qquad (21)$$

$$\zeta^{1/2} = 1 - \frac{\tilde{G}_\varphi\tilde{G}_\chi}{8\pi^2(\tilde{\Lambda}^2 - \tilde{m}^2)}$$

$$\times \ln\frac{\kappa^2}{\tilde{\Lambda}^2}\begin{pmatrix} 0 & \tilde{\Lambda}^2 - 6\tilde{M}^2 \\ -\tilde{m}^2 - 6\tilde{M}^2 & 0 \end{pmatrix}.$$

The appropriate $\tilde{\beta}$ functions

$$\tilde{\beta}_\varphi = \frac{5\tilde{G}_\varphi^3}{16\pi^2},$$
$$\tilde{\beta}_\chi = \frac{1}{16\pi^2}(2\tilde{G}_\chi^3 + 3\tilde{G}_\chi\tilde{G}_\varphi^2) \quad (22)$$

contain no terms connected with mixing between light and heavy scalars. Thus, the fourth term in equation (20) is removed, and the RG relation for the *S*-matrix element becomes

$$\mathcal{D}(S_{1PR} + S_{box}) = \frac{\partial\tilde{S}_{1PR}^{(1)}}{\partial\ln\kappa} + \tilde{\mathcal{D}}^{(1)}\tilde{S}_{1PR}^{(0)} = 0, \quad (23)$$

$$\tilde{S}_{1PR}^{(0)} = \left(\frac{\tilde{G}_\varphi^2}{s-\tilde{m}^2} - \tilde{\alpha} + O\left(\frac{s^2}{\tilde{\Lambda}^4}\right)\right)\bar{\tilde{\psi}}\tilde{\psi}\times\bar{\tilde{\psi}}\tilde{\psi}, \quad (24)$$

$$\frac{\partial\tilde{S}_{1PR}^{(1)}}{\partial\ln\kappa} = \frac{\bar{\tilde{\psi}}\tilde{\psi}\times\bar{\tilde{\psi}}\tilde{\psi}}{4\pi^2}\left(-\frac{\tilde{G}_\varphi^4}{s-\tilde{m}^2}\right.$$
$$\left. + \frac{\tilde{G}_\varphi^2[-6\tilde{\lambda}\tilde{m}^2 + \tilde{G}_\varphi^2(6\tilde{M}^2 - s)]}{(s-\tilde{m}^2)^2} + \tilde{\alpha}\tilde{G}_\varphi^2 + O\left(\frac{s^2}{\tilde{\Lambda}^4}\right)\right). \quad (25)$$

At $\tilde{\alpha} = 0$, equation (23) is just the RG identity for the scattering amplitude calculated in the absence of the heavy particles. The terms of order $\tilde{\alpha}$ describe the RG relation for the effective low-energy four-fermion interaction in the decoupling region. The last one can be reduced in the RG relation for the vertex describing the scattering of the light particle (fermion) on the external field $\sqrt{\tilde{\alpha}}$ substituting the virtual heavy scalar:

$$\mathcal{D}(\sqrt{\tilde{\alpha}}\bar{\tilde{\psi}}\tilde{\psi}) = \frac{\tilde{G}_\varphi^2}{8\pi^2}\sqrt{\tilde{\alpha}}\bar{\tilde{\psi}}\tilde{\psi} + \tilde{\mathcal{D}}^{(1)}(\sqrt{\tilde{\alpha}}\bar{\tilde{\psi}}\tilde{\psi}) = 0, \quad (26)$$

where

$$\tilde{\mathcal{D}}^{(1)} = \tilde{\beta}_\varphi\frac{\partial}{\partial\tilde{G}_\varphi} - \tilde{\gamma}_\alpha\frac{\partial}{\partial\ln\tilde{\alpha}} - \tilde{\gamma}_m\frac{\partial}{\partial\ln\tilde{m}^2} - \tilde{\gamma}_\psi\frac{\partial}{\partial\ln\tilde{\psi}},$$
$$\tilde{\gamma}_\alpha = -\mathcal{D}\tilde{\alpha} = -\frac{1}{8\pi^2}(3\tilde{G}_\varphi^2 + O(\tilde{\alpha})). \quad (27)$$

Equations (23)–(27) are the main result of our investigation. One can derive them with only the knowledge about the effective Lagrangian (13) and the Lagrangian of the model with no heavy particles. One also has to ignore all the heavy-particle loop contributions to the RG relation and the one-loop mixing between the heavy and light fields. Equations (23)–(27) depend on the effective low-energy parameters only. But as the difference between the original set of parameters and the low-energy one is of one-loop order, one may freely substitute them in equations (23)–(26).

4. DISCUSSION

Let us discuss the results obtained. The RG relation for the four-fermion scattering amplitude is derived in the decoupling region $s \ll \Lambda^2$. It was shown that one can redefine the parameters and the fields of the model in order to remove all the heavy-particle loop contributions to the RG relation. Then, the RG relation becomes dependent on the low-energy physics parameters, only. As the RG operator coefficients and the difference between the original parameters and the redefined ones are of the one-loop order, one can replace one set of parameters by another at the lowest level. Thus, we extend the result of [4] to the case when mixing terms are present. The additional transformation of fields and charges allows one to diagonalize the leading logarithm terms of the scalar polarization operator and to avoid the contributions to the RG relation originated from the one-loop mixing between the heavy and light field. Since the difference between the diagonalized fields and charges and the original ones is of one-loop order, one may simply omit one-loop mixing terms in the RG relation at the lower level. Then, it is possible to reduce the RG relation for the *S*-matrix element to the one for the vertex describing the scattering of light particles on the external field induced by the heavy virtual particle. In fact, this result is independent of the specific features of the considered model, as was shown in [4].

The RG relations of the considered type may be used in searching for the dependences between the parameters of effective Lagrangians describing physics beyond the SM. For example, let a symmetry require the same charge structure for some effective Lagrangians. Then, the number of unknown $\tilde{\beta}$ and $\tilde{\gamma}$ functions is less than the number of RG relations, and it is possible to derive nontrivial solutions for the parameters. The present results allow one to omit the one-loop mixing diagrams in construction of the RG relations for the tree-level effective Lagrangians.

REFERENCES

1. J. Wudka, Int. J. Mod. Phys. A **9**, 2301 (1994).
2. C. Arzt, M. Einhorn, and J. Wudka, Nucl. Phys. B **433**, 41 (1995).
3. N. N. Bogoliubov and D. V. Shirkov, *Introduction to the Theory of Quantized Fields* (Nauka, Moscow, 1984; Wiley, New York, 1980).
4. A. V. Gulov and V. V. Skalozub, Yad. Fiz. **62**, 341 (1999) [Phys. At. Nucl. **62**, 306 (1999)].
5. T.-P. Cheng and L.-F. Li, *Gauge Theory of Elementary Particle Physics* (Clarendon, Oxford, 1984).
6. M. Bando, T. Kugo, N. Maekawa, *et al.*, Prog. Theor. Phys. **90**, 405 (1993).

Physics of Atomic Nuclei, Vol. 63, No. 1, 2000, pp. 31–39. Translated from Yadernaya Fizika, Vol. 63, No. 1, 2000, pp. 36–45.

NUCLEI
Experiment

Photofission of ^{238}Pu, ^{240}Pu, and ^{242}Pu in the Energy Range 5–10 MeV

A. S. Soldatov, A. I. Blokhin, A. V. Ignatyuk, and A. N. Storozhenko

Institute of Physics and Power Engineering, pl. Bondarenko 1, Obninsk, Kaluga oblast, 249020 Russia

Received November 4, 1998; in final form, January 22, 1999

Abstract—The cross sections for the photofission of plutonium isotopes ^{238}Pu, ^{240}Pu, and ^{242}Pu in the energy range 5–10 MeV have been measured by using a beam of bremsstrahlung photons from the microtron installed at the Institute of Physics and Power Engineering (Obninsk). The energy regions below the fission barrier and above 6 MeV have been scanned with pitches of 0.05 and 0.1 MeV, respectively. In deriving the absolute cross section for ^{238}Pu photofission, ^{238}U photofission has been employed as a reference reaction. In measurements involving ^{240}Pu and ^{242}Pu nuclei, the neptunium isotope ^{237}Np, which is characterized by a more regular dependence of the photofission cross section on excitation energy than ^{238}U, has been chosen for the first time as a reference nucleus. The measured cross sections as functions of energy show resonance structures in the vicinity of the fission threshold that are consistent with those previously observed in the energy dependences of fissilities for corresponding direct reactions. The partial-wave cross sections for the $J^\pi K = 1^-0$, 1^-1, and 2^+0 photofission channels have been determined as functions of energy. At energies below some 5.5 MeV, the total cross section for photofission of each plutonium isotope being studied receives a significant contribution from quadrupole interaction. Within the one-dimensional model of a two-humped fission barrier, the parameters of the barriers for ^{238}Pu, ^{240}Pu, and ^{242}Pu have been extracted from data and have then been compared with estimates based on previous measurements. *© 2000 MAIK "Nauka/Interperiodica".*

1. INTRODUCTION

The structure of the fission barrier in a given nucleus is investigated through fission reactions induced by nuclear projectiles (such as neutrons, deuterons, and tritons) and by incident photons. From the viewpoint of data analysis, an important advantage of the photon probe is that the photon–nucleus cross section decreases fast with increasing angular momentum, so that the angular-momentum transfer to the nucleus is largely restricted to $l = 1$ and 2; as a result, the cross section picks negligibly small contributions from multipoles higher than $E2$ and $M1$. For this reason, the reaction of photofission is particularly effective for probing even–even nuclei of zero spin. As soon as the total cross section of photofission and the angular distributions of fragments have been measured in the threshold region, we can derive the partial-wave cross sections for the $J^\pi K = 1^-0$, 1^-1, and 2^+0 reaction channels as functions of excitation energy (here, J^π denotes the spin–parity of the fragmenting nucleus, and K is the spin projection onto the line along which fragments fly apart and which coincides with the axis of the nucleus).

This article reports on an investigation of the photofission of three even–even isotopes of plutonium: ^{238}Pu, ^{240}Pu, and ^{242}Pu. The angular distributions of fragments $W(\theta)$ originating from the photofission of these nuclei were measured previously [1] in a beam of bremsstrahlung photons generated by the microtron installed at the Institute of Physics Problems. The estimates of the total cross sections from [1] were based on data of previous experiments that aimed largely at measuring angular distributions. That there have been no precision data on the total cross sections for the photofission of ^{238}Pu, ^{240}Pu, and ^{242}Pu nuclei in the near-threshold region E = 5–7 MeV has prompted us to measure these cross sections in a dedicated experiment. The reported measurement also covers the energy region between the threshold and the giant dipole resonance, E = 7–10 MeV, where the data for ^{240}Pu and ^{242}Pu are totally lacking and where the cross section for ^{238}Pu has been measured only for $E > 7.5$ MeV (up to 11 MeV in this case) [2]. The present measurements, carried out in a beam of bremsstrahlung photons, rely on the reference method, which was described in detail elsewhere [3, 4]. The cross section for ^{238}Pu photofission was measured here with respect to that for ^{238}U [3], a nucleus that was employed as a reference one in all of our previous measurements. In our measurements for ^{240}Pu and ^{242}Pu isotopes, the reference was taken to be, for the first time, ^{237}Np, a nucleus that is characterized by a more regular behavior of the photofission cross section in the threshold region than ^{238}U.

The cross sections for the photofission of three even–even isotopes of plutonium as measured in this study for energies near the fission threshold are then analyzed for partial-wave content by using our earlier data from [1] on the angular distributions of fragments in the same reactions. This analysis relies on experience gained in studying ^{234}U [5] and updates our earlier partial-wave analysis of the cross sections for the

Table 1. Thicknesses of fissile targets (t) and distances from them to the tungsten section of the braking target (L)

Composition of fissile-target assemblies	Assembly number	t for the isotope under investigation, mg/cm^2	t for the reference isotope, mg/cm^2	L, mm
^{238}Pu–^{238}U	1	0.06	0.61	35
	2	0.06	0.57	42
^{240}Pu–^{237}Np	1	0.49	0.75	84
	2	0.56	0.73	91
^{242}Pu–^{237}Np	1	0.64	0.77	70
	2	0.60	0.79	77
^{237}Np–^{238}U	1	0.76	2.00	98

Table 2. Admixtures of extraneous fissile nuclei in the samples of the isotopes under investigation and reference isotopes

Irradiated sample	Admixture content, %					
	^{235}U	^{239}Pu	^{240}Pu	^{241}Pu	^{242}Pu	^{244}Pu
^{238}Pu	–	0.4	1	–	0.3	–
^{240}Pu	–	0.04	–	1.2	0.004	–
^{242}Pu	–	0.00005	0.0002	0.08	–	0.00002
^{237}Np	0.01	0.001	–	–	–	–
^{238}U	0.003	–	–	–	–	–

photofission of ^{238}Pu, ^{240}Pu, and ^{242}Pu nuclei [6]. In particular, we were able to reveal the dependence of the reaction parameters on the number of neutrons in a nucleus undergoing fission from a higher excited state.

2. EXPERIMENTAL RESULTS

Actually measured was the ratio R of the yields from the photofission of the nucleus being investigated, Y, and of the reference nucleus, Y_0,

$$R(E_{\max}) = Y(E_{\max})/Y_0(E_{\max}), \quad (1)$$

as a function of the endpoint energy of bremsstrahlung photons, $E_{\max}$. For the photofission of the nucleus being investigated, the yield of the reaction is expressed in terms of its cross section $\sigma_f(E)$ as

$$Y(E_{\max}) = C(E_{\max}) \int_0^{E_{\max}} \sigma_f(E) N(E, E_{\max}) dE, \quad (2)$$

where $N(E, E_{\max})$ stands for the energy spectrum of bremsstrahlung photons and $C(E_{\max})$ is a normalization factor that takes into account the total number of irradiated nuclei and the total flux of incident photons. The yield of the reference reaction, $Y_0(E_{\max})$, is similarly expressed in terms of its own cross section $\sigma_f^0(E)$.

The photon beam used was generated by an electron beam from the microtron of the Institute of Physics and Power Engineering and was moderated in a braking target made of 1-mm-thick tungsten and 12-mm-thick aluminum. Over the energy region $4.9 < E_{\max} < 6.1$ MeV, the ratio $R(E_{\max})$ for each nucleus under study was measured with a pitch of 0.05 MeV. Higher values of $E_{\max}$ (up to 9 MeV for ^{238}Pu and up to 9.4 MeV for ^{240}Pu and ^{242}Pu) were scanned with a cruder pitch of 0.1 MeV. Additionally, the ratio $R(E_{\max})$ for ^{238}Pu was sampled in the interval 9.4–10.0 MeV with a still cruder pitch of 0.2 MeV.

The apparatus was very similar to those described in [3–5]. A layer of the isotope being investigated and a layer of the reference isotope (in oxide forms) were placed back to back in a container that was rigidly attached to the braking target. For each isotope of plutonium, we used two containers. An additional container housed the layers of ^{237}Np and ^{238}U: this was needed for calibrating the cross section for the photofission of ^{237}Np, which was used for the first time as a reference nucleus. For each two-isotope assembly, Table 1 quotes the thicknesses of active layers, t, and the distance between the assembly and the tungsten part of the braking target, L.

The irradiated areas of the active layers were restricted by diaphragms with circular holes of diameter 10 mm. Fission fragments were detected by mica counters positioned at a distance of 1.5 mm from the active layers.

The ^{240}Pu–^{237}Np, ^{242}Pu–^{237}Np, and ^{237}Np–^{238}U assemblies were irradiated simultaneously. The two ^{238}Pu–^{238}U assemblies were irradiated separately from the others, since much thinner layers of ^{238}Pu (see Table 1) dictated a much longer exposure to the photon beam.

The admixtures of extraneous nuclei in the irradiated samples of a fissile material are listed in Table 2.

Since the cross sections for the photofission of different plutonium isotopes are on the same order of magnitude, the systematic shifts due to the admixtures of extraneous isotopes prove to be much less than statistical uncertainties. Therefore, the measured cross sections are not corrected for the isotope composition of the plutonium samples.

For the three isotopes of plutonium, the measured ratios R as functions of E_{max} are plotted in Fig. 1 (in numerical form, they are also tabulated in [7]). Shown by error bars are the experimental uncertainties that have been described in detail elsewhere [5]. For each of the even–even plutonium isotopes, the photofission reaction must be discriminated against the background of spontaneous fission, which was estimated to a precision of some 1%. Its relative contribution to the signal does not exceed 3 to 4% for energies above 6 MeV, but it increases toward lower energies, reaching 92–95% at the lower boundary of the interval studied here. The measured cross sections were corrected for the angular acceptance of the apparatus by using data from [1] on the angular distribution of photofission fragments. For each plutonium isotope, the photofission cross section was estimated with an overall systematic uncertainty of nearly 15%, which arises, in particular, from the uncertainty in the ratio of the total numbers of nuclei investigated here and reference nuclei in the assembly. This ratio was measured to within 3% by irradiating the same assembly with 2.7-MeV neutrons (see also [5]).

For each plutonium isotope, the yield of the reaction was then derived as $Y(E_{max}) = R(E_{max})Y_0(E_{max})$ [see equation (1)], where $R(E_{max})$ is the measured value of the ratio and $Y_0(E_{max})$ is the yield of the reference reaction; the latter was estimated by integrating the reference cross section over the bremsstrahlung spectrum [8] according to (2). The uncertainty in the reference cross section was neglected. In the reported measurements for the isotope ^{238}Pu, as in our previous measurements for other nuclei [3–5, 9, 10], ^{238}U was employed as a reference nucleus; the cross section for its photofission was estimated in [3]. That the cross section for photofission of ^{238}U shows a resonance structure in the vicinity of the fission threshold—this structure is usually associated with vibrational states in the second well of the potential barrier—poses serious problems for the relative measurements using this even–even nucleus for a reference. In our measurements for the isotopes ^{240}Pu and ^{242}Pu, we therefore chose ^{237}Np as a reference nucleus: in relation to ^{238}U, this A-odd nucleus shows a larger density of internally excited states and, as a consequence, a more regular dependence of the cross section on excitation energy. That the angular distribution of fragments from ^{237}Np photofission is isotropic effectively reduces the uncertainty arising from the limited angular acceptance of the apparatus. Using ^{237}Np photofission as a reference reaction was proposed in [4], where the cross section for its photofission was measured in detail. It is these results that were employed here for the reference cross section below 7 MeV. At higher energies, we relied on the cross section for ^{237}Np photofission from measurements with a beam of monochromatic photons [11].

For each plutonium isotope studied here, the photofission cross section as a function of excitation energy, $\sigma_f(E)$, was extracted from the measured yield $\Delta Y(E_{max})$ by applying the method of minimization of directed divergences [12] for solving the integral equation (2). The $\sigma_f(E)$ values obtained in this way are illustrated in Fig. 2 (in numerical form, they were tabulated in [7]). The uncertainty in the cross section, as shown by error bars in Fig. 2, was estimated by randomizing the yield $\Delta Y(E_{max})$ in accordance with its uncertainty and by analyzing the resulting dispersion of the solutions to equation (2). The uncertainty in $Y(E_{max})$ was estimated by propagating the measurement error in the ratio $R(E_{max})$.

Also illustrated in Fig. 2 are the results of previous measurements of the cross sections for photofission of the isotopes ^{238}Pu [2], ^{240}Pu [13], and ^{242}Pu [14], as well as our earlier estimates [1] thereof, which were based on a measurement of $W(\theta, E_{max})$. Note that all these measurements, like that which is reported in the present article, were performed with bremsstrahlung photons. Our preliminary estimates [1] are seen to be largely confirmed by the thorough and systematic measurements reported in this article, but there are nevertheless some distinctions.

Measured simultaneously was the ratio of the yields from ^{237}Np and ^{238}U photofission (see above). That the ^{237}Np–^{238}U and ^{240}Pu–^{237}Np assemblies were arranged at a small distance allowed us to measure, in addition, the ratio of the yields from ^{240}Pu and ^{238}U photofissions, but the layers of ^{240}Pu and ^{238}U were not, strictly speaking, in a back-to-back configuration. Thereby, we obtained an independent estimate of the absolute yield $Y(E_{max})$ and, finally, of the cross section $\sigma_f(E)$ for the photofission of the isotope ^{240}Pu, this time using ^{238}U as a reference nucleus. Good agreement between the two estimates of $\sigma_f(E)$ for the isotope ^{240}Pu, which are based on different reference nuclei, demonstrates the self-consistency of the adopted approach. (Likewise, the two independent measurements of the cross section for ^{232}Th photofission, with either ^{238}U or ^{237}Np as a reference nucleus, yield compatible results.)

The accuracy of the reported measurements allowed us to probe the resonance structure of the cross section in the near-threshold region. On the whole, the cross sections for the photofission of the isotopes ^{238}Pu, ^{240}Pu, and ^{242}Pu are characterized by similar magnitudes and E dependences, but the positions of the resonances in the energy region $E < 7$ MeV are not identical for the three nuclear species.

Throughout the energy region 7–10 MeV, the cross sections for the photofission of all three plutonium isotopes proved to be regular. For the ^{238}Pu isotope, our

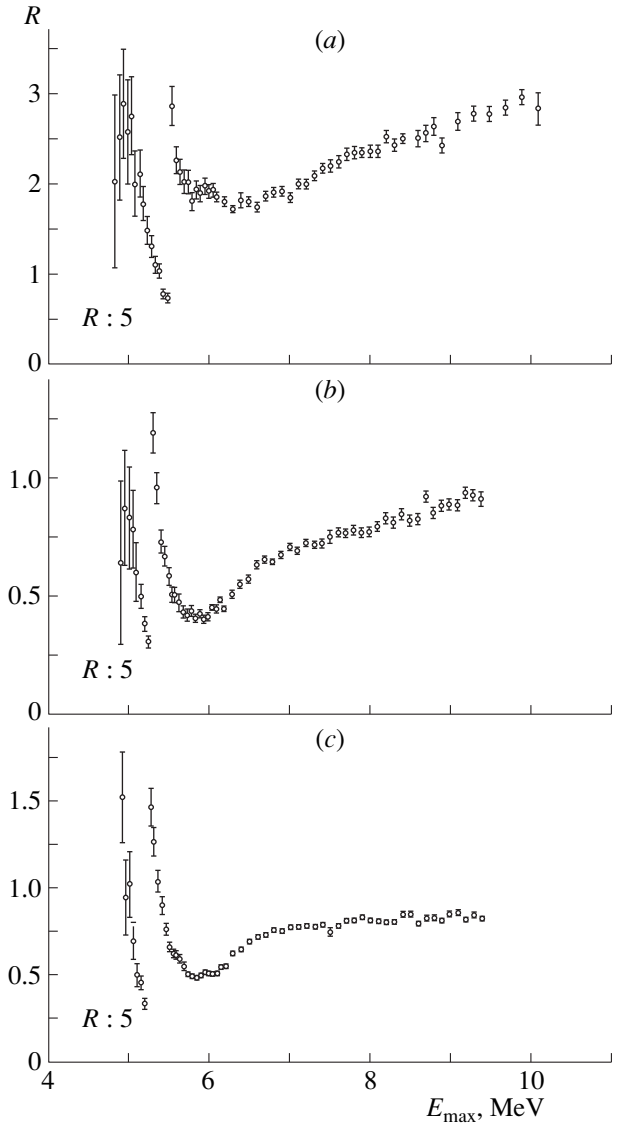

Fig. 1. Photofission-yield ratio R as a function of the endpoint energy of bremsstrahlung photons, E_{max}, for (*a*) ^{238}Pu and ^{238}U, (*b*) ^{240}Pu and ^{237}Np, and (*c*) ^{242}Pu and ^{237}Np nuclei.

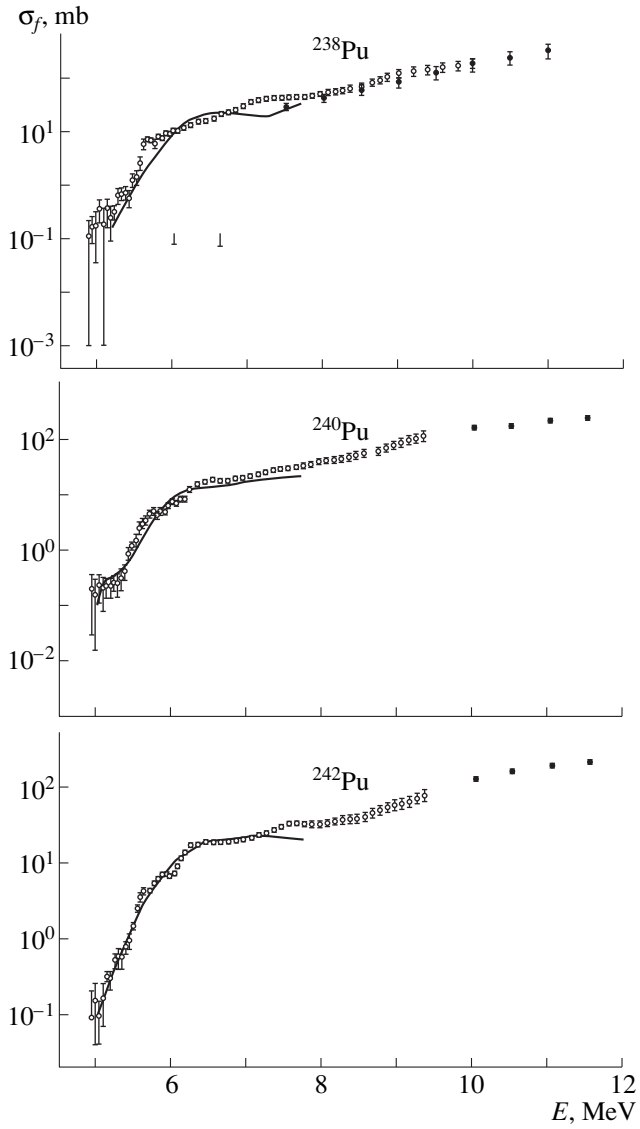

Fig. 2. Total cross sections for ^{238}Pu, ^{240}Pu, and ^{242}Pu photofission as functions of excitation energy: (○) present data and (●) data from [2, 13, 14] for ^{238}Pu, ^{240}Pu, and ^{242}Pu, respectively. Solid curves represent cross-section estimates from [1].

estimate of the cross section exceeds the previous estimate from [2] by some 10–15% throughout the energy region 7.5–10.0 MeV, which is common to the two measurements. For the ^{240}Pu and ^{242}Pu isotopes, our estimates of $\sigma_f(E)$ match well with the results from [13] and [14], respectively, at $E \simeq 10$ MeV, but they begin to deviate from those at higher energies. Comparing the cross sections for the photofission of the even–even isotopes ^{238}Pu, ^{240}Pu, ^{242}Pu, and ^{244}Pu (the last was studied in [15]) among themselves, we see that an increase in the atomic number A by two units effectively reduces $\sigma_f(E)$ by some 20–30%. Such an A dependence of $\sigma_f(E)$ suggests that, for an excited nucleus, the probability to relax through neutron emission increases with A.

The reported measurements of the cross sections for the photofission of three even–even isotopes of plutonium on the basis of a single procedure (reference method) are very similar to the earlier measurements for the nuclei ^{231}Pa [9], ^{232}Th [10], ^{234}U [5], and ^{237}Np [4]. They complement and refine the previous results from [2, 13, 14].

The angular distribution of photofission fragments can be represented as

$$W(\theta) = a + b\sin^2\theta + c\sin^2 2\theta, \qquad (3)$$

where θ is the angle between the photon-beam direction and the line along which the fragments fly apart.

Accordingly, the cross section can be written as $\sigma_f(E) = \sigma_a(E) + \sigma_b(E) + \sigma_c(E)$, where the components correspond to the three terms in (3). By invoking the experimental results from [1] on the angular distributions of fragments, we were able to determine the energy dependences of the cross-section components σ_a, σ_b, and σ_c from the plutonium isotopes under study.

As in [5], where such a decomposition was performed for ^{234}U photofission, the component σ_c is estimated rather roughly. By using the equations that are quoted in [5] and which relate the components σ_a, σ_b, and σ_c to the partial-wave cross sections $\sigma_f^{JK}(E)$ corresponding to definite values of the total angular momentum (J) and of its projection onto the direction of fragment emission (K), we determined the partial-wave cross sections $\sigma_f^{10}(E)$, $\sigma_f^{11}(E)$, and $\sigma_f^{20}(E)$ (only a rough estimate was obtained in the last case) as functions of excitation energy. These results are depicted in Figs. 3, 4, and 5 for ^{238}Pu, ^{240}Pu, and ^{242}Pu, respectively.

The quoted uncertainties in the partial-wave cross sections reflect the experimental errors in the total yield $Y(E_{max})$ and in the parameters a, b, and c of the angular distribution of fragments [see equation (3)]. At excitation energies below 5.5 MeV, the total cross section for photofission of each even–even plutonium isotope features a significant quadrupole component.

It is physically meaningful to compare the resonance structures of the cross sections for the photofission of a given nucleus and for its direct fission in reactions like (t, pf). Direct fission reactions are characterized by a broad spectrum of angular-momentum transfers; therefore, they may involve a large number of fission channels, including the $J^\pi = 2^+$ and 1^- channels, which are excited in the photofission of the even–even nuclei [16]. The comparison is done in terms of the fissility $P_f(E)$ that, for the reaction of photofission, is computed as a ratio of the cross sections for photofission and for photoabsorption:

$$P_f(E) = \sigma_f(E)/\sigma_{cJ}(E). \quad (4)$$

The photoabsorption cross section $\sigma_{cJ}(E)$ was parametrized as a superposition of two Lorentzian forms:

$$\sigma_{cJ} = \sum_{i=1}^{2} \sigma_i \frac{E^2\Gamma_i^2}{(E^2 - E_i^2)^2 + E^2\Gamma_i^2}. \quad (5)$$

Its dipole contribution $\sigma_{c1}(E)$, assumed to take the same value for all three even–even isotopes of plutonium, was set to that for the ^{239}Pu isotope as parametrized in the same form (5) and as calculated with the parameter values of $\sigma_1 = 325$ mb, $\Gamma_1 = 2.48$ MeV, $E_1 = 10.28$ MeV, $\sigma_2 = 384$ mb, $\Gamma_2 = 4.25$ MeV, and $E_2 = 13.73$ MeV, which were derived in [11].

Data on the quadrupole contribution to the photoabsoprtion cross section, $\sigma_{c2}(E)$, are scarce. Therefore, estimates of $\sigma_{c2}(E)$ are usually based on electrodynamics calculations for the ratio of the cross sections for electric-dipole and electric-quadrupole photoabsorption: $\sigma_{c1}/\sigma_{c2} \approx 25$–$30$. We note, however, that, according to some measurements (for an overview, see [17,

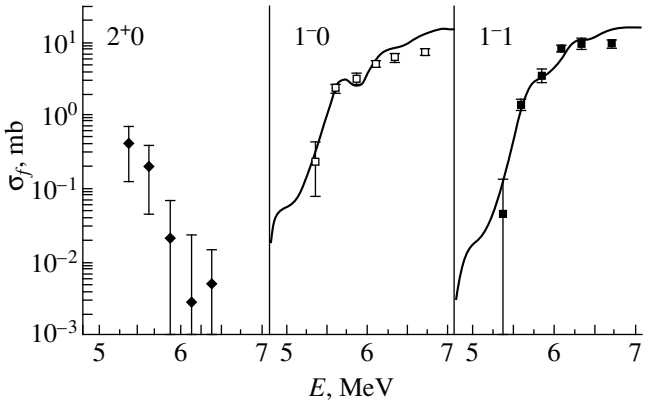

Fig. 3. Results of the analysis of the cross-section components for ^{238}Pu versus excitation energy: (◆) rough estimate of the cross section for quadrupole photofission, (□) cross section for photofission through the $J^\pi K = 1^-0$ channel, and (■) cross section for photofission through the $J^\pi K = 1^-1$ channel. Solid curves represent fits of the cross-section components to forms predicted theoretically.

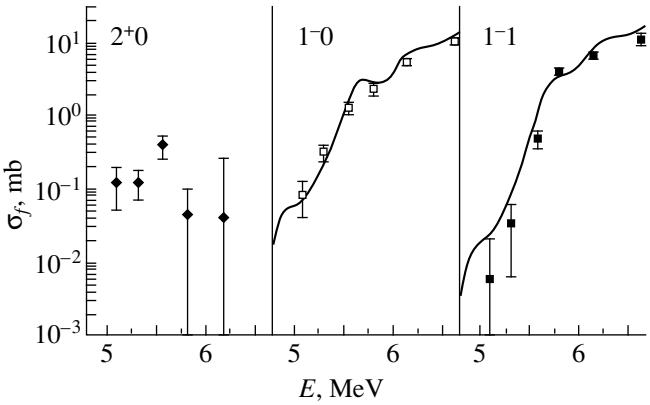

Fig. 4. As in Fig. 3, but for ^{240}Pu.

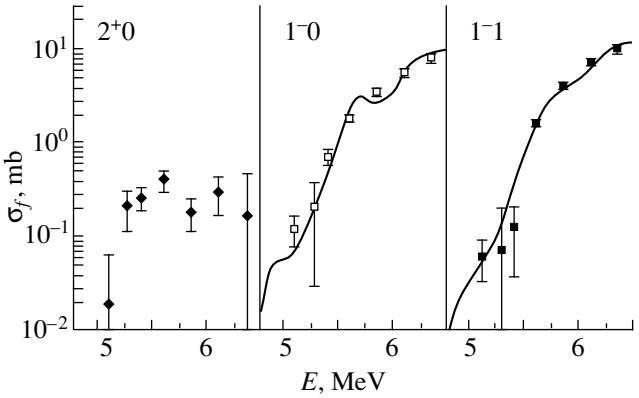

Fig. 5. As in Fig. 3, but for ^{242}Pu.

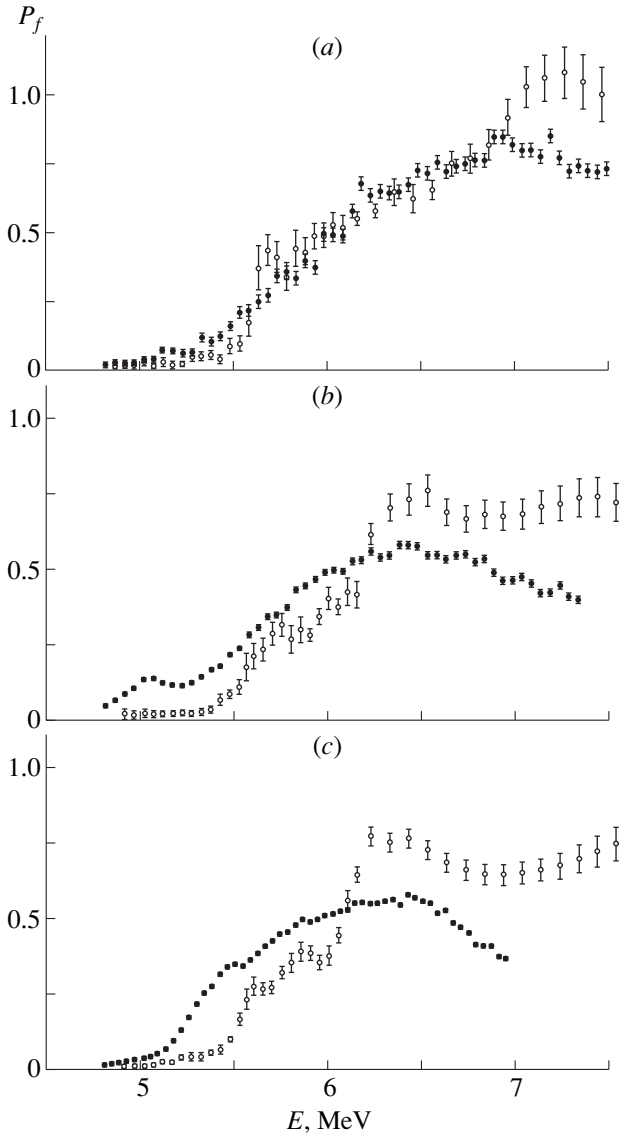

Fig. 6. Comparison of fissilities as functions of energy in (○) photofission reactions and (●) direct reactions: (*a*) ^{238}Pu(γ, *f*) and ^{237}Np(^{3}He, *df*)^{238}Pu [20], (*b*) ^{240}Pu(γ, *f*) and ^{238}Pu(*t*, *pf*)^{240}Pu [20], and (*c*) ^{242}Pu (γ, *f*) and ^{240}Pu(*t*, *pf*)^{242}Pu [20].

18]), the cross sections for quadrupole photoabsorption feature giant isoscalar quadrupole resonances at $E = (60–65)A^{-1/3}$ MeV, where A is the atomic number of the nucleus. The analysis performed in [19] for this giant resonance in terms of an additional Lorentzian yielded the optimal parameter values of $\sigma_1 = 2.8$ mb, $\Gamma_1 = 6.8$ MeV, and $E_1 = 9.9$ MeV.

The direct reactions were chosen as ^{237}Np(^{3}He, *df*)^{238}Pu for ^{238}Pu, ^{238}Pu(*t*, *pf*)^{240}Pu for ^{240}Pu, and ^{240}Pu(*t*, *pf*)^{242}Pu for ^{242}Pu [20]. For each even–even plutonium isotope, the fissilities for the photofission and direct reactions are compared in Fig. 6 as functions of excitation energy. For the ^{238}Pu and ^{240}Pu isotopes in particular, the resonance patterns of the fissilities under comparison are seen to be largely similar (Figs. 6*a* and 6*b*, respectively). The agreement for ^{242}Pu is somewhat poorer (Fig. 6*c*).

3. THEORETICAL ANALYSIS OF DATA

In analyzing the measured cross sections for ^{238}Pu, ^{240}Pu, and ^{242}Pu photofission, the penetrabilities of the fission barriers were computed theoretically only for excitation energies below the binding energy of a constituent neutron. In this energy region, the excitation of a nucleus can be relaxed either through fission or through photon emission. Accordingly, the photofission cross section $\sigma_f(E)$ and photoabsorption cross sections σ_{cJ} are related by equation

$$\sigma_f(E) = \sum_{J^\pi}\sum_{K}\sigma_{cJ}\frac{T_f^{J^\pi K}}{T_f^{J^\pi K} + T_\gamma^{J^\pi}}, \qquad (6)$$

where $T_f^{J^\pi K}$ and $T_\gamma^{J^\pi}$ are, respectively, the total and the radiative penetrability of the barrier for the channel characterized by the quantum numbers $J^\pi K$. Only two channels, those that have $J^\pi K = 1^-0$ and 1^-1 and which make a dominant contribution to the total cross section for photofission, are analyzed here.

The radiative penetrability was estimated as

$$T_\gamma^{J^\pi} = \frac{2\pi\Gamma_\gamma^{J^\pi}(E)}{D^{J^\pi}(E)}, \qquad (7)$$

where $\Gamma_\gamma^{J^\pi}$ is the average radiative-decay width, while D^{J^π} is the mean spacing between the energy levels in the well. Under the assumption that dipole transitions are dominant, the radiative width can be expressed as

$$\Gamma_\gamma = \frac{R}{\rho(E)}\int_0^E \varepsilon_\gamma^3\rho(E-\varepsilon_\gamma)d\varepsilon_\gamma, \qquad (8)$$

where the factor R was fixed by normalizing the total radiative-decay width to the measured value of the radiative width for excitation energies close to the neutron binding energy. The level density $\rho(E)$ was estimated within the superfluid-nucleus model taking phenomenologically into account collective and shell effects [21]. The neutron binding energy, the mean radiative width, and the mean spacing between neutron resonances were set to the values quoted in [22], and the level density was parametrized according to [23].

The probability for an excited nucleus to decay through fission was calculated on the basis of the one-dimensional model of the fission process. The penetrability of the fission barrier was determined by numerically solving the Schrödinger equation. We assumed a two-humped fission barrier that consists of three smoothly matched parabolic sections and which depends on six parameters, E_A, $\hbar\omega_A$, E_B, $\hbar\omega_B$, E_{II}, and

Table 3. Parameters (in MeV) of the two-humped fission barriers as extracted from data on photofission

$J^\pi K$	E_A		$\hbar\omega_A$		E_{II}		$\hbar\omega_{II}$		E_B		$\hbar\omega_B$	
	This study	[26]	This study	[26]	This study	[26]	This study	[26]	This study	[26]	This study	[26]
						^{238}Pu						
1^-0	7.0	6.95	1.35	1.3	3.45	–	1.0	–	6.1	5.9	0.6	0.8
1^-1	6.9	6.8	1.35	1.3	3.6	–	0.9	–	6.3	6.25	0.63	0.8
						^{240}Pu						
1^-0	7.0	7.35	1.35	1.4	3.45	–	1.0	–	6.1	5.5	0.6	0.6
1^-1	6.9	7.2	1.35	1.4	3.6	–	0.9	–	6.3	5.85	0.63	0.6
						^{242}Pu (This study)						
1^-0	7.0		1.35		3.00		0.8		6.1		0.6	
1^-1	6.9		1.35		3.6		0.9		6.3		0.67	

$\hbar\omega_{II}$ (the subscripts *A*, *B*, and II refer to the parameters of the lower hump, of the upper hump, and of the second well, respectively). The interaction that couples the vibrational fission mode to states of nonfission origin and which leads to the fragmentation of purely fission resonances in the second well was taken into account by adding an imaginary component to the potential for the second well. The probability for absorption in the second well was assumed to be linear in energy and was parametrized as

$$W(E) = w \times (E - E_{II} - \Delta_n - \Delta_p) + W_0, \qquad (9)$$

where Δ_n and Δ_p are the energy gaps in the spectra of internal excitations for the neutron and proton subsystems, respectively, while w and W_0 are parameters whose values were determined directly from a data analysis. In our calculations, the energy gaps Δ_p and Δ_n for ^{238}Pu, ^{240}Pu, and ^{242}Pu were set to the values of 0.49 and 0.61, 0.43 and 0.61, and 0.50 and 0.61 MeV, respectively, which were derived in [24]. The above assumptions and approximations lead to a second-order differential equation, which was solved by using the numerical algorithm developed in [25]. The penetrability of the fission barrier is finally obtained in the form

$$T_f = T_D + A\frac{T_B}{T_A + T_B}, \qquad (10)$$

where T_D is the direct barrier penetrability, A is the flux fraction absorbed in the second well, and T_A and T_B are the penetrabilities of the corresponding humps of the two-humped barrier.

The predictions obtained in this way were then compared with the actually measured cross sections for ^{238}Pu, ^{240}Pu, and ^{242}Pu photofission. The fission-barrier parameters E_A, $\hbar\omega_A$, E_B, $\hbar\omega_B$, E_{II}, and $\hbar\omega_{II}$ and the quantities w and W_0, which govern the E dependence of absorption in the second well [see equation (9)] can be varied in fitting the data. Figures 3, 4, and 5 show the results of our data analysis of the dipole components of the cross sections for the photofission of ^{238}Pu, ^{240}Pu, and ^{242}Pu, respectively. The corresponding fitted values of the above parameters are listed in Tables 3 and 4. At these parameter values, we were able to reproduce the distinctly observed structure between 5.6 and 5.7 MeV. We interpret this structure as a superposition of two resonances with slightly different positions in the $J^\pi K = 1^-0$ and 1^-1 channels. For each plutonium isotope under study, the total cross section for photofission at energies below 5.5 MeV could be adequately reproduced upon supplementing the dipole contributions with the quadrupole contribution taken here in the experimentally estimated form $\sigma_c(E) \cong \sigma_f^{20}$.

Also quoted in Table 3 are the parameters of the two-humped barrier for ^{238}Pu and ^{240}Pu as derived in [26] by analyzing the combined data on the (*d*, *pf*), (^{3}He, *df*), and (γ, *f*) reactions over a relatively narrow range of excitation energies. Here, we used only data on photofission, but we performed our analysis in the much broader excitation-energy interval from 4.7 to 7.0 MeV. Our estimates for the widths of the two barrier humps are seen to be largely consistent with those in [26] (for each plutonium isotope and for either dipole channel, the widths of the humps *A* and *B* prove to be close to 1.3 and 0.6 MeV, respectively). However, the hump heights as estimated here are not always consistent with those from [26]: for ^{238}Pu, they comply well,

Table 4. Fitted values of the absorption parameters w and W_0 (in MeV)

Isotope	$J^\pi K$			
	1^-0		1^-1	
	w	W_0	w	W_0
^{238}Pu	0.08	0.088	0.1	0.11
^{240}Pu	0.08	0.083	0.1	0.104
^{242}Pu	0.1	0.111	0.13	0.14

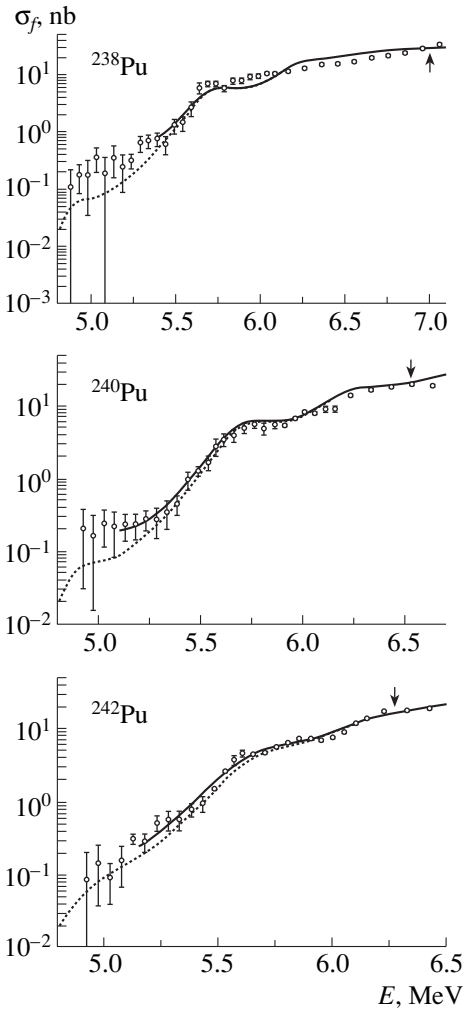

Fig. 7. Measured cross sections for the photofission of ^{238}Pu, ^{240}Pu, and ^{242}Pu versus excitation energy (points) along with the sum of the estimated partial-wave cross sections for $J^\pi K = 1^-0$, 1^-1, and 2^+0 channels (solid curves) and the sum of the estimated partial-wave cross sections for $J^\pi K = 1^-0$ and 1^-1 channels (dotted curves). The partial-wave cross sections for $J^\pi K = 1^-0$ and 1^-1 were fitted to predicted forms, whereas that for $J^\pi K = 2^+0$ was interpolated on the basis of experimental values. The arrow indicates the neutron binding energy.

but for ^{240}Pu, the disagreement reaches some 500 keV. That the two derivations of barrier parameters sometimes diverge may be due to the use of the different theoretical schemes and assumptions. It should also be noted that extra systematic shifts in the analysis may have resulted from combining the heterogeneous data of different experiments in [26].

We proceed to supplement the partial-wave cross sections for the $J^\pi K = 1^-0$ and 1^-1 dipole channels in their fitted forms with that for the $J^\pi K = 2^+0$ quadrupole channel in the directly measured (and then interpolated) form. For each of the ^{238}Pu, ^{240}Pu, and ^{242}Pu isotopes, Fig. 7 demonstrates that the sum of the three partial-wave cross sections (solid curve) adequately reproduces the total cross section measured for photofission (data points), whereas only the two dipole components (dotted curve) fail to saturate the total cross section in the subthreshold region.

4. CONCLUSION

The cross sections for ^{238}Pu, ^{240}Pu, and ^{242}Pu photofission have been measured with a fine pitch in excitation energy by using photofission of either ^{238}U or ^{237}Np as a reference. The neptunium isotope ^{237}Np, which shows a more regular E dependence of the photofission cross section than ^{238}U, has been employed as a reference nucleus for the first time. The independent measurements with the different reference nuclei have yielded compatible results. By invoking our previous measurements of the angular distributions of fragments, we have been able to extract, from the measured cross section, the partial-wave cross sections for the $J^\pi K = 1^-0$ and 1^-1 dipole channels and to estimate the cross section for the $J^\pi K = 2^+0$ quadrupole channel. The data on partial-wave cross sections for the dipole channels have been analyzed in the one-dimensional model of a two-humped barrier with allowance for the interaction of vibrational states in the second well with states of nonfission origin, and the parameters of the fission barrier have been derived. On the whole, the measured cross sections for ^{238}Pu, ^{240}Pu, and ^{242}Pu photofission in the subthreshold region have been adequately described within the aforementioned model.

ACKNOWLEDGMENTS

This work was supported in part by the Russian Foundation for Basic Research (project no. 96-02-17982).

REFERENCES

1. N. S. Rabotnov *et al.*, Yad. Fiz. **11**, 508 (1970) [Sov. J. Nucl. Phys. **11**, 285 (1970)].
2. A. Shapiro and W. F. Stubbins, Nucl. Sci. Eng. **45**, 47 (1971).
3. A. S. Soldatov and G. N. Smirenkin, Yad. Fiz. **55**, 3153 (1992) [Sov. J. Nucl. Phys. **55**, 1757 (1992)].
4. A. S. Soldatov *et al.*, Yad. Fiz. **56** (10), 16 (1993) [Phys. At. Nucl. **56**, 1307 (1993)].
5. A. S. Soldatov *et al.*, Yad. Fiz. **61**, 1427 (1998) [Phys. At. Nucl. **61**, 1325 (1998)].
6. A. V. Ignatyuk *et al.*, Zh. Éksp. Teor. Fiz. **61**, 1284 (1971) [Sov. Phys. JETP **34**, 684 (1971)].
7. A. S. Soldatov, *Vopr. At. Nauki Tekh., Ser. Yad. Konstanty* (Tsentr. Nauch. Issled. Inst. Atominform, Moscow, 1997), no. 3/4, p. 3.
8. M. Z. Tarasko *et al.*, At. Énerg. **65**, 290 (1988).
9. A. N. Soldatov *et al.*, At. Énerg. **78**, 400 (1995).
10. G. N. Smirenkin and A. S. Soldatov, Yad. Fiz. **59**, 203 (1996) [Phys. At. Nucl. **59**, 185 (1996)].
11. B. L. Berman *et al.*, Phys. Rev. C **34**, 2201 (1986).

12. M. Z. Tarasko, Preprint No. 1446, Institute of Physics and Power Engineering (Obninsk, 1983).
13. H. Thierens *et al.*, Phys. Rev. C **23**, 2104 (1981).
14. H. Thierens *et al.*, Phys. Rev. C **29**, 498 (1984).
15. H. Thierens *et al.*, Phys. Rev. C **27**, 1117 (1983).
16. G. N. Smirenkin and Yu. M. Tsipenyuk, in *Proceedings of International Symposium on Physics and Chemistry of Fission* (IAEA, Vienna, 1980), Vol. 1, p. 31.
17. G. R. Satchler, Phys. Rep. **14**, 99 (1974).
18. I. N. Borzov and S. P. Kamerdzhiev, Preprint No. 580, Institute of Physics and Power Engineering (Obninsk, 1975).
19. Yu. B. Ostapenko *et al.*, Fiz. Élem. Chastits. At. Yadra **12**, 1364 (1981) [Sov. J. Part. Nucl. **12**, 545 (1981)].
20. B. B. Back *et al.*, in *Proceedings of the International Symposium on Physics and Chemistry of Fission* (IAEA,Vienna, 1974), Vol. 1, p. 25.
21. A. V. Ignatyuk *et al.*, Yad. Fiz. **29**, 875 (1979) [Sov. J. Nucl. Phys. **29**, 450 (1979)].
22. T. S. Belanova *et al.*, *Handbook on Radiative Capture of Neutrons* (Énergoatomizdat, Moscow, 1986).
23. G. V. Antsipov, V. A. Kon'shin, and V. M. Maslov, *Vopr. At. Nauki Tekh., Ser. Yad. Konstanty* (Tsentr. Nauch. Issled. Inst. Atominform, Moscow, 1985), no. 3, p. 25.
24. B. B. Back *et al.*, Phys. Rev. C **9**, 1924 (1974).
25. A. N. Storozhenko *et al.*, in *Proceedings of 5th International Seminar on Neutron–Nucleus Interactions (ISINN-5): Neutron Spectroscopy, Nuclear Structure, and Related Topics* (JINR, Dubna, 1997) p. 155.
26. M. Just *et al.*, in *Proceedings of International Symposium on Physics and Chemistry of Fission* (IAEA, Vienna, 1980), Vol. 1, p. 71.

Translated by A. Asratyan

Physics of Atomic Nuclei, Vol. 63, No. 1, 2000, pp. 40–42. Translated from Yadernaya Fizika, Vol. 63, No. 1, 2000, pp. 46–49.

NUCLEI
Theory

Exponential–Trigonometric Basis Functions in the Coulomb Four-Body Problem

V. S. Zotev and T. K. Rebane

Institute of Physics (Petrodvorets Branch), St. Petersburg State University, ul. Ul'yanovskaya 1, Petrodvorets, 198904 Russia

Received July 24, 1998; in final form, October 6, 1998

Abstract—Basis functions of a new type—specifically, exponential–trigonometric functions depending on all six interparticle distances—have been proposed for the Coulomb four-body problem. A method has been developed for computing nine-dimensional integrals determining the matrix elements of the Hamiltonian for a four-body system and featuring these functions. The efficiency of the approach that relies on the proposed basis functions has been tested by calculating the $e^+e^-e^+e^-$, $p^+\mu^-p^+\mu^-$, $\mu^+e^-\mu^+e^-$, and $p^+e^-p^+e^-$ molecules. © *2000 MAIK "Nauka/Interperiodica".*

Over the last decade, basis functions depending exponentially on all interparticle distances have been widely used in quantum-mechanical calculations of Coulomb three-body systems. Such basis functions allow for correlations in particle motion and make it possible to perform computations by taking fully into account the kinetic energy of the system without resort to the adiabatic approximation (where the effect of the operator of the kinetic energy of heavy particles on the wave function of light particles is neglected). In such a basis, the ground-state energies of three-particle atomic and mesic molecular systems can be estimated to a high precision. However, this basis loses its efficiency when we go over to adiabatic molecular systems, where coupled particles (nuclei) are a few thousand times more massive than the coupling ones (electrons) [1]. This is because exponential functions, which change monotonically, cannot approximate adequately the oscillating part of the wave function, which has a sharp maximum in the vicinity of the equilibrium interatomic distance and which transforms into a delta function in the limit of infinitely heavy nuclei.

To sidestep this flaw, it was proposed in [2] to replace exponential basis functions by exponential–trigonometric functions of interparticle distances. In just the same way as the former, the latter secure a simple and rapid analytic computation of all the required integrals in the perimetric coordinates of three-body systems. In treating three-body molecular systems with well-distinct particle masses, a single exponential–trigonometric function appeared to be sufficient to replace some tens of ordinary exponential functions.

A transition to a broad basis of exponential–trigonometric functions in [3] made it possible to calculate the ground-state energies for typical adiabatic systems (isotopic modifications of the molecular hydrogen ion) up to the tenth decimal place. This accuracy corresponds to that of precision computations [4–6] within an adiabatic basis by the method of artificial scattering channels [7]. For example, 300 exponential–trigonometric basis functions were used in [3] to calculate the variational values of the ground-state energy for the H_2^+, HD^+, and D_2^+ molecules. The results, –0.5971390631, –0.5987887942, and –0.5978979684, respectively, in Hartree atomic units, comply well with the values of –0.5971390631 [4], –0.5987887943 [5], and –0.5978979686 [6], which were calculated in the adiabatic basis.

Later on, the exponential–trigonometric basis functions proposed in [2, 3] were used to improve the accuracy of variational calculations for a number of three-body mesic molecular systems [8].

Until recently, exponential basis functions were applied only to three-body systems because there were no procedures for calculating the Hamiltonian matrix elements for systems featuring more than three particles. In [9], a method was proposed for a variational computation of four-body Coulomb systems in the basis of exponential functions dependent on all six interparticle distances:

$$\phi = \exp\left(-\sum_{j<k}^{4} a_{jk} r_{jk}\right). \qquad (1)$$

This method is based on the analytic algorithm [10] reducing the computation of nine-dimensional four-body integrals (with nonseparable variables of integration) to a computation of a dilogarithmic function [11] and its derivatives. An effective procedure allowing for variations of the branches of multifunctions was developed in [9], variations that arise in computing four-body integrals featuring arbitrary values of the exponential parameters a_{jk}. Concurrently, the results from [12] that are based on the Hellmann–Feynman theorem for the auxiliary Schrödinger equation and which reduce substantially the number of the nine-dimen-

1063-7788/00/6301-0040$20.00

Ground-state energy E_{var}, mean values of the inverse interparticle distances, and parameters of the exponential–trigonometric variational wave function for the four-body Coulomb systems with particle masses m and M (E_{prec} stands for the most accurate energy values known at present)

Quantities	System			
	$e^+e^-e^+e^-$	$p^+\mu^-p^+\mu^-$	$\mu^+e^-\mu^+e^-$	$p^+e^-p^+e^-$
m/M	1	0.1126095	0.00483633	0.000544617
E_{var}	−0.514957	−198.206	−1.11320	−1.122378
E_{prec}	−0.516002 [14]	−199.626 [14]	−1.14100 [16]	−1.16402 [15]
$\langle 1/r_{12}\rangle$	0.3695	148.7	0.8592	0.8688
$\langle 1/r_{13}\rangle$	0.2240	104.1	0.6604	0.6736
$\langle 1/r_{24}\rangle$	0.2240	93.59	0.5500	0.5563
α_{12}	0.160209	79.6286	0.170868	0.177518
α_{13}	0.149632	113.3199	0.562708	0.562203
α_{14}	0.514090	224.5581	0.692597	0.695909
α_{23}	0.405251	137.0178	1.349148	1.358794
α_{24}	0.022991	−35.4691	−0.209043	−0.211919
α_{34}	0.075871	37.3005	0.481728	0.487454
β_{12}	0.015133	−7.6626	−0.024687	−0.028472
β_{13}	−0.081245	75.9794	1.022433	1.080718
β_{14}	0.073363	−29.9707	0.011286	0.007994
β_{23}	−0.052736	13.5675	−0.0624432	−0.055856
β_{24}	0.011487	−1.18311	−0.010328	−0.010781
β_{34}	−0.005591	11.5900	−0.013141	−0.010987
γ	3.063754	−3.093388	2.940814	2.907504

Note: All values are presented here in atomic units.

sional integrals needed to derive the Hamiltonian matrix elements for a four-body system were used there. This made it possible to express these matrix elements in terms of seven basic integrals (six integrals of Coulomb particle interaction and a normalization integral).

Application of the exponential basis functions (1) to computing the positronium molecule $e^+e^-e^+e^-$ [9], which represents an extreme case of nonadiabatic system, and to some four-particle mesic molecules [13] has confirmed the efficiency of this approach to the Coulomb four-body problem.

In just the same way as in the three-body problem, however, the convergence of the variational expansion in terms of exponential basis functions of the type (1) becomes slower with increasing heavy-to-light particle-mass ratio.

In this connection, the application of an exponential–trigonometric basis instead of an exponential one seems reasonable in the four-body Coulomb problem. A solution to this problem is presented here.

We construct the wave function of a four-body Coulomb system as an expansion in terms of exponential–trigonometric functions of the form

$$\psi = \exp\left(-\sum_{j<k}^{4}\alpha_{jk}r_{jk}\right)\sin\left(\sum_{j<k}^{4}\beta_{jk}r_{jk}+\gamma\right). \qquad (2)$$

Each of the basis functions ψ (2) involves twelve nonlinear parameters (α_{jk} and β_{jk}) and one linear parameter ($\tan\gamma$) and can be considered as a linear combination of two exponential functions of the type (1), with the complex exponents $a_{jk} = \alpha_{jk} \pm i\beta_{jk}$.

In order to generalize the algorithm for an analytic calculation of four-body integrals to the case of complex exponential parameters, it was necessary to take into account in detail the variations in the branches of multifunctions in response to an arbitrary motion of a point in the twelve-dimensional space of the parameters α_{jk} and β_{jk}. Mathematically, this problem is much more involved than that in the case of the six-dimensional space of real exponential parameters a_{jk}. Here, we will not describe the procedure that we used to solve it.

In order to demonstrate the potential of the method that employs exponential–trigonometric basis functions in dealing with four-body Coulomb systems, we performed calculations for the ground states of the $e^+e^-e^+e^-$, $p^+\mu^-p^+\mu^-$, $\mu^+e^-\mu^+e^-$, and $p^+e^-p^+e^-$ systems (where e^-, e^+, p^+, and μ^- stand for an electron, a positron, a proton, and a negative muon, respectively) by using a single coordinate basis function that has the form (2) and which is symmetrized with respect to permutations of identical particles:

$$\Psi = (1 + P_{13})(1 + P_{24})\psi. \qquad (3)$$

Here, positively and negatively charged particles are labeled with the subscripts 1, 3 and 2, 4, respectively.

In the case of the positronium molecule, we performed an additional symmetrization of the wave function with respect to a permutation that corresponds to a simultaneous reversal of all particle-charge signs:

$$\Psi = (1 + P_{12}P_{34})(1 + P_{13})(1 + P_{24})\psi. \qquad (4)$$

Twelve nonlinear parameters (α_{jk} and β_{jk}) of the trial wave function Ψ were carefully optimized by means of the gradient-descent method, while the linear parameter $\tan\gamma$ was found from a relevant quadratic equation.

The results of our calculations are presented in the table, which also quotes the most precise energy values from [14–16] obtained thus far for the systems under consideration.

A comparison with the results of variational calculations based on the exponential functions (1) shows that a single symmetrized exponential–trigonometric function Ψ replaces seven symmetrized exponential functions in computing the positronium molecule, nine such functions in computing the $p^+\mu^-p^+\mu^-$ molecule, and a few tens of them in computing the adiabatic molecular systems $\mu^+e^-\mu^+e^-$ and $p^+e^-p^+e^-$.

Owing to a doubled number of nonlinear parameters, the compact exponential–trigonometric function Ψ enables us to take into account in detail correlations in the motion of particles. The trigonometric factor of this function is responsible for the improved description of the wave-function behavior versus the distance between heavy particles.

It is interesting to compare the efficiency of an exponential–trigonometric basis in the four-body case under consideration with that in the three-body case [2]. The relative error in computing the ground-state energy for the four-body systems $e^+e^-e^+e^-$, $p^+\mu^-p^+\mu^-$, $\mu^+e^-\mu^+e^-$, and $p^+e^-p^+e^-$ with a single symmetrized exponential–trigonometric basis function was estimated at 0.2, 0.71, 2.4, and 3.6%, respectively. For the three-body systems $e^+e^-e^+$, $p^+\mu^-p^+$, $\mu^+e^-\mu^+$, and $p^+e^-p^+$, a single symmetrized exponential–trigonometric basis function reproduces the ground-state energy with relative errors of, respectively, 0.17, 0.41, 2.7, and 3.9% [2]. Thus, the exponential–trigonometric basis is equally efficient for four-body and for three-body problems.

In summary, a high precision peculiar to the computation of three-body Coulomb systems within a vast exponential–trigonometric basis [3] can be achieved in computing four-body systems as well. Since the codes for computing four-body integrals are much more complicated than those for three-body integrals, the amount of calculations will be three to four orders of magnitude greater in the former case; therefore, this will require the use of supercomputers.

REFERENCES

1. A. N. Frolov, Zh. Éksp. Teor. Fiz. **92**, 1959 (1987) [Sov. Phys. JETP **65**, 1100 (1987)].
2. T. K. Rebane and O. N. Yusupov, Zh. Éksp. Teor. Fiz. **98**, 1870 (1990) [Sov. Phys. JETP **71**, 1050 (1990)].
3. V. S. Zotev and T. K. Rebane, Opt. Spektrosk. **77**, 733 (1994) [Opt. Spectrosk. **77**, 654 (1994)].
4. R. E. Moss, Mol. Phys. **80**, 1541 (1993).
5. R. E. Moss, J. Chem. Soc. Faraday Trans. **89**, 3851 (1993).
6. R. E. Moss, Mol. Phys. **78**, 371 (1993).
7. M. Shapiro and G. G. Balint-Kurti, J. Chem. Phys. **71**, 1461 (1979).
8. A. M. Frolov, J. Phys. B **28**, 1449 (1995).
9. T. K. Rebane, V. S. Zotev, and O. N. Yusupov, Zh. Éksp. Teor. Fiz. **110**, 59 (1996) [JETP **83**, 28 (1996)].
10. D. M. Fromm and R. N. Hill, Phys. Rev. A **36**, 1013 (1987).
11. L. Levin, *Polylogarithms and Associated Functions* (Amsterdam, 1981).
12. T. K. Rebane, Opt. Spektrosk. **75**, 945 (1993) [Opt. Spectrosk. **75**, 557 (1993)].
13. V. S. Zotev and T. K. Rebane, submitted for publication in Opt. Spektrosk.
14. A. M. Frolov and V. H. Smith, J. Phys. B **29**, 1433 (1996).
15. D. M. Bishop and L. M. Cheung, Adv. Quantum Chem. **12**, 1 (1980).
16. T. K. Rebane, Yad. Fiz. **60**, 1628 (1997) [Phys. At. Nucl. **60**, 1483 (1997)].

Translated by O. Chernavskaya

Physics of Atomic Nuclei, Vol. 63, No. 1, 2000, pp. 43–54. Translated from Yadernaya Fizika, Vol. 63, No. 1, 2000, pp. 50–62.

NUCLEI
Theory

Microscopic Calculation of a Pairing Gap in Semi-Infinite Nuclear Matter

M. Baldo[1)], U. Lombardo[1), 2)], É. E. Sapersteĭn, and M. V. Zverev

Russian Research Centre Kurchatov Institute, pl. Kurchatova 1, Moscow, 123182 Russia

Received March 25, 1999

Abstract—The pairing gap in semi-infinite nuclear matter has been calculated microscopically by solving the gap equation for a nonlocal interaction with the aid of the method proposed by V.A. Khodel, A.V. Khodel, and J.W. Clark [Nucl. Phys. A **598**, 390 (1996)] for the case of infinite nuclear matter. The calculation employs the effective pairing interaction obtained previously for semi-infinite geometry on the basis of the separable 3×3 representation of the Paris nucleon–nucleon potential. The gap found in this way changes sharply in the surface region, where it has a pronounced maximum. The dependence of the surface effect on the chemical potential of nuclear matter has been investigated. © *2000 MAIK "Nauka/Interperiodica".*

1. INTRODUCTION

The present article reports on a continuation of studies that were described in [1–3] and which were devoted to developing a method for directly solving the equation for a pairing gap in semi-infinite nuclear matter without recourse to the local approximation. This method, based on the concept of effective pairing interaction, was constructed for a separable nucleon–nucleon potential. In order to implement it, the full Hilbert space of the problem is broken down into two subspaces. In the first, model, subspace S_0, we derive an equation for the gap Δ in terms of an effective interaction $\mathcal{V}^{\mathrm{p}}_{\mathrm{eff}}$. In the second, complementary, subspace S', the effective interaction $\mathcal{V}^{\mathrm{p}}_{\mathrm{eff}}$ is determined in terms of the vacuum nucleon–nucleon potential $\mathcal{V}$. In the equation for $\mathcal{V}^{\mathrm{p}}_{\mathrm{eff}}$, pairing effects can be disregarded, which substantially simplifies the situation, validating the two-step approach to solving the problem of pairing via the introduction of an effective interaction.

The implementation of the method is considerably facilitated for a separable form of the nucleon–nucleon potential. By using the mixed coordinate–momentum representation, the problem of determining the effective interaction is reduced to numerically solving the set of several one-dimensional integral equations. In [2], the effective interaction in the ${}^1S_0$ channel was explicitly obtained for the separable 3×3 form [4, 5] of the Paris nucleon–nucleon potential [6]. It was defined in such a way that the model subspace S_0 contained all negative-energy single-particle states. In this model subspace, the equation for the gap represents a set of three integral equations in coordinate space, the kernels of these equations being expressed in terms of functions u and v that obey the Bogolyubov equations with a nonlocal gap Δ. In that case, the Bogolyubov equations are integro-differential ones, so that the resulting problem presents a real challenge. A method for solving such equations was developed in [3], but it proved rather cumbersome. It is well known that a conventional iterative procedure for solving the gap equation in nuclear systems is characterized by a very slow convergence; as a result a few thousand iterations are required for obtaining an accurate result. Since it is necessary to solve integro-differential Bogolyubov equations at each step of the iterative process, a direct method of iterations consumes an enormous amount of machine time.

In order to simplify the problem of determining the gap Δ, we make use here of the method proposed by V.A. Khodel, A.V. Khodel, and J.W. Clark (KKC) [7] for solving the gap equation in the case of a nonlocal interaction. Originally, this method was developed for infinite nuclear matter, but it is applicable to any case where the gap Δ is much less than the Fermi energy ε_{F}. The main computational difficulties within the conventional iterative process stem from the fact that the integral gap equation is essentially nonlinear, so that a large number of iterations are required to solve it. Here, the convergence of an iterated series greatly depends on the choice of a zero-order iteration. In the KKC method, the problem of nonlinearity is sidestepped by considering that a nonlinear character of the equation is important for the gap magnitude, but not for its momentum dependence. As a matter of fact, the momentum dependence is determined by integrals over vast regions of momentum space, the region near the Fermi surface, where the nonlinearity in question is sizable, contributing insignificantly to those integrals. If the parameter $\Delta/\varepsilon_{\mathrm{F}}$ is small, the functional form of the momentum

[1)] Istituto Nazionale di Fisica Nucleare, Sezione di Catania, Corso Italia 57, I-95129 Catania, Italy.
[2)] Dipartimento di Fisica, Università di Catania, Corso Italia 57, I-95129 Catania, Italy.

1063-7788/00/6301-0043$20.00

dependence of the gap does not change with its magnitude. For the gap $\Delta(k)$, the authors of [7] used the ansatz $\Delta(k) = \Delta_F\chi(k)$, where the first factor is a constant $\Delta_F = \Delta(k_F)$, while the second factor is a gap-shape function normalized by the condition $\chi(k_F) = 1$. Upon the substitution of this ansatz, the original nonlinear integral equation reduces to a set of two equations. Of these, the first, that which determines the gap-shape function $\chi(k)$, is a nonhomogeneous integral equation whose kernel is virtually independent of Δ_F, a circumstance that simplifies significantly the problem of finding its solution. If the function $\chi(k)$ is known, the equation for the gap amplitude Δ_F becomes a nonlinear algebraic equation, which can be solved be conventional methods.

In the zero-order approximation of the KKC method, the gap-shape function $\chi^{(0)}(k)$ is calculated at $\Delta_F = 0$. After that, the gap amplitude in the zero-order approximation, $\Delta_F^{(0)}$, can easily be found for a given form of the momentum dependence. In the next approximation, the quantity $\Delta_F^{(0)}$ is substituted in the equation for the function $\chi^{(1)}(k)$, which in turn determines $\Delta_F^{(1)}$. The entire procedure is then repeated as many times as is required for achieving convergence. Conceptually, the KKC method does not introduce additional approximations in relation to the conventional method relying on direct iterations of the gap equation; it only rearranges the conventional iterative scheme improving the convergence. As a rule, even the zero-order approximation of the KKC method yields a fairly accurate result [7, 8]. Concurrently, arbitrariness in choosing the zero-order iterative approximation $\Delta^{(0)}(k)$ is removed in this method.

The KKC method can be extended to the case of nonzero temperatures ($T \neq 0$) [7, 8]. As a result, it turns out that the gap-shape function is virtually independent of T. This is because, at low temperatures, which are of prime interest in the problem being considered (the critical temperature $T_c \simeq 0.57\Delta_F \ll \varepsilon_F$), particles are redistributed only in a narrow interval of width $T \leq T_c$ near the Fermi surface, but this has virtually no effect on the gap-shape function. In other words, the dependence of Δ on k and T can be factorized, to a high accuracy, as

$$\Delta(\mathbf{k}, T) = \Delta_F(T)\chi(\mathbf{k}). \quad (1)$$

In semi-infinite nuclear matter, there arises an additional coordinate dependence of all quantities. However, all physical validations of relation of the type (1) with a gap-shape function that depends on the coordinates and momenta, but which is independent of T, and with a gap amplitude $\Delta_F(T)$ dependent only on T are preserved. This gap amplitude can be determined from the asymptotic value within nuclear matter, a value that obviously coincides with that for infinite nuclear matter and which can be determined quite straightforwardly. In order to determine the gap-shape function, we can make use of the gap equation for $T \longrightarrow T_c$; in this limit, the equation in question becomes linear, and its kernel is determined by the properties of the normal system. In the present study, we apply this method to semi-infinite nuclear matter because, in that case, it is much simpler than the direct iterative method.

2. KKC METHOD FOR SEMI-INFINITE NUCLEAR MATTER

In a symbolic form, the gap equation at a nonzero temperature can be written as [9, 10]

$$\Delta(T) = \mathcal{V}^{\mathrm{p}}_{\mathrm{eff}} A_0^{\mathrm{s}}(T)\Delta(T), \quad (2)$$

where $\mathcal{V}^{\mathrm{p}}_{\mathrm{eff}}$ is the effective pairing interaction in the model subspace S_0, while A_0^{s} is the superfluid two-particle propagator defined in this subspace.

According to [7, 8], the temperature and momentum dependences of the gap operator $\Delta(\mathbf{k}, T)$ in homogeneous nuclear matter can be factorized in the form (1), where the gap-shape function $\chi(\mathbf{k})$ can be considered to be independent of T up to the critical temperature T_c. If the temperature T is close to T_c, the gap Δ is negligible, whereas the propagator $A_0^{\mathrm{s}}(T)$ in equation (2) tends to the two-particle propagator $A_0(T)$ for the normal system. Thus, equation (2) taken at $T = T_c$ reduces to a homogeneous linear integral equation, which can be treated as an equation for $\chi(\mathbf{k})$. Its solution corresponding to the eigenvalue of $\lambda = 1$ is the required gap-shape function.

We will now use the KKC method to calculate the gap operator in semi-infinite nuclear matter nonhomogeneous along the x axis. As in [2], its boundary is taken for the $x = 0$ plane, nuclear matter itself is assumed to occupy the region $x < 0$, and the Woods–Saxon potential $U(x)$ having the depth of $U_0 = 50$ MeV and the diffuseness parameter of $d = 0.65$ fm is used for a mean field. We assume that the temperature dependence can be factored out of the coordinate and momentum dependences in a form similar to (1):

$$\Delta(x_1, x_2, k_\perp^2; T) = \Delta_F(T)\chi(x_1, x_2, k_\perp^2). \quad (3)$$

Here, $\mathbf{k}_\perp$ stands for a two-dimensional momentum in the plane **s** orthogonal to the x axis. We will use the effective pairing interaction that was calculated in [2] for the Paris potential [6] taken in the separable form [4, 5]

$$V(\mathbf{k}, \mathbf{k}') = \sum_{i,j=1}^{3} \lambda_{ij} g_i(k^2) g_j(k'^2), \quad (4)$$

where $\mathbf{k}$ and $\mathbf{k}'$ are the relative momenta prior to and after scattering, respectively. As in [2], the original normalization of the form factors from [4, 5] was changed in such a way as to ensure fulfillment of the conditions

$g_i(0) = 1$. For this choice of the nucleon–nucleon potential, the effective interaction also assumes a separable form [2]. Specifically, we have

$$\begin{aligned} &{}^{\circ}V^{\mathrm{p}}_{\mathrm{eff}}(x_1, x_2, x_3, x_4; k_\perp^2, k_\perp'^2) \\ &= \sum_{ij} \Lambda_{ij}(X, X') g_i(k_\perp^2, x) g_j(k_\perp'^2, x'), \end{aligned} \tag{5}$$

where $X = (x_1 + x_2)/2$, $X' = (x_3 + x_4)/2$, $x = x_1 - x_2$, $x' = x_3 - x_4$, and $g_i(k_\perp^2, x)$ is determined by the inverse Fourier transformation of the form factor $g_i(k_\perp^2 + k_x^2)$ with respect to the variable k_x. Obviously, the gap-shape function can also be represented as

$$\chi(x_1, x_2, k_\perp^2) = \sum_i \chi_i(X) g_i(k_\perp^2, x). \tag{6}$$

Substituting relations (3)–(6) into (2) at $T = T_c$, we find that the components χ_i satisfy the equations

$$\begin{aligned} \chi_i(X) &= \sum_{lm} \int dX_1 dX_2 \Lambda_{il}(X, X_1) \\ &\times B^0_{lm}(X_1, X_2; T_c) \chi_m(X_2), \end{aligned} \tag{7}$$

where

$$\begin{aligned} B^0_{lm}(X_1, X_2; T) &= \int \frac{dk_\perp}{(2\pi)^2} dx_1 dx_2 g_l^*(k_\perp^2, x_1) \\ &\times g_m(k_\perp^2, x_2) A_0\Big(X_1 + \frac{x_1}{2}, X_1 - \frac{x_1}{2}, X_2 + \frac{x_2}{2}, \\ &X_2 - \frac{x_2}{2}; \; k_\perp^2; \; T\Big). \end{aligned} \tag{8}$$

In order to calculate the propagator $A_0(T)$, we will make use of the Matsubara temperature technique [11]. For $T > 0$, it is necessary to evaluate the sum

$$\begin{aligned} &A_0(\mathbf{r}_1, \mathbf{r}_2, \mathbf{r}_3, \mathbf{r}_4; T) \\ &= -T \sum_n \mathcal{G}(\mathbf{r}_1, \mathbf{r}_3, \zeta_n; T) \mathcal{G}(\mathbf{r}_2, \mathbf{r}_4, -\zeta_n; T) e^{\zeta_n \tau}\Big|_{\tau \to +0}. \end{aligned} \tag{9}$$

Here, $\zeta_n = (2n + 1)\pi i T$, while $\mathcal{G}(\mathbf{r}_i, \mathbf{r}_k, \zeta_n; T)$ are the temperature Green's functions, for which we employ the pole expansion

$$\mathcal{G}(\mathbf{r}, \mathbf{r}', \zeta_n; T) = \sum_\lambda \frac{\varphi_\lambda(\mathbf{r}) \varphi_\lambda(\mathbf{r}')}{\zeta_n - \varepsilon_\lambda + \mu}, \tag{10}$$

where μ is the chemical potential, ε_λ stands for the single-particle energies of the system without allowance for pairing, and $\varphi_\lambda(\mathbf{r})$ are the corresponding single-particle eigenfunctions. In the case of semi-infinite geometry, the index λ represents the set of quantum numbers $\{n, \mathbf{k}_\perp\}$; that is,

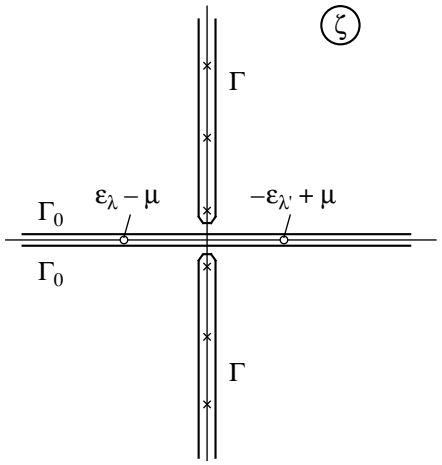

Fig. 1. Contour of integration in (14).

$$\varphi_\lambda(\mathbf{r}) = y_n(x) e^{i\mathbf{k}_\perp \cdot \mathbf{s}}, \tag{11}$$

where $y_n(x)$ is a function that is obtained as a solution to the one-dimensional Schrödinger equation with a potential $U(x)$ and which corresponds to the energy ε_n related to ε_λ by the equation $\varepsilon_\lambda = \varepsilon_n + k_\perp^2/2m$.

Substituting (10) into (9), we obtain

$$\begin{aligned} A_0(\mathbf{r}_1, \mathbf{r}_2, \mathbf{r}_3, \mathbf{r}_4; T) &= \sum_n A_{\lambda\lambda'}(T) \\ &\times \varphi_\lambda(\mathbf{r}_1) \varphi_\lambda^*(\mathbf{r}_3) \varphi_{\lambda'}(\mathbf{r}_2) \varphi_{\lambda'}^*(\mathbf{r}_4), \end{aligned} \tag{12}$$

where

$$A_{\lambda\lambda'}(T) = -T \sum_n \frac{e^{\zeta_n \tau}}{(\zeta_n - \varepsilon_\lambda + \mu)(-\zeta_n - \varepsilon_{\lambda'} + \mu)}\Big|_{\tau \to +0}. \tag{13}$$

Following the Luttinger–Ward method [11], we replace the sum in [13] by the integral

$$\begin{aligned} &A_{\lambda\lambda'}(T) \\ &= \frac{1}{2\pi i} \int_\Gamma \frac{e^{\zeta\tau}}{(\zeta - \varepsilon_\lambda + \mu)(\zeta + \varepsilon_{\lambda'} - \mu)(e^{\zeta/T} + 1)}\Big|_{\tau \to +0} \end{aligned} \tag{14}$$

along the contour Γ (see Fig. 1) circumventing the poles of the function

$$f(\zeta) = 1/(e^{\zeta/T} + 1) \tag{15}$$

in the ζ plane.

The contour Γ can be transformed into Γ_0, and the integral in (14) can easily be calculated. The result can

be represented as

$$A_{\lambda\lambda'}(T) = -\frac{1 - N_\lambda(T) - N_{\lambda'}(T)}{\varepsilon_\lambda + \varepsilon_{\lambda'} - 2\mu}, \quad (16)$$

where

$$N_\lambda(T) = 1/(e^{(\varepsilon_\lambda - \mu)/T} + 1). \quad (17)$$

In a more detailed notation, we have

$$A_0(x_1, x_2, x_3, x_4; k_\perp^2; T) = -\sum_{n_1 n_2} \frac{1 - N_{n_1}(k_\perp^2, T) - N_{n_2}(k_\perp^2, T)}{\varepsilon_{n_1} + \varepsilon_{n_2} + k_\perp^2/m - 2\mu} \times y_{n_1}(x_1) y_{n_1}^*(x_3) y_{n_2}(x_2) y_{n_2}^*(x_4). \quad (18)$$

Substituting (18) into (8), we obtain

$$B_{lm}^0(X, X'; T) = -\sum_{n_1 n_2} \int \frac{dk_\perp}{(2\pi)^2} \times \frac{1 - N_{n_1}(k_\perp, T) - N_{n_2}(k_\perp, T)}{\varepsilon_{n_1} + \varepsilon_{n_2} + k_\perp^2/m - 2\mu} g_{n_1 n_2}^l(k_\perp^2, X) g_{n_1 n_2}^m(k_\perp^2, X'), \quad (19)$$

where

$$g_{n_1 n_2}^l(k_\perp^2, X) = \int g_l(k_\perp^2, x) y_{n_1}\left(X + \frac{x}{2}\right) y_{n_2}\left(X - \frac{x}{2}\right) dx. \quad (20)$$

We note that, in [2], the effective interaction $\mathcal{V}_{\text{eff}}^{\text{p}}$ was defined for a model subspace such that the propagator A_0^{s} includes all negative-energy single-particle states. For this reason, summation over the indices n_1 and n_2 and integration with respect to $\mathbf{k}_\perp$ is constrained by the condition

$$\varepsilon_n + k_\perp^2/2m < 0. \quad (21)$$

The above formulas determine the kernels of the set of equations (7) for the components of the gap-shape function $\chi(x_1, x_2, k_\perp^2)$. A solution to this set of equations must be substituted into (3), together with the factor $\Delta_{\text{F}}(T)$, which can be found for $X \longrightarrow -\infty$ (see above) and which therefore coincides with the gap value in nuclear matter at the Fermi surface.

3. KKC METHOD FOR INFINITE NUCLEAR IN THE CASE OF A SEPARABLE NUCLEON–NUCLEON POTENTIAL

In the present study, the equations presented in the preceding section will be solved for semi-infinite nuclear matter. Prior to doing this, however, we will test here the accuracy to which relation (1) holds in infinite nuclear matter (that is, the accuracy of the zero-order approximation of the KKC method) for the specific form that we use for nucleon–nucleon interaction—the separable form [4, 5] of the Paris potential. Initially, this potential was used in [12, 13] to study superfluidity in neutron matter and in nuclear matter within Brueckner theory. Here, we present some results of these calculations in a form that is convenient for analyzing the temperature dependence of the gap-shape function. For the separable potential (4), the momentum dependence of the gap Δ is determined by the coefficients C_i in the sum

$$\Delta(k, T) = \sum_i C_i(T) g_i(k^2). \quad (22)$$

As a matter of fact, it is necessary to demonstrate that the ratios of the coefficients C_i are independent of T. These ratios are displayed in Tables 1 and 2 for neutron matter and nuclear matter, respectively, at several Fermi momentum (k_{F}) values for which the gap Δ is sufficiently large.

From these tables, it can be seen that, although the coefficients C_i themselves change noticeably with temperature, the ratios C_2/C_1 and C_3/C_1 are independent of T to within 2 to 3% up to the critical temperature T_c.

Let us now investigate the convergence of the KKC method for an infinite system in the case of a separable potential. It should be noted that the calculations presented below differ somewhat from those in [12, 13] because, here—in just the same way as in [2]—we use the simplified version of Brueckner theory, setting the effective nucleon mass m^* to the nucleon mass in a vacuum and fixing the depth of the mean field at $U_0 = 50$ MeV.

Let us present basic relations of the KKC method for the potential (4). We will first consider the case of $T = 0$. The Bardeen–Cooper–Schrieffer (BCS) equation for the gap has the form

$$\Delta(k) = -\int V(\mathbf{k}, \mathbf{k}') \frac{\Delta(k')}{2E_{k'}} d\tau', \quad (23)$$

where $d\tau = d^3k/(2\pi)^3$ and $E_k = \sqrt{\xi_k^2 + \Delta^2(k)}$ with $\xi_k = \varepsilon_k - \varepsilon_{\text{F}}$. As was indicated above, basic mathematical difficulties encountered in solving equation (23) are associated with a singular behavior of its kernel for $\Delta_{\text{F}} \longrightarrow 0$. Within the KKC method, this kernel is transformed in such a way as to simplify its singular part to the highest possible degree. This is achieved by isolating a separable term in the potential V, which is represented accordingly as [7, 8]

$$V(\mathbf{k}, \mathbf{k}') = V_{\text{F}} \phi(k) \phi(k') + W(\mathbf{k}, \mathbf{k}'), \quad (24)$$

where

$$V_{\text{F}} = V(k_{\text{F}}, k_{\text{F}}), \quad (25)$$

$$\phi(k) = V(k, k_{\text{F}})/V_{\text{F}}. \quad (26)$$

Table 1. $^1S_0$ pairing in neutron matter: calculated temperature dependence of the coefficients C_i in (22) for various values of the Fermi momentum k_F

T	C_1	C_2	C_3	C_2/C_1	C_3/C_1
			$k_F = 0.60$ fm^{-1}		
0.00	1.736	0.552	-4.82×10^{-3}	0.318	-2.78×10^{-3}
0.75	1.598	0.507	-4.43×10^{-3}	0.318	-2.77×10^{-3}
1.20	0.751	0.238	-2.06×10^{-3}	0.317	-2.75×10^{-3}
1.25	0.484	0.153	-1.33×10^{-3}	0.316	-2.75×10^{-3}
1.35 ($\simeq T_c$)	1.06×10^{-3}	3.39×10^{-4}	-2.99×10^{-6}	0.320	-2.83×10^{-3}
			$k_F = 0.84$ fm^{-1}		
0.00	1.933	1.356	-8.43×10^{-3}	0.701	-4.36×10^{-3}
1.00	1.678	1.172	-7.28×10^{-3}	0.699	-4.34×10^{-3}
1.25	1.313	0.915	-5.67×10^{-3}	0.697	-4.32×10^{-3}
1.50	0.413	0.284	-1.76×10^{-3}	0.689	-4.27×10^{-3}
1.60 ($\simeq T_c$)	1.44×10^{-3}	9.88×10^{-4}	-6.42×10^{-6}	0.688	-4.47×10^{-3}
			$k_F = 1.10$ fm^{-1}		
0.00	1.226	1.827	-1.68×10^{-2}	1.491	-1.37×10^{-2}
0.75	1.021	1.522	-1.39×10^{-2}	1.490	-1.36×10^{-2}
1.00	0.568	0.841	-7.64×10^{-3}	1.480	-1.35×10^{-2}
1.15	2.22×10^{-3}	3.27×10^{-3}	-2.96×10^{-5}	1.469	-1.33×10^{-2}
1.25 ($\simeq T_c$)	1.08×10^{-6}	1.57×10^{-6}	-1.43×10^{-8}	1.459	-1.33×10^{-2}

Note: All values of the coefficients and temperature are presented in MeV units.

By virtue of the definition in (24), we have $W(k_F, k') \equiv W(k, k_F) \equiv 0$.

The representation of $\Delta(k)$ in the form (1) leads to a set of coupled equations [12, 13] for the gap amplitude and the gap-shape function. Specifically, we have

$$1 = -V_F \int \phi(k) \frac{\chi(k)}{2\sqrt{\xi_k^2 + \Delta_F^2 \chi^2(k)}} d\tau, \quad (27)$$

$$\chi(k) = \phi(k) - \int W(\mathbf{k}, \mathbf{k}') \frac{\chi(k')}{2\sqrt{\xi_{k'}^2 + \Delta_F^2 \chi^2(k')}} d\tau'. \quad (28)$$

By using the potential (4) and relation (26), we arrive at

$$\phi(k) = \sum_i \phi_i g_i(k^2), \quad (29)$$

where

$$\phi_i = \sum_j \lambda_{ij} g_j(k_F^2)/V_F \quad (30)$$

with

$$V_F = \sum_{ij} \lambda_{ij} g_i(k_F^2) g_j(k_F^2). \quad (31)$$

Further, we have

$$W(\mathbf{k}, \mathbf{k}') = \sum_{ij} \gamma_{ij} g_i(k^2) g_j(k'^2), \quad (32)$$

where

$$\gamma_{ij} = \lambda_{ij} - V_F \phi_i \phi_j. \quad (33)$$

The gap-shape function can be sought in the form

$$\chi(k) = \sum_i \chi_i g_i(k^2). \quad (34)$$

Equations (27) and (28) then become

$$1 = -V_F \sum_{ij} \phi_i B_{ij} \chi_j, \quad (35)$$

$$\chi_i = \phi_i - \sum_{jl} \gamma_{ij} B_{jl} \chi_l, \quad (36)$$

where

$$B_{ij} = \int \frac{g_i(k^2) g_j(k^2)}{2E_k} d\tau \quad (37)$$

Table 2. $^1S_0$ pairing in nuclear matter: calculated temperature dependence of the coefficients C_i in (22) for various values of the Fermi momentum k_F

T	C_1	C_2	C_3	C_2/C_1	C_3/C_1
			$k_F = 0.80$ fm^{-1}		
0.00	2.008	0.831	-6.20×10^{-2}	0.414	-3.09×10^{-2}
0.75	1.906	0.786	-5.88×10^{-2}	0.413	-3.09×10^{-2}
1.20	1.327	0.542	-4.07×10^{-2}	0.409	-3.07×10^{-2}
1.30	1.045	0.425	-3.20×10^{-2}	0.407	-3.07×10^{-2}
1.40	0.572	0.231	-1.75×10^{-2}	0.406	-3.06×10^{-2}
1.45	0.128	5.21×10^{-2}	-3.93×10^{-3}	0.405	-3.06×10^{-2}
1.50 ($\simeq T_c$)	3.85×10^{-3}	1.56×10^{-3}	-1.18×10^{-4}	0.405	-3.07×10^{-2}
			$k_F = 0.90$ fm^{-1}		
0.00	1.587	0.869	-6.98×10^{-2}	0.547	-4.40×10^{-2}
0.80	1.327	0.724	-5.83×10^{-2}	0.546	-4.39×10^{-2}
1.20	1.07×10^{-2}	5.76×10^{-3}	-4.68×10^{-4}	0.539	-4.38×10^{-2}
1.25	2.03×10^{-4}	1.09×10^{-4}	-8.94×10^{-6}	0.538	-4.39×10^{-2}
1.30 ($\simeq T_c$)	3.65×10^{-6}	1.96×10^{-6}	-1.61×10^{-7}	0.536	-4.41×10^{-2}
			$k_F = 1.08$ fm^{-1}		
0.00	0.791	0.729	-6.02×10^{-2}	0.921	-7.60×10^{-2}
0.40	0.684	0.630	-5.20×10^{-2}	0.920	-7.59×10^{-2}
0.50	0.533	0.491	-4.05×10^{-2}	0.919	-7.59×10^{-2}
0.60	1.87×10^{-3}	1.72×10^{-3}	-1.42×10^{-4}	0.919	-7.58×10^{-2}
0.65 ($\simeq T_c$)	1.74×10^{-3}	1.59×10^{-3}	-1.31×10^{-4}	0.914	-7.56×10^{-2}

Note: All values of the coefficients and temperature are presented in MeV units.

with

$$E_k = \sqrt{\xi_k^2 + \Delta_F^2\left(\sum_l \chi_l g_l(k^2)\right)^2}.$$

The KKC equations are more convenient than the original BCS equation in that the kernel of the integral equation (28) features no singularity for $\Delta_F \longrightarrow 0$ because the residual interaction W vanishes at the Fermi surface. For the separable forces considered here, this corresponds to the identity $\sum_i \gamma_{ij} g_i(k_F^2) = 0$; by virtue of it, the singular part of the contribution of the integral in (37) to the sum in (36) vanishes. It should be recalled that, for equations with nonsingular kernels, iterative procedures work well, ensuring a comparatively fast convergence. As to the singular equation (27), it is in fact an algebraic equation, which can be solved by standard methods (for example, by Newton's method) not requiring the use of an iterative process. In the zero-order approximation of the KKC method, we can set $\Delta_F = 0$ in the denominator on the right-hand side of (28) [for a separable version, in the denominator on the right-hand side of (37)]. The set of equations (36) then reduces to a set of linear equations for the functions $\chi_i^{(0)}$ because, in this approximation, the coefficients

$$B_{ij}^{(0)} = \int \frac{g_i(k^2) g_i(k^2)}{2\xi_k} d\tau \qquad (38)$$

feature no unknown quantities. It was shown in [7, 8] that even the gap-shape function of the zero-order approximation, $\chi^{(0)}(k)$ [it is obtained by substituting the resulting coefficients $\chi_i^{(0)}$ into the sum in (36)], describes the momentum dependence $\Delta(p)$ quite accurately. In the next approximation, the substitution of $\chi_i^{(0)}$ into the denominator on the right-hand side of (37) determines the matrix $B_{ij}^{(1)}(\Delta_F)$, which depends on Δ_F parametrically. The substitution $B_{ij}^{(1)}(\Delta_F)$ and $\chi_i^{(0)}$ into (35) leads to an equation for Δ_F. Its solution $\Delta_F^{(0)}$ represents the gap amplitude in the zero-order approximation of the KKC method. At the next iteration step, the matrix $B_{ij}^{(1)}(\Delta_F^{(0)})$ is substituted into (36), whereby the gap-shape function $\chi_i^{(1)}$ is determined in the next approximation; after that, the process is reiterated.

Table 3. Illustration of convergence within the KKC method at $T = 0$: coefficients χ_i in equation (34) versus the number N of iteration

N	Δ_F, MeV	χ_1	χ_2	χ_3
		$\mu = -16$ MeV		
0	0.98508579	0.51496182	1.7332633	$-8.3303282 \times 10^{-4}$
1	0.97535836	0.51247844	1.7354232	$-9.0958849 \times 10^{-4}$
2	0.97551858	0.51252118	1.7353864	$-9.0834607 \times 10^{-4}$
3	0.97551858	0.51252047	1.7353870	$-9.0836649 \times 10^{-4}$
4	0.97551858	0.51252047	1.7353870	$-9.0836649 \times 10^{-4}$
		$\mu = -8$ MeV		
0	0.19878907	0.30019636	2.6898012	$-1.8056271 \times 10^{-2}$
1	0.19863648	0.30006468	2.6899770	$-1.8068021 \times 10^{-2}$
2	0.19863648	0.30006487	2.6899768	$-1.8068005 \times 10^{-2}$
3	0.19863648	0.30006487	2.6899768	$-1.8068005 \times 10^{-2}$
		$\mu = -2$ MeV		
0	0.011648583	0.083704097	4.1089851	$-5.6122312 \times 10^{-2}$
1	0.011648583	0.083703371	4.1089871	$-5.6122463 \times 10^{-2}$
2	0.011648583	0.083703371	4.1089871	$-5.6122463 \times 10^{-2}$

A fast convergence of the KKC interaction scheme for separable forces is illustrated in Table 3, where solutions to the KKC equations are displayed versus the number of iterations, N, for several values of the chemical potential μ.

It can be seen from Table 3 that even the zero-order iteration of the KKC method ensures a precision at a level of a few percent and that, upon the second or the third iteration, eight decimal places prove to be stable. It should be noted that the smallness of Δ_F (at small $|\mu|$) improves here the convergence of the iteration process, in contrast to what usually occurs in applying a direct method of iterations, where such a smallness generates serious problems. Owing to this, the use of the KKC method is especially appealing for $T \neq 0$, because the gap amplitude Δ_F tends to zero as T approaches T_c.

The gap-shape functions of the zero-order approximation, $\chi^{(0)}(k)$, are displayed in Fig. 2 for several values of μ (or k_F). These functions were obtained by substituting the coefficients $\chi_i^{(0)}$ (rows in Table 3 that correspond to $N = 0$) into the sum in (34). It was indicated in [7, 8] that these functions determined at different μ values have many features in common—in particular, they vanish at close values of $k = k_0(k_F)$, which determine approximately the critical Fermi momentum k_F^c corresponding to disappearance of superfluidity in nuclear matter [7, 8]. This is confirmed by data in Fig. 3, which shows Δ_F as a function of μ. The critical value μ_c at which Δ_F vanishes is about 9.2 MeV, which corresponds to the Fermi momentum of $k_F^c \simeq 1.69$ fm^{-1}.

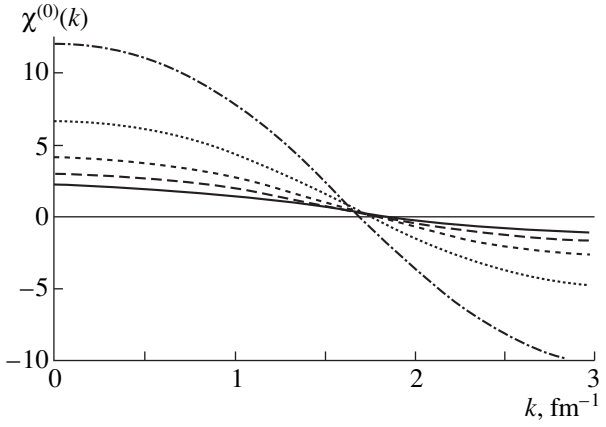

Fig. 2. Gap-shape function $\chi^{(0)}(k)$ in homogeneous nuclear matter at the chemical-potential values of μ = (solid curve) –16, (long dashes) –8, (short dashes) –2, and (dotted curve) 3 MeV. The dash-dotted curve represents the function $\chi(k)/10$ at $\mu = 9.2$ MeV.

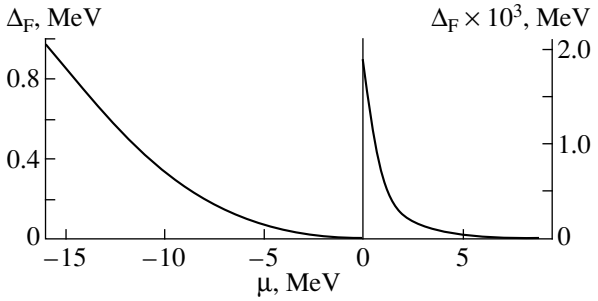

Fig. 3. Gap-operator amplitude Δ_F in homogeneous nuclear matter as a function of μ.

Table 4. Illustration of convergence within the KKC method for $T \neq 0$ ($\mu = -16$ MeV): coefficients χ_i in equation (34) versus the number N of iteration

T, MeV	N	Δ_F, MeV	χ_1	χ_2	$\chi_3 \times 10^{-4}$
0	0	0.985085	0.514961	1.73326	–8.33032
	1	0.975358	0.512478	1.73542	–9.09588
	2	0.975518	0.512521	1.73538	–9.08346
	3	0.975518	0.512520	1.73538	–9.08366
0.100	0	0.982225	0.513799	1.73418	–8.48253
	1	0.975357	0.512491	1.73541	–9.09220
	2	0.975470	0.512521	1.73538	–9.08346
0.200	0	0.973900	0.513798	1.73418	–8.48265
	1	0.966927	0.512528	1.73537	–9.07982
	2	0.967046	0.512559	1.73535	–9.07095
0.300	0	0.923231	0.513805	1.73418	–8.48160
	1	0.916257	0.512746	7.73518	–9.00720
	2	0.916389	0.512775	1.73516	–8.99854
0.400	0	0.794579	0.513872	1.73412	–8.47207
	1	0.788421	0.513239	1.73475	–8.84127
	2	0.788558	0.513261	1.73473	–8.83438
0.500	0	0.517052	0.514033	1.73399	–8.44951
	1	0.514330	0.514038	1.73404	–8.56942
	2	0.514400	0.514044	1.73404	–8.56732
0.520	0	0.423078	0.514427	1.73368	–8.39659
	1	0.419142	0.514230	1.73387	–8.50364
	2	0.419249	0.514237	1.73387	–8.50113
0.540	0	0.286995	0.514502	1.73362	–8.38632
	1	0.284619	0.514439	1.73369	–8.43175
	2	0.284686	0.514443	1.73368	–8.43071
0.550	0	0.178203	0.514540	1.73359	–8.38096
	1	0.177372	0.514549	1.73359	–8.39412
	2	0.177395	0.514550	1.73359	–8.39389
0.552	0	0.147605	0.514595	1.73355	–8.37362
	1	0.146167	0.514571	1.73357	–8.38672
	2	0.146208	0.514572	1.73357	–8.38639
0.554	0	0.107134	0.514603	1.73354	–8.37248
	1	0.106174	0.514593	1.73355	–8.37903
	2	0.106202	0.514593	1.73355	–8.37888
0.556 ($\simeq T_c$)	0	3.24171×10^{-2}	0.514611	1.73353	–8.37134
	1	3.26736×10^{-2}	0.514615	1.73353	–8.37129
	2	3.26660×10^{-2}	0.514615	1.73353	–8.37130

A transition to nonzero temperatures is rather straightforward. All the relations presented in this section remain in force, with the exception of expression (37) for B_{ij}, where there arises a temperature-dependent factor; that is,

$$B_{ij}(T) = \int \frac{g_i(k^2)g_j(k^2)}{2E_k} \tanh\left(\frac{E_k}{2T}\right) d\tau. \qquad (39)$$

Table 4 illustrates the convergence of the KKC procedure for nonzero temperatures. It can be seen that the rate at which the iterations converge is close to that at $T = 0$. To avoid encumbering the table, the result that is obtained upon the third iteration and which is virtually coincident with the result of the second iteration is presented only for $T = 0$. The last of the temperatures listed in the table is virtually coincident with the critical tem-

perature for $\mu = -16$ MeV ($T_c = 0.5562$ MeV). It should be emphasized that a conventional iterative procedure for solving the BCS equation for $\Delta(T)$ near T_c requires a few thousand iterations and that a determination of T_c to a satisfactory precision is very difficult within this method. In the present study, T_c is determined by directly solving equation (37) with the quantity $B_{ij}(T)$ specified by expression (39) at $\Delta = 0$ [recall that, at a nonzero temperature, this expression features no singularity at the Fermi surface since the temperature-dependent factor in (39) vanishes there]. The critical temperature found in this way is $T_c = 0.1127$ MeV at $\mu = -8$ MeV and $T_c = 0.0065$ MeV at $\mu = -2$ MeV. By using the values of $\Delta_F(T = 0)$ from Table 3, it can easily be shown that, for all three values of the chemical potential μ that are considered here, the ratio $T_c/\Delta_F(T = 0)$ is very close to the BCS value of 0.57. This is in accord with the results obtained in [7, 8] for nonseparable potentials.

4. RESULTS OF THE CALCULATION FOR SEMI-INFINITE NUCLEAR MATTER

Let us now return to the problem of semi-infinite nuclear matter. Equation (7) can be considered as a particular case of a more general set of homogeneous integral equations

$$\chi_i(X) = \lambda(T)\sum_j \int dX' K_{ij}(X, X'; T)\chi_j(X), \qquad (40)$$

where $K_{ij}(X, X'; T)$ stands for the kernels of these equations at an arbitrary temperature T, while $\lambda(T)$ is the corresponding eigenvalue. The critical temperature can be determined from the condition that the minimal eigenvalue $\lambda_1(T_c)$ is equal to unity. This method, which relies on solving equations (40) for many values of T, is possible in principle, but it is very cumbersome. In the case being considered, where pairing takes place in infinite nuclear matter, the value of T_c for semi-infinite nuclear matter is identical to that for infinite matter. A much simpler way therefore consists in determining the critical temperature T_c for infinite matter and in using T_c in equation (7) as a known parameter. In particular, we have already seen that, at the value of $\mu = -8$ MeV considered here, $T_c = 0.1127$ MeV.

Given immediately below is a brief account of the computational scheme used here to solve the set of integral equations (7). The kernels $K_{im}(X, X')$ of these equations are determined by the convolution of the coefficients $\Lambda_{il}(X, X_1)$ in the expansion (5) of the effective interaction $\mathcal{V}^{p}_{\text{eff}}$ with the analogous coefficients $B^0_{lm}(X_1, X'; T_c)$ in the expansion of the propagator $A_0(T = T_c)$. The former were calculated in [2] for the chemical-potential value of $\mu = -8$ MeV, which was chosen in such a way as to approximate more closely the situation in actual nuclei. As a matter of fact, the calculation was performed only for the interval -8 fm $< X < 8$ fm, because the calculation of $\Lambda_{il}(X, X')$ for greater $|X|$ values is trivial. On one hand, it was shown in [2] that, in the region $X, X' < -4$ fm, the quantities $\Lambda_{ij}(X, X')$ are virtually coincident with the corresponding coefficients in the effective interaction calculated for infinite nuclear matter. For $X, X' > 4$ fm, the interaction $\mathcal{V}^{p}_{\text{eff}}$ tends fast to the free T matrix continued analytically to the region of negative energies and taken at two-particle energy of $E = 2\mu$. On the other hand, it was also shown in [2] that, at a fixed value of $X_0 = (X + X')/2$, the effective interaction $\mathcal{V}^{p}_{\text{eff}}(X, X')$ decreases fast with increasing $t = X - X'$, so that the integrals involving $\Lambda_{ij}(X, X')$ can be cut off at $|t| > 4$ fm. Taking all the above into account, we conclude that the interval (–8 fm, 8 fm) is quite sufficient for obtaining all values of the effective interaction necessary for ensuing calculations. As to equation (7) for the gap-shape function, a much vaster region of X, $\{X\} = (-L_{\text{in}}, L_{\text{ex}})$, with a minimal value of $L_{\text{in}} \simeq 40$ fm (the value of $L_{\text{ex}} = 8$ fm is sufficiently large), is required for solving it. The reason why it is necessary to extend this region is associated with the smallness of Δ_F ($\Delta_F \lesssim 1$ MeV), which leads to a large correlation length ($\xi \sim v_F/\Delta_F \gtrsim 10$ fm). In order that effects of the left boundary condition not distort substantially the asymptotic behavior of the gap-shape function within nuclear matter, the distance between the left boundary and the point being considered (for example $X \gtrsim -10$ fm) must not be less than the correlation length. The minimal value of $L_{\text{in}} = 40$ fm was determined empirically. For $X, X' < -8$ fm, the calculation employed the effective interaction $\mathcal{V}^{\infty}_{\text{eff}}(t)$ that was found for infinite nuclear matter and which is dependent only on the difference $t = X - X'$.

The propagators B^0_{lm} represent a new element in the problem being considered. They can be calculated by formulas (17)–(19), where the wave functions $y_n(x)$ are solutions to the one-dimensional Schrödinger equation with the Woods–Saxon potential $U(x)$. Here, we are obviously dealing with a continuous spectrum; therefore, summation over n_1 and n_2 in equation (18) actually means integration with respect to the one-dimensional momenta p_1 and p_2 (for details, see [2]). Recall that the model subspace S_0 includes only negative-energy single-particle states; therefore, the regions of integration in (18) with respect to p_1, p_2, and $q_\perp$ do not contain high momenta, so that the evaluation of the relevant integrals does not involve considerable difficulties.

That the X space is vast generates considerable difficulties in directly solving equation (6) in coordinate space (this method was used in [2] to solve the analogous equation for $\mathcal{V}^{p}_{\text{eff}}$). The point is that constructing a solution by this method requires inverting a $3N \times 3N$ matrix, where N is the number of nodes in the interval

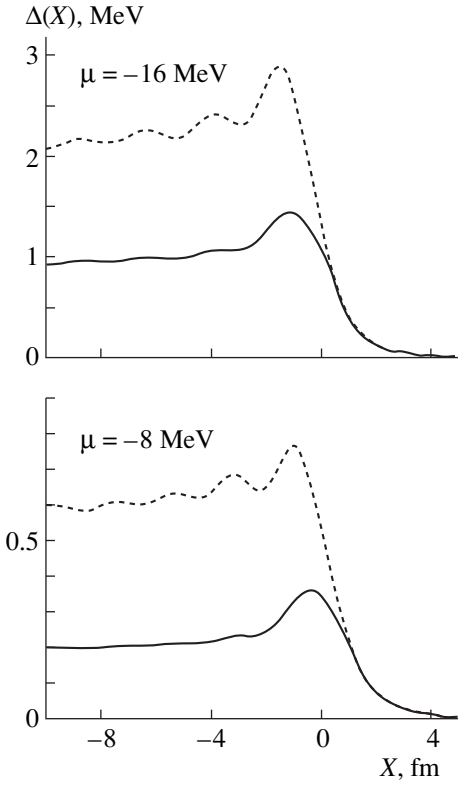

Fig. 4. Zero moment $\Delta_0(X)$ of the gap operator (dashed curves) and function $\Delta_F(X)$ (solid curves) for two values of the chemical potential μ.

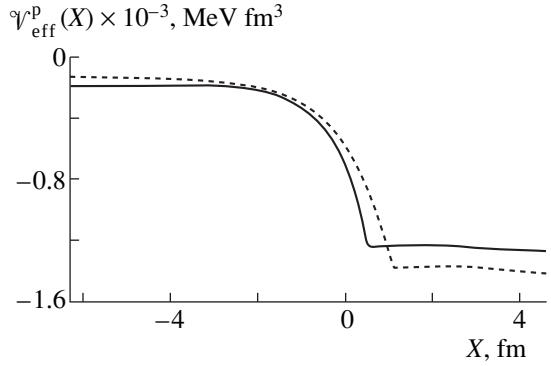

Fig. 5. Effective interaction $\mathcal{V}^{p}_{eff}(X)$ at μ = (solid curve) –16 and (dashed curve) –8 MeV.

$(-L_{in}, L_{ex})$. A minimal step in X necessary for achieving reasonable accuracy is $h = 0.1$ fm, in which case we obtain a 2000 × 2000 matrix. The inversion of such matrices is not always stable.

It is much more convenient to expand the gap-shape function in a Fourier series in the interval $(-L_{in}, L_{ex})$. We have

$$\chi_i(X) = \sum_n \chi_i^n f_n(X), \qquad (41)$$

where $f_n(x)$ stands for $\sin(2\pi n(X - X_c)/L)$ and $\cos(2\pi n(X - X_c)/L)$, $L = L_{in} + L_{ex}$ and $X_c = (L_{ex} - L_{in})/2$. The kernels $K_{ij}(X, X')$ are expanded in double Fourier series. As a result, we obtain a set of homogeneous linear equations for the Fourier coefficients χ_i^n,

$$\chi_i^n = \sum_{j=1}^{3} \sum_{n'=1}^{N} K_{ij}^{nn'} \chi_j^{n'}, \qquad (42)$$

with a matrix $K_{ij}^{nn'}$ of moderately large dimensions. Here, we have used the interval $\{X\} = (-40$ fm, 10 fm) $(X_c = -15$ fm), in which case a precision better than 1% could be achieved with $N = 101$ functions. Once the coefficients χ_i^n have been determined, the gap-shape function $\chi(X, x, k_\perp^2)$ can be found by formula (6). In order to obtain the full gap at zero temperature, $\Delta(X, x, k_\perp^2; T = 0)$, it is necessary to multiply χ by the constant $\Delta_F = 0.200$ MeV, which was found in the calculation for infinite nuclear matter.

In order to represent the results in clearer form, we will evaluate the zeroth moment of the function $\chi(X, x, \mathbf{s})$ in the relative coordinate:

$$\chi_0(X) = \int d\mathbf{s} \int dt \chi(X + t/2, X - t/2, \mathbf{s}) = \sum_i \chi_i(X). \qquad (43)$$

In accordance with [2], we have used here the normalization condition $g(k^2 = 0) = 1$. Let us also consider the function

$$\chi_F(X) = \sum_i \chi_i(X) g_i(k^2 = k_F^2(X)), \qquad (44)$$

where $k_F(X) = \sqrt{2m(\mu - U(X))}$ is the local Fermi momentum [$k_F(X) = 0$ for $\mu - U(X) < 0$]. The corresponding moments of the gap operator are $\Delta_0(X) = \Delta_F\chi_0(X)$ and $\Delta_F(X) = \Delta_F\chi_F(X)$. The last function is of paramount importance for the interpretation of the results. It determines approximately the matrix elements of Δ for single-particle states occurring near the Fermi surface. For semi-infinite matter, this approximation was analyzed in [2, 14]. We note that this version of the local approximation is usually used to describe pairing in finite nuclei [15]. Its accuracy for neutron stars was investigated in [16]. It should be emphasized that, here, this approximation is invoked only to obtain a clearer representation of the results that were computed without using it.

Similar calculations were also performed for the chemical-potential value of μ = –16 MeV, which is self-consistent for semi-infinite nuclear matter and which obviously coincides with the chemical potential of infinite matter. In this case, $T_c = 0.556$ MeV and $\Delta_F = 0.975$ MeV.

The functions $\Delta_0(X)$ and $\Delta_F(X)$ are depicted in Fig. 4 for the two values of μ. It can be seen that all curves

have pronounced surface maxima. In order to assess the extent to which the existence of these maxima is due to a large effective pairing interaction in the surface region [2] (see Fig. 5), we considered a model situation where the propagator is calculated for semi-infinite matter, while effective interaction is determined for infinite matter. The functions $\Delta_F(X)$ computed for the realistic and model situations are displayed in Fig. 6 for the two values of the chemical potential μ. It can be seen that the enhancement of the effective interaction is responsible for one-half of the surface effect in Δ at $\mu = -8$ MeV and only for one-quarter of it at $\mu = -16$ MeV.

In order to render the analysis of the μ dependence of the surface effect more convenient, the gap-shape function is displayed in Fig. 7 for the two values of μ in question. It can be seen that the surface effect in Δ is more pronounced at $\mu = -8$ MeV. Indeed, the ratio of the surface-maximum height to the asymptotic value in the interior of nuclear matter is about 1.8 in this case; at the same time, this ratio is about 1.5 at $\mu = -16$ MeV. Moreover, the position of the maximum is closer to the surface ($X = 0$) at $\mu = -8$ MeV than at $\mu = -16$ MeV.

It should be noted that the surface effect for Δ proved to be weakened considerably in relation to the effective interaction itself. This is because of a strong coupling between the volume and the surface, an effect that is peculiar to the gap equation owing to a large pair correlation length, much larger than the surface-layer thickness. This coupling is realized in any purely quantum calculation, but it can be lost in part if some version of the local approximation is used. The coupling in question suppresses somewhat the surface maximum in Δ and weakens the μ dependence of the surface effect.

The μ dependence of the gap is determined by several factors. First of all, the effective pairing interaction depends on μ, as can be seen from Fig. 5. The asymptotic value of $|\mathcal{V}^{p}_{eff}|$ for $X > 0$ is greater for the smaller value of $|\mu|$. This is due to a direct dependence of $\mathcal{V}^{p}_{eff}$ on the two-particle energy $E = 2\mu$ [2]. An inverse pattern is observed for negative X and in the vicinity of the point $X = 0$, where $|\mathcal{V}^{p}_{eff}|$ takes a smaller value for the smaller value of $|\mu|$—this is associated with the momentum dependence of the form factors $g_i(k^2)$, which are taken at $k^2 = k_F^2(X) = 2m(\mu - U(X))$. As a result, the change in $\mathcal{V}^{p}_{eff}$ near the surface is greater for smaller $|\mu|$, and this is the circumstance that enhances the surface effect in Δ with decreasing $|\mu|$. However, there exists an effect that contributes oppositely, rendering the μ dependence of the height of the surface maximum in Δ less pronounced. We mean here that with decreasing $|\mu|$, Δ_F decreases, which results in the growth of the correlation length. This in turn leads to the weakening of the surface effect as such and of its μ dependence.

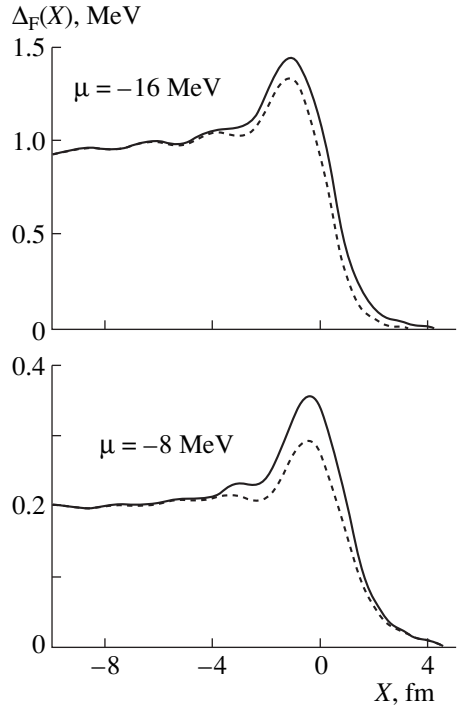

Fig. 6. Function $\Delta_F(X)$ as calculated with the effective interaction in (solid curves) semi-infinite and (dashed curves) infinite matter.

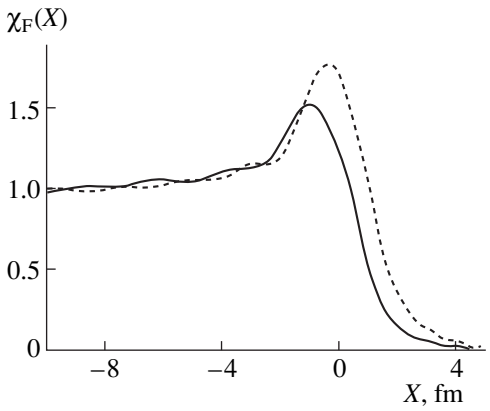

Fig. 7. Gap-shape function $\chi_F(X)$ at μ = (solid curve) –16 and (dashed curve) –8 MeV.

The inclusion of the energy dependence of pairing can prove important in considering the nucleon-stability boundary (drip line), at which the chemical potential μ vanishes. An analysis of the situation that arises at small μ will be performed in a separate study.

5. CONCLUDING REMARKS

The present article completes a series of studies devoted to a microscopic analysis of pairing in the $^1S_0$ channel in semi-infinite nuclear matter. The approach developed in these studies relies on considering the equations of the theory directly in the coordinate space

without recourse to any version of the local approximation. In the present study, we have solved the gap equation for the model subspace containing only negative-energy single-particle states. In doing this, we have employed the effective pairing interaction that was calculated previously in [1, 2] and which takes into account correlations in the complementary subspace incorporating positive-energy single-particle states. Since this effective interaction is nonlocal, it induces a nonlocal gap Δ; as a result, the corresponding Bogolyubov equations are integro-differential ones. A method for solving such equations in the case of semi-infinite geometry was developed in [3], but it proved rather cumbersome. Therefore, a direct iterative method for solving the gap equation has been abandoned here as uneconomic—this method, which requires solving such integro-differential equations at each iterative step, consumes an enormous amount of machine time—in favor of the KKC method developed recently in [7, 8] for solving the gap equation in infinite nuclear matter and infinite neutron matter. We have confirmed the efficiency of the KKC method for infinite nuclear matter in the case of separable nucleon–nucleon forces that we use. For semi-infinite nuclear matter, we have restricted our consideration to the zero-order approximation in the temperature version of this method, in which case the gap Δ dependent on temperature, coordinates, and momenta can be represented as the product of the factor $\Delta_F(T)$ dependent only on the temperature and the gap-shape function $\chi(x_1, x_2, k_\perp)$ that is independent of temperature, but which depends on coordinates and momenta. The gap-shape function χ has been found by solving the gap equation linearized near the critical temperature $T = T_c$, so that the resulting kernel of this equation is determined by the properties of the normal system. The factor $\Delta_F(T)$, which coincides with the corresponding quantity in infinite nuclear matter, can be found straightforwardly. The gap operator at zero temperature is determined as the product of the function $\chi(x_1, x_2, k_\perp)$ and the factor $\Delta_F(T = 0)$. This method for solving the gap equation in the case of a semi-infinite system is much simpler than a direct iterative method.

Our calculations have been performed for two values of the chemical potential, $\mu = -16$ and -8 MeV. Of these, the first corresponds to the actual value of the chemical potential of semi-infinite nuclear matter—needless to say, it coincides with that for infinite matter—while the second was chosen in such a way that the calculations could reproduce more closely the situation in finite nuclei. The gap magnitude at the Fermi boundary, $\Delta_F(T = 0)$, depends on μ for two reasons. The first stems from a direct dependence of the effective pairing interaction $\mathcal{V}^{\mathrm{p}}_{\mathrm{eff}}$ on the energy $E = 2\mu$. The second is associated with the momentum dependence of the form factors $g_i(k^2)$, which are taken at $k^2 = k_F^2(X) = 2m(\mu - U(X))$. As the result of the concerted effect of these two factors, the surface effect is enhanced both in the effective pairing interaction and in the gap Δ with decreasing $|\mu|$. Because of a strong coupling between the volume and the surface, a phenomenon that is inherent in the gap equation, the surface effect is much less pronounced in $\Delta_F(X)$ than in the effective interaction. However, this effect and its dependence on the chemical potential μ are important even in the case of Δ. This dependence is expected to be important in calculating the drip line, near which the chemical potential tends to zero.

ACKNOWLEDGMENTS

We are grateful to V.A. Khodel for the advice to use the temperature independence of the gap-shape function to calculate the gap in semi-infinite nuclear matter. Thanks are also due to P. Schuck, S.V. Tolokonnikov, and S.A. Fayans for stimulating discussions. É.E. Sapersteĭn and M.V. Zverev gratefully acknowledge the hospitality extended to them at Istituto Nazionale di Fisica Nucleare, Sezione di Catania (Catania, Italy) and Università di Catania.

This work was supported in part by the Russian Ministry for Higher Education (grant no. 97-0-6.1-7).

REFERENCES

1. M. Baldo, U. Lombardo, É. E. Sapersteĭn, *et al.*, Yad. Fiz. **58**, 1572 (1995) [Phys. At. Nucl. **58**, 1483 (1995)]; Phys. Lett. B **350**, 135 (1995); Yad. Fiz. **60**, 1206 (1997) [Phys. At. Nucl. **60**, 1081 (1997)].
2. M. Baldo, U. Lombardo, É. E. Sapersteĭn, *et al.*, Nucl. Phys. A **628**, 503 (1998).
3. M. Baldo, U. Lombardo, É. E. Sapersteĭn, *et al.*, Yad. Fiz. **62**, 71 (1999) [Phys. At. Nucl. **62**, 66 (1999)].
4. J. Haidenbauer and W. Plessas, Phys. Rev. C **30**, 1822 (1984).
5. J. Haidenbauer and W. Plessas, Phys. Rev. C **32**, 1424 (1985).
6. M. Lacombe, B. Loiseau, J. M. Richard, *et al.*, Phys. Rev. C **21**, 861 (1980).
7. V. A. Khodel, V. V. Khodel, and J. W. Clark, Nucl. Phys. A **598**, 390 (1996).
8. V. A. Khodel, Yad. Fiz. **60**, 1157 (1997) [Phys. At. Nucl. **60**, 1033 (1997)].
9. A. B. Migdal, *Theory of Finite Fermi Systems and Applications to Atomic Nuclei* (Nauka, Moscow, 1982; Interscience, New York, 1967).
10. P. Ring and P. Schuck, *The Nuclear Many-Body Problem* (Springer-Verlag, Berlin, 1980).
11. A. A. Abrikosov, L. P. Gor'kov, and I. E. Dzyaloshinskiĭ, *Methods of Quantum Field Theory in Statistical Physics* (Fizmatgiz, Moscow, 1962; Prentice-Hall, Englewood Cliffs, 1963).
12. M. Baldo, J. Cugnon, A. Lejeune, *et al.*, Nucl. Phys. A **515**, 409 (1990).
13. M. Baldo, I. Bombaci, G. Giansiracusa, *et al.*, Nucl. Phys. A **545**, 741 (1992).

Translated by A. Isaakyan

Physics of Atomic Nuclei, Vol. 63, No. 1, 2000, pp. 55–68. Translated from Yadernaya Fizika, Vol. 63, No. 1, 2000, pp. 63–78.

NUCLEI
Theory

Investigation of Low-Energy Scattering in the *nnpp* System on the Basis of Differential Equations for Yakubovsky Components in Configuration Space

I. N. Filikhin and S. L. Yakovlev*

St. Petersburg State University, Universitetskaya nab. 7/9, St. Petersburg, 199164 Russia

Received May 19, 1998; in final form, December 16, 1998

Abstract—The *s*-wave differential equations for the Yakubovsky components characterizing the *nnpp* system have been solved by the method of cluster reduction. Two-cluster scattering at energies below the three-particle threshold in the singlet and triplet spin states has been considered. The MT I–III potential model has been used to simulate nucleon–nucleon interaction, and the Coulomb interaction between the protons has been taken into account. The singlet and triplet scattering lengths have been calculated for proton interaction with the triton (^{3}H) and for neutron interaction with the ^{3}He nucleus, and the deuteron–deuteron scattering length has also been determined. The low-energy behavior of the phase shifts and inelasticity factors in the corresponding scattering channels has been investigated. The features of the 0^+ resonance in the ^{4}He nucleus have been determined.

1. INTRODUCTION

The resonating-group method (RGM) is traditionally used to study theoretically the continuum states of the *nnpp* system. Various RGM versions were employed in [1–6]. The development of the formalism based on the Faddeev–Yakubovsky equations [7, 8] provided a tool for studying scattering in the *nnpp* system more consistently. However, the integral form of these equations is not quite appropriate in dealing with systems featuring Coulomb interaction. For this reason, the Coulomb interaction of protons was disregarded in [9–13], where scattering in four-nucleon systems was investigated on the basis integral equations—in particular, on the basis of the Yakubovsky integral equations [9–12]. Coulomb interaction is easily incorporated in the general formalism of the Faddeev–Yakubovsky equations within their differential formulation [14–16], but this leads to cumbersome sets of three-dimensional integro-differential equations even in the simplest case of the *s*-wave approximation. Only by using supercomputers is it possible to solve such sets directly. In the present study, the method of cluster reduction [17–19] is used to solve the differential equations for the Faddeev components characterizing the *nnpp* system. With the aid of this method, reduced equations can be solved by employing computers with quite a moderate volume of memory.

This article reports on a continuation of studies that were devoted to the application of equations for Yakubovsky components to four-nucleon systems and which were initiated by the present authors in [18–20], where scattering in the n^3He system and bound states in the ^{4}He nuclear system, as well as scattering in the four-nucleon system, have been considered without taking into account the Coulomb interaction between the protons involved. Here, we analyze scattering in the singlet ($S = 0$) and triplet ($S = 1$) spin states of the *nnpp* system. We employ the *s*-wave approximation. For nucleon–nucleon interaction, we take the MT I–III potential model [20] modified as in [21]. In addition, we allow for the Coulomb interaction between the protons.

The ensuing exposition is organized as follows. In Section 2, we describe equations for the Yakubovsky components corresponding to the system of identical fermions. We perform a spin–isospin analysis of these equations, consider the *s*-wave approximation, and formulate boundary-value problems that correspond to elastic scattering and rearrangement in the case of two-cluster scattering in the *nnpp* system. In Section 3, we explain the crucial points of the procedure that implements the cluster reduction of the equation and derive effective equations that describe the relative motion of relevant clusters. In Section 4, we discuss the results obtained by numerically solving these effective equations and present the calculated values of the singlet and triplet scattering lengths for proton interaction with the triton ($^{2S+1}A_{pt}$) and for neutron interaction with the ^{3}He nucleus ($^{2S+1}A_{nh}$), as well as the calculated value of the spin-singlet deuteron–deuteron scattering length A_{dd}. Values obtained in this way for the n^3He system are then compared with experimental data. Further, we investigate the low-energy behavior of the singlet and triplet phase shifts and inelasticity parameters for all possible scattering channels in the *nnpp* system. The singlet phase shift for proton–neutron scattering is used

* e-mail: yakovlev@snoopy.phys.spbu.ru

1063-7788/00/6301-0055$20.00

to calculate the features of the 0^+ resonance in the ^{4}He nucleus.

2. DIFFERENTIAL EQUATIONS FOR THE YAKUBOVSKY COMPONENTS CORRESPONDING TO THE *nnpp* SYSTEM

Let us consider a four-particle system consisting of two protons and two neutrons. Here, a pair interaction potential appears to be the sum of a short-range and a Coulomb component. In order to describe the system in configuration space, we make use of the Jacobi coordinates $\mathbf{X} = \{\mathbf{x}_i, \mathbf{y}_i, \mathbf{z}_i\}$, $i = 1, 2$, where the different values of the subscript i correspond to different partitions of the system ($i = 1$ for partition chains of the 3 + 1 type and $i = 2$ for partition chains of the 2 + 2 type). The Jacobi coordinates are expressed in terms of the particle radius vectors $\mathbf{r}_k$ ($k = 1, 2, 3, 4$) as

$$\mathbf{x}_1 = \mathbf{r}_2 - \mathbf{r}_1, \quad \mathbf{y}_1 = (\mathbf{r}_1 + \mathbf{r}_2)/2 - \mathbf{r}_3,$$

$$\mathbf{z}_1 = (\mathbf{r}_1 + \mathbf{r}_2 + \mathbf{r}_3)/3 - \mathbf{r}_4, \quad \mathbf{x}_2 = \mathbf{r}_2 - \mathbf{r}_1,$$

$$\mathbf{y}_2 = \mathbf{r}_4 - \mathbf{r}_3, \quad \mathbf{z}_2 = (\mathbf{r}_1 + \mathbf{r}_2)/2 - (\mathbf{r}_3 + \mathbf{r}_4)/2.$$

The wave function Ψ of the system is a spinor in the $\mathcal{H} = \mathcal{H}_T \otimes \mathcal{H}_S$ space, where $\mathcal{H}_S$ ($\mathcal{H}_T$) is a linear space where spin (isospin) states of the system are specified. In the isospin formalism, the particles in question are assumed to be identical. In the present case, the Yakubovsky components U_1 and U_2 satisfy the modified differential equations [15]

$$\begin{aligned}(H_0 + V - E + V^{\mathrm{Coul}})U_1 + V(P_4^+ + P_4^-)U_1 \\ = -V[(P_1^+ - P^+)U_1 + (P_1^+ + P_4^+)U_2], \\ (H_0 + V - E + V^{\mathrm{Coul}})U_2 + V(P^+P^+)U_2 \\ = -V[(P^+ - P_1^+)P^+U_1],\end{aligned} \tag{1}$$

where H_0 is the kinetic-energy operator; V is a pair nuclear nucleon–nucleon potential; V^{Coul} is the potential of the Coulomb interaction between the protons; and $P_k^\pm$ is the operator of permutation of three particles, with k being the subscript that indicates the particle not involved in this permutation. The Yakubovsky components U_1 and U_2 are spinors in $\mathcal{H}$.

2.1. Spin–Isospin Analysis

For the potential of nucleon–nucleon interaction, we will make use of the MT I–III model. Since this potential involves no spin–orbit and tensor components, the total spin moment and the total orbital angular momentum are conserved separately. Bases in the subspaces $\mathcal{H}_S$ and $\mathcal{H}_T$ are consistent with the two possible chains of partitions, and this actually fixes the scheme of addition of the subsystem angular momenta in the total angular momentum.

In the subspace $\mathcal{H}_S$, the basis elements for the two schemes of addition of the angular momenta are given by

$$|\chi^{(1)}\rangle = |(((1/2, 1/2)s_{12}, 1/2)s_{123})S, S_z\rangle,$$

$$|\chi^{(2)}\rangle = |((1/2, 1/2)s_{12}(1/2, 1/2)s_{34})S, S_z\rangle.$$

The basis elements in the subspace $\mathcal{H}_T$ are constructed in a similar way and are denoted by $|\eta^{(k)}\rangle$. The basis elements of the space $\mathcal{H}$ have the form

$$|e^{(k)}\rangle = |\chi^{(k)}\rangle|\eta^{(k)}\rangle. \tag{2}$$

The corresponding quantum-number sets $e^{(k)}$ can be represented as

$$e^{(1)} = (s_{12}, s_{123}, S, S_z)(t_{12}, t_{123}, T, T_z),$$

$$e^{(2)} = (s_{12}, s_{34}, S, S_z)(t_{12}, t_{34}, T, T_z).$$

The expansion of the Yakubovsky components U_k in the above bases has the form

$$U_k(\mathbf{X}) = \sum_e \mathcal{U}_e^k(\mathbf{x}_k, \mathbf{y}_k, \mathbf{z}_k)|e^{(k)}\rangle. \tag{3}$$

By substituting expansions (3) into equations (1) and projecting these equations onto the basis elements, we arrive at a set of equations for coordinate functions. Let us separate the spin–isospin variables in equations (1) for the $S = 1$ spin state of the system (for the case of $S = 0$, the spin–isospin analysis can be performed in a similar way). Since there is no interaction in the singlet–singlet and triplet–triplet states of a nucleon pair, the elements of the spin–isospin basis that correspond to these states must be eliminated from the expansion in (3). As a result, the spin–isospin bases will consist of eight elements $e_k^{(i)}$, $k = 1, 2, \ldots, 8$, where the superscript values of $i = 1, 2$ are used as before to label basis elements that correspond to different rules of composition of particle spins (isospins). For the triplet state, the elements of the spin–isospin basis and the corresponding quantum numbers are displayed in Tables 1 and 2. (For the singlet case, these quantities are compiled in Tables 3 and 4). Further, we must find the representation of the operators from equations (1) in the basis given by (2). Presented below are the results of this calculation. Nuclear interaction depends only on the pair spin; therefore, the operator V has a diagonal matrix representation of the form

$$V = \mathrm{diag}\{V^{\mathrm{t}}, V^{\mathrm{t}}, V^{\mathrm{s}}, V^{\mathrm{s}}, V^{\mathrm{t}}, V^{\mathrm{t}}, V^{\mathrm{s}}, V^{\mathrm{s}}\},$$

where V^{s} and V^{t} are, respectively, the singlet and triplet components of the nucleon–nucleon potential. The representations of the permutation operators are specified

by 8×8 matrices:

$$\langle 1|P_4^{\pm}|1\rangle = \begin{pmatrix} \frac{1}{4} & 0 & -\frac{3}{4} & & & & & \\ 0 & -\frac{1}{2} & 0 & & & 0 & & \\ -\frac{3}{4} & 0 & \frac{1}{4} & & & & & \\ & & & -\frac{1}{2} & & & & \\ & & & & \frac{1}{4} & 0 & -\frac{3}{4} & 0 \\ & 0 & & & 0 & -\frac{1}{2} & 0 & 0 \\ & & & & -\frac{3}{4} & 0 & \frac{1}{4} & 0 \\ & & & & 0 & 0 & 0 & -\frac{1}{2} \end{pmatrix},$$

$$\langle 2|P^+P^+|2\rangle = \begin{pmatrix} -1 & 0 & 0 & 0 & 0 & 0 & 0 & 0 \\ 0 & 0 & 0 & 0 & 0 & 0 & 0 & 0 \\ 0 & 0 & 0 & 0 & 0 & 0 & 0 & 0 \\ 0 & 0 & 0 & 0 & 0 & 0 & 0 & 0 \\ 0 & 0 & 0 & 0 & 0 & 0 & 0 & 0 \\ 0 & 0 & 0 & 0 & 0 & 0 & 0 & 1 \\ 0 & 0 & 0 & 0 & 0 & 0 & 0 & 0 \\ 0 & 0 & 0 & 0 & 0 & 1 & 0 & 0 \end{pmatrix},$$

$$\langle 1|P_1^+|1\rangle = \begin{pmatrix} \frac{1}{12} & \frac{\sqrt{2}}{6} & \frac{3}{4} & 0 & 0 & 0 & 0 & 0 \\ -\frac{\sqrt{2}}{3} & \frac{1}{6} & 0 & 0 & 0 & 0 & 0 & 0 \\ -\frac{1}{4} & -\frac{1}{\sqrt{2}} & -\frac{1}{4} & 0 & 0 & 0 & 0 & 0 \\ 0 & 0 & 0 & \frac{1}{2} & 0 & 0 & 0 & 0 \\ 0 & 0 & 0 & 0 & -\frac{1}{12} & -\frac{\sqrt{2}}{6} & \frac{1}{4} & \frac{1}{\sqrt{2}} \\ 0 & 0 & 0 & 0 & \frac{\sqrt{2}}{3} & -\frac{1}{6} & 0 & 0 \\ 0 & 0 & 0 & 0 & \frac{1}{4} & \frac{1}{\sqrt{2}} & -\frac{1}{12} & -\frac{\sqrt{2}}{6} \\ 0 & 0 & 0 & 0 & 0 & 0 & \frac{\sqrt{2}}{3} & -\frac{1}{6} \end{pmatrix},$$

Table 1. Elements of the spin–isospin basis for 3 + 1 partitions and corresponding states of the *nnpp* system (total spin of $S = 1$)

Basis elements	S_{12}	T_{12}	S_{123}	T_{123}	S	T
$e_1^{(1)}$	1	0	1/2	1/2	1	0
$e_2^{(1)}$	1	0	3/2	1/2	1	0
$e_3^{(1)}$	0	1	1/2	1/2	1	0
$e_4^{(1)}$	0	1	1/2	3/2	1	2
$e_5^{(1)}$	1	0	1/2	1/2	1	1
$e_6^{(1)}$	1	0	3/2	1/2	1	1
$e_7^{(1)}$	0	1	1/2	1/2	1	1
$e_8^{(1)}$	0	1	1/2	3/2	1	1

Table 2. Elements of the spin–isospin basis for 2 + 2 partitions and corresponding states of the *nnpp* system (total spin of $S = 1$)

Basis elements	S_{12}	T_{12}	S_{34}	T_{34}	S	T
$e_1^{(1)}$	1	0	1	0	1	0
$e_2^{(1)}$	1	0	0	0	1	0
$e_3^{(1)}$	0	1	1	1	1	0
$e_4^{(1)}$	0	1	1	1	1	2
$e_5^{(1)}$	1	0	1	1	1	1
$e_6^{(1)}$	1	0	0	1	1	1
$e_7^{(1)}$	0	1	1	1	1	1
$e_8^{(1)}$	0	1	1	0	1	1

Table 3. Elements of the spin–isospin basis for 3 + 1 partitions and corresponding states of the *nnpp* system (total spin of $S = 0$)

Basis elements	S_{12}	T_{12}	S_{123}	T_{123}	S	T
$e_1^{(1)}$	0	1	1/2	1/2	0	0
$e_2^{(1)}$	0	1	1/2	3/2	0	2
$e_3^{(1)}$	1	0	1/2	1/2	0	0
$e_4^{(1)}$	0	1	1/2	1/2	0	1
$e_5^{(1)}$	0	1	1/2	3/2	0	1
$e_6^{(1)}$	1	0	1/2	1/2	0	1

$$\langle 1|P^+|1\rangle = \langle 1|P_1^+|1\rangle,$$

$$\langle 1|P_4^+|2\rangle$$

$$= \begin{pmatrix}
\frac{1}{2\sqrt{6}} & -\frac{1}{4\sqrt{3}} & -\frac{3}{4} & 0 & 0 & 0 & 0 & 0 \\
-\frac{1}{2\sqrt{3}} & -\frac{1}{\sqrt{6}} & 0 & 0 & 0 & 0 & 0 & 0 \\
-\frac{3}{2\sqrt{6}} & \frac{\sqrt{3}}{4} & \frac{1}{4} & 0 & 0 & 0 & 0 & 0 \\
0 & 0 & 0 & \frac{1}{2} & 0 & 0 & 0 & 0 \\
0 & 0 & 0 & 0 & \frac{1}{2\sqrt{6}} & -\frac{1}{2\sqrt{3}} & -\frac{3}{2\sqrt{6}} & \frac{\sqrt{3}}{4} \\
0 & 0 & 0 & 0 & -\frac{1}{2\sqrt{3}} & -\frac{1}{\sqrt{6}} & 0 & 0 \\
0 & 0 & 0 & 0 & -\frac{3}{2\sqrt{6}} & \frac{\sqrt{3}}{4} & \frac{1}{2\sqrt{6}} & -\frac{1}{4\sqrt{3}} \\
0 & 0 & 0 & 0 & 0 & 0 & -\frac{1}{2\sqrt{3}} & -\frac{1}{\sqrt{6}}
\end{pmatrix},$$

$$\langle 1|P_1^+|2\rangle$$

$$= \begin{pmatrix}
\frac{1}{2\sqrt{6}} & \frac{1}{4\sqrt{3}} & \frac{3}{4} & 0 & 0 & 0 & 0 & 0 \\
-\frac{1}{2\sqrt{3}} & \frac{1}{\sqrt{6}} & 0 & 0 & 0 & 0 & 0 & 0 \\
-\frac{3}{2\sqrt{6}} & -\frac{\sqrt{3}}{4} & -\frac{1}{4} & 0 & 0 & 0 & 0 & 0 \\
0 & 0 & 0 & \frac{1}{2} & 0 & 0 & 0 & 0 \\
0 & 0 & 0 & 0 & -\frac{1}{2\sqrt{6}} & -\frac{1}{2\sqrt{3}} & \frac{3}{2\sqrt{6}} & \frac{\sqrt{3}}{4} \\
0 & 0 & 0 & 0 & \frac{1}{2\sqrt{3}} & -\frac{1}{\sqrt{6}} & 0 & 0 \\
0 & 0 & 0 & 0 & \frac{3}{2\sqrt{6}} & \frac{\sqrt{3}}{4} & -\frac{1}{2\sqrt{6}} & -\frac{1}{4\sqrt{3}} \\
0 & 0 & 0 & 0 & 0 & 0 & \frac{1}{2\sqrt{3}} & -\frac{1}{\sqrt{6}}
\end{pmatrix},$$

$$\langle 2|P^+P^+|1\rangle = \begin{pmatrix}
-\frac{2}{\sqrt{6}} & -\frac{1}{\sqrt{3}} & 0 & 0 & 0 & 0 & 0 & 0 \\
0 & 0 & 0 & 0 & 0 & 0 & 0 & 0 \\
0 & 0 & 0 & 0 & 0 & 0 & 0 & 0 \\
0 & 0 & 0 & 0 & 0 & 0 & 0 & 0 \\
0 & 0 & 0 & 0 & 0 & 0 & 0 & 0 \\
0 & 0 & 0 & 0 & 0 & 0 & -\frac{1}{\sqrt{3}} & \frac{2}{\sqrt{6}} \\
0 & 0 & 0 & 0 & 0 & 0 & 0 & 0 \\
0 & 0 & 0 & 0 & -\frac{1}{\sqrt{3}} & \frac{2}{\sqrt{6}} & 0 & 0
\end{pmatrix}.$$

The upper block of each of the above matrices corresponds to the $S = 1$, $T = 0, 2$ states of the system, while the lower block corresponds to the $S = 1$, $T = 1$ state.

The Coulomb potential of the problem is given by

$$V^{\mathrm{Coul}} = \sum_{j>i} V_{ji} \frac{(1 + 2\tau_i^z)(1 + 2\tau_j^z)}{4},$$

where τ_i^z is the operator projecting the isospin of the ith particle onto the z axis, while $V_{ji} = n/|\mathbf{x}_{ji}|$. Here, $i, j = 1, 2, 3, 4$; $\mathbf{x}_{ji} = \mathbf{r}_j - \mathbf{r}_i$; and n is the reduced proton charge given by $n = (e^2m)/\hbar^2$, with m being the nucleon mass. In the spin–isospin basis (2), the representation matrices for the Coulomb interaction can be written as

$$W_1 = 1/2 \begin{pmatrix}
w_{11} & 0 & 0 & 0 & w_{11} & 0 & 0 & 0 \\
0 & w_{11} & 0 & 0 & 0 & w_{11} & 0 & 0 \\
0 & 0 & w_{33} & w_{34} & 0 & 0 & w_{33} & w_{34} \\
0 & 0 & w_{34} & w_{44} & 0 & 0 & w_{34} & w_{44} \\
w_{11} & 0 & 0 & 0 & w_{11} & 0 & 0 & 0 \\
0 & w_{11} & 0 & 0 & 0 & w_{11} & 0 & 0 \\
0 & 0 & w_{33} & w_{34} & 0 & 0 & w_{33} & w_{34} \\
0 & 0 & w_{34} & w_{44} & 0 & 0 & w_{34} & w_{44}
\end{pmatrix},$$

$$\overline{W}_1 = 1/2$$

$$\times \begin{pmatrix}
\overline{w}_{11} & 0 & 0 & 0 & -\overline{w}_{11} & 0 & 0 & 0 \\
0 & \overline{w}_{11} & 0 & 0 & 0 & -\overline{w}_{11} & 0 & 0 \\
0 & 0 & \overline{w}_{33} & \overline{w}_{34} & 0 & 0 & -\overline{w}_{33} & -\overline{w}_{34} \\
0 & 0 & \overline{w}_{34} & \overline{w}_{44} & 0 & 0 & -\overline{w}_{34} & -\overline{w}_{44} \\
-\overline{w}_{11} & 0 & 0 & 0 & \overline{w}_{11} & 0 & 0 & 0 \\
0 & -\overline{w}_{11} & 0 & 0 & 0 & \overline{w}_{11} & 0 & 0 \\
0 & 0 & -\overline{w}_{33} & -\overline{w}_{34} & 0 & 0 & \overline{w}_{33} & \overline{w}_{34} \\
0 & 0 & -\overline{w}_{34} & -\overline{w}_{44} & 0 & 0 & \overline{w}_{34} & \overline{w}_{44}
\end{pmatrix},$$

$$W^1 = W_1 + \overline{W}_1,$$

where

$$w_{11} = (V_{12} + V_{23})/2, \quad \overline{w}_{11} = (V_{14} + V_{24})/2,$$
$$w_{33} = 2V_{12}/3 + (V_{13} + V_{23})/6,$$
$$\overline{w}_{33} = 2V_{34}/3 + (V_{13} + V_{23})/6,$$
$$w_{44} = (V_{13} + V_{23} + V_{13})/3,$$
$$\overline{w}_{44} = (V_{34} + V_{14} + V_{24})/3,$$
$$w_{34} = \sqrt{2}(V_{12} - (V_{13} + V_{23})/2)/3,$$
$$\overline{w}_{34} = \sqrt{2}(V_{34} - (V_{14} + V_{24})/2)/3$$

for components of the 3 + 1 type and as

$$W_2 = 1/2\begin{pmatrix} w_{11} & 0 & 0 & 0 & w_{11} & 0 & 0 & 0 \\ 0 & w_{11} & 0 & 0 & 0 & w_{11} & 0 & 0 \\ 0 & 0 & w_{33} & w_{34} & 0 & 0 & w_{37} & w_{38} \\ 0 & 0 & w_{34} & w_{44} & 0 & 0 & w_{47} & w_{48} \\ w_{11} & 0 & 0 & 0 & w_{11} & 0 & 0 & 0 \\ 0 & w_{11} & 0 & 0 & 0 & w_{11} & 0 & 0 \\ 0 & 0 & w_{37} & w_{47} & 0 & 0 & w_{77} & 0 \\ 0 & 0 & w_{38} & w_{48} & 0 & 0 & 0 & w_{11} \end{pmatrix},$$

$$\overline{W}_2 = 1/2$$

$$\times\begin{pmatrix} \overline{w}_{11} & 0 & 0 & 0 & -\overline{w}_{11} & 0 & 0 & 0 \\ 0 & \overline{w}_{11} & 0 & 0 & 0 & -\overline{w}_{11} & 0 & 0 \\ 0 & 0 & \overline{w}_{33} & \overline{w}_{34} & 0 & 0 & -\overline{w}_{37} & -\overline{w}_{38} \\ 0 & 0 & \overline{w}_{34} & \overline{w}_{44} & 0 & 0 & -\overline{w}_{47} & -\overline{w}_{48} \\ -\overline{w}_{11} & 0 & 0 & 0 & \overline{w}_{11} & 0 & 0 & 0 \\ 0 & -\overline{w}_{11} & 0 & 0 & 0 & \overline{w}_{11} & 0 & 0 \\ 0 & 0 & -\overline{w}_{37} & -\overline{w}_{47} & 0 & 0 & \overline{w}_{77} & 0 \\ 0 & 0 & -\overline{w}_{38} & -\overline{w}_{48} & 0 & 0 & 0 & \overline{w}_{11} \end{pmatrix},$$

$$W^2 = W_2 + \overline{W}_2,$$

where

$$w_{11} = ((V_{13} + V_{23})/2), \quad \overline{w}_{11} = (V_{14} + V_{24})/2,$$
$$w_{33} = 2V_{12}/3 + (V_{13} + V_{23})/6,$$
$$\overline{w}_{33} = 2V_{34}/3 + (V_{14} + V_{24})/6,$$
$$w_{38} = -\sqrt{3}(V_{13} + V_{23})/6, \quad \overline{w}_{38} = \sqrt{3}(V_{14} + V_{24})/6,$$
$$w_{34} = -\sqrt{2}(V_{12} - (V_{13} + V_{23})/2)/3,$$

Table 4. Elements of the spin–isospin basis for 2 + 2 partitions and corresponding states of the *nnpp* system (total spin of $S = 0$)

Basis elements	S_{12}	T_{12}	S_{34}	T_{34}	S	T
$e_1^{(1)}$	0	1	0	1	0	0
$e_2^{(1)}$	0	1	0	1	0	2
$e_3^{(1)}$	1	0	1	0	0	0
$e_4^{(1)}$	0	1	0	1	0	1
$e_5^{(1)}$	0	1	0	0	0	1
$e_6^{(1)}$	1	0	1	1	0	1

$$\overline{w}_{34} = \sqrt{2}(V_{34} - (V_{14} + V_{24})/2)/3,$$
$$w_{44} = (V_{12} + V_{13} + V_{23})/3,$$
$$\overline{w}_{44} = (V_{34} + V_{14} + V_{24})/3,$$
$$w_{47} = \sqrt{3}V_{12}/3, \quad \overline{w}_{47} = \sqrt{3}V_{34}/3,$$
$$w_{77} = V_{12}, \quad \overline{w}_{77} = V_{34},$$
$$w_{37} = 2V_{12}/\sqrt{6}, \quad \overline{w}_{37} = 2V_{34}/\sqrt{6},$$
$$w_{48} = (V_{13} + V_{23})/\sqrt{6}, \quad \overline{w}_{48} = (V_{14} + V_{24})/\sqrt{6}$$

for components of the 2 + 2 type.

In order to single out the individual channels of n^3He and p^3H scattering, we go over to a new spin–isospin basis for 3 + 1 components. This is done by means of the orthogonal transformation

$$e_i^{(1)'} = \sum_{j=1}^{8} A_{ij} e_j^{(1)}, \quad i = 1, 2, \ldots, 8, \qquad (4)$$

where the transformation matrix A has the form

$$A = \begin{pmatrix} 1 & 0 & 0 & 0 & 1 & 0 & 0 & 0 \\ 0 & 1 & 0 & 0 & 0 & 1 & 0 & 0 \\ 0 & 0 & 1 & 0 & 0 & 0 & 1 & 0 \\ 0 & 0 & 0 & 1 & 0 & 0 & 0 & 1 \\ 1 & 0 & 0 & 0 & -1 & 0 & 0 & 0 \\ 0 & 1 & 0 & 0 & 0 & -1 & 0 & 0 \\ 0 & 0 & 1 & 0 & 0 & 0 & -1 & 0 \\ 0 & 0 & 0 & 1 & 0 & 0 & 0 & -1 \end{pmatrix}.$$

Under this transformation, the representation matrices for the operators $P_4^{\pm}$ undergo no changes; that is, we

have

$$A\langle 1|P_4^{\pm}|1\rangle A^{-1} = \langle 1|P_4^{\pm}|1\rangle.$$

The Coulomb matrix W^1 then reduces to the form

$$W^1 = \begin{pmatrix} w_{11} & 0 & 0 & & & & & \\ 0 & w_{11} & 0 & & 0 & & & \\ 0 & 0 & w_{33} & w_{34} & & & & \\ 0 & 0 & w_{34} & w_{44} & & & & \\ & & & & \bar{w}_{11} & & & \\ & & & & 0 & \bar{w}_{11} & 0 & 0 \\ & 0 & & & 0 & 0 & \bar{w}_{33} & \bar{w}_{34} \\ & & & & 0 & 0 & \bar{w}_{34} & \bar{w}_{44} \end{pmatrix},$$

where

$$w_{11} = (V_{12} + V_{23})/2, \quad \bar{w}_{11} = (V_{14} + V_{24})/2,$$

$$w_{33} = 2V_{12}/3 + (V_{13} + V_{23})/6,$$

$$\bar{w}_{33} = 2V_{34}/3 + (V_{13} + V_{23})/6,$$

$$w_{44} = (V_{12} + V_{23} + V_{13})/3,$$

$$\bar{w}_{44} = (V_{34} + V_{14} + V_{24})/3,$$

$$w_{34} = \sqrt{2}(V_{12} - (V_{13} + V_{23})/2)/3,$$

$$\bar{w}_{34} = \sqrt{2}(V_{34} - (V_{14} + V_{24})/2)/3.$$

Thus, we can see that, on the left-hand sides of equations (1), the matrices of the operator representations are decomposed into blocks that describe the individual channels of n^3He and p^3H scattering. These channels are coupled through the right-hand sides of equations (1).

2.2. s-Wave Approximation

Our further consideration will be restricted to the *s*-wave approximation—that is, we assume that all angular momenta of the system in question and of its subsystems are equal to zero. In the case of $S = 1$, equations (1) take the form of a set of 16 equations for the components $\mathcal{U}_i^k$ ($k = 1, 2$; $i = 1, 2, \ldots, 8$). [In the case of $S = 0$, we have a set of 12 equations for the components $\mathcal{U}_i^k$ ($k = 1, 2$; $i = 1, 2, \ldots, 6$).] We then combine the above components into the vectors $\mathcal{U}^1 \in R^{n_1}$ and $\mathcal{U}^2 \in R^{n_2}$ ($n_1 = 8, n_2 = 6$) and represent the set of *s*-wave equations for these vectors as

$$\begin{aligned} &(h_0^1 + V_1(x) - \varepsilon)\mathcal{U}^1(x, y, z) \\ &+ V_1(x)\int_{-1}^{1} dv \frac{xy}{x_1 y_1} B_1 \mathcal{U}^1(x_1, y_1, z_1) + V_1^{\mathrm{Coul}}\mathcal{U}^1(x, y, z) \\ &= -\frac{1}{2}V_1(x)\int_{-1}^{1} du \int_{-1}^{1} dv \left\{ \frac{xyz}{x_2 y_2 z_2} D\mathcal{U}^1(x_2, y_2, z_2) \right. \\ &\left. + \frac{xyz}{x_3 y_3 z_3} C_1 \mathcal{U}^2(x_3, y_3, z_3) \right\} \\ &(h_0^2 + V_2(x) - \varepsilon)\mathcal{U}^2(x, y, z) \\ &+ V_2(x)B_2\mathcal{U}^2(x, y, z) + V_2^{\mathrm{Coul}}\mathcal{U}^2(x, y, z) \\ &= -\frac{1}{2}V_2(x)\int_{-1}^{1} dv \frac{xyz}{x_4 y_4 z_4} C_2 \mathcal{U}^1(x_4, y_4, z_4), \end{aligned} \tag{5}$$

where $\varepsilon = \frac{m}{\hbar^2}E$, $V_k = \frac{m}{\hbar^2}\langle e^k|V|e^k\rangle$, and V_k^{Coul} are the *s*-wave projections of the Coulomb matrices W^k. By B_k ($k = 1, 2$), C_k, and D, we denote numerical matrices generated by the representations of the permutation operators in the spin–isospin bases (2) and (4) from equations (1); that is,

$$B_1 = \langle 1|P_4^+ + P_1^-|1\rangle,$$

$$D = \langle 1|P_1^+ - P^+|1\rangle,$$

$$B_2 = \langle 2|P^+P^+|2\rangle,$$

$$C_1 = \langle 1|P_1^+ + P_4^+|2\rangle,$$

$$C_2 = \langle 2|P^+ - P_1^+|1\rangle.$$

For the singlet and triplet spin states of the *nnpp* system, the matrices B_k ($k = 1, 2$), C_k, V_k^{Coul}, and D are presented in the Appendix. The operators h_0^k are given by

$$h_0^1 = -\left(\partial_x^2 + \frac{3}{4}\partial_y^2 + \frac{2}{3}\partial_z^2\right),$$

$$h_0^2 = -\left(\partial_x^2 + \partial_y^2 + \frac{1}{2}\partial_z^2\right).$$

The operators $V_k(x)$ are diagonal, and their matrices have the form

$$V_k(x) = \mathrm{diag}\{V^s(x), V^s(x), V^t(x), V^s(x), V^s(x), V^t(x)\},$$

where $V^s(x)$ and $V^t(x)$ are, respectively, the singlet and triplet components of the nucleon–nucleon potential.

The coordinates x_l, y_l, and z_l ($l = 1, 2, 3, 4$) in the integral terms of equations (5) are computed by the for-

mulas

$$x_1 = \left[\frac{x^2}{4} + y^2 - xy\sqrt{}\right]^{1/2},$$

$$y_1 = \left[\left(\frac{3x}{4}\right)^2 + \frac{y^2}{4} + \frac{3}{4}xy\sqrt{}\right]^{1/2},$$

$$x_2 = x_1, \quad x_3 = x_1, \quad x_4 = y,$$

$$y_2 = \left[\left(\frac{y_1}{3}\right)^2 + z^2 + \frac{2}{3}y_1 zu\right]^{1/2},$$

$$z_2 = \left[\left(\frac{8y_1}{9}\right)^2 + \frac{z^2}{9} - \frac{16}{27}y_1 zu\right]^{1/2},$$

$$y_3 = \left[\left(\frac{2y_1}{3}\right)^2 + z^2 + \frac{4}{3}y_1 zu\right]^{1/2},$$

$$z_3 = \left[\left(\frac{2y_1}{3}\right)^2 + \frac{z^2}{4} - \frac{2}{3}y_1 zu\right]^{1/2},$$

$$y_4 = \left[\left(\frac{x}{2}\right)^2 + z^2 - xz\sqrt{}\right]^{1/2}, \quad z_4 = \frac{2}{3}[x^2 + z^2 + 2xz\sqrt{}]^{1/2}.$$

2.3. Boundary-Value Problems

The set of equations (5) is supplemented with asymptotic boundary conditions. We denote by $\mathcal{U}_i^{(k)}(x, y, z)$, $k = 1, 2$ and $i = 1, 2, \ldots, N$ (we have $N = 8$ for the triplet spin state and $N = 6$ for the singlet spin state), the vector column formed by the coordinate parts of the *s*-wave Yakubovsky components. At $x = 0$, $y = 0$, and $z = 0$, zero boundary conditions are imposed on the functions $\mathcal{U}_i^{(k)}(x, y, z)$. Let us consider asymptotic boundary conditions for low-energy triplet p^3H scattering. Only the elastic scattering channel is open at energies below the threshold for the reaction ^{3}H$(p, n)^3$He. For the open channel, the asymptotic behavior of the relevant Yakubovsky components in the limit $z \longrightarrow \infty$ is given by

$$\mathcal{U}^1(x, y, z) \sim (0, 0, 0, 0, \Phi_t(x, y)(\chi_p(z) + \tan(\delta_{pt})G_0(\eta, p)), 0)^T, \quad (6)$$
$$\mathcal{U}^2(x, y, z) \sim 0,$$

where $\Phi_t(x, y)$ stands for the Faddeev components of the wave functions of the ground-state ^{3}H nucleus. The function $\chi_p(z)$ describes the initial, asymptotically free state of the system, $\chi_p(z) = F_0(\eta, pz)$, $F_0(\eta, pz)$ being the regular Coulomb function. The corresponding singular function is denoted by $G_0(\eta, pz)$. In these functions, the parameter η is given by $\eta = (3/4)n/p$. At energies of relative motion in the system that are higher than the threshold for the reaction ^{3}H$(p, n)^3$He, the asymptotic expression for the component $U^1(x, y, z)$ can be represented in the form

$$\mathcal{U}^1(x, y, z) \sim (\Phi_h a_1(p_1)\exp(ip_1 z), 0, \Phi_t(x, y)(\chi_p(z) + a(p)(G_0(\eta, pz) + iF_0(\eta, pz))), 0)^T, \quad (7)$$

where $\Phi_h(x, y)$ are the Faddeev components of the wave function of the ground-state ^{3}He nucleus. The relative momenta p and p_1 in the c.m. frame are determined from the relation

$$E = 2p^2/3 + \varepsilon_t = 2p_1^2/3 + \varepsilon_h,$$

where ε_t and ε_h are the binding energies of the triton and the ^{3}He nucleus, respectively. The diagonal elements of the *S* matrix are parametrized in the conventional form $S_{11} = {}^3\eta_{pt}\exp(2i^3\delta_{pt})$, where $^3\eta_{pt}$ is the inelasticity factor. The amplitude $a(p)$ is related to the matrix element S_{11} by the equation $a(p) = (S_{11} - 1)/2i$. The scattering length $^3A_{pt}$ is calculated as the zero-energy limit of the function $-\tan(\delta_{pt})/pC_0^2$, where $C_0^2 = 2\pi\eta/[\exp(2\pi\eta) - 1]$.

For triplet neutron scattering on a ^{3}He nucleus, the asymptotic boundary conditions in the limit $z \longrightarrow \infty$ must take into account two open channels; that is,

$$\mathcal{U}^1(x, y, z) \sim (\Phi_h(x, y)(\chi_{1p_1}(z) + a(p_1)\exp(ip_1 z)), 0, \Phi_t(x, y)a_1(p)(G_0(\eta, pz) + iF_0(\eta, pz)), 0)^T, \quad (8)$$
$$\mathcal{U}^2(x, y, z) \sim 0,$$

where $S_{22} = {}^3\eta_{nh}\exp(2i^3\delta_{nh})$, $a(p) = (S_{22} - 1)/2i$, and $\chi_{1p_1}(z) = \sin(p_1 z)/p_1$. The scattering length A_{nh} for neutron interaction with a ^{3}He nucleus is calculated as the limit $A_{nh} = -\lim_{p_1 \to 0} a(p_1)$.

Singlet-scattering states in the *nnpp* system correspond to the continuous spectrum of the ^{4}He nucleus. In the case of singlet scattering, the possible channels include, in addition to the p^3H and n^3He channels, the channel of deuteron–deuteron scattering. This corresponds to a nonzero asymptotic value of the component $\mathcal{U}^2(x, y, z)$ in the limit $z \longrightarrow \infty$. The asymptotic behavior of the component $\mathcal{U}^1(x, y, z)$ is similar to that given by equations (6)–(8). By way of example, we indicate that, for singlet deuteron–deuteron scattering, the asymptotic expressions for the components in question can be represented as

$$\mathcal{U}^1(x, y, z) \sim (\Phi_h a_1(p_1)\exp(ip_1 z), 0, \Phi_t(x, y)a_2(p_2)(G_0(\eta_2, p_2 z) + iF_0(\eta_2, p_2 z)), 0)^T,$$

$$\mathcal{U}^2(x, y, z) \sim (0, 0, \Phi_d(x, y)(\chi_d(pz) + a(p)(G_0(\eta_d, pz) + iF_0(\eta_d, pz))), 0, 0, 0, 0, 0)^T.$$

Here, $\chi_d(pz) = F_0(\eta_d, pz)$; $\eta_d = n/p$; $\eta_2 = (3/4)n/p_2$; and the relative momenta p, p_1, and p_2 are determined from the relations

$$E = p^2/2 + 2\varepsilon_d = 2p_1^2/3 + \varepsilon_h = 2p_2^2/3 + \varepsilon_t,$$

where ε_d is the deuteron binding energy. By $\Phi_d(x, y)$, we denote that Faddeev component of the wave function which corresponds to a state of two noninteracting deuterons. The deuteron–deuteron scattering length A_{dd} is calculated as $A_{dd} = -\lim_{p\to 0} \frac{a(p)}{pC_0^2}$.

3. CLUSTER REDUCTION

A general scheme for implementing the reduction of equations for the Yakubovsky components is described elsewhere [18, 19]. Here, we only recall the basis points of this procedure as applied to the s-wave equations (5). Solutions to these equations can be represented in the form

$$^{0}u^{i}(x, y, z) = \sum_{l=0}^{\infty} \phi_l^i(x, y) F_l^i(z), \tag{9}$$

where the basis functions $\phi_l^i(x, y)$ are solutions to the Faddeev equations for the 3 + 1 and 2 + 2 partitions; that is,

$$\begin{aligned}
&\left\{-\partial_x^2 - \frac{3}{4}\partial_y^2 + V_1(x)\right\}\phi_l^1(x, y) \\
&+ V_1(x)\int_{-1}^{1} dv \frac{xy}{x_1y_1} B_1\phi_l^1(x_1, y_1) \\
&+ \hat{V}_1^{\text{Coul}}(x, y)\phi_l^1(x, y) = \varepsilon_1^l\phi_l^1(x, y), \\
&\{-\partial_x^2 - \partial_y^2 + V_2(x)\}\phi_l^2(x, y) + V_2(x)B_2\phi_l^2(y, x) \\
&= \varepsilon_2^l\phi_l^2(x, y),
\end{aligned} \tag{10}$$

where $\hat{V}_1^{\text{Coul}}$ is the truncated Coulomb matrix obtained from W^1 by setting its right lower block to zero. A set of functions that is biorthogonal to $\{\phi_l^k\}$ is determined by conjugate Faddeev equations [23, 24]. In the case being considered, these equations have the form

$$\begin{aligned}
&\left\{-\partial_x^2 - \frac{3}{4}\partial_y^2 + V_1(x)\right\}\psi_l^1(x, y) \\
&+ \int_{-1}^{1} dv \frac{xy}{x_1y_1} B_1V_1(x_1)\psi_l^1(x_1, y_1) \\
&+ \hat{V}_1^{\text{Coul}}(x, y)\psi_l^1(x, y) = \varepsilon_1^l\psi_l^1(x, y), \\
&\{-\partial_x^2 - \partial_y^2 + V_2(x)\}\psi_l^2(x, y) \\
&+ B_2V_2(y)\psi_l^2(y, x) = \varepsilon_2^l\psi_l^2(x, y).
\end{aligned} \tag{11}$$

Upon the substitution of expansions (9) into equations (5) and projecting the result onto the elements of the basis $\{\psi_l^k\}$, we eventually find that the functions $F_l^k(z)$ satisfy the equations

$$\begin{aligned}
&\left\{-\frac{2}{3}\partial_z^2 - E + \varepsilon_1^k\right\}F_k^1(z) + \sum_{l\geq 0}\langle\psi_k^1|\tilde{V}_1^{\text{Coul}}|\phi_l^1\rangle F_l^1(z) \\
&= -\frac{1}{2}\sum_{l\geq 0}\frac{1}{2}\left\langle\psi_k^1\middle|V_1(x)\int_{-1}^{1} du\int_{-1}^{1} dv\left\{\frac{xyz}{x_2y_2z_2} D\phi_l^1(x_2, y_2)F_l^1(z_2)\right.\right. \\
&\left.\left. + \frac{xyz}{x_3y_3z_3} C_1\phi_l^2(x_3, y_3)F_l^2(z_3)\right\}\right\rangle,
\end{aligned} \tag{12}$$

$$\begin{aligned}
&\left\{-\frac{1}{2}\partial_z^2 - E + \varepsilon_2^k\right\}F_k^2(z) + \sum_{l\geq 0}\langle\psi_k^2|V_2^c|\phi_l^2\rangle F_l^2(z) \\
&= -\frac{1}{2}\sum_{l\geq 0}\left\langle\psi_k^2\middle|V_2(x)\int_{-1}^{1} dv\frac{xyz}{x_4y_4z_4} C_2\phi_l^1(x_4, y_4)F_l^1(z_4)\right\rangle,
\end{aligned}$$

where $\langle\ldots|\ldots\rangle$ denotes integration with respect to the variables x and y.

The number of equations in the set that we obtained depends on the number of terms that are taken into account in expansions (9) (needless to say, a finite number of such terms must be retained in solving the above equations numerically).

Table 5. Singlet and triplet scattering lengths for the *nnpp* system

References	$^1A_{pt}$, fm	$^1A_{nh}$, fm	$^1A_{dd}$, fm	$^3A_{pt}$, fm	$^3A_{nh}$, fm
Our study	–22.6	7.5 – 4.2i	10.2 – 0.2i	4.6	3.0 + 0i
[4]	–21.46	7.25 – 3.92i	–	–	–
[25]	4.2	6.05 – 0.72i	–	5.2	4.25 + 0.005i

Table 6. Calculated triplet scattering lengths in the *nnpp* system versus the number N of terms retained in expansions (9)

N	${}^3A_{pt}$, fm	${}^3A_{nh}$, fm
1	3.82	2.56
5	4.20	2.86
10	4.50	2.95
15	4.55	2.98
20	4.56	3.00
25	4.55	–

4. RESULTS OF THE CALCULATIONS

The first step in solving equations (12) must consist in constructing relevant bases. This problem is solved by using equations (10) and (11) with zero boundary conditions at the boundaries of the regions $\Omega^1 = \{x, y | \sqrt{x^2 + 3/4y^2} \leq \rho^{3+1}\}$ and $\Omega^2 = \{x, y | x \in [0, R_x^{2+2}], y \in [0, R_y^{2+2}]\}$, respectively. The functions are numbered in such a way that the eigenvalues corresponding to them form an increasing sequence.

A numerical solution to equations (12) for the functions describing relative motion is constructed by using a finite-difference approximation on a homogeneous mesh in the relative coordinate z. We denote by R_z the radius in z where we impose the asymptotic boundary conditions (6)–(8) and by N_z the number of mesh nodes in the coordinate z. In our calculations, we take into account a finite number of terms in expansions (9). We denote this number by N. The parameters of the calculations were chosen as $\rho^{(3+1)} = R^{(2+2)} = 17$ fm, $R_z = 17$ fm, $N_z = 23$, and $N = 40$ for the spin-singlet state of the system and as $\rho^{(3+1)} = 21$ fm, $R^{(2+2)} = 20$ fm, $R_z = 21$ fm, $N_z = 30$, and $N = 20$ for the spin-triplet state. Table 5 displays the calculated singlet and triplet scattering length in the *nnpp* system for the p^3H, n^3He, and *dd* channels. It can be seen that our results are quite close to the RGM results from [4]. Belyaev and Pupyshev [25] used an integral form of the equations of motion and specified nucleon–nucleon interaction in a separable form.

The efficiency of the cluster-reduction method is determined primarily by the number N of terms that must be taken into account in expansions (9) in order that the results of the calculations for observables, such as scattering lengths and phase shifts, be convergent. From the above values of the parameters used in the calculations, it can be seen that, for the different spin states of the system, different numbers of terms must be retained in expansions (9). Obviously, the higher the degree of 3 + 1 clustering in the system being considered (or the degree of 2 + 2 clustering in the *dd* system), the smaller the value of N. The data quoted in Table 6 illustrate the convergence of the results of the calculations for the triplet scattering length in the p^3H and n^3He systems versus N. It can be seen that the contribution of the first term ($N = 1$) in expansion (9) saturates 85% of the result. The convergence for singlet scattering in the *dd* system has a similar character. The situation is totally different for the spin-singlet states of the p^3H and n^3He systems: the calculations employing only the first term in expansion (9) lead to scattering length values that differ from ${}^1A_{pt}$ and ${}^1A_{nh}$ not only in magnitude but also in sign.

Let us now contrast the results of our calculations for the singlet and triplet scattering of neutrons on ^{3}He nuclei against available experimental data. Specifically, we compare theoretical and experimental values of relevant scattering lengths (see Table 7, which also quotes the coherent scattering length, whose theoretical values are calculated by the formula $A_{\text{coh}} = {}^1A_{nh}/4 + 3{}^3A_{nh}/4$).

The imaginary part of the singlet scattering length for neutron interaction with a ^{3}He nucleus was precisely determined in terms of the cross section for thermal-neutron capture by the ^{3}He nucleus [26]. The imaginary part of the triplet scattering length was also determined precisely by using data on the cross section for radiative capture [26]. Experiments give no way to determine unambiguously the real parts of the singlet and triplet scattering lengths. The analysis of experimental data that was performed in [11] yielded the

Table 7. Real and imaginary parts of the scattering lengths in the n^3He system

		${}^1A_{nh}$, fm	${}^3A_{nh}$, fm	A_{coh}, fm
Experimental data	Re	6.53 ± 0.32 [29]	$3.5^{+0.8}_{-0.4}$ [11]	4.29 ± 0.04 [28]
		$6.6^{+1.0}_{-2.3}$ [11]		
	Im	-4.4448 ± 0.0009 [26]	$(1.7 \pm 0.08) \times 10^{-8}$ [27]	-1.1112 ± 0.0003 [11]
Results of our calculations	Re	7.5	3.0	4.1
	Im	–4.2	0.0	–1.1
[4]	Re	7.25	–	–
	Im	–3.92	–	–

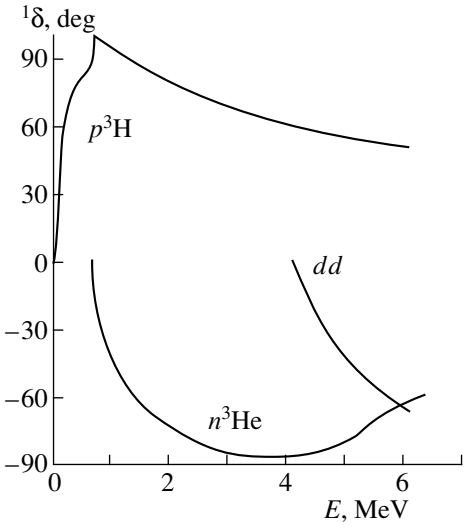

Fig. 1. Phase shifts for singlet scattering in the *nnpp* system.

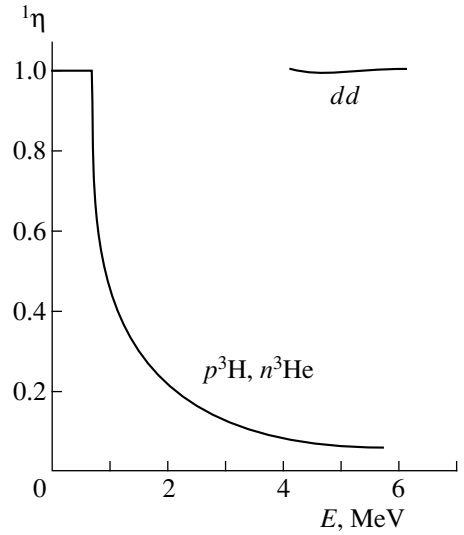

Fig. 2. Inelasticity factors for singlet scattering in the *nnpp* system.

value of $\mathrm{Re}(^1A) = 6.6^{+1.0}_{-2.3}$ fm. The close value of $\mathrm{Re}(^1A) = 6.53 \pm 0.3$ fm was obtained in the later study of Alfimenkov *et al.* [29]. As can be seen from Table 7, our results comply well with those experimental values that are thought to be the most reliable ones (the imaginary parts of the singlet and triplet scattering lengths and the real part of the coherent scattering length [28]).

Let us now consider phase shifts and inelasticity factors. The results of our calculations are presented in Figs. 1 and 2 for the spin-singlet state of the *nnpp* system and in Fig. 3 for its spin-triplet state. The energy is reckoned from the threshold of p^3H scattering in the c.m. frame. In Fig. 1, the phase shift for singlet p^3H scattering shows a distinct resonance behavior between the thresholds for ^{4}He breakup through the p^3H and n^3He channels. Available experimental data [30, 31] indicate that, in this energy region, the ^{4}He nucleus has a 0^+ resonance state. Thus, our calculations reproduce basic physical conditions under which the *nnpp* system has an above-threshold resonance state. The resonance energy, E_r, is determined as the value at which the function $d\delta/dE$ attains a maximum. The resonance width, Γ, is calculated by the formula $\Gamma = 2(d\delta/dE)^{-1}|_{E = E_r}$. The results of these calculations are displayed in Table 8. They comply well with the results of the RGM calculations of Vasilevsky *et al.* [4], who used the Nasagawa–Nagata potential, and with the experimental value from [30]. The phase shift for proton scattering on a ^{3}He nucleus shows a threshold anomaly at the proton energy of $E = 0.76$ MeV, which corresponds to the opening of the second scattering channel. The derivative of the phase shift has a discontinuity at this point. This is the well-known Baz' effect [4]. The third scattering channel, ^{3}H(p, d)d, is weakly coupled to the input channel (for dd scattering, the inelasticity factor is close to unity), and its effect on the phase shifts for p^3H and n^3He scatterings is negligibly small. The triplet phase shifts for n^3He and p^3H scatterings are shown in Fig. 3. It can be seen that these channels are coupled to each other only slightly as well. The inelasticity factors in triplet scattering are close to unity. By and large, our results comply qualitatively with the dependences obtained in [1–6] for the singlet and triplet phase shifts and inelasticity factors.

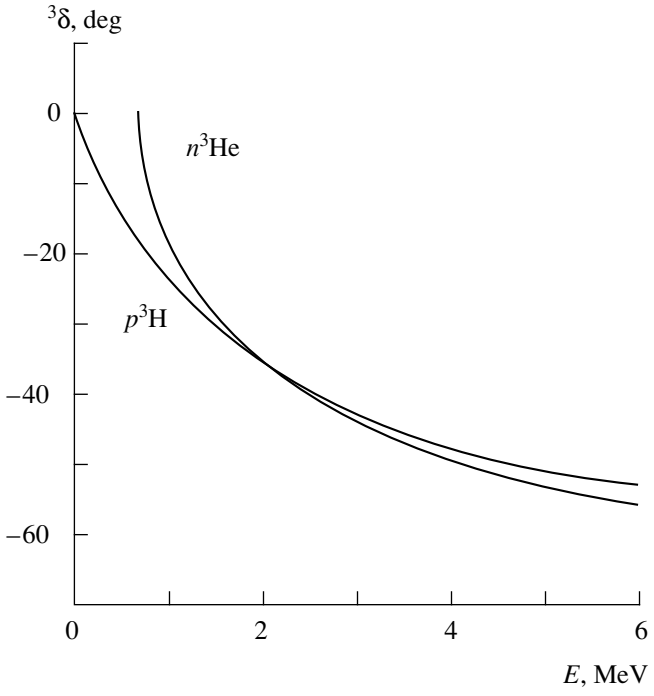

Fig. 3. Phase shifts for triplet scattering in the *nnpp* system.

Table 8. Features of the 0^+ resonance in the ^{4}He nucleus (the energy is reckoned from the threshold for ^{4}He breakup through the p^3H channel)

References	E_r, MeV	Γ, MeV
Our study	0.15	0.3
[4]	0.12	0.26
[27]	0.3 ± 0.05	0.27 ± 0.05

ACKNOWLEDGMENTS

This work was supported by the Russian Foundation for Basic Research (project no. 96-02-17021).

APPENDIX

Here, we present numerical matrices implementing the representation for the operators of particle permutations for the *s*-wave equations (5) determining the Yakubovsky components. For the $S = 1$ spin state of the system, the numerical matrices B_k, D, and C_k are given by

$$B_1 = \begin{pmatrix}
1/4 & 0 & -3/4 & & & & & \\
0 & -1/2 & 0 & & & 0 & & \\
-3/4 & 0 & 1/4 & & & & & \\
 & & & -1/2 & & & & \\
 & & & & 1/4 & 0 & -3/4 & 0 \\
 & 0 & & & 0 & -1/2 & 0 & 0 \\
 & & & & -3/4 & 0 & 1/4 & 0 \\
 & & & & 0 & 0 & 0 & -1/2
\end{pmatrix},$$

$$B_2 = \begin{pmatrix}
-1 & 0 & 0 & 0 & 0 & 0 & 0 & 0 \\
0 & 0 & 0 & 0 & 0 & 0 & 0 & 0 \\
0 & 0 & 0 & 0 & 0 & 0 & 0 & 0 \\
0 & 0 & 0 & 0 & 0 & 0 & 0 & 0 \\
0 & 0 & 0 & 0 & 0 & 0 & 0 & 0 \\
0 & 0 & 0 & 0 & 0 & 0 & 0 & 1 \\
0 & 0 & 0 & 0 & 0 & 0 & 0 & 0 \\
0 & 0 & 0 & 0 & 0 & 1 & 0 & 0
\end{pmatrix},$$

$$D = \begin{pmatrix}
0 & 0 & 1/2 & 1/(2\sqrt{2}) & 1/12 & \sqrt{2}/6 & 1/4 & -1/(2\sqrt{2}) \\
0 & 0 & 0 & 0 & -\sqrt{2}/6 & -1/6 & 0 & 0 \\
0 & 0 & -1/6 & -\sqrt{2}/12 & -1/4 & -1/\sqrt{2} & -1/12 & \sqrt{2}/12 \\
0 & 0 & \sqrt{2}/6 & -1/3 & 0 & 0 & -\sqrt{2}/6 & -1/6 \\
1/12 & \sqrt{2}/6 & 1/4 & -1/(2\sqrt{2}) & 0 & 0 & 1/2 & 1/(2\sqrt{2}) \\
-\sqrt{2}/6 & -1/6 & 0 & 0 & 0 & 0 & 0 & 0 \\
-1/4 & -1/\sqrt{2} & -1/22 & \sqrt{2}/12 & 0 & 0 & -1/6 & -\sqrt{2}/12 \\
0 & 0 & -\sqrt{2}/6 & -1/6 & 0 & 0 & \sqrt{2}/6 & -1/3
\end{pmatrix},$$

$$C_1 = \begin{pmatrix}
1/(2\sqrt{6}) & 0 & 0 & 0 & 0 & -1/(4\sqrt{3}) & 0 & 0 \\
-1/(2\sqrt{3}) & 0 & 0 & 0 & 0 & -1/(2\sqrt{6}) & 0 & 0 \\
-3/2\sqrt{6} & 0 & 0 & 0 & \sqrt{3}/4 & 0 & 0 & 0 \\
0 & 0 & 0 & 1/2 & 0 & 0 & 0 & -1/\sqrt{6} \\
1/(2\sqrt{6}) & 0 & 0 & 0 & 0 & 1/(4\sqrt{3}) & 0 & 0 \\
-1/(2\sqrt{3}) & 0 & 0 & 0 & 0 & 1/(2\sqrt{6}) & 0 & 0 \\
-3/2\sqrt{6} & 0 & 0 & 0 & -\sqrt{3}/4 & 0 & 0 & 0 \\
0 & 0 & 0 & 1/2 & 0 & 0 & 0 & 1/\sqrt{6}
\end{pmatrix},$$

$$C_2 = \begin{pmatrix} -2/\sqrt{6} & -1/\sqrt{3} & 0 & 0 & -2/\sqrt{6} & -1/\sqrt{3} & 0 & 0 \\ 0 & 0 & 0 & 0 & 0 & 0 & 0 & 0 \\ 0 & 0 & 0 & 0 & 0 & 0 & 0 & 0 \\ 0 & 0 & 0 & 0 & 0 & 0 & 0 & 0 \\ 0 & 0 & 0 & 0 & 0 & 0 & 0 & 0 \\ 0 & 0 & -1/\sqrt{3} & 2/\sqrt{6} & 0 & 0 & 1/\sqrt{3} & -2/\sqrt{6} \\ 0 & 0 & 0 & 0 & 0 & 0 & 0 & 0 \\ -1/\sqrt{3} & 2/\sqrt{6} & 0 & 0 & 1/\sqrt{3} & -2/\sqrt{6} & 0 & 0 \end{pmatrix}.$$

The representation matrices for the Coulomb potential, V_k^{Coul}, $k = 1, 2$, can be written as

$$V_1^{\mathrm{Coul}} = \begin{pmatrix} w_{11}^{(1)} & 0 & 0 & 0 & 0 & 0 & 0 & 0 \\ 0 & w_{11}^{(1)} & 0 & 0 & 0 & 0 & 0 & 0 \\ 0 & 0 & w_{33}^{(1)} & w_{34}^{(1)} & 0 & 0 & 0 & 0 \\ 0 & 0 & w_{34}^{(1)} & w_{44}^{(1)} & 0 & 0 & 0 & 0 \\ 0 & 0 & 0 & 0 & \bar{w}_{11}^{(1)} & 0 & 0 & 0 \\ 0 & 0 & 0 & 0 & 0 & \bar{w}_{11}^{(1)} & 0 & 0 \\ 0 & 0 & 0 & 0 & 0 & 0 & \bar{w}_{33}^{(1)} & \bar{w}_{34}^{(1)} \\ 0 & 0 & 0 & 0 & 0 & 0 & \bar{w}_{34}^{(1)} & \bar{w}_{44}^{(1)} \end{pmatrix},$$

where

$$w_{33}^{(1)} = \frac{2n}{3x} + v_2^{(1)}/3, \quad w_{44}^{(1)} = \frac{1}{3}\left(\frac{n}{x} + 2v_2^{(1)}\right),$$

$$w_{34}^{(1)} = \frac{\sqrt{2}}{3}\left(\frac{n}{x} - v_2^{(1)}\right), \quad w_{11}^{(1)} = v_2^{(1)},$$

$$\bar{w}_{33}^{(1)} = \frac{2}{3}v_6^{(1)} + v_4^{(1)}/3, \quad \bar{w}_{44}^{(1)} = \frac{1}{3}(v_6^{(1)} + 2v_4^{(1)}),$$

$$\bar{w}_{34}^{(1)} = \frac{\sqrt{2}}{3}(v_6^{(1)} - v_4^{(1)}), \quad \bar{w}_{11}^{(1)} = v_4^{(1)};$$

$$V_2^{\mathrm{Coul}} = \begin{pmatrix} w_{11}^{(2)} & 0 & 0 & 0 & 0 & 0 & 0 & 0 \\ 0 & w_{11}^{(2)} & 0 & 0 & 0 & 0 & 0 & 0 \\ 0 & 0 & w_{33}^{(2)} & w_{34}^{(2)} & 0 & 0 & w_{37}^{(2)} & 0 \\ 0 & 0 & w_{34}^{(2)} & w_{44}^{(2)} & 0 & 0 & w_{47}^{(2)} & 0 \\ 0 & 0 & 0 & 0 & w_{11}^{(2)} & 0 & 0 & 0 \\ 0 & 0 & 0 & 0 & 0 & w_{11}^{(2)} & 0 & 0 \\ 0 & 0 & w_{37}^{(2)} & w_{47}^{(2)} & 0 & 0 & w_{77}^{(2)} & 0 \\ 0 & 0 & 0 & 0 & 0 & 0 & 0 & w_{11}^{(2)} \end{pmatrix},$$

where

$$w_{33}^{(2)} = \frac{1}{3}\left(\frac{n}{x} + \frac{n}{y} + v_2^{(2)}\right), \quad w_{34}^{(2)} = \frac{\sqrt{2}}{6}\left(\frac{n}{x} + \frac{n}{y} - 2v_2^{(2)}\right),$$

$$w_{44}^{(2)} = \frac{1}{6}\left(\frac{n}{x} + \frac{n}{y} + 4v_2^{(2)}\right), \quad w_{11}^{(2)} = v_2^{(2)},$$

$$w_{77}^{(2)} = \frac{1}{2}\left(\frac{n}{x} + \frac{n}{y}\right), \quad w_{37}^{(2)} = \frac{1}{\sqrt{6}}\left(\frac{n}{x} - \frac{n}{y}\right),$$

$$w_{47}^{(2)} = \frac{\sqrt{3}}{6}\left(\frac{n}{x} - \frac{n}{y}\right),$$

$$v_2^{(1)} = n\begin{cases} 2/x & \text{for } x > 2y \\ 1/y & \text{for } x < 2y, \end{cases}$$

$$v_4^{(1)} = n\begin{cases} \dfrac{1}{z} & \text{for } z > \dfrac{x}{2} + \dfrac{y}{3} \\ \dfrac{1}{xy}\left(\dfrac{2}{3}\dfrac{1}{z}\left(z^2 - \left(\dfrac{3}{4}x - \dfrac{1}{2}y\right)^2\right) + 2\left(\dfrac{3}{4}x + \dfrac{1}{2}y - z\right)\right) & \text{for } \left|\dfrac{1}{2}x - \dfrac{1}{3}y\right| < z < \dfrac{1}{2}x + \dfrac{1}{3}y \\ \dfrac{2}{x} & \text{for } x > \dfrac{2}{3}y, \quad z < \left|\dfrac{1}{2}x - \dfrac{1}{3}y\right| \\ \dfrac{3}{y} & \text{for } x < \dfrac{2}{3}y, \quad z < \left|\dfrac{1}{2}x - \dfrac{1}{3}y\right|, \end{cases}$$

$$v_6^{(1)} = n\begin{cases} \dfrac{1}{z} & \text{for } x > \dfrac{2}{3}y \\ \dfrac{3}{2}\dfrac{1}{y} & \text{for } x < \dfrac{3}{2}y, \end{cases}$$

$$v_2^{(2)} = n\begin{cases} \dfrac{1}{z} \ \text{for} \ z > \dfrac{x+y}{2} \\ \dfrac{1}{xy}\left(-\dfrac{1}{z}\left(\left(\dfrac{x-y}{2}\right)^2 + x + y - z\right)\right) \\ \quad \text{for} \ \left|\dfrac{x-y}{2}\right| < z < \dfrac{x+y}{2} \\ \dfrac{2}{x} \ \text{for} \ x > y, \quad z < \left|\dfrac{x-y}{2}\right| \\ \dfrac{2}{y} \ \text{for} \ x < y, \quad z < \left|\dfrac{x-y}{2}\right|. \end{cases}$$

For the spin-singlet state of the system, we further present explicit expressions for the operators $V_k(x)$ and for the numerical matrices B_k, C_k, and D ($k = 1, 2$). The operators $V_k(x)$ are diagonal, and their matrices have the form

$$V_k(x) = \mathrm{diag}\{V^{\mathrm{s}}(x), V^{\mathrm{s}}(x), V^{\mathrm{t}}(x), V^{\mathrm{s}}(x), V^{\mathrm{s}}(x), V^{\mathrm{t}}(x)\}.$$

The 6×6 numerical matrices B_k, D, and C_k, $k = 1, 2$, are then given by

$$B_1 = \begin{pmatrix} 1/4 & 0 & -3/4 & 0 & 0 & 0 \\ 0 & -1/2 & 0 & 0 & 0 & 0 \\ -3/4 & 0 & 1/4 & 0 & 0 & 0 \\ 0 & 0 & 0 & 1/4 & 0 & -3/4 \\ 0 & 0 & 0 & 0 & -1/2 & 0 \\ 0 & 0 & 0 & -3/4 & 0 & 1/4 \end{pmatrix},$$

$$B_2 = \begin{pmatrix} 1 & 0 & 0 & 0 & 0 & 0 \\ 0 & 1 & 0 & 0 & 0 & 0 \\ 0 & 0 & 1 & 0 & 0 & 0 \\ 0 & 0 & 0 & -1 & 0 & 0 \\ 0 & 0 & 0 & 0 & 0 & 0 \\ 0 & 0 & 0 & 0 & 0 & 0 \end{pmatrix},$$

$$D = \begin{pmatrix} 1/6 & \sqrt{2}/6 & 0 & 1/12 & -\sqrt{2}/12 & -3/4 \\ -\sqrt{2}/6 & -1/6 & 0 & \sqrt{2}/6 & -1/3 & 0 \\ -1/2 & -1/(2\sqrt{2}) & 0 & -1/4 & 1/(2\sqrt{2}) & 1/4 \\ 1/12 & -\sqrt{2}/12 & -3/4 & 1/6 & \sqrt{2}/12 & 0 \\ \sqrt{2}/6 & -1/3 & 0 & -\sqrt{2}/6 & -1/6 & 0 \\ -1/4 & 1/(2\sqrt{2}) & 1/4 & -1/2 & -1/(2\sqrt{2}) & 0 \end{pmatrix},$$

$$C_1 = \begin{pmatrix} 1/4 & 0 & -3/4 & 1/2\sqrt{6} & 0 & 0 \\ 0 & -1/2 & 0 & -1/2\sqrt{3} & 0 & 0 \\ -3/4 & 0 & 1/4 & -3/2\sqrt{6} & 0 & 0 \\ 1/4 & 0 & -3/4 & -1/2\sqrt{6} & 0 & 0 \\ 0 & -1/2 & 0 & 1/2\sqrt{3} & 0 & 0 \\ -3/4 & 0 & 1/4 & 3/2\sqrt{6} & 0 & 0 \end{pmatrix},$$

$$C_2 = \begin{pmatrix} 1 & 0 & 0 & 1 & 0 & 0 \\ 0 & 1 & 0 & 0 & 1 & 0 \\ 0 & 0 & 1 & 0 & 0 & 1 \\ -2/\sqrt{6} & -1/\sqrt{3} & 0 & 2/\sqrt{6} & 1/\sqrt{3} & 0 \\ 0 & 0 & 0 & 0 & 0 & 0 \\ 0 & 0 & 0 & 0 & 0 & 0 \end{pmatrix}.$$

The representation matrices for the Coulomb potential, V_k^{Coul}, $k = 1, 2$, can be written as

$$V_1^{\mathrm{Coul}} = \begin{pmatrix} w_{11}^{(1)} & w_{12}^{(1)} & 0 & 0 & 0 & 0 \\ w_{12}^{(1)} & w_{22}^{(1)} & 0 & 0 & 0 & \\ 0 & 0 & w_{33}^{(1)} & 0 & 0 & 0 \\ 0 & 0 & 0 & \bar{w}_{11}^{(1)} & \bar{w}_{12}^{(1)} & 0 \\ 0 & 0 & 0 & \bar{w}_{12}^{(1)} & \bar{w}_{22}^{(1)} & 0 \\ 0 & 0 & 0 & 0 & 0 & \bar{w}_{33}^{(1)} \end{pmatrix},$$

where

$$w_{11}^{(1)} = \frac{2}{3}\frac{n}{x} + v_2^{(1)}/3, \quad w_{22}^{(1)} = \frac{1}{3}\left(\frac{n}{x} + 2v_2^{(1)}\right),$$

$$w_{12}^{(1)} = \frac{\sqrt{2}}{3}\left(\frac{n}{x} - v_2^{(1)}\right), \quad w_{33}^{(1)} = v_2^{(1)},$$

$$\bar{w}_{11}^{(1)} = \frac{2}{3}v_6^{(1)} + v_4^{(1)}/3, \quad \bar{w}_{22}^{(1)} = \frac{1}{3}(v_6^{(1)} + 2v_4^{(1)}),$$

$$\bar{w}_{12}^{(1)} = \frac{\sqrt{2}}{3}(v_6^{(1)} - v_4^{(1)}), \quad \bar{w}_{33}^{(1)} = v_4^{(1)};$$

$$V_2^{\mathrm{Coul}} = \begin{pmatrix} w_{11}^{(2)} & w_{12}^{(2)} & 0 & w_{14}^{(2)} & 0 & 0 \\ w_{12}^{(2)} & w_{22}^{(2)} & 0 & w_{24}^{(2)} & 0 & 0 \\ 0 & 0 & w_{33}^{(2)} & 0 & 0 & w_{33}^{(2)} \\ w_{14}^{(2)} & w_{24}^{(2)} & 0 & w_{44}^{(2)} & 0 & 0 \\ 0 & 0 & 0 & 0 & w_{33}^{(2)} & 0 \\ 0 & 0 & w_{33}^{(2)} & 0 & 0 & w_{33}^{(2)} \end{pmatrix},$$

where

$$w_{11}^{(2)} = \frac{1}{3}\left(\frac{n}{x} + \frac{n}{y} + v_2^{(2)}\right), \quad w_{12}^{(2)} = \frac{\sqrt{2}}{6}\left(\frac{n}{x} + \frac{n}{y} - 2v_2^{(2)}\right),$$

$$w_{22}^{(2)} = \frac{1}{6}\left(\frac{n}{x} + \frac{n}{y} + 4v_2^{(2)}\right), \quad w_{33}^{(2)} = v_2^{(2)}$$

$$w_{44}^{(2)} = \frac{1}{2}\left(\frac{n}{x} + \frac{n}{y}\right), \quad w_{14}^{(2)} = \frac{1}{\sqrt{6}}\left(\frac{n}{x} - \frac{n}{y}\right),$$

$$w_{24}^{(2)} = \frac{\sqrt{3}}{6}\left(\frac{n}{x} - \frac{n}{y}\right).$$

REFERENCES

1. D. R. Thompson, Nucl. Phys. A **143**, 304 (1970).
2. H. M. Hofman, W. Zahn, and H. Stowe, Nucl. Phys. A **357**, 139 (1981).
3. H. Kanada, T. Kaneko, and Y. C. Tang, Phys. Rev. C **34**, 22 (1986).
4. V. C.Vasilevskiĭ, T. N. Kovalenko, and G. F. Filippov, Yad. Fiz. **48**, 346 (1988) [Sov. J. Nucl. Phys. **48**, 217 (1988)].
5. V. C.Vasilevskiĭ, I. Yu. Rybkin, and G. F. Filippov, Yad. Fiz. **51**, 112 (1990) [Sov. J. Nucl. Phys. **51**, 71 (1990)].
6. S. B. Dubovichenko, Yad. Fiz. **58**, 1973 (1995) [Phys. At. Nucl. **58**, 1866 (1995)].
7. L. D. Faddeev, Zh. Éksp. Teor. Fiz. **39**, 1459 (1961) [Sov. Phys. JETP **12**, 1014 (1961)].
8. O. A. Yakubovsky, Yad. Fiz. **5**, 1312 (1966) [Sov. J. Nucl. Phys. **5**, 937 (1966)].
9. J. A. Tjon, Phys. Lett. B **56**, 217 (1975); **63**, 391 (1976).
10. H. Kröger and W. Sandhas, Phys. Rev. Lett. **40**, 834 (1978).
11. V. F. Kharchenko, Fiz. Élem. Chastits At. Yadra **10**, 884 (1979) [Sov. J. Part. Nucl. **10**, 349 (1979)].
12. V. P. Levashev, Yad. Fiz. **38**, 566 (1983) [Sov. J. Nucl. Phys. **38**, 336 (1983)].
13. A. C. Fonseca, Phys. Rev. C **30**, 35 (1984); Few-Body Syst. **1**, 69 (1986).
14. S. P. Merkuriev and S. L. Yakovlev, Dokl. Akad. Nauk SSSR **262**, 591 (1982); Teor. Mat. Fiz. **56**, 60 (1983); S. P. Merkuriev and L. D. Faddeev, *Quantum Scattering Theory for Few-Body Systems* (Nauka, Moscow, 1985).
15. S. P. Merkuriev and S. L. Yakovlev, Yad. Fiz. **39**, 1580 (1984) [Sov. J. Nucl. Phys. **39**, 1002 (1984)]; S. P. Merkuriev, S. L. Yakovlev, and C. Gignoux, Nucl. Phys. A **431**, 125 (1984).
16. A. A. Kvitsinskiĭ, Yu. A. Kuperin, *et al.*, Fiz. Élem. Chastits At. Yadra **17**, 267 (1986).
17. S. L. Yakovlev and I. N. Filikhin, Yad. Fiz. **56** (12), 98 (1993) [Phys. At. Nucl. **56**, 1676 (1993)]; Vestn. S.-Peterb. Univ., Ser. 4: Fiz. Khim., No. 3, 24 (1992).
18. S. L. Yakovlev and I. N. Filikhin, Yad. Fiz. **58**, 817 (1995) [Phys. At. Nucl. **58**, 754 (1995)].
19. S. L. Yakovlev and I. N. Filikhin, Yad. Fiz. **60**, 1962 (1997) [Phys. At. Nucl. **60**, 1794 (1997)].
20. S. L. Yakovlev and I. N. Filikhin, Yad. Fiz. **62**, 1585 (1999) [Phys. At. Nucl. **62**, 1490 (1999)].
21. R. A. Malfliet and J. A. Tjon, Ann. Phys. (N.Y.) **61**, 425 (1970).
22. N. W. Schelligerhout, J. J. Schut, and L. P. Kok, Phys. Rev. C **46**, 1192 (1992).
23. S. L. Yakovlev, Teor. Mat. Fiz. **102**, 323 (1995); **107**, 513 (1996).
24. V. A. Rudnev and S. L. Yakovlev, Yad. Fiz. **58**, 1762 (1995) [Phys. At. Nucl. **58**, 1662 (1995)].
25. V. B. Belyaev and V. V. Pupyshev, Yad. Fiz. **35**, 905 (1982) [Sov. J. Nucl. Phys. **35**, 526 (1982)].
26. V. F. Sears and F. C. Khanna, Phys. Lett. B **56**, 1 (1975).
27. J. Als-Nielsen and O. Dietrich, Phys. Rev. B **133**, 925 (1964).
28. H. Kaiser *et al.*, Phys. Lett. B **71**, 321 (1977).
29. V. P. Alfimenkov *et al.*, Yad. Fiz. **33**, 33 (1981) [Sov. J. Nucl. Phys. **33**, 467 (1981)].
30. S. Firman and W. E. Meyerhof, Nucl. Phys. A **206**, 1 (1973).
31. G. Kobschal *et al.*, Nucl. Phys. A **405**, 648 (1983).

Translated by A. Isaakyan

Physics of Atomic Nuclei, Vol. 63, No. 1, 2000, pp. 69–75. Translated from Yadernaya Fizika, Vol. 63, No. 1, 2000, pp. 79–86.

NUCLEI
Theory

Solving the Differential Yakubovsky Equations for p^3He Scattering by the Cluster-Reduction Method

I. N. Filikhin and S. L. Yakovlev*

St. Petersburg State University, Universitetskaya nab. 7/9, St. Petersburg, 199164 Russia

Received July 1, 1998; in final form, December 16, 1998

Abstract—The cluster-reduction method has been used to solve numerically the differential equations for the *s*-wave Yakubovsky components in the *nppp* system. Proton scattering on a ^{3}He nucleus has been considered for energies below the three-body threshold in the singlet and triplet spin states of the system. Nucleon–nucleon interaction has been simulated by the MT I–III potential, and the Coulomb interaction between the protons has been taken into account. Effective equations that describe the relative motion of clusters have been derived. The low-energy behavior of phase shifts has been analyzed. The values of ^1A = 8.2 fm and ^3A = 7.7 fm have been obtained for, respectively, the singlet and triplet scattering lengths. The calculated phase shifts agree well with experimental data. © *2000 MAIK "Nauka/Interperiodica".*

1. INTRODUCTION

The Yakubovsky equations [1] have long since been used to analyze scattering in four-nucleon systems [2–5]. The majority of authors employed the integral form of these equations and, for this reason, disregarded the Coulomb interaction of protons. Only for the *nnnp* system, which features no Coulomb interaction, could theoretical results obtained in [2–5] therefore be directly compared with experimental data. It is obvious that a consistent analysis of systems like *nnpp* and *nppp* is impossible without taking into account Coulomb interaction. The differential form of the Faddeev–Yakubovsky equations [6] admits a rather straightforward inclusion of the Coulomb interaction in the general scheme of analysis. For example, the characteristics of low-energy scattering in the *nnpp* system were calculated in [7] on the basis of the differential equations for the Yakubovsky components. This was done by the cluster-reduction method proposed in [8]. In the present study, we apply this method to the problem of low-energy scattering in the *nppp* system.

We note that, even in the simplest case of the *s*-wave approximation, the inclusion of Coulomb interaction in the equations for the Yakubovsky components leads to cumbersome sets of integro-differential equations. Such sets can be solved directly only with a supercomputer. The approach based on the cluster reduction of these equations makes it possible to construct numerical solutions to reduced equations by means of conventional computer facilities. The method essentially consists in expanding the sought solution of the original set of equations in the basis formed by the components of the eigenfunctions of the Hamiltonians of the three-body subsystems. Upon such an expansion, the original set of equations is diagonalized partly, which reduces considerably the machine time required for solving it. Here, we analyze scattering in the singlet (S = 0) and triplet (S = 1) spin states of the p^3He system in the *s*-wave approximation. The nucleon–nucleon interaction is described by the MT I–III potentials [9] modified as in [10].

The ensuing exposition is organized as follows. In Section 2, we present the equations for the Yakubovsky components describing the system of identical fermions and the results of a spin–isospin analysis of these equations, consider the *s*-wave approximation, and formulate the boundary-value problems corresponding to elastic two-cluster scattering in the *nppp* system. The explanation of the cluster-reduction procedure for the equations from Section 2 and effective equations describing the relative motion of clusters can be found in Section 3. Numerical solutions of these effective equations are described in Section 4. There, we display the low-energy behavior of the singlet and triplet phase shifts, which were obtained by numerically solving the effective equations for the functions describing the relative motion of the clusters. In addition, we compare the resulting theoretical values of the phase shifts with experimental data and analyze the convergence of our numerical algorithm. We also present the calculated scattering lengths for proton interaction with the ^{3}He nucleus in the singlet and triplet states.

2. DIFFERENTIAL EQUATIONS FOR THE YAKUBOVSKY COMPONENTS IN THE *nppp* SYSTEM

In order to describe the *nppp* system in configuration space, we use modified differential equations for the Yakubovsky components where the Coulomb inter-

* e-mail: yakovlev@snoopy.phys.spbu.ru

Table 1. Components of the spin–isospin bases for the 3 + 1 type of clustering and corresponding states of the *nppp* system

Basis components	S_{12}	T_{12}	S_{123}	T_{123}	S	T
$e_1^{(1)}$	0	1	1/2	1/2	0	1
$e_2^{(1)}$	1	0	1/2	1/2	0	1
$e_1^{(1)}$	0	1	1/2	1/2	1	1
$e_2^{(1)}$	1	0	1/2	1/2	1	1

action V^{Coul} is included in the unperturbed Hamiltonian [11]. We have

$$\begin{aligned}(H_0 + V^{\mathrm{Coul}} + V - E)U_1 + V(P_4^+ + P_4^-)U_1 \\ = -V[(P_1^+ - P^+)U_1 + (P_1^+ + P_4^+)U_2], \\ (H_0 + V^{\mathrm{Coul}} + V - E)U_2 + V(P^+P^+)U_2 \\ = -V[(P^+ - P_1^+)P^+U_1],\end{aligned} \tag{1}$$

where H_0 is the kinetic-energy operator, V is the pair potential of nuclear interaction, $P^{\pm}$ stands for the operators of the cyclic permutation of four particles, and $P_i^{\pm}$ stands for the operators of the cyclic permutation of three particles (the subscript i indicates a particle that is not involved in a given permutation). The components U_i are spinors in the linear spin–isospin space of the system, where the subscript values of $i = 1$ and 2 specify components corresponding to the 3 + 1 and 2 + 2 types of clustering, respectively. The coordinate dependence of the components is described by using relative Jacobi coordinates. For $i = 1$ and 2, these coordinates are determined in terms of the particle radius vectors $\mathbf{r}_i$ as

$$\begin{aligned}\mathbf{x}_1 = \mathbf{r}_2 - \mathbf{r}_1, \quad \mathbf{y}_1 = (\mathbf{r}_1 + \mathbf{r}_2)/2 - \mathbf{r}_3, \\ \mathbf{z}_1 = (\mathbf{r}_1 + \mathbf{r}_2 + \mathbf{r}_3)/3 - \mathbf{r}_4, \quad \mathbf{x}_2 = \mathbf{r}_2 - \mathbf{r}_1, \\ \mathbf{y}_2 = \mathbf{r}_4 - \mathbf{r}_3, \quad \mathbf{z}_2 = (\mathbf{r}_1 + \mathbf{r}_2)/2 - (\mathbf{r}_3 + \mathbf{r}_4)/2.\end{aligned}$$

For nucleon–nucleon interaction, we take the MT I–III potential [9], which has only a central component. The four-body system *nppp* is obtained from the *nnnp* system by means of a mirror-symmetry transformation. Since these systems are identical within the isospin formalism, the spin–isospin analysis of the equations for the Yakubovsky components that was performed in the first reference from [8] is applicable to the *nppp* system as well. However, the Coulomb potential is added here to the nuclear-interaction potential. For this reason, the representations of the Coulomb interaction operators in the spin–isospin bases must be derived for the above two types of clustering. The Coulomb potential is specified as

$$V^{\mathrm{Coul}} = \sum_{j>i} V_{ji} \frac{(1 + 2\tau_i^z)(1 + 2\tau_j^z)}{4},$$

where τ_i^z is the isospin-projection operator for the ith particle, while $V_{ji} = n/|\mathbf{x}_{ji}|$ with $\mathbf{x}_{ji} = \mathbf{r}_j - \mathbf{r}_i$ and $n = me^2/\hbar^2$, m being the nucleon mass.

Omitting intermediate manipulations, which can be found in [8], we go over to the differential equations for the s-wave Yakubovsky components. There are four equations for the components $\mathcal{U}_i^k$, $k = 1, 2$ and $i = 1, 2$, in the case where $S = 1$ and three equations for the components $\mathcal{U}_i^1$, $i = 1, 2$, and $\mathcal{U}_1^2$ in the case where $S = 0$. Specifically, we have

$$\begin{aligned}(h_0^1 + V_1(x) - \varepsilon)\mathcal{U}^1(x, y, z) \\ + V_1(x)\int_{-1}^{1} dv \frac{xy}{x_1y_1} B_1 \mathcal{U}^1(x_1, y_1, z_1) + \mathcal{W}_1\mathcal{U}^1(x, y, z) \\ = -\frac{1}{2}V_1(x)\int_{-1}^{1} du \int_{-1}^{1} dv \left\{ \frac{xyz}{x_2y_2z_2} D\mathcal{U}^1(x_2, y_2, z_2) \right. \\ \left. + \frac{xyz}{x_3y_3z_3} C_1 \mathcal{U}^2(x_3, y_3, z_3) \right\},\end{aligned} \tag{2}$$

$$\begin{aligned}(h_0^2 + V_2(x) - \varepsilon)\mathcal{U}^2(x, y, z) \\ + V_2(x)B_2\mathcal{U}^2(x, y, z) + \mathcal{W}_2\mathcal{U}^2(x, y, z) \\ = -\frac{1}{2}V_2(x)\int_{-1}^{1} dv \frac{xyz}{x_4y_4z_4} C_2 \mathcal{U}^1(x_4, y_4, z_4).\end{aligned}$$

Here, $\varepsilon = (m/\hbar^2)E$; $V_k = (m/\hbar^2)\langle k|V|k\rangle$ is the representation of the nuclear interaction in the spin–isospin bases; $\mathcal{W}_1 = W_1 + \overline{W}_1$, where the first term is dependent on the intracluster coordinates x and y, while the second term is dependent on these coordinates and additionally on the intercluster coordinate z, is the representation matrix of the Coulomb interaction; and $B_1 = \langle 1|P_4^+ + P_1^-|1\rangle$, $D = \langle 1|P_1^+ - P^+|1\rangle$, $B_2 = \langle 2|P^+P^+|2\rangle$, $C_1 = \langle 1|P_1^+ + P_4^+|2\rangle$, and $C_2 = \langle 2|P^+ - P_1^+|1\rangle$ are numerical matrices that are generated by the spin–isospin representations of the permutation operators appearing in equations (1). For the singlet and triplet spin states of the *nppp* system, these matrices are presented explicitly in the Appendix. For two possible schemes of coupling of spin and isospin moments, Tables 1 and 2 establish the correspondence between their components and nontriv-

ial quantum numbers of the system and subsystems. The operators h_0^k are given by

$$h_0^1 = -\left(\partial_x^2 + \frac{3}{4}\partial_y^2 + \frac{2}{3}\partial_z^2\right),$$

$$h_0^2 = -\left(\partial_x^2 + \partial_y^2 + \frac{1}{2}\partial_z^2\right).$$

The coordinates x_l, y_l, and z_l, where $l = 1, 2, 3, 4$, which appear in the integral terms of equations (2), are obtained by transforming the relative coordinates x, y, and z with the aid of the corresponding particle-permutation operators. These coordinates are given by

$$x_1 = \left[\frac{x^2}{4} + y^2 - xyv\right]^{1/2},$$

$$y_1 = \left[\left(\frac{3x}{4}\right)^2 + \frac{y^2}{4} + \frac{3}{4}xyv\right]^{1/2},$$

$$x_2 = x_1, \quad x_3 = x_1, \quad x_4 = y,$$

$$y_2 = \left[\left(\frac{y_1}{3}\right)^2 + z^2 + \frac{2}{3}y_1zu\right]^{1/2},$$

$$z_2 = \left[\left(\frac{8y_1}{9}\right)^2 + \frac{z^2}{9} - \frac{16}{27}y_1zu\right]^{1/2},$$

$$y_3 = \left[\left(\frac{2y_1}{3}\right)^2 + z^2 + \frac{4}{3}y_1zu\right]^{1/2},$$

$$z_3 = \left[\left(\frac{2y_1}{3}\right)^2 + \frac{z^2}{4} - \frac{2}{3}y_1zu\right]^{1/2},$$

$$y_4 = \left[\left(\frac{x}{2}\right)^2 + z^2 - xzv\right]^{1/2},$$

$$z_4 = \frac{2}{3}[x^2 + z^2 + 2xzv]^{1/2}.$$

The set of equations (2) is supplemented with asymptotic boundary conditions. We denote by $\mathcal{U}_i^k(x, y, z)$, $k = 1, 2$ and $i = 1, 2, \ldots, n$ ($n = 2$ for the triplet spin state; for the singlet spin state, $n = 2$ and 1 at $k = 1$ and 2, respectively), the column vector of the coordinate parts of the s-wave Yakubovsky components. We impose the boundary condition $\mathcal{U}_i^k(0, 0, 0) = 0$. When elastic scattering is the only open channel, the asymptotic boundary conditions for low-energy s-wave p^3He scattering for $z \longrightarrow \infty$ are written as

$$\mathcal{U}^1(x, y, z) \sim \Phi_h(x, y)[\chi_p(z) + \tan({}^1\delta)G_0(\eta, p)], \qquad \mathcal{U}^2(x, y, z) \sim 0 \tag{3}$$

Table 2. Components of the spin–isospin bases for the 2 + 2 type of clustering and corresponding states of the *nppp* system

Basis components	S_{12}	T_{12}	S_{34}	T_{34}	S	T
$e_1^{(2)}$	0	1	0	1	0	1
$e_1^{(2)}$	0	1	1	0	1	1
$e_2^{(2)}$	1	0	0	1	1	1

for the singlet spin state and as

$$\mathcal{U}^1(x, y, z) \sim \Phi_h(x, y)[\chi_p(z) + \tan({}^3\delta)G_0(\eta, p)], \qquad \mathcal{U}^2(x, y, z) \sim (0, 0)^T \tag{4}$$

for the triplet spin state. Here, $\Phi_h(x, y)$ stands for the coordinate parts of the Faddeev component of the wave function of the ground-state ^{3}He nucleus; the function $\chi_p(z) = F_0(\eta, pz)$ [$F_0(\eta, pz)$ is the regular Coulomb function, its irregular counterpart being $G_0(\eta, pz)$] describes the asymptotically free state of our system; and $\eta = (3/4)n/p$ is the Coulomb parameter.

3. CLUSTER REDUCTION

In the case under consideration, the general scheme [8] for reducing the equations for the Yakubovsky components is as follows. The components $\mathcal{U}^i$ are represented as the expansions

$$\mathcal{U}^i(x, y, z) = \sum_{l=0}^{\infty} \phi_l^i(x, y)F_l^i(z), \quad i = 1, 2, \tag{5}$$

where the basis functions ϕ_l^i are solutions to the following s-wave Faddeev equations for the subsystems corresponding to clustering of the 3 + 1 ($i = 1$) and 2 + 2 ($i = 2$) types:

$$\left\{-\partial_x^2 - \frac{3}{4}\partial_y^2 + V_1(x) + W_1(x, y)\right\}\phi_l^1(x, y) + V_1(x)\int_{-1}^{1} dv\,\frac{xy}{x_1y_1}B_1\phi_l^1(x_1, y_1) = \varepsilon_1^l\phi_l^1(x, y),$$
$$\{-\partial_x^2 - \partial_y^2 + V_2(x) + W_2(x, y)\}\phi_l^2(x, y) + V_2(x)B_2\phi_l^2(y, x) = \varepsilon_2^l\phi_l^2(x, y). \tag{6}$$

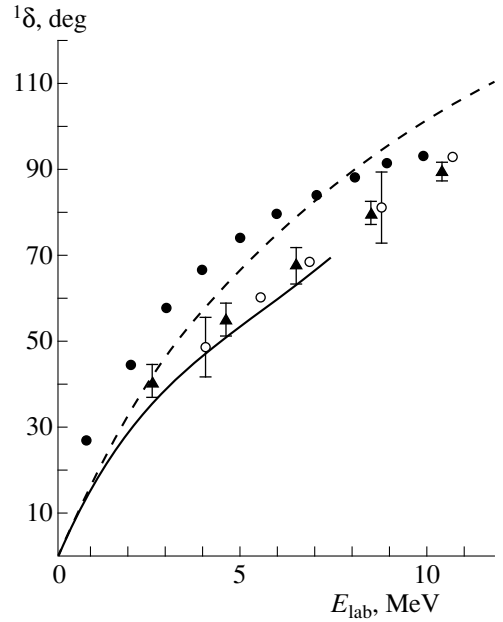

Fig. 1. Phase shift $^1\delta$ for singlet *s*-wave p^3He scattering as calculated in (solid curve) this study and (dashed curve) [17]. Experimental data were taken from (open circles) [14], (triangles) [15], and (solid circles) [16].

The set of functions $\{\phi_l^i\}$ biorthogonal to the set $\{\psi_l^i\}$ involves the eigenfunctions of the equations [12, 13]

$$\left\{-\partial_x^2 - \frac{3}{4}\partial_y^2 + V_1(x) + W_1(x,y)\right\}\psi_l^1(x,y)$$
$$+ \int_{-1}^{1} dv \frac{xy}{x_1 y_1} B_1 V_1(x_1)\psi_l^1(x_1,y_1) = \varepsilon_1^l \psi_l^1(x,y),$$
$$\{-\partial_x^2 - \partial_y^2 + V_2(x) + W_2(x,y)\}\psi_l^2(x,y)$$
$$+ B_2 V_2(y)\psi_l^2(y,x) = \varepsilon_2^l \psi_l^2(x,y),$$

which are conjugate to equations (6).

Substituting expansions (5) into equations (2) and taking projections onto the elements of the conjugate basis $\{\psi_l^i\}$, we find that the functions $F_l^i(z)$ describing the relative motion of the clusters satisfy the set of integro-differential equations

$$\left\{-\frac{2}{3}\partial_z^2 + \varepsilon_1^l - E\right\}F_l^1(z) + \sum_{k=0}^{\infty}\langle\psi_l^1|\overline{W}_1|\phi_k^1\rangle F_k^1(z)$$
$$= -\frac{1}{2}\sum_{k=0}^{\infty}\left\langle\psi_l^1(x,y)|V_1(x)\int_{-1}^{1}du\int_{-1}^{1}dv\left\{\frac{xyz}{x_2y_2z_2}D\right.\right.$$
$$\left.\left.\times\phi_k^1(x_2,y_2)F_k^1(z_2) + \frac{xyz}{x_3y_3z_3}C_1\phi_k^2(x_3,y_3)F_k^2(z_3)\right\}\right\rangle, \quad (7)$$

$$\{-\partial_z^2 + \varepsilon_2^l - E\}F_l^2(z) + \sum_{k=0}^{\infty}\langle\psi_l^2|\overline{W}_2|\phi_k^2\rangle F_k^2(z) = -\frac{1}{2}$$
$$\times\sum_{k=0}^{\infty}\left\langle\psi_l^2(x,y)\Big|V_2(x)\int_{-1}^{1}dv\frac{xyz}{x_4y_4z_4}C_2\phi_k^1(x_4,y_4)F_k^1(z_4)\right\rangle,$$

where the symbol $\langle\ldots|\ldots\rangle$ denotes integration with respect to the variables *x* and *y*. The number of equations in the above set is determined by the number of terms that are retained in expansions (5). In numerically solving these equations, we have to take into account a finite number of such terms. The boundary conditions for the functions $F_l^i(z)$ are obtained by taking the projections of formulas (3) and (4).

4. RESULTS OF THE CALCULATIONS

Equations (7) for the functions of relative motion will be solved numerically by a finite-difference technique on an equidistant grid in the relative coordinate *z*. In this coordinate, we denote by R_z the radius at which we impose the asymptotic boundary conditions (3) and (4), by N_z the number of grid nodes in the coordinate *z*, and by *N* the number of terms retained in expansions (5). The value of *N* determines the efficiency of the cluster-reduction method. The values of R_z = 20 fm, N_z = 25, and *N* = 14 ensure a precision not poorer than 1% in the calculations for the singlet and triplet spin states.

Let us now discuss the results of four-body calculations. In Figs. 1 and 2, the calculated *s*-wave phase shifts for singlet and triplet p^3He scattering are contrasted against relevant experimental data. The results are presented as functions of the laboratory energy measured from the threshold of p^3He scattering. The scattering phase shifts calculated here agree well with experimental data from [14–16]. The dashed curves represent the results obtained in [17] on the basis of available experimental data analyzed by using a modified effective-range expansion.

A problem that deserves a dedicated consideration is that of the number *N* of terms that must retained in expansion (5) for the results to be convergent. The calculated singlet phase shift for p^3He scattering is presented in Table 3 versus *N* for some energy values. It can be seen that even the first term (*N* = 1) in expansions (5) saturates no less than 85% of the result. This suggests a high degree of clustering in the system. It should also be noted that the rate of convergence in *N* depends on energy. As the energy approaches the three-body threshold *E* = 5.63 MeV, a greater number of basis functions must be taken into account, because the p^3He system becomes looser. In general, four to fourteen terms from expansions (5) are required for ensuring a precision of about 1%. The properties of convergence for triplet p^3He scattering are similar.

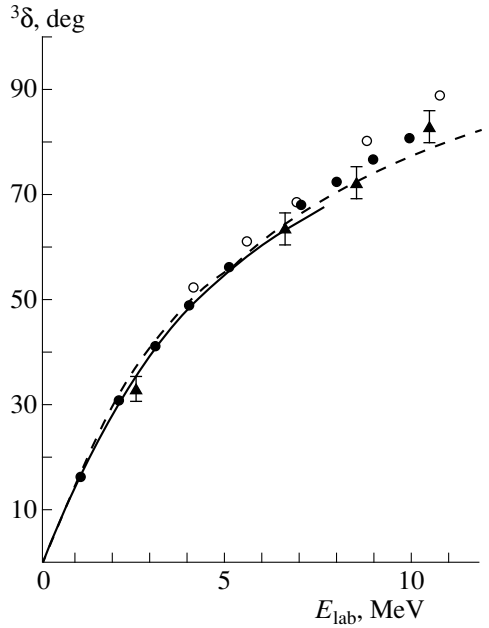

Fig. 2. As in Fig. 1, but for triplet scattering.

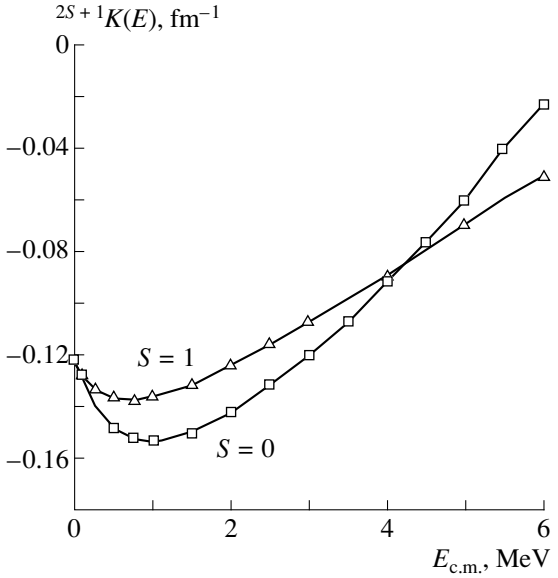

Fig. 3. Functions (squares) $^1K(E)$ and (triangles) $^3K(E)$ calculated for *s*-wave p^3He scattering. Curves represent the approximations of these functions by polynomials of eighth degree.

It is well known that, for charged-particle scattering, in which case there is long-range Coulomb interaction in addition to the short-range nuclear potential, the effective-range expansion is valid for the function

$$^{2S+1}K(E) = C_0^2(\eta)p\cot(^{2S+1}\delta(p)) + \frac{3}{2}nh(\eta),$$

where $h(\eta) = -\ln\eta + \mathrm{Re}\psi(1 + \eta i)$, $\psi(z)$ being a digamma function. The evaluated phase shifts $^{2S+1}\delta$ are used to calculate the function $^{2S+1}K(E)$. In Fig. 3, the squares and triangles represent the results for singlet and triplet scatterings, respectively. The functions $^{2S+1}K(E)$ can be expanded in a convergent power series in the variable E. To illustrate this circumstance, the approximations of the functions $^{2S+1}K(E)$ by polynomials of eighth degree are represented by curves in Fig. 3. For this case, the expansion coefficients are quoted in Table 4. A similar parametrization of the functions $^{2S+1}K(E)$ was previously used in [17]. We note that the energy-independent term in the expansion of the functions $^{S+1}K(E)$ represents the inverse scattering length defined as the limit of the function $\tan(^{2S+1}\delta)/pC_0^2$ for $p \longrightarrow 0$. The triplet and singlet scattering lengths for p^3He interaction were found to be 7.7 and 8.2 fm, respectively. The calculated singlet and triplet scattering lengths for p^3He interaction are presented in Table 5 along with the results of Belyaev and

Table 3. Calculated singlet phase shift for p^3He scattering at some values of c.m. energy versus the number N of terms retained in expansions (5)

$E_{c.m.}$, MeV / N	0.25	1.5	3	5
1	−4.4	−30.1	−44.1	−52.4
2	−3.6	−26.5	−43.5	−53.5
4	−3.9	−28.1	−45.3	−56.9
6	−4.1	−27.9	−45.0	−62.1
8	−4.0	−27.6	−45.0	−62.3
10	−3.9	−27.4	−44.9	−62.4
12	−3.9	−27.8	−45.5	−63.4
14	−3.9	−27.8	−45.6	−63.7

Table 4. Coefficients in the polynomials approximating the functions $^{2S+1}K(E)$

Power	$S = 0$	$S = 1$
0	−0.120367	−0.123628
1	−0.087201	−0.051790
2	0.080153	0.074081
3	−0.031458	−0.053538
4	0.005295	0.025249
5	0.000485	−0.007413
6	−0.000348	0.001291
7	0.521684×10^{-4}	0.000122
8	-0.267058×10^{-5}	0.474590×10^{-6}

Table 5. Singlet and triplet scattering lengths in the p^3He system

References	^1A, fm	^3A, fm
This study	8.2	7.7
[18]	8.1	5.2

Pupyshev [18], who used integral equations and took the nucleon–nucleon potential in a separable form.

ACKNOWLEDGMENTS

This work was supported by the Russian Foundation for Basic Research (project no. 98-02-18190).

APPENDIX

Here, we present the numerical matrices representing the particle-permutation operators that appear in equations (2) for the *s*-wave Yakubovsky components in the triplet and singlet states of the *nppp* system. For the triplet spin state of the system ($S = 1$), the matrices B_k, D, and C_k, $k = 1, 2$, are given by

$$B_1 = \begin{pmatrix} 1/4 & -3/4 \\ -3/4 & 1/4 \end{pmatrix}, \quad B_2 = \begin{pmatrix} 0 & 1 \\ 1 & 0 \end{pmatrix},$$

$$D = \begin{pmatrix} -1/12 & 1/4 \\ 1/4 & -1/12 \end{pmatrix},$$

$$C_1 = \begin{pmatrix} -1/(4\sqrt{3}) & \sqrt{3}/4 \\ \sqrt{3}/4 & -1/(4\sqrt{3}) \end{pmatrix},$$

$$C_2 = \begin{pmatrix} 0 & -1/\sqrt{3} \\ -1/\sqrt{3} & 0 \end{pmatrix}.$$

The nuclear interaction is controlled only by the pair spin; therefore, the operator V has the diagonal form

$$V = \mathrm{diag}\{V^{\mathrm{s}}, V^{\mathrm{t}}\},$$

where V^{s} and V^{t} are, respectively, the singlet and triplet components of the potential.

For the triplet state, the representation matrices for the Coulomb interaction can be written as

$$\mathcal{W}_1 = W_1 + \overline{W}_1,$$

$$W_1 = \begin{pmatrix} w_{11}^{(1)} & 0 \\ 0 & w_{22}^{(1)} \end{pmatrix},$$

$$w_{11}^{(1)} = \frac{2}{3}\frac{n}{x} + v_2^{(1)}/3, \quad w_{22}^{(1)} = v_2^{(1)},$$

$$\overline{W}_1 = \begin{pmatrix} \overline{w}_{11}^{(1)} & 0 \\ 0 & \overline{w}_{22}^{(1)} \end{pmatrix},$$

$$\overline{w}_{11}^{(1)} = \frac{5}{3}v_4^{(1)} + \frac{1}{3}v_6^{(1)}, \quad \overline{w}_{22}^{(1)} = v_4^{(1)} + v_6^{(1)},$$

$$\mathcal{W}_2 = W_2 + \overline{W}_2,$$

$$W_2 = \begin{pmatrix} w_{11}^{(2)} & 0 \\ 0 & w_{22}^{(2)} \end{pmatrix},$$

$$w_{11}^{(2)} = \frac{n}{x} + 2v_2^{(2)}, \quad w_{22}^{(2)} = \frac{n}{y} + 2v_2^{(2)},$$

where

$$v_2^{(1)} = n\begin{cases} 2/x & \text{for} \quad x > 2y \\ 1/y & \text{for} \quad x < 2y, \end{cases}$$

$$v_4^{(1)} =$$

$$n\begin{cases} \dfrac{1}{z} & \text{for} \quad z > \dfrac{x}{2} + \dfrac{y}{3} \\ \dfrac{1}{xy}\left(\dfrac{2}{3}\dfrac{1}{z}\left(z^2 - \left(\dfrac{3}{4}x - \dfrac{1}{2}y\right)^2\right) + 2\left(\dfrac{3}{4}x + \dfrac{1}{2}y - z\right)\right) & \text{for} \quad \left|\dfrac{1}{2}x - \dfrac{1}{3}y\right| < z < \dfrac{1}{2}x + \dfrac{1}{3} \\ \dfrac{2}{x} & \text{for} \quad x > \dfrac{2}{3}y, \quad z < \left|\dfrac{1}{2}x - \dfrac{1}{3}y\right| \\ \dfrac{3}{y} & \text{for} \quad x < \dfrac{2}{3}y, \quad z < \left|\dfrac{1}{2}x - \dfrac{1}{3}y\right|, \end{cases}$$

$$v_6^{(1)} = n\begin{cases} \dfrac{1}{z} & \text{for} \quad x > \dfrac{2}{3}y \\ \dfrac{3}{2}\dfrac{1}{y} & \text{for} \quad x < \dfrac{2}{3}y, \end{cases}$$

$$v_2^{(2)} = n\begin{cases} \dfrac{1}{z} & \text{for} \quad z > \dfrac{x+y}{2} \\ \dfrac{1}{xy}\left(-\dfrac{1}{z}\left(\left(\dfrac{x-y}{2}\right)^2 + x + y - z\right)\right) & \text{for} \quad \left|\dfrac{x-y}{2}\right| < z < \dfrac{x+y}{2} \\ \dfrac{2}{x} & \text{for} \quad x > y, \quad z < \left|\dfrac{x-y}{2}\right| \\ \dfrac{2}{y} & \text{for} \quad x < y, \quad z < \left|\dfrac{x-y}{2}\right|. \end{cases}$$

Further, we present the corresponding operators $V_k(x)$ and the matrices B_k, D, and C_k, $k = 1, 2$ for the singlet spin state ($S = 0$) of the *nppp* system. The operators $V_k(x)$ have the diagonal form

$$V_k(x) = \mathrm{diag}\{V^s(x), V^t(x)\}.$$

The matrices B_k, D, and C_k, $k = 1, 2$, are given by

$$B_1 = \begin{pmatrix} 1/4 & -3/4 \\ -3/4 & 1/4 \end{pmatrix}, \quad B_2 = -1,$$

$$D = \begin{pmatrix} 1/12 & 3/4 \\ -1/4 & -1/4 \end{pmatrix},$$

$$C_1 = \begin{pmatrix} 1/2\sqrt{6} \\ -3/2\sqrt{6} \end{pmatrix}, \quad C_2 = \begin{pmatrix} -2/\sqrt{6} & 0 \end{pmatrix}.$$

The matrices representing the Coulomb interaction can be written as

$$\mathcal{W}_1 = W_1 + \overline{W}_1,$$

$$W_1 = \begin{pmatrix} w_{11}^{(1)} & 0 \\ 0 & w_{22}^{(1)} \end{pmatrix}, \quad \overline{W}_1 = \begin{pmatrix} \overline{w}_{11}^{(1)} & 0 \\ 0 & \overline{w}_{22}^{(1)} \end{pmatrix},$$

$$\mathcal{W}_2 = W_2 + \overline{W}_2,$$

$$W_2 = \frac{n}{x},$$

$$\overline{W}_2 = 2\nu_2^{(2)}.$$

REFERENCES

1. O. A. Yakubovsky, Yad. Fiz. **5**, 1312 (1967) [Sov. J. Nucl. Phys. **5**, 937 (1967)].
2. J. A. Tjon, Phys. Lett. B **56**, 217(1975); **63**, 391 (1976).
3. H. Kröger and W. Sandhas, Phys. Rev. Lett. **40**, 834 (1978).
4. V. F. Kharchenko, Fiz. Élem. Chastits At. Yadra **10**, 884 (1979) [Sov. J. Part. Nucl. **10**, 349 (1979)].
5. V. P. Levashev, Yad. Fiz. **38**, 566 (1983) [Sov. J. Nucl. Phys. **38**, 336 (1983)].
6. S. P. Merkuriev and S. L. Yakovlev, Dokl. Akad. Nauk SSSR **262**, 591 (1982); Teor. Mat. Fiz. **56**, 60 (1983); S. P. Merkuriev and L. D. Faddeev, *Quantum Scattering Theory for Few-Body Systems* (Nauka, Moscow, 1985).
7. S. L. Yakovlev and I. N. Filikhin, in *Handbook of 15th International IUPAP Conference on Few-Body Problems in Physics, Groningen, 1997*, p. 155; I. N. Filikhin and S. L. Yakovlev, Yad. Fiz. **63**, 63 (2000) [Phys. At. Nucl. **63**, 55 (2000)].
8. S. L. Yakovlev and I. N. Filikhin, Yad. Fiz. **58**, 817 (1995) [Phys. At. Nucl. **58**, 754 (1995)]; Yad. Fiz. **60**, 1962 (1997) [Phys. At. Nucl. **60**, 1794 (1997)]; I. N. Filikhin and S. L. Yakovlev, Yad. Fiz. **62**, 1585 (1999) [Phys. At. Nucl. **62**, 1490 (1999)].
9. R. A. Malfliet and J. A. Tjon, Ann. Phys. (N. Y.) **61**, 425 (1970).
10. N. W. Schellingerhout, J. J. Schut, and L. P. Kok, Phys. Rev. C **46**, 1192 (1992).
11. S. P. Merkur'ev and S. L. Yakovlev, Yad. Fiz. **39**, 1580 (1984) [Sov. J. Nucl. Phys. **39**, 1002 (1984)].
12. S. L. Yakovlev, Teor. Mat. Fiz. **102**, 323 (1995); **107**, 513 (1996).
13. V. A. Rudnev and S. L. Yakovlev, Yad. Fiz. **58**, 1762 (1995) [Phys. At. Nucl. **58**, 1662 (1995)].
14. D. H. McSherry and S. D. Baker, Phys. Rev. C **1**, 888 (1970).
15. G. Szaloky and F. Seiler, Nucl. Phys. A **303**, 57 (1978).
16. L. Beltramin, R. Dei Frate, and G. Pisent, Nucl. Phys. A **442**, 266 (1985).
17. M. T. Alley and L. D. Knutson, Phys. Rev. C **48**, 1901 (1993).
18. V. B. Belyaev and V. V. Pupyshev, Yad. Fiz. **35**, 905 (1982) [Sov. J. Nucl. Phys. **35**, 526 (1982)].

Translated by R. Tyapaev

Physics of Atomic Nuclei, Vol. 63, No. 1, 2000, pp. 76–81. Translated from Yadernaya Fizika, Vol. 63, No. 1, 2000, pp. 87–92.

ELEMENTARY PARTICLES AND FIELDS
Theory

Description of Initial- and Final-State-Interaction Effects for the Reaction $\gamma p \longrightarrow \pi^- \Delta^{++}$ in the Region of Nucleon-Resonance Excitation

M. Anghinolfi[1)], M. Battaglieri[1)], E. N. Golovach[1)], B. S. Ishkhanov[2)], V. I. Mokeev[1)], M. V. Osipenko[2)], G. Ricco[1), 3)], M. Ripani[1)], V. V. Sapunenko[1)], M. Taiuti[1)], and G. V. Fedotov[2)]

Institute of Nuclear Physics, Moscow State University, Vorob'evy gory, Moscow, 119899 Russia

Received December 8, 1998; in final form, February 18, 1999

Abstract—A model has been developed for describing the cross section for the reaction $\gamma_{r,v} p \longrightarrow \pi^- \Delta^{++}$ in the energy region of nucleon-resonance excitation, and relevant calculations have been performed. The model takes into account the contribution of all reliably established resonances with masses less than 2 GeV and the contributions of nonresonance mechanisms in the approximation of Born diagrams. On the basis of data on the amplitudes of pion–nucleon interactions, a method has been evolved for phenomenologically describing the coupling of initial and final states with open inelastic channels. Calculations performed in this study represent a first step in developing a method for determining the electromagnetic form factors for nucleon resonances in exclusive reactions of pion-pair production on a nucleon by real and virtual photons. © *2000 MAIK "Nauka/Interperiodica".*

1. INTRODUCTION

Presently, a vast experimental program aimed at studying the structure of nucleon resonances in various exclusive channels of interactions induced by real and virtual photons is being performed at the electron accelerator of the TJNAF research center (USA) [1]. In this program, much attention is being given to studying pion-pair production on a proton by real and virtual photons [2, 3]. These experiments will make it possible to extract form factors for high-lying nucleon resonances ($M_{N^*} > 1.6$ GeV), whose branching fractions for decays into final-state pion pairs are significant. Investigation of pion-pair production on a proton by photons is a promising method of searches for resonances that are predicted by quark models [4, 5], but which have not yet been discovered experimentally (so-called missing resonances).

A dominant contribution of nonresonance processes, in excess of 70%, is a distinctive feature of pion-pair-production reactions on a proton at the photon point. As a result, traditional methods—a partial-wave expansion followed by a parametrization of partial waves [6, 7]—are insufficiently efficient for extracting nucleon-resonance form factors N^*. It follows that, in reactions like $\gamma p \longrightarrow \pi^+\pi^- p$, such form factors can be extracted only within model approaches that relate them to measured cross sections and which make it possible to determine nucleon-resonance form factors by fitting experimental data.

An appropriate model was developed in [8, 9], where the reaction $\gamma p \longrightarrow \pi^+\pi^- p$ was described as a set of two processes,

$$\gamma p \longrightarrow \pi^- \Delta^{++}, \quad (1)$$

$$\gamma p \longrightarrow \rho p, \quad (2)$$

and where the concept of phase space was used. It was shown in [9] that effects of initial- and final-state interactions (ISI and FSI, respectively) play an important role in describing reaction (1). Only for c.m. emission angles smaller than 30° can calculations that disregard ISI and FSI effects reproduce data from [10] on the angular distributions of pions from reaction (1). At larger emission angles, the calculated cross sections exceed the measured values by a factor of 2 to 3; in the case of pion emission into the backward hemisphere, the discrepancy is still greater.

In [9], ISI and FSI effects were taken into account within the approach proposed in [11]. In this approach, ISI and FSI are considered as the absorption of particles in the initial and final states. There, the absorption factor is related to the amplitudes of the elastic-scattering processes $\pi\Delta \longrightarrow \pi\Delta$ and $\rho p \longrightarrow \rho p$ (FSI and ISI, respectively). Owing to the photon–rho-meson transition, the absorption in the photon–proton initial state actually reduces to rho-meson absorption by the proton. The absorption factors in the input and output

[1)] Istituto Nazionale di Fisica Nucleare, Sezione di Genova, Genova, Italy.
[2)] Department of Physics, Moscow State University, Vorob'evy Gory, Moscow, 119899 Russia.
[3)] Universitá di Genova, via Dodecaneso 33, I-16146 Genova, Italy.

channels were determined in [9] by using their exponential parametrizations that were chosen phenomenologically and which involved the following free parameters: (i) the constants of coupling to inelastic channels in the initial and final states, C_{in} and C_{out}, and (ii) the diffraction-cone slopes A_{in} and A_{out} in the elastic-scattering processes $\pi\Delta \longrightarrow \pi\Delta$ and $\rho p \longrightarrow \rho p$. These parameters were chosen by fitting experimental data on the cross sections for the reaction $\gamma p \longrightarrow \pi^-\Delta^{++}$. The values of C_{in} and C_{out} that were determined in this way proved to be strongly dependent on W, varying from zero to unity as W changed from 1.5 to 1.7 GeV. Although the calculations presented in [9] reproduced satisfactorily data from [10] on the angular distributions of pions from reaction (1), the method used there cannot ensure an accurate description of physical mechanisms that govern the processes of absorption in the initial and final states. The procedure that relies on a fit to data alone may lead to significant and uncontrollable uncertainties in extracting the nucleon-resonance form factors.

Nonresonance processes for $W > 1.6$ GeV, in which case many open inelastic channels can compete, present one of the most challenging problems in studying the structure of high-lying nucleon resonances in electromagnetic interactions. The current status of strong-interaction theory gives no way to describe consistently the entire body of such processes on the basis of first principles. Thus, nonresonance amplitudes can be determined only within phenomenological approaches that relate them to the measured amplitudes of strong-interaction-induced processes. The present study relies on the approach proposed in [11] for obtaining corrections that arise in nonresonance amplitudes for reaction (1) because of absorptive effects in the initial and final states. It was indicated above that, in this approach, the correction factors are related to the amplitudes of the elastic-scattering processes $\pi\Delta \longrightarrow \pi\Delta$ and $\rho p \longrightarrow \rho p$.

Here, we develop a method for describing the amplitudes for the reactions $\pi\Delta \longrightarrow \pi\Delta$ and $\rho p \longrightarrow \rho p$ on the basis of experimental data on pion–nucleon interactions. Within the approach proposed in [11], the absorption factors are determined in the initial and final states of reaction (1). The differential cross sections for reaction (1) are computed, and the results are compared with data from [10].

2. DESCRIPTION OF THE CROSS SECTIONS FOR REACTION $\gamma p \longrightarrow \pi^-\Delta^{++}$

A detailed account of the model for describing the cross sections for the reaction $\gamma p \longrightarrow \pi^-\Delta^{++}$ is given in [9]. For this reason, we describe here only briefly the model and the method for taking into account ISI and FSI effects in calculating the cross sections for reaction (1).

The amplitude of reaction (1) is represented by the set of diagrams in Fig. 1, which correspond to the contribution of the excitation of nucleon resonances in the s channel (Fig. 1a) and to the contributions of nonresonance Born terms (Figs. 1b–1e). The contribution of resonance terms (Fig. 1a) is taken into account in the Breit–Wigner approximation [9]. In doing this, the results obtained from an analysis [12] of data on pion–nucleon interactions are used to determine the amplitudes of the strong-interaction-induced decays of nucleon resonances. The electromagnetic amplitudes for the excitation nucleon resonances are related to the helicity amplitudes $A_{1/2}$, $A_{3/2}$, and $C_{1/2}$, which were determined from data on pion-photoproduction reactions and which are presented in [13].

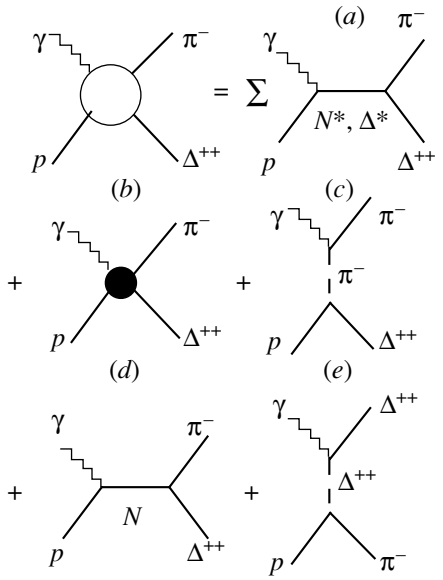

Fig. 1. Basic mechanisms of the reaction $\gamma p \longrightarrow \pi^-\Delta^{++}$.

Born terms (Figs. 1b–1d) are described in the approximation of effective Lagrangians [14]. In order to take correctly into account interactions with virtual pions and to reproduce faithfully the t dependences of the Born amplitudes, the form factors for the electromagnetic and for the $\pi p\Delta$ vertex are introduced in the diagrams in Figs. 1b–1e. For processes featuring pion exchange in the t channel, we invoke experimental data from [15] on the electromagnetic form factor for the pion and the results of an analysis of nucleon–nucleon scattering for the $\pi p\Delta$ form factor [16]. The $\pi p\Delta$ form factor calculated according to [16] suppresses the contribution of the delta-isobar-exchange diagram (Fig. 1e). The vertex functions for the contact term (Fig. 1b) are recovered on the basis of requirements of gauge invariance.

3. ABSORPTIVE EFFECTS IN THE INITIAL AND FINAL STATES OF THE REACTION $\gamma p \longrightarrow \pi^-\Delta^{++}$

A method for describing ISI and FSI effects was proposed in [11]. In this approach, the coupling of ini-

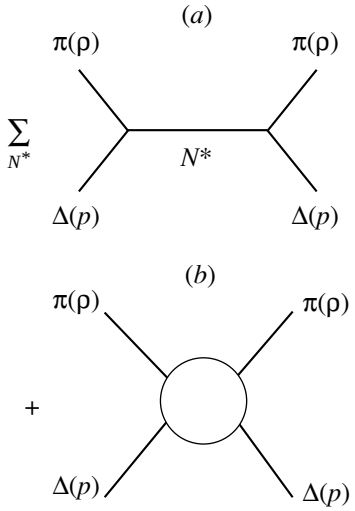

Fig. 2. Mechanisms of the elastic-scattering processes $\pi\Delta \longrightarrow \pi\Delta$ and $\rho p \longrightarrow \rho p$: (*a*) resonance mechanisms and (*b*) background

tial and final states of a reaction featuring open inelastic channels is described as the absorption of incident particles prior to occurrence of the reaction and as a partial absorption of nascent reaction products. The approach in question is based on the assumption that the reaction being studied proceeds through a sequence of ISIs, the reaction proper, and FSI. The absorption factors in the initial and final states depend on the spin J of a given channel. Therefore, the amplitude T of reaction (1) is expanded in states characterized by a definite value of the total channel spin; after that, each partial-wave amplitude T^J is appropriately corrected.

By using the approach proposed in [11], it can be shown that ISI and FSI effects modify the amplitude of reaction (1) in the channel characterized by the total spin j, $\langle \pi : \lambda_\Delta | T^j | \lambda_\gamma \lambda_p \rangle$, as follows:

$$\langle \pi : \lambda_\Delta | T^j | \lambda_\gamma \lambda_p \rangle_{\text{corr}} = (\langle \pi : \lambda_\Delta | S^j | \pi : \lambda_\Delta \rangle)^{1/2} \times \langle \pi : \lambda_\Delta | T^j | \lambda_\gamma \lambda_p \rangle (\langle \lambda_\gamma \lambda_p | S^j | \lambda_\gamma \lambda_p \rangle)^{1/2}. \quad (3)$$

Here, $\langle \pi : \lambda_\Delta | S^j | \pi : \lambda_\Delta \rangle$ is the S-matrix element for the elastic-scattering process $\pi\Delta \longrightarrow \pi\Delta$ with the delta-isobar helicity equal to λ_Δ both in the initial and in the final state, while $\langle \lambda_\gamma \lambda_p | S^j | \lambda_\gamma \lambda_p \rangle$ is the S-matrix element for the elastic-scattering process $\rho p \longrightarrow \rho p$ with the rho-meson helicities in the initial and final states equal, respectively, to the incident-photon helicity λ_γ and the proton helicity λ_p. The S- and T-matrix elements are related by the conventional equation

$$S = 1 + 2iT. \quad (4)$$

The number of terms retained in the expansion in j is determined by the magnitudes of the correcting factors $\langle \pi : \lambda_\Delta | S^j | \pi : \lambda_\Delta \rangle$ and $\langle \lambda_\gamma \lambda_p | S^j | \lambda_\gamma \lambda_p \rangle$; it will be shown below that, to a high precision, we can restrict our analysis to $j \le 5/2$. There are no experimental data on the amplitudes for the elastic-scattering processes $\pi\Delta \longrightarrow \pi\Delta$ and $\rho p \longrightarrow \rho p$; therefore, we can only calculate these amplitudes within some model approaches. In the present study, we propose an approach for determining them on the basis of experimental data on pion–nucleon interactions.

4. AMPLITUDES FOR THE ELASTIC-SCATTERING PROCESSES $\pi\Delta \longrightarrow \pi\Delta$ AND $\rho p \longrightarrow \rho p$

The elastic-scattering processes $\pi\Delta \longrightarrow \pi\Delta$ and $\rho p \longrightarrow \rho p$ are described in terms of the set of nucleon-resonance excitations in the s channel and a nonresonance background (see Fig. 2). The amplitude of the resonance processes (Fig. 2*a*) is parametrized in the Breit–Wigner form

$$\left\langle \pi : \lambda_\Delta(\lambda_\rho \lambda_p) \middle| T^j_{\text{res}} \middle| \lambda_\Delta : \pi(\lambda_\rho \lambda_p) \right\rangle = \sum_{N^*} \frac{\left\langle \lambda_R \middle| T^j_{\text{res}} \middle| \lambda_\Delta : \pi(\lambda_\rho \lambda_p) \right\rangle \left\langle \lambda_\Delta : \pi(\lambda_\rho \lambda_p) \middle| T^j_{\text{res}} \middle| \lambda_R \right\rangle}{W^2 - M^2_{N^*} + i\Gamma_{N^*}(W) M_{N^*}}, \quad (5)$$

where $\langle \lambda_R | T^j_{\text{res}} | \lambda_\Delta : \pi(\lambda_\rho \lambda_p) \rangle$ is the amplitude of the resonance decay $N^* \longrightarrow \pi\Delta(\rho p)$ for the resonance helicity of $\lambda_R = -\lambda_\Delta(\lambda_\rho - \lambda_p)$; W is the c.m. energy of the products of nucleon-resonance decay; and M_{N^*} and $\Gamma_{N^*}(W)$ are the nucleon-resonance mass and width, respectively. In order to describe consistently the off-mass-shell behavior of the nucleon resonance N^*, we introduce the W dependence of the total decay width. The amplitudes $\langle \lambda_R | T^j_{\text{res}} | \lambda_\Delta : \pi(\lambda_\rho \lambda_p) \rangle$ and the partial widths $\Gamma_{\lambda_\Delta(\lambda_\rho, \lambda_p)}$ with respect to the decays $N^* \longrightarrow \pi\Delta(\rho p)$ into a final state characterized by a helicity $\lambda_\Delta(\lambda_\rho, \lambda_p)$ are related by the equation

$$\langle \lambda_R | T^j_{\text{res}} | \lambda_\Delta : \pi(\lambda_\rho \lambda_p) \rangle = \sqrt{\frac{P_{\pi(\rho)}}{8\pi(2j+1)W}} \left[\frac{\sqrt{\Gamma_{\lambda_\Delta(\lambda_\rho \lambda_p)}} \times 2\sqrt{2\pi} M_{N^*} \sqrt{2j+1}}{\sqrt{P_{\pi(\rho)}}} \right] = \frac{\sqrt{\Gamma_{\lambda_\Delta(\lambda_\rho \lambda_p)}} M_{N^*}}{\sqrt{W}}, \quad (6)$$

where $P_{\pi(\rho)}$ is the absolute value of the pion (rho-meson) 3-momentum in the c.m. frame. The bracketed factor in (6) is explained in [9]. The factor in front of the bracketed expression represents a transformation factor relating the matrix elements used in the calculations from [9] to the relevant T-matrix elements. This factor was determined from the condition requiring that $|S^j_{\text{res}}|$ be equal to unity at the resonance point, provided that only one nucleon resonance N^* contributes and that only the elastic-scattering channel is open. In order

to determine the partial nucleon-resonance decay widths $\sqrt{\Gamma(LS)(N^* \longrightarrow \pi\Delta)}$ and $\sqrt{\Gamma(LS)(N^* \longrightarrow \rho p)}$ in the representation of LS coupling, we used the results of an analysis of data on pion–nucleon interactions [12] as recast into the helicity representation ($\sqrt{\Gamma_{\lambda_\Delta}}$ and $\sqrt{\Gamma_{\lambda_\rho\lambda_p}}$). The W dependence of the widths $\sqrt{\Gamma_{\lambda_\Delta}}$ and $\sqrt{\Gamma_{\lambda_\rho\lambda_p}}$ are introduced in just the same way as in [9]. The total decay width of the nucleon resonance N^* is the sum of the partial decay widths over all possible channels; that is,

$$\Gamma_{N^*} = \sum_i \Gamma_{i_{N^*}}. \quad (7)$$

The W dependence of the decay width with respect to each partial channel, $\Gamma_{i_{N^*}}(W)$, was calculated under the assumption that the effects of the centrifugal-barrier penetrability have a dominant impact on the W evolution of the widths. According to the parametrization adopted in [12], the W dependence of the nucleon-resonance width with respect to decay through the ith partial channel is given by

$$\Gamma_{i_{N^*}}(W) = \Gamma_{i_{N^*}}(W = M_{N^*})\frac{M_{N^*}}{W}\frac{P_{c(\rho,\pi)}}{P_{R(\rho,\pi)}}\frac{B_l^2(P_{c(\rho,\pi)}R)}{B_l^2(P_{R(\rho,\pi)}R)}, \quad (8)$$

where $\Gamma_{i_{N^*}}(W = M_{N^*})$ is the nucleon-resonance width with respect to decay through the ith channel at the resonance point $W = M_{N^*}$; $P_{c(\rho,\pi)}$ and $P_{R(\rho,\pi)}$ are the pion (rho-meson) momenta at a current value of W and at the resonance point, respectively; and B_l are the penetrability factors [17]. Summation in (5) is performed over all nucleon resonances that contribute to states with definite values of the total channel spin j and which are presented in the table.

Our estimates reveal that, in the energy region of nucleon-resonance excitation, the contribution of $j > 5/2$ states to corrections to Born amplitudes does not exceed 10%. In view of this, we disregarded the absorption in the initial and final states of reaction (1) for $j > 5/2$ states.

In order to describe the nonresonance components of the amplitudes for the elastic-scattering processes $\pi\Delta \longrightarrow \pi\Delta$ and $\rho p \longrightarrow \rho p$, we made use of data from [18] on the nonresonance component of the s-wave $\pi N \longrightarrow \pi N$ amplitude T_s. The nonresonance $\pi N \longrightarrow \pi N$ amplitudes for nonzero orbital angular momenta were calculated as

$$T_{\text{backgr}} = T_s B_l^2(P_{\rho(\pi)}R). \quad (9)$$

The nonresonance amplitudes for the elastic-scattering processes $\pi\Delta \longrightarrow \pi\Delta$ and $\rho p \longrightarrow \rho p$ were determined from the nonresonance amplitudes for $\pi N \longrightarrow \pi N$ scattering under the assumption of $SU(3)$ flavor symmetry.

Nucleon resonances taken into account in calculating the amplitudes $\langle \pi : \lambda_\Delta | T^j_{\text{res}} | \pi : \lambda_\Delta \rangle$ and $\langle \lambda_\rho\lambda_p | T^j_{\text{res}} | \lambda_\rho\lambda_p \rangle$

Total channel spin j	Nucleon resonances N^* included in the calculation
1/2	$S11(1535)$ $S31(1620)$ $S11(1650)$
	$P11(1440)$ $P11(1710)$ $P31(1910)$
3/2	$P13(1720)$ $P33(1600)$ $P33(1920)$
	$D13(1520)$ $D13(1700)$ $D33(1700)$
5/2	$D15(1675)$
	$F15(1680)$ $F35(1905)$

From a comparison of the calculated resonance and nonresonance contributions to the amplitudes for elastic $\pi\Delta$ and ρp scatterings, it can clearly be seen that resonance processes are dominant over the entire energy region of nucleon-resonance excitation ($W < 2$ GeV). It obviously follows that, in constructing an effective description of coupling between initial and final states featuring open inelastic channels, we must take into account s-channel mechanisms.

In calculating the amplitude for the elastic-scattering process $\rho p \longrightarrow \rho p$, we allowed for effects of a finite rho-meson width. The $\rho p \longrightarrow \rho p$ amplitude $\langle \lambda_\rho\lambda_p | T | \lambda_\rho\lambda_p \rangle$ was determined as the convolution of the amplitude calculated at a specific rho-meson mass m_ρ, $\langle \lambda_\rho\lambda_p | T | \lambda_\rho\lambda_p \rangle|_{m_\rho}$, with the mass distribution of the rho meson, $w(m_\rho)$; that is,

$$\langle \lambda_\rho\lambda_p | T | \lambda_\rho\lambda_p \rangle = \int \langle \lambda_\rho\lambda_p | T | \lambda_\rho\lambda_p \rangle|_{m_\rho} w(m_\rho^2) dm_\rho^2. \quad (10)$$

In turn, the rho-meson mass distribution $w(m_\rho)$ was chosen in the form of the Breit–Wigner distribution

$$w(m_\rho) = \frac{1}{\pi}\frac{M\Gamma}{(m_\rho^2 - M^2)^2 + M^2\Gamma^2}, \quad (11)$$

where M and Γ are the rho-meson mass and width [13], respectively, and where the normalization factor is chosen in such a way that the distribution in (11) is normalized to unity.

5. DISCUSSION OF THE RESULTS

Within the approach described above, we have calculated the cross sections for the reaction $\gamma p \longrightarrow \pi^-\Delta^{++}$. In Fig. 3, the results of these calculations are contrasted against experimental data from [10]. In the calculation, we included the same nucleon resonances as in [9]. In accordance with [16], the cutoff parameter Λ for the $\pi p\Delta$ form factor was chosen to be 0.75 GeV.

Two solid curves in Fig. 3 correspond to the results of the calculations performed for different values cho-

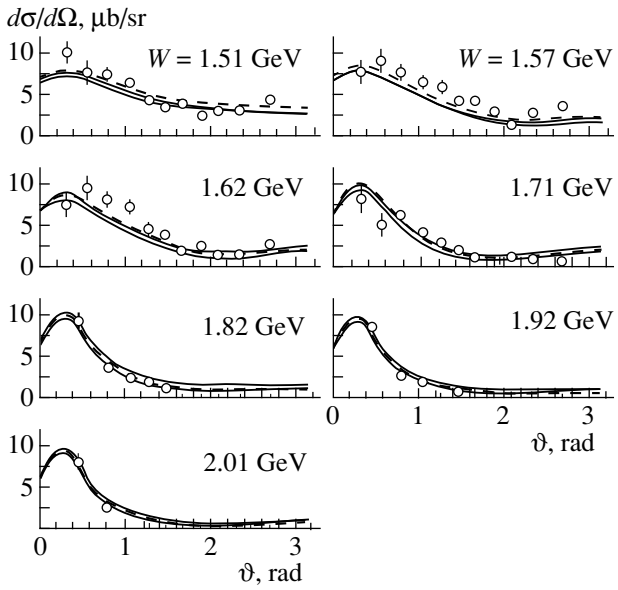

Fig. 3. Differential cross sections calculated for the reaction $\gamma p \longrightarrow \pi^-\Delta^{++}$ at (solid curves) the maximal values of the partial nucleon-resonance widths with respect to decays through the $\pi\Delta$ and ρp channels and the minimal values of the analogous widths with respect to all other channels and (dashed curves) the minimal values of the partial nucleon-resonance widths with respect to decays through the $\pi\Delta$ and ρp channels and the maximal values of the analogous widths with respect to all other channels. Points represent experimental data from [10].

sen for the partial widths with respect to nucleon-resonance decays within the uncertainties of the analysis reported in [12]. The cross section for the reaction $\gamma p \longrightarrow \pi^-\Delta^{++}$ and the absorptive effects in the initial and final states receive contributions from many nucleon resonances. For the nucleon resonances, it is next to impossible to choose partial-decay-width values that would correspond to the corridor between the maximal and minimal values of the cross section for reaction (1). For this reason, we performed the calculation for two options: (i) for the maximal partial widths with respect nucleon-resonance decays through the $\pi\Delta$ and ρp channels and the minimal partial widths with respect to all other channels and (ii) for the minimal partial widths with respect nucleon-resonance decays through the $\pi\Delta$ and ρp channels and the maximal partial widths with respect to all other channels. Either calculation gives the idea of errors that the calculated cross sections may have because of uncertainties in data from [12] on the partial decay widths of nucleon resonances. From the data in Fig. 3, it can be seen that the scatter of the results of the calculations is much less than the uncertainties in experimental data from [10]. Thus, we can state that the proposed model produces results that are stable to variations in the input parameters.

The data in Fig. 3 show that, by and large, the results of the calculations reproduce faithfully experimental values from [10]. At angles larger than 100° and W values in excess of 1.8 GeV, the calculated differential cross sections are smaller than 1.5 μb/sr. Because of the uncertainties in the experimental data from [10], it was possible to establish only upper limits on the differential cross sections in this kinematical region (1 μb/sr). Such small values of the differential cross sections are due to absorption in the initial and final states of the reaction $\gamma p \longrightarrow \pi^-\Delta^{++}$. The calculations taking no account of ISI and FSI effects lead to differential-cross-section values within a few μb/sr in this kinematical region. Thus, the inclusion of channel-coupling effects is of key importance in describing reaction (1) for W values in excess of 1.7 GeV. At the same time, our calculations demonstrate that, for $W < 1.6$ GeV, the absorption in the initial and final states is small, which is in accord with the estimates of ISI and FSI effects from [19, 20]. In the region of moderately small values of W, the calculated cross sections for reaction (1) reproduce faithfully the data from [10] at $W = 1.51$ GeV, but they fall systematically short of the cross-section values measured at $W = 1.57$ and 1.62 GeV. Because of the approximations used to describe the amplitudes for the elastic-scattering processes $\pi\Delta \longrightarrow \pi\Delta$ and $\rho p \longrightarrow \rho p$ and because of the absence of experimental data on relevant amplitudes, any hypotheses on the reasons behind these discrepancies would be mere speculation. In order to obtain a reliable description of ISI and FSI effects in the reaction $\gamma p \longrightarrow \pi^-\Delta^{++}$, it is necessary that the amplitudes calculated for the elastic-scattering processes $\pi\Delta \longrightarrow \pi\Delta$ and $\rho p \longrightarrow \rho p$ within different approaches that employ available data on the amplitudes of pion–nucleon interactions be consistent. A promising approach would be to reconstruct the $\pi\Delta$ and ρp amplitudes for these reactions on the basis of the results that an analysis of the entire body of data on meson–nucleon interactions could produce, provided that this analysis is performed with allowance for requirements of S-matrix unitarity used along the same lines as in [21].

6. CONCLUSION

An approach has been developed for describing ISI and FSI for the reaction $\gamma p \longrightarrow \pi^-\Delta^{++}$ on the basis of experimental data on pion–nucleon scattering amplitudes. The angular distributions of pions from reaction (1) have been calculated with allowance for absorption in the initial and final states that was determined within the method proposed here. The results comply well with experimental data from [10]. This gives grounds to hope that the dominant nonresonance processes in reaction (1) have been treated adequately. It is worth noting that the proposed approach features no free parameters to be determined from data on reaction (1). All the input parameters have been determined from an analysis of a vast body of data on πN interactions. At present, the problem of describing nonresonance processes in pion production by photons at $W > 1.6$ GeV is one of the most important unresolved problems in studying the

structure of high-lying nucleon resonances in electromagnetic processes. The approach developed in this study provides a phenomenological description of nonresonance processes induced by photons in the energy region of nucleon-resonance excitation.

REFERENCES

1. V. D. Burkert, Nucl. Phys. A **623**, 59 (1997).
2. M. Ripani, Nucl. Phys. A **623**, 110 (1997).
3. V. D. Burkert, M. Ripani, *et al.*, CEBAF Experiment E-93-006.
4. R. Koniuk and N. Isgur, Phys. Rev. Lett. **44**, 845 (1980); Phys. Rev. D **21**, 1868 (1980); R. Koniuk, Nucl. Phys. B **195**, 452 (1982),
5. S. Capstic and W. Roberts, Phys. Rev. D **49**, 4570 (1994).
6. F. A. Berens and A. Donnachie, Nucl. Phys. B **84**, 342 (1975).
7. R. A. Arndt, I. I. Strakovsky, and R. L. Workman, Phys. Rev. C **53**, 430 (1996).
8. V. I. Mokeev, M. Anghinolfi, M. Battaglieri, *et al.*, Few-Body Syst. Suppl. (in press).
9. M. Anghinolfi, M. Battaglieri, E. N. Golovach, *et al.*, Yad. Fiz. **62**, 1522 (1999) [Phys At. Nucl. **62**, 1437 (1999)].
10. Cambridge Bubble Chamber Group, Phys. Rev. **155**, 1477 (1967); ABBHM Collab., Phys. Rev. **175**, 1669 (1968).
11. K. Gottfried and J. D. Jackson, Nuovo Cimento **34**, 736 (1964).
12. D. M. Manley and E. M. Salesky, Phys. Rev. D **45**, 4002 (1992).
13. Particle Data Group, Phys. Rev. D **54**, 1 (1996).
14. A. Bartl, W. Majerotto, and D. Schildknecht, Nuovo Cimento A **12**, 703 (1972).
15. C. J. Bebek *et al.*, Phys. Rev. D **17**, 1693 (1978).
16. R. Machleidt, Adv. Nucl. Phys. **19**, 189 (1979).
17. J. M. Blatt and U. F. Weisskopf, *Theoretical Nuclear Physics* (Wiley, New York, 1952).
18. S. A. Dytman, T. P. Vrana, and T.-S. H. Lee, nucl-th/9702033.
19. J. A. Gómez-Tejedor and E. Oset, Nucl. Phys. A **571**, 667 (1994); **600**, 413 (1996).
20. C. Mukhopadhyay, J. F. Zhang, and M. Benmerrouche, nucl-th/9612061.
21. S. A. Dytman, T. P. Vrana, and T.-S. H. Lee, πN Newsletters **13**, 90 (1997).

Translated by A. Isaakyan

Physics of Atomic Nuclei, Vol. 63, No. 1, 2000, pp. 82–93. Translated from Yadernaya Fizika, Vol. 63, No. 1, 2000, pp. 93–105.

ELEMENTARY PARTICLES AND FIELDS
Theory

BFKL Pomeron in the Reaction $\gamma_\perp^*(Q^2)p \longrightarrow \rho_\perp^0 p$ at Large Q^2 and W

V. V. Anisovich, L. G. Dakhno, D. I. Melikhov, V. A. Nikonov, and M. G. Ryskin

Petersburg Nuclear Physics Institute, Russian Academy of Sciences, Gatchina, 188350 Russia

Received September 21, 1998; in final form, February 15, 1999

Abstract—The reaction $\gamma_\perp^*(Q^2)p \longrightarrow \rho_\perp^0 p$ has been studied at large Q^2 and W^2/Q^2 and low momentum transfers to the nucleon, $\kappa_\perp^2$ —that is, in the region where the Pomeron exchange mechanism is operative. At sufficiently large Q^2, the Pomeron interacts with quarks occurring at small distances, whereby the hard component of the Pomeron is separated, so that the process is governed by the Pomeron of perturbative QCD (BFKL Pomeron). Our calculations indicate that, in vector-meson electroproduction at low $\kappa_\perp^2$, the perturbative regime cannot set in fast because, for $Q^2 \le 100$ GeV^2 and, accordingly, for $W^2/Q^2 \le 10^7$, comparatively large distances of $\rho_{q\bar{q}} > 0.2$ fm are important. © *2000 MAIK "Nauka/Interperiodica".*

1. INTRODUCTION

A direct verification of perturbative QCD predictions is an important problem in itself. At currently available energies, there are two lines of investigation that make it possible to observe a transition from the physics of soft processes to the physics of hard processes. These are an investigation of hadron form factors [1, 2] and an investigation of the hard Pomeron [3, 4].

In performing a quantitative analysis of hard processes, it is of paramount importance to answer the question of where the regime of perturbative QCD commences. The problem was discussed comprehensively in studying form factors [5–7]. Chernyak and Zhitnitsky [5] considered a possible scheme for perturbatively calculating form factors at comparatively low Q^2. At the same time, Isgur and Llevelyn-Smith argued [6] that the perturbative regime is reached at very high Q^2, those on the order of 50 GeV^2 or even higher. Their arguments were confirmed by the calculations performed in [7]. In [7, 8], the charge form factor for the pion and the electromagnetic transition form factors for $\gamma\gamma^*(Q^2) \longrightarrow \pi^0$, $\gamma\gamma^*(Q^2) \longrightarrow \eta$, and $\gamma\gamma^*(Q^2) \longrightarrow \eta'$ were calculated in the interval $0 \le Q^2 \le 25$ GeV^2. The region of low Q^2 made it possible to reconstruct the soft wave functions of pseudoscalar mesons and of the photon, while the region of high Q^2 was represented by the convolution of the block of hard one-gluon exchange and the soft wave functions. The calculation presented in [8] demonstrated that perturbative-gluon-exchange diagrams, which yield contributions of order α_s, become dominant only at $Q^2 \simeq 50$ GeV^2; at lower momentum transfers, the nonperturbative contribution of the triangle diagram (direct convolution of the wave functions) is significant.

Here, we study the diffractive electroproduction of ρ^0 mesons by transversely polarized photons, $\gamma_\perp^*(Q^2)p \longrightarrow \rho_\perp^0 p$. This process is driven by the BFKL Pomeron exchange. Indeed, this proceeds as follows at high Q^2: a virtual photon $\gamma^*(Q^2)$ produces a quark–antiquark pair at a small distance (see Fig. 1), which is converted into a ρ^0 meson, emitting t-channel gluons; since these gluons also have, owing to small interquark distances, small impact parameters, there arises the t-channel exchange of a perturbative BFKL Pomeron.

Thus, it is the quark loop that separates small distances at high Q^2. The quark loop is determined by two wave (or vertex) functions, that of the photon and that of the ρ^0 meson. In terms of the light-cone variables, the photon wave function was reconstructed in [8] on the basis of experimental data on the $\gamma \longrightarrow \pi^0$ transition form factor. The photon wave function is determined by two processes: the direct production of a quark–antiquark pair—this results in the pointlike $\gamma \longrightarrow q\bar{q}$ transition vertex at large $q\bar{q}$ invariant masses $M_{q\bar{q}}$ (the wave function corresponding to the direct production of a quark–antiquark pair by a photon was discussed in detail elsewhere [9])—and the interaction of low-energy quarks. The latter process enhances the relative contribution of small $M_{q\bar{q}}$ and, hence, of large interquark distances of about 0.5–1 fm (vector-dominance effect).

The low-energy component of the rho-meson wave function is close to the quark wave function of the pion, because either particle belongs to the same $q\bar{q}$ nonet. Moreover, vector dominance dictates that the low-energy component of the rho meson be similar to that of the photon. In our calculations, we assume that the

1063-7788/00/6301-0082$20.00

rho-meson and pion wave functions coincide in the region of low-energy $q\bar{q}$ excitations (specifically, for $M_{q\bar{q}} \leq 3$ GeV); the low-energy pion wave function was determined in [7] from data on the pion form factor.

The high-energy component of the ρ-meson wave function requires a dedicated discussion. The point is that, despite the similarity of the problems, it cannot be found by using the same procedure as that which was followed in [7, 8] in dealing with the meson form factors. In [7], a consideration of the pion form factor was based on isolating the strong-interaction contribution with allowance for corrections linear in α_s. For this purpose, the pion wave function was broken down into a soft and a hard component, Ψ^S and Ψ^H, respectively, in such a way that Ψ^S is large for $M^2_{q\bar{q}} = (m^2 + k_\perp^2)/x(1 + x) < M_0^2$ (here, $k_\perp$ and x are the light-cone quark variables, while m is the quark mass) and that Ψ^H is dominant for $M^2_{q\bar{q}} > M_0^2$; the parameter M_0, which represents the boundary between the soft and hard regions, is about a few GeV. Specifically, the simplest way of partitioning the wave function in terms of a Heaviside step function was chosen in [7] to implement the above procedure: $\Psi_\pi = \Psi^S\theta(M^0 - M_{q\bar{q}}) + \Psi^H\theta(M_{q\bar{q}} - M^0)$. In this case, the hard component Ψ^H is the convolution of the soft wave function Ψ^S with the kernel V^{α_s} determined by one-gluon exchange:

$$\Psi^H = V^{\alpha_s} \otimes \Psi^S. \quad (1)$$

When Ψ^H is defined in this way, the expansion of the form factor in power series in terms of α_s has the form

$$F = F^{SS} + 2F^{SH} + O(\alpha_s^2), \quad (2)$$

where F^{SS} is the soft form factor, while F^{SH} is the $O(\alpha_s)$ contribution determined by the one-gluon-exchange diagram. In this case, we take into account all $O(\alpha_s)$ contributions in the first two terms on the right-hand side of (2) by including the Sudakov form factor in the quark–photon vertex and by renormalizing the quark mass.

It is more difficult to allow for all $O(\alpha_s)$ contributions in the reaction $\gamma^*(Q^2)p \longrightarrow \rho^0 p$, which involves a few hadrons and a Pomeron. Here, it is necessary to take into account $O(\alpha_s)$ corrections not only to the ρ^0-meson wave function, but also to the vertices of quark interaction with t-channel gluons and to include next-to-leading corrections (NLC) in the QCD Pomeron eigenfunctions, but this seems impossible at present. At the same time, it is hazardous take into account all $O(\alpha_s)$ terms only in the rho-meson wave function, because this is not a consistent procedure. In this situation, we deem it reasonable to rely on phenomenological information about the $V \longrightarrow q\bar{q}$ vertex. It is worth noting that, phenomenologically, the $V \longrightarrow q\bar{q}$ vertex is well known up to $M^2_{q\bar{q}} \sim 3$ GeV^2. At extremely large masses (in the asymptotic region), the contribution corresponding to the leading-twist wave function is dominant. For the transverse ρ^0 meson, however, this contribution can be neglected almost always for numerical reasons—it is proportional to the very small current mass of the light quark. In the intermediate region, we apply the idea of quark–hadron duality for this process [10] and assume that, at large $M^2_{q\bar{q}}$, the $V \longrightarrow q\bar{q}$ transition form factor behaves, according to the law of generalized vector dominance, as

$$G_V(M^2_{q\bar{q}}) \sim M^{-2}_{q\bar{q}}. \quad (3)$$

In order to test the stability of our main conclusions with respect to the above assumptions in the region of high $q\bar{q}$ excitations, we study other versions, those where $G_V(M^2_{q\bar{q}})$ decreases faster at large $M^2_{q\bar{q}}$.

For processes characterized by a low momentum transfer to the nucleon, κ—and we discuss here precisely such processes—the use of the leading-twist rho-meson wave function leads to an infrared divergence in the integral associated with the quark block [11]. The low-energy rho-meson wave function constructed by analogy with the pion wave function [7] does not generate such a divergence, making a finite contribution to the cross section from large distances between hadrons.

This article is organized as follows. We present the expression for the $\gamma^* \longrightarrow V$ vertex associated with Pomeron exchange in Section 2 and the expression for the total amplitude with allowance for the exchange of a BFKL Pomeron in Section 3. We consider two versions: (i) in the process of t-channel evolution, a hard BFKL Pomeron transforms into a soft Pomeron, which interacts with the target nucleon; (ii) a BFKL Pomeron does not have time to transform into the system of soft gluons. Our calculations reveal that the two versions lead to very close Q and W (total invariant energy of the γp system) dependences of the cross section. The results of these calculations are displayed in Section 4.

The main objective of this study is to assess the Q^2 scale above which a virtual photon selects small distances. Therefore, we performed two versions of the calculation for the reaction $\gamma^*_\perp(Q^2)p \longrightarrow \rho^0_\perp p$: (a) that within the standard procedure featuring no additional selection of small distances and (2) that where there is an additional selection of small distances by a Heaviside step function. In the phase space of the quark loop, only the contribution of small distances ($\rho_{q\bar{q}} \leq 0.2$ fm) is retained in the latter version. The cross-section values calculated within the two versions differ significantly in the region $Q^2 \sim 5$–20 GeV^2, but they approach each other for Q^2 in excess of 100 GeV^2. This means that perturbative QCD becomes applicable in Pomeron

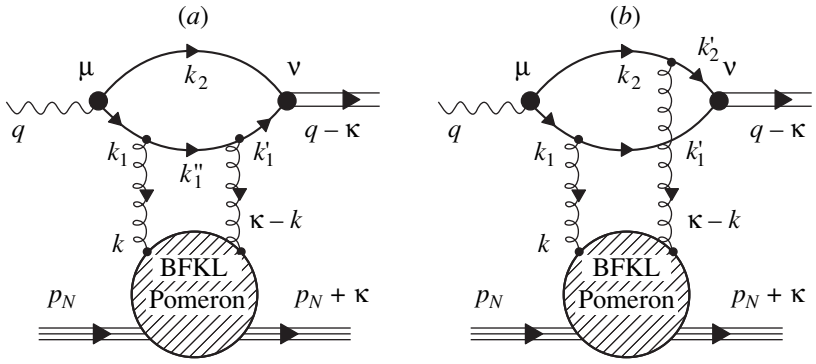

Fig. 1. Diagrams that determine the process $\gamma^*(Q^2)p \longrightarrow \rho^0 p$.

exchanges at approximately the same Q^2 values as in form-factor processes.

2. PHOTON–POMERON–MESON VERTEX

At high W, the process $\gamma^*(Q^2)p \longrightarrow Vp$ (where $V = \rho, \omega, \phi$) is determined by two diagrams in Figs. 1*a* and 1*b*. In Fig. 1*a*, two Reggeized gluons interact with a quark; there is a similar diagram where two gluons interact with an antiquark. In Fig. 1*b*, one gluon interacts with the quark, while the other interacts with the antiquark. The conventions for the momenta are illustrated in the figure.

The kinematics corresponding to the process is the following (the virtual photon has a high momentum along the z axis):

$$q = (q_0, \mathbf{q}_\perp, q_z) \simeq \left(q_z + \frac{-Q^2}{2q_z}, 0, q_z\right). \tag{4}$$

The value of Q^2 is assumed to be large, but $q_z \gg Q$. The target proton is at rest; that is,

$$p_N = (m_N, 0, 0), \tag{5}$$

in which case, we have $W^2 \simeq 2m_N q_z + m_N^2 - Q^2$.

We consider the process at low momentum transfers to the nucleon, $|\kappa^2| < m_N^2$. From the conditions $(p+\kappa)^2 = m_N^2$ and $(q-\kappa)^2 = \mu_V^2$, where μ_V is the vector-meson mass, it then follows that

$$\kappa = (\kappa_0, \boldsymbol{\kappa}_\perp, \kappa_z)$$
$$\simeq \left(\frac{-\kappa^2}{2m_N}, \boldsymbol{\kappa}_\perp, \frac{\mu_V^2 - \kappa^2 + Q^2}{2q_z} - \frac{\kappa^2}{2m_N}\right) \simeq (0, \boldsymbol{\kappa}_\perp, 0); \tag{6}$$

that is, $\kappa^2 \approx -\kappa_\perp^2$. Let us consider the upper block of the diagram in Fig. 1*a*. The quark loop of this diagram is calculated by using the spectral-integration technique; the corresponding cuts of the diagram are shown in Fig. 2*a*. The amplitude of the quark block in Fig. 2*a* is

$$A_{qq} = \int \frac{dM_{q\bar{q}}^2}{\pi} G_\gamma(M_{q\bar{q}}^2) \frac{d\Phi_2(p; k_1, k_2)}{M_{q\bar{q}}^2 - q^2 - i0} \frac{dM_{q\bar{q}}^{''2}}{\pi}$$
$$\times \frac{d\Phi_1(p''; k_1'', k_2)}{M_{q\bar{q}}^{''2} - (q-k)^2 - i0} \frac{dM_{q\bar{q}}^{'2}}{\pi} \frac{d\Phi_1(p'; k_1', k_2)}{M_{q\bar{q}}^{'2} - (q-\kappa)^2 - i0} \tag{7}$$
$$\times G_V(M_{q\bar{q}}^{'2}) g^2 (-1) S_\mathrm{I},$$

where $p^2 = M_{q\bar{q}}^2$, $p'^2 = M_{q\bar{q}}^{'2}$, and $p''^2 = M_{q\bar{q}}^{''2}$ are the squares of the energies in the corresponding intermediate states. The spin-dependent factor is

$$S_\mathrm{I} = \mathrm{tr}[\gamma_\nu^\perp (\hat{k}_1' + m) \hat{n} (\hat{k}_1'' + m)$$
$$\times \hat{n} (\hat{k}_1 + m) \gamma_\mu^\perp (-\hat{k}_2 + m)], \tag{8}$$
$$n = \frac{1}{2q_z}(1, 0, -1),$$

where $\hat{n}$ is the vertex function for the quark and the Reggeized gluon [12], while the subscripts μ and ν refer to, respectively, photon and vector-meson polarizations.

The phase spaces are given by

$$d\Phi_2(p; k_1, k_2) = \frac{1}{2} \frac{d^3 k_1}{(2\pi)^3 2k_{10}} \frac{d^3 k_2}{(2\pi)^3 2k_{20}} (2\pi)^4$$
$$\times \delta^4(p - k_1 - k_2) = \frac{1}{(4\pi)^2} \frac{dx_1 dx_2}{x_1 x_2} \delta(1 - x_1 - x_2)$$
$$\times d^2 k_{1\perp} d^2 k_{2\perp} \delta(\mathbf{k}_{1\perp} + \mathbf{k}_{2\perp}) \delta\left(M_{q\bar{q}}^2 - \frac{m_{1\perp}^2}{x_1} - \frac{m_{2\perp}^2}{x_2}\right), \tag{9}$$
$$d\Phi_1(p''; k_1'', k_2) = \frac{1}{2} \frac{d^3 k_1''}{(2\pi)^3 2k_{10}''} (2\pi)^4$$

$$\times \delta^4(p'' - k_1'' - k_2) = \pi \frac{dx_1''}{x_1''} \delta(1 - x_1'' - x_2)$$

$$\times d^2k_{1\perp}'' \delta(\mathbf{k}_{1\perp}'' + \mathbf{k}_\perp + \mathbf{k}_{2\perp}) \delta\left(M_{q\bar{q}}''^2 + k_\perp^2 - \frac{m_{1\perp}''^2}{x_1''} - \frac{m_{2\perp}^2}{x_2} \right),$$

$$d\Phi_1(p'; k_1', k_2) = \frac{1}{2} \frac{d^3k_1'}{(2\pi)^3 2k_{10}'} (2\pi)^4$$

$$\times \delta^4(p' - k_1' - k_2) = \pi \frac{dx_1'}{x_1'} \delta(1 - x_1' - x_2)$$

$$\times d^2k_{1\perp}' \delta(\mathbf{k}_{1\perp}' + \boldsymbol{\kappa}_\perp + \mathbf{k}_{2\perp}) \delta\left(M_{q\bar{q}}'^2 + \kappa_\perp^2 - \frac{m_{1\perp}'^2}{x_1'} - \frac{m_{2\perp}^2}{x_2} \right).$$

Integration with respect to k_z is removed owing to the pole $(M_{q\bar{q}}''^2 + Q^2 - 2q_z k_z - i0)^{-1}$, which is replaced by the corresponding half-residue; the delta functions in equations (9) remove the remaining integrations. As a result, we obtain

$$A_{qq} = \frac{1}{4\pi} \int_0^1 \frac{dx}{x(1-x)^3} \int \frac{d^2k_{2\perp}}{(2\pi)^2} dk_z \frac{G_\gamma(M_{q\bar{q}}^2)}{M_{q\bar{q}}^2 + Q^2}$$

$$\times \frac{1}{M_{q\bar{q}}''^2 + Q^2 - 2q_z k_z - i0} \frac{G_V(M_{q\bar{q}}'^2)}{M_{q\bar{q}}'^2 - \mu_V^2} g^2(-1) S_{\mathrm{I}} \qquad (10)$$

$$= \int_0^1 \frac{dx}{x(1-x)^3} \int \frac{d^2k_{2\perp}}{(4\pi)^2} \frac{G_\gamma(M_{q\bar{q}}^2)}{M_{q\bar{q}}^2 + Q^2} \frac{G_V(M_{q\bar{q}}'^2)}{M_{q\bar{q}}'^2 - \mu_V^2} \frac{-ig^2}{2q_z} S_{\mathrm{I}},$$

where

$$M_{q\bar{q}}^2 = \frac{m^2 + k_{2\perp}^2}{x(1-x)}, \quad M_{q\bar{q}}''^2 = \frac{m^2 + (\mathbf{k}_{2\perp} + x\mathbf{k}_\perp)^2}{x(1-x)}, \qquad (11)$$

$$M_{q\bar{q}}'^2 = \frac{m^2 + (\mathbf{k}_{2\perp} + x\boldsymbol{\kappa}_\perp)^2}{x(1-x)}, \quad x \equiv x_2.$$

The quark loop (upper block) in Fig. 1*b* is considered in a similar way. The triple spectral representation (see Fig. 2*b*) leads to the spectral integral

$$A_{q\bar{q}} = \int \frac{dM_{q\bar{q}}^2}{\pi} G_\gamma(M_{q\bar{q}}^2) \frac{d\Phi_2(p; k_1, k_2)}{M_{q\bar{q}}^2 - q^2 - i0} \frac{dM_{q\bar{q}}''^2}{\pi}$$

$$\times \frac{d\Phi_1(p''; k_1', k_2)}{M_{q\bar{q}}''^2 - (q-k)^2 - i0} \frac{dM_{q\bar{q}}'^2}{\pi} \frac{d\Phi_1(p'; k_1', k_2')}{M_{q\bar{q}}'^2 - (q-\kappa)^2 - i0} \qquad (12)$$

$$\times G_V(M_{q\bar{q}}'^2) g^2(-1) S_{\mathrm{II}},$$

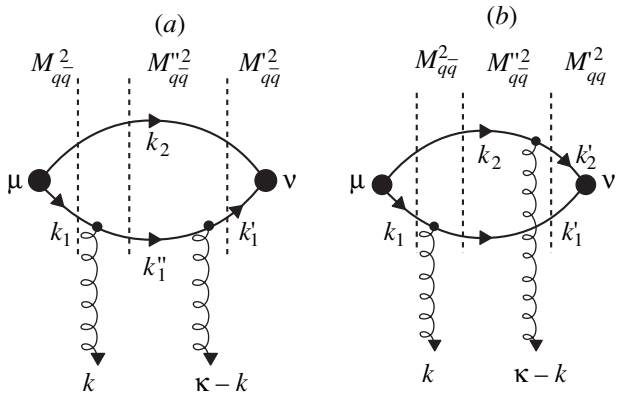

Fig. 2. Quark loop for the process $\gamma^*(Q^2) \longrightarrow V$ in the case of gluon interaction with (*a*) a quark and (*b*) a quark and an antiquark. The dashed lines show loop cuts corresponding to the spectral integrals in equations (7) and (12).

where

$$S_{\mathrm{II}} = \mathrm{tr}[\gamma_\nu^\perp(\hat{k}_1' + m)\hat{n}(\hat{k}_1 + m)$$
$$\times \gamma_\mu^\perp(-\hat{k}_2 + m)\hat{n}(-\hat{k}_2' + m)]. \qquad (13)$$

The phase spaces are determined in the same way as above; that is,

$$d\Phi_2(p; k_1, k_2) = \frac{1}{(4\pi)^2} \frac{dx_1 dx_2}{x_1 x_2} \delta(1 - x_1 - x_2)$$

$$\times d^2k_{1\perp} d^2k_{2\perp} \delta(\mathbf{k}_{1\perp} + \mathbf{k}_{2\perp}) \delta\left(M_{q\bar{q}}^2 - \frac{m_{1\perp}^2}{x_1} - \frac{m_{2\perp}^2}{x_2} \right),$$

$$d\Phi_1(p''; k_1', k_2) = \pi \frac{dx_1'}{x_1'} \delta(1 - x_1' - x_2) d^2k_{1\perp}' \qquad (14)$$

$$\times \delta(\mathbf{k}_{1\perp}' + \mathbf{k}_\perp + \mathbf{k}_{2\perp}) \delta\left(M_{q\bar{q}}''^2 + k_\perp^2 - \frac{m_{1\perp}'^2}{x_1'} - \frac{m_{2\perp}^2}{x_2} \right),$$

$$d\Phi_1(p'; k_1', k_2') = \pi \frac{dx_2'}{x_2'} \delta(1 - x_1' - x_2') d^2k_{2\perp}'$$

$$\times \delta(\mathbf{k}_{1\perp}' + \boldsymbol{\kappa}_\perp + \mathbf{k}_{2\perp}') \delta\left(M_{q\bar{q}}'^2 + \kappa_\perp^2 - \frac{m_{1\perp}'^2}{x_1'} - \frac{m_{2\perp}'^2}{x_2'} \right).$$

Integration performed in just the same way as in deriving expression (10) yields

$$A_{q\bar{q}} = \int_0^1 \frac{dx}{x^2(1-x)^2} \int \frac{d^2k_{2\perp}}{(4\pi)^2} \frac{G_\gamma(M_{q\bar{q}}^2)}{M_{q\bar{q}}^2 + Q^2} \frac{G_V(M_{q\bar{q}}'^2)}{M_{q\bar{q}}'^2 - \mu_V^2} \frac{-ig^2}{2q_z} S_{\mathrm{II}}, \qquad (15)$$

where

$$M_{q\bar{q}}^2 = \frac{m^2 + k_{2\perp}^2}{x(1-x)}, \quad M_{q\bar{q}}^{''2} = \frac{m^2 + (\mathbf{k}_{2\perp} + (1-x)\mathbf{k}_\perp)^2}{x(1-x)},$$
$$M_{q\bar{q}}^{'2} = \frac{m^2 + (\mathbf{k}_{2\perp} + \mathbf{k} - x\boldsymbol{\kappa}_\perp)^2}{x(1-x)}, \quad x \equiv x_1. \tag{16}$$

We calculate S_I and S_II for the case of transverse polarization in the (x, y) plane; for this reason, we make the substitution

$$g_{\mu\nu} \longrightarrow -\delta_{ab}, \quad k_{i\mu}k_{j\nu} \longrightarrow k_{ia}k_{jb}, \quad a, b = 1, 2. \tag{17}$$

The resulting expressions for S_I and S_II are

$$S_\mathrm{I} = -8\frac{(1-x)}{x} \times \delta_{ab}[m^2 + (1-2x(1-x))k_{2\perp}^2 + x^2(\boldsymbol{\kappa}_\perp \cdot \mathbf{k}_{2\perp})], \tag{18}$$

$$S_\mathrm{II} = 8\delta_{ab}[m^2 + (1-2x(1-x)) \times (k_{2\perp}^2 + (\mathbf{k} \cdot \mathbf{k}_{2\perp}) - x(\boldsymbol{\kappa}_\perp \cdot \mathbf{k}_{2\perp}))]. \tag{19}$$

3. $\gamma_\perp^*(Q^2)p \longrightarrow \rho_\perp^0 p$ AMPLITUDE

Let us now address quark loop diagrams featuring a BFKL Pomeron.

A. First, we consider the version where the BFKL Pomeron transforms into a soft Pomeron, which interacts with the target nucleon. Following [3, 4, 13], we represent the contribution of the diagram in Fig. 1*a* in the form

$$A_{qq}^\mathrm{BFKL}(\gamma^* p \longrightarrow Vp) = 4i\delta_{ab}\int_0^1 \frac{dx}{x^2(1-x)^2} \times \int \frac{d^2k_{2\perp}}{(2\pi)^2}\frac{d^2k}{(2\pi)^2}\Psi_\gamma(k_{2\perp}^2)\Psi_V((\mathbf{k}_{2\perp} + x\boldsymbol{\kappa}_\perp)^2) \times (m^2 + (1-2x(1-x))k_{2\perp}^2 + x^2\mathbf{k}_{2\perp}\cdot\boldsymbol{\kappa}_\perp) \times \int_{-\infty}^{\infty} \frac{d\nu\nu^2}{(\nu^2+1/4)^2}\left(\frac{W^2}{Q^2+\mu_V^2}\right)^{\omega(\nu)} \int d^2\rho_1 d^2\rho_2 \times e^{i\mathbf{k}\cdot(\boldsymbol{\rho}_1-\boldsymbol{\rho}_2)}e^{i\boldsymbol{\kappa}_\perp\cdot\boldsymbol{\rho}_2}\left(\left[\frac{(\boldsymbol{\rho}_1-\boldsymbol{\rho}_2)^2}{\rho_1^2\rho_2^2}\right]^{1/2+i\nu} - \left[\frac{1}{\rho_1^2}\right]^{1/2+i\nu} - \left[\frac{1}{\rho_2^2}\right]^{1/2+i\nu}\right) g^2\tilde{g}e^{-B\kappa_\perp^2}, \tag{20}$$

where $\boldsymbol{\rho}_1$ and $\boldsymbol{\rho}_2$ are the gluon coordinates in the impact-parameter space and where we have introduced the photon and vector-meson wave functions

$$\Psi_\gamma(k_{2\perp}^2) = \frac{G_\gamma(M_{q\bar{q}}^2)}{M_{q\bar{q}}^2 + Q^2}, \quad \Psi_V((\mathbf{k}_{2\perp} + x\boldsymbol{\kappa}_\perp)^2) = \frac{G_V(M_{q\bar{q}}^{'2})}{M_{q\bar{q}}^{'2} - \mu_V^2}, \tag{21}$$

with $M_{q\bar{q}}^{'2}$ being given by (11). The energy dependence is determined by the function

$$\omega(\nu) = \frac{2\alpha_s C_A}{\pi}\mathrm{Re}\left(\frac{\Gamma'(1)}{\Gamma(1)} - \frac{\Gamma'(1/2+i\nu)}{\Gamma(1/2+i\nu)}\right), \tag{22}$$

where $C_A = N_c = 3$, and $\Gamma(z)$ is a gamma function.

For the diagram in Fig. 1*b*, we arrive at

$$A_{q\bar{q}}^\mathrm{BFKL}(\gamma^* p \longrightarrow Vp) = -4i\delta_{ab}\int_0^1 \frac{dx}{x^2(1-x)^2} \times \int \frac{d^2k_{2\perp}}{(2\pi)^2}\frac{d^2k}{(2\pi)^2}\Psi_\gamma(k_{2\perp}^2)\Psi_V((\mathbf{k}_{2\perp} + \mathbf{k} - x\boldsymbol{\kappa}_\perp)^2) \times (m^2 + (1-2x(1-x))(k_{2\perp}^2 + \mathbf{k}\cdot\mathbf{k}_{2\perp} - x\boldsymbol{\kappa}_\perp\cdot\mathbf{k}_{2\perp})) \times \int_{-\infty}^{\infty} \frac{d\nu\nu^2}{(\nu^2+1/4)^2}\left(\frac{W^2}{Q^2+\mu_V^2}\right)^{\omega(\nu)} \int d^2\rho_1 d^2\rho_2 \times e^{i\mathbf{k}\cdot(\boldsymbol{\rho}_1-\boldsymbol{\rho}_2)}e^{i\boldsymbol{\kappa}_\perp\cdot\boldsymbol{\rho}_2}\left(\left[\frac{(\boldsymbol{\rho}_1-\boldsymbol{\rho}_2)^2}{\rho_1^2\rho_2^2}\right]^{1/2+i\nu} - \left[\frac{1}{\rho_1^2}\right]^{1/2+i\nu} - \left[\frac{1}{\rho_2^2}\right]^{1/2+i\nu}\right) g^2\tilde{g}e^{-B\kappa_\perp^2}. \tag{23}$$

The momentum transfer to the Pomeron, $\kappa_\perp^2$, is not high; therefore, small distances are not permanently selected along the Pomeron ladder: the distance between the *t*-channel gluons in the impact-parameter space gradually increases as we move from the $\gamma^*(Q^2) \longrightarrow V$ block to the nucleon. For a sufficiently developed comb (that is, at large W), the distances between gluons reach ordinary hadron values, in which case we are dealing with a soft Pomeron. Accordingly, the Pomeron–nucleon vertex for the soft Pomeron has the standard form—we defined it as $\tilde{g}F_{PNN}(\kappa_\perp^2)$. To a high accuracy, the nucleon form factor can be approximated as $F_{PNN}(\kappa_\perp^2) = e^{-B\kappa_\perp^2}$ with $B \simeq 2.5$ GeV^{-2}.

It can easily be seen that the total amplitude satisfies the condition

$$A^\mathrm{BFKL}(\gamma^* p \longrightarrow Vp) = A_{qq}^\mathrm{BFKL}(\gamma^* p \longrightarrow Vp) + A_{\bar{q}\bar{q}}^\mathrm{BFKL}(\gamma^* p \longrightarrow Vp) + 2A_{q\bar{q}}^\mathrm{BFKL}(\gamma^* p \longrightarrow Vp). \tag{24}$$

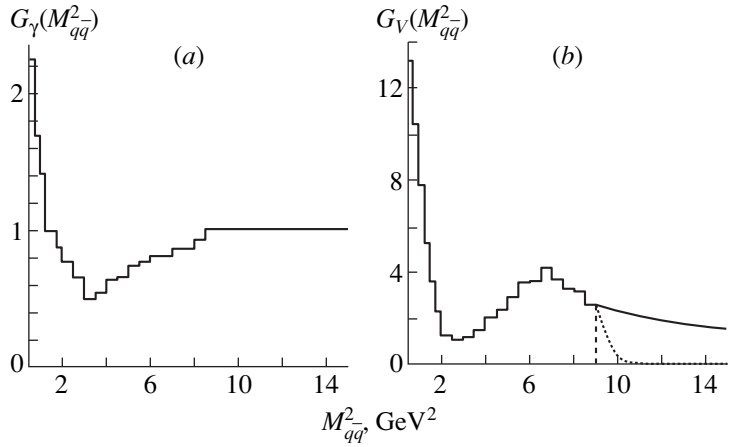

Fig. 3. (*a*) Vertex $G_\gamma(M^2_{q\bar{q}})$ obtained from an analysis of the $\gamma \longrightarrow \pi^0, \eta, \eta'$ transition form factors [8] and used here to calculate the reaction $\gamma^*_\perp(Q^2)p \longrightarrow \rho^0_\perp p$. (*b*) Rho-meson vertex function used in the calculations; the wave functions of the 1^1S_0 and 1^3S_1 $q\bar{q}$ nonets (pseudoscalar and vector mesons, respectively) are identical in the region of low $q\bar{q}$ excitations $M_{q\bar{q}} < 3$ GeV (the pseudoscalar-meson vertex function was determined in [7]). Three versions of the behavior of $G_V(M^2_{q\bar{q}})$ for $M^2_{q\bar{q}} > 9$ GeV^2 have been considered: (I) a decrease of $G_V(M^2_{q\bar{q}})$ in proportion to $1/M^2_{q\bar{q}}$ (solid curve), (II) the exponential decrease $G_V(M^2_{q\bar{q}}) \sim \exp(-M^2_{q\bar{q}}/M_0^2)$ with $M_0^2 = 0.5$ GeV^2 (dotted curve), and (III) $G_V = 0$ (dashed curve).

Making use of it and taking into account all cancellations, we arrive at

$$A^{\mathrm{BFKL}}(\gamma^* p \longrightarrow Vp) = -8i\delta_{ab}\int_0^1 \frac{dx}{x^2(1-x)^2}$$
$$\times \int \frac{d^2k_{2\perp}}{(2\pi)^2}\frac{d^2k}{(2\pi)^2}\Psi_\gamma(k^2_{2\perp})\Psi_V((\mathbf{k}_{2\perp}+\mathbf{k}-x\boldsymbol{\kappa}_\perp)^2)$$
$$\times (m^2 + (1-2x(1-x))(k^2_{2\perp} + \mathbf{k}\cdot\mathbf{k}_{2\perp} - x\boldsymbol{\kappa}_\perp\cdot\mathbf{k}_{2\perp})) \quad (25)$$
$$\times \int_0^\infty \frac{2d\nu\nu^2}{(\nu^2+1/4)^2}\left(\frac{W^2}{Q^2+\mu_V^2}\right)^{\omega(\nu)}\int d^2\rho_1 d^2\rho_2$$
$$\times e^{i\mathbf{k}\cdot(\boldsymbol{\rho}_1-\boldsymbol{\rho}_2)}e^{i\boldsymbol{\kappa}_\perp\cdot\boldsymbol{\rho}_2}\left[\frac{(\boldsymbol{\rho}_1-\boldsymbol{\rho}_2)^2}{\rho_1^2\rho_2^2}\right]^{1/2+i\nu} g^2\tilde{g}e^{-B\kappa_\perp^2}.$$

Introducing the variables

$$\mathbf{k}' \equiv (\mathbf{k}_{2\perp} + \mathbf{k} - x\boldsymbol{\kappa}_\perp), \quad \mathbf{k} \equiv \mathbf{k}_{2\perp}, \quad (26)$$

we obtain

$$A^{\mathrm{BFKL}}(\gamma^* p \longrightarrow Vp) = -8i\delta_{ab}\int_0^1 \frac{dx}{x^2(1-x)^2}$$
$$\times \int_0^\infty \frac{2d\nu\nu^2}{(\nu^2+1/4)^2}\left(\frac{W^2}{Q^2+\mu_V^2}\right)^{\omega(\nu)}\int d^2\rho_1 d^2\rho_2$$
$$\times e^{i\boldsymbol{\kappa}_\perp\cdot\boldsymbol{\rho}_2}e^{ix\boldsymbol{\kappa}_\perp\cdot(\boldsymbol{\rho}_1-\boldsymbol{\rho}_2)}\left[\frac{(\boldsymbol{\rho}_1-\boldsymbol{\rho}_2)^2}{\rho_1^2\rho_2^2}\right]^{1/2+i\nu} \quad (27)$$
$$\times \int \frac{d^2k'}{(2\pi)^2}\frac{d^2k}{(2\pi)^2}\Psi_V(k'^2)\Psi_\gamma(k^2)e^{i\mathbf{k}'\cdot(\boldsymbol{\rho}_1-\boldsymbol{\rho}_2)}e^{-i\mathbf{k}\cdot(\boldsymbol{\rho}_1-\boldsymbol{\rho}_2)}$$
$$\times (m^2 + (1-2x(1-x))\mathbf{k}'\cdot\mathbf{k})g^2\tilde{g}e^{-B\kappa_\perp^2}.$$

In terms of the auxiliary variables

$$\mathbf{R} = \frac{\boldsymbol{\rho}_1+\boldsymbol{\rho}_2}{2}, \quad \boldsymbol{\rho} = \boldsymbol{\rho}_1 - \boldsymbol{\rho}_2, \quad (28)$$

the amplitude can finally be represented as

$$A^{\mathrm{BFKL}}(\gamma^* p \longrightarrow Vp) = -8i\delta_{ab}\int_0^1 \frac{dx}{x^2(1-x)^2}$$
$$\times \int_0^\infty \frac{2d\nu\nu^2}{(\nu^2+1/4)^2}\left(\frac{W^2}{Q^2+\mu_V^2}\right)^{\omega(\nu)}\int d^2\rho_1 d^2R$$
$$\times e^{i\boldsymbol{\kappa}_\perp\cdot(\mathbf{R}-(1/2-x)\boldsymbol{\rho})}\left[\frac{\rho^2}{(\mathbf{R}+\boldsymbol{\rho}/2)^2(\mathbf{R}-\boldsymbol{\rho}/2)^2}\right]^{1/2+i\nu} \quad (29)$$
$$\times \int \frac{d^2k'}{(2\pi)^2}\frac{d^2k}{(2\pi)^2}\Psi_V(k'^2)\Psi_\gamma(k^2)e^{i\mathbf{k}'\cdot\boldsymbol{\rho}}e^{-i\mathbf{k}'\cdot\boldsymbol{\rho}}$$
$$\times (m^2 + (1-2x(1-x))\mathbf{k}'\cdot\mathbf{k})g^2\tilde{g}e^{-B\kappa_\perp^2}.$$

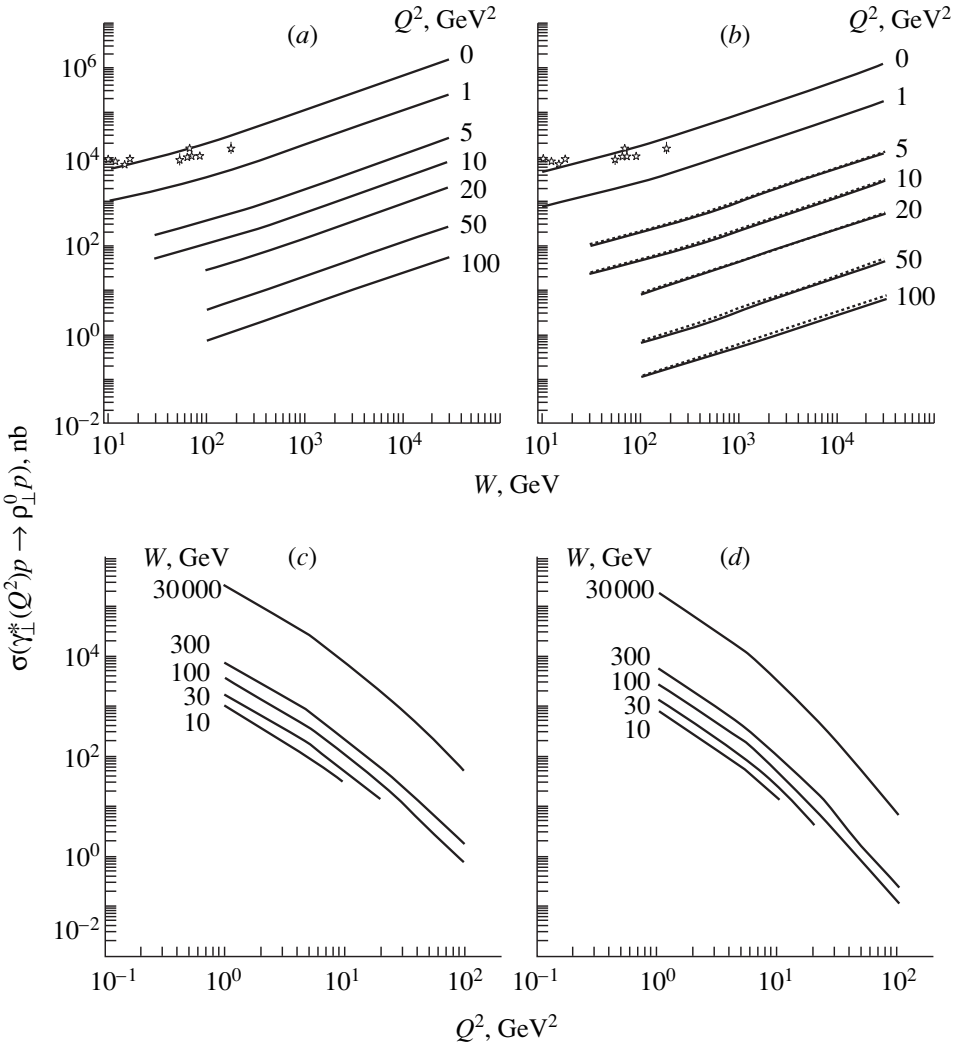

Fig. 4. (*a*) Cross section $\sigma(\gamma_\perp^*(Q^2)p \longrightarrow \rho_\perp^0 p)$ in version IA for various Q^2 versus W (experimental data on the cross section for the photoproduction process $\gamma p \longrightarrow \rho^0 p$ from [14] are shown as guidelines). (*b*) Cross section $\sigma(\gamma_\perp^*(Q^2)p \longrightarrow \rho_\perp^0 p)$ at various Q^2 versus W for versions (solid curves) IIA and (dotted curves) IIIA. (*c* and *d*) Cross section $\sigma(\gamma_\perp^*(Q^2)p \longrightarrow \rho_\perp^0 p)$ for various W versus Q^2 in versions IA and IIA (IIIA), respectively.

The last integral can be recast into a form that is more convenient for a numerical integration; that is,

$$A^{\mathrm{BFKL}}(\gamma^* p \longrightarrow Vp) = -8i\delta_{ab}\int_0^1 \frac{dx}{x^2(1-x)^2} \times \int_0^\infty \frac{2d\nu\nu^2}{(\nu^2+1/4)^2}\left(\frac{W^2}{Q^2+\mu_V^2}\right)^{\omega(\nu)} \int d^2\rho d^2R \times e^{i\boldsymbol{\kappa}_\perp\cdot(\mathbf{R}-(1/2-x)\boldsymbol{\rho})}\left[\frac{\rho^2}{(\mathbf{R}+\boldsymbol{\rho}/2)^2(\mathbf{R}-\boldsymbol{\rho}/2)^2}\right]^{1/2+i\nu} \quad (30)$$

$$\times \frac{1}{(2\pi)^2} g^2\tilde{g} e^{-B\kappa_\perp^2}(m^2\Phi_V(\rho^2)\Phi_\gamma(\rho^2) + 2(1-2x(1-x))\Phi_V^{(1)}(\rho^2)\Phi_\gamma^{(1)}(\rho^2)),$$

where

$$\Phi(\rho^2) = \int_0^\infty dk k\Psi(k^2)J_0(k\rho), \qquad \Phi^{(1)}(\rho^2) = \int_0^\infty dk k^2\Psi(k^2)J_1(k\rho). \quad (31)$$

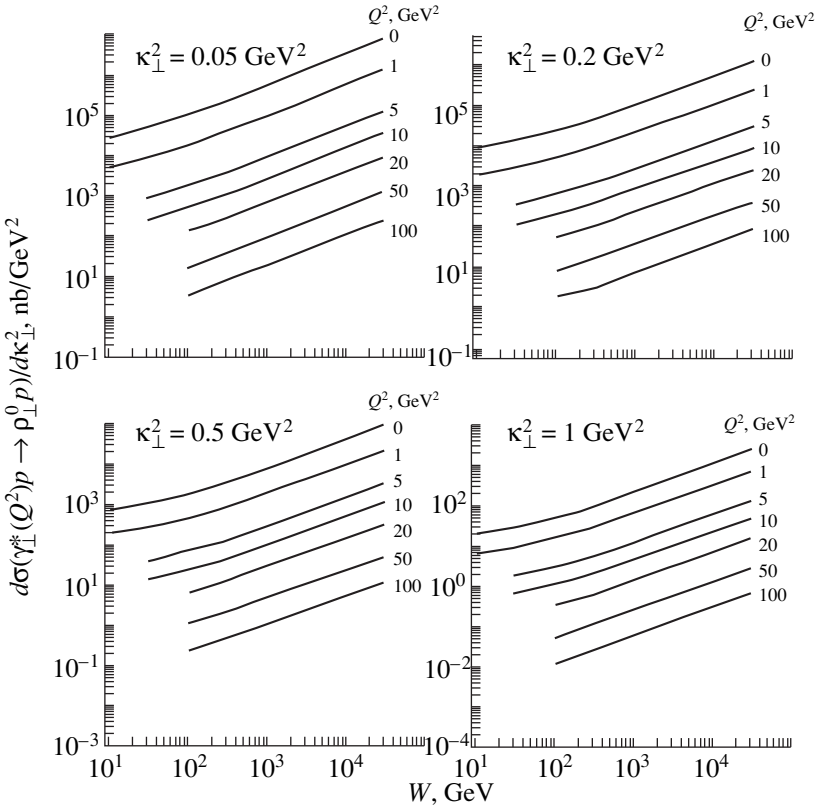

Fig. 5. Cross section $d\sigma(\gamma_\perp^*(Q^2)p \longrightarrow \rho_\perp^0 p)/d\kappa_\perp^2$ for various Q^2 and $\kappa_\perp^2$ versus the total energy W in version IA.

B. In the second version of the calculation, we assume that the gluon ladder of the BFKL Pomeron is rather short; therefore, the BFKL Pomeron is not converted into a soft Pomeron. In this case, the $\gamma_\perp^*(Q^2)p \longrightarrow \rho_\perp^0 p$ transition amplitude has the form

$$A^{\mathrm{BFKL}}(\gamma^* p \longrightarrow Vp) = -8i\delta_{ab}\int_0^1 \frac{dx}{x^2(1-x)^2}$$
$$\times \int_0^\infty \frac{2d\nu\nu^2}{(\nu^2+1/4)^2}\left(\frac{W^2}{Q^2+\mu_V^2}\right)^{\omega(\nu)} \int d^2\rho d^2R$$
$$\times e^{i\boldsymbol{\kappa}_\perp\cdot(\mathbf{R}-(1/2-x)\boldsymbol{\rho})}\left[\frac{\rho^2}{(\mathbf{R}+\boldsymbol{\rho}/2)^2(\mathbf{R}-\boldsymbol{\rho}/2)^2}\right]^{1/2+i\nu} \quad (32)$$
$$\times \frac{1}{(2\pi)^2} g^2\tilde{g} A_N(\nu, \boldsymbol{\kappa}_\perp)(m^2\Phi_V(\rho^2)\Phi_\gamma(\rho^2)$$
$$+ 2(1-2x(1-x))\Phi_V^{(1)}(\rho^2)\Phi_\gamma^{(1)}(\rho^2)),$$

where

$$A_N(\nu, \boldsymbol{\kappa}_\perp) = \int d^2\rho_1' d^2\rho_2' \left(\left[\frac{(\boldsymbol{\rho}_1'-\boldsymbol{\rho}_2')^2}{\rho_1'^2\rho_2'^2}\right]^{1/2-i\nu}$$
$$-\left[\frac{1}{\rho_1'^2}\right]^{1/2-i\nu} - \left[\frac{1}{\rho_2'^2}\right]^{1/2-i\nu}\right)\exp\left(i\boldsymbol{\kappa}_\perp\frac{\boldsymbol{\rho}_1'+\boldsymbol{\rho}_2'}{2}\right) \quad (33)$$
$$\times\left(\exp\left(-\frac{2(\rho_1'^2+\rho_2'^2)}{3\langle r^2\rangle}\right) - \delta(\boldsymbol{\rho}_1'-\boldsymbol{\rho}_2')\frac{3}{2}\pi\right.$$
$$\left.\times\langle r^2\rangle\exp\left(-\frac{(\boldsymbol{\rho}_1'+\boldsymbol{\rho}_2')^2}{6\langle r^2\rangle}\right)\right),$$

with $\langle r^2\rangle$ being 0.8 fm^2. This choice of the nucleon wave function corresponds to a decrease of the nucleon–Pomeron vertex in proportion to an exponential $\exp(-B\kappa_\perp^2)$ with $B \simeq 2$ GeV^{-2}.

4. RESULTS OF THE CALCULATIONS

The vertex function that couples the Pomeron to the *virtual photon* $\longrightarrow$ *vector meson* block is determined by the vertex functions $G_\gamma(M_{q\bar{q}}^2)$ and $G_V(M_{q\bar{q}}^2)$. The vertex function $G_\gamma(M_{q\bar{q}}^2)$ was evaluated in [8]; here, we make use of the results of those calculations. Figure 3*a* displays the function $G_\gamma(M_{q\bar{q}}^2)$. It can be seen that, for

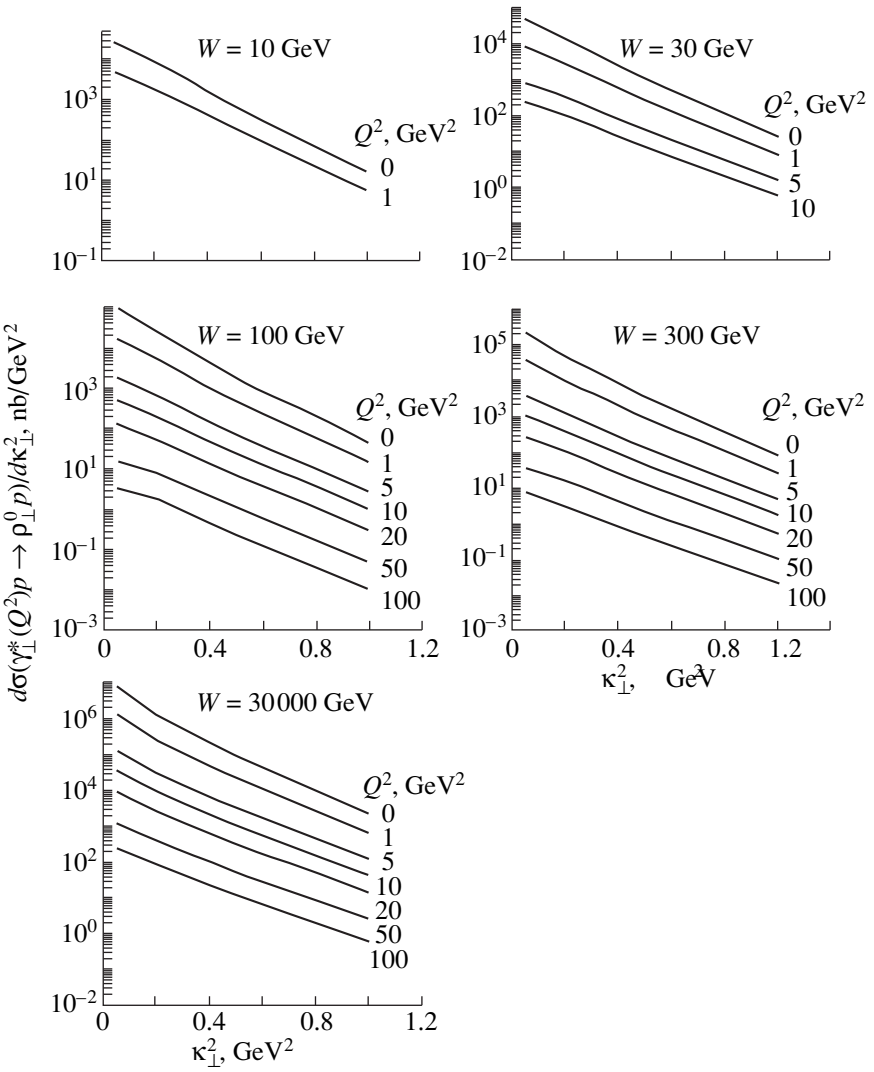

Fig. 6. Cross section $d\sigma(\gamma_\perp^*(Q^2)p \longrightarrow \rho_\perp^0 p)/d\kappa_\perp^2$ for various Q^2 and W versus the momentum transfer $\kappa_\perp^2$ to the nucleon in version IA.

$M_{q\bar{q}}^2 < 2$ GeV^2, this vertex function decreases with increasing $M_{q\bar{q}}^2$ and that, at large $M_{q\bar{q}}^2$, it reduces to $G_\gamma(M_{q\bar{q}}^2) = 1$.

We consider various versions of the ρ-meson wave function; they differ from one another only for $M_{q\bar{q}}^2 >$ 9 GeV^2. Figure 3*b* shows the vertex function $G_V(M_{q\bar{q}}^2)$ used in the calculations; we assume that, for $M_{q\bar{q}}^2 <$ 9 GeV^2, the soft wave functions of the vector mesons belonging to the $1^3S_1 q\bar{q}$ nonet are identical to the wave functions of the $1^1S_0 q\bar{q}$ pseudoscalar mesons (the latter were determined in [7, 8]). For the high-energy component, $M_{q\bar{q}}^2 > 9$ GeV^2, we consider three versions:

(I) $G_V(M_{q\bar{q}}^2) \sim M_{q\bar{q}}^{-2}$,

(II) $G_V(M_{q\bar{q}}^2) \sim \exp[-aM_{q\bar{q}}^2]$ with $a = 2$ GeV^{-2},

(III) $G_V(M_{q\bar{q}}^2) = 0$.

The amplitude also depends on the coupling constant $g^2\tilde{g}$, which is treated here as a free parameter. Figure 4 illustrates the cross section $\sigma(\gamma_\perp^*(Q^2)p \longrightarrow \rho_\perp^0 p)$ as a function of W and Q^2 for version IA; we fixed the coupling constant $g^2\tilde{g}$ at 12.3 by fitting the value of the photoproduction cross section $\sigma(\gamma p \longrightarrow \rho^0 p)$ at $W =$ 30 GeV.

The results of our calculations for the cross section $\sigma(\gamma_\perp^*(Q^2)p \longrightarrow \rho_\perp^0 p)$ are presented in Fig. 4. On the

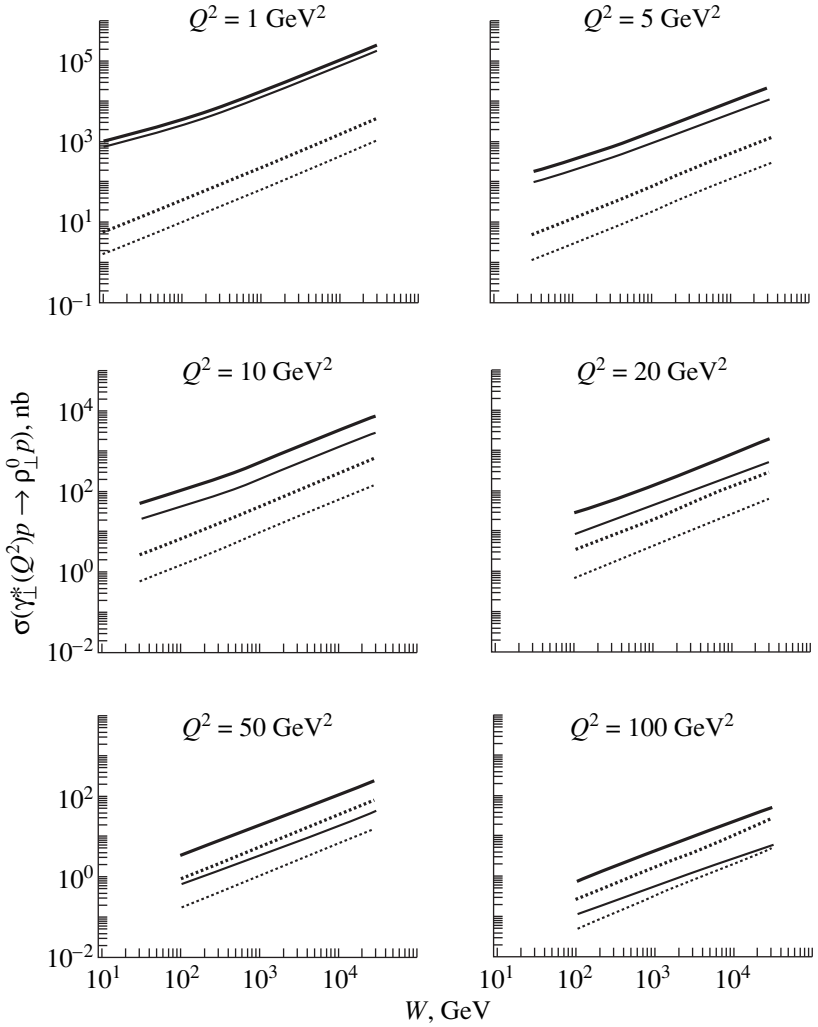

Fig. 7. Cross section $\sigma(\gamma_\perp^*(Q^2)p \longrightarrow \rho_\perp^0 p)$ calculated with allowance for all possible interquark distances (thick and thin solid curves correspond to versions IA and IIA, respectively) and cross section $\sigma(\gamma_\perp^*(Q^2)p \longrightarrow \rho_\perp^0 p)_{\rho < r_{cut}}$ representing the contribution of small interquark distances of $\rho < 0.2$ fm (thick and thin dotted curves correspond to versions IA and IIA, respectively). The difference $\sigma(\gamma_\perp^*(Q^2)p \longrightarrow \rho_\perp^0 p) - \sigma(\gamma_\perp^*(Q^2)p \longrightarrow \rho_\perp^0 p)_{\rho < r_{cut}}$ is small (on the order of 10%) only for $Q^2 > 100$ GeV^2 in the region $W \geq 10^4$ GeV.

basis of these results, we can draw the following conclusions:

(a) Versions IIA and IIIA yield nearly the same results.

(b) For all versions, the growth of the cross section with increasing W at constant Q^2 is described by the same expression

$$\sigma(\gamma_\perp^*(Q^2)p \longrightarrow \rho_\perp^0 p) \sim W^{2\Delta} \tag{34}$$

with $\Delta \approx 0.37$.

(c) With increasing Q, the cross section decreases faster in versions IIA and IIIA than in version IA.

The differential cross section

$$\frac{d\sigma(\gamma_\perp^*(Q^2)p \longrightarrow \rho_\perp^0 p)}{d\kappa_\perp^2} = \frac{1}{2}\sum_{a,b}\left|A^{\mathrm{BFKL}}(\gamma_\perp^* p \longrightarrow Vp)\right|^2 \tag{35}$$

is illustrated in Figs. 5 and 6. Figure 5 shows it as a function of W at various values of Q^2. It can be seen that the W dependences of this cross section have nearly the same form over a broad interval of $\kappa_\perp$. Figure 6 demonstrates that its $\kappa_\perp$ dependence weakly changes with Q^2.

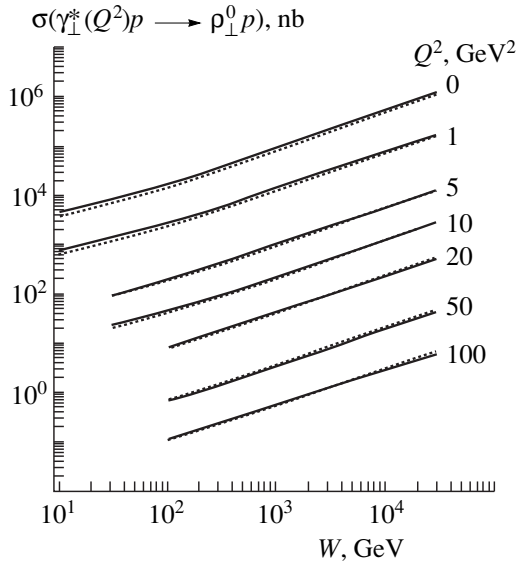

Fig. 8. Calculated cross section $\sigma(\gamma_\perp^*(Q^2)p \longrightarrow \rho_\perp^0 p)$ for versions IIA and IIB: solid curves correspond to the case where a hard Pomeron transforms into a soft Pomeron during the *t*-channel evolution of gluons [equations (30) and (31)], while dotted curves correspond to the case where a hard Pomeron does not transform into a soft Pomeron system [equations (32) and (33)].

The BFKL Pomeron is defined as a system that is formed by gluons separated by comparatively small (on the hadronic scale) distances. In order to clarify the way in which large Q^2 select small interquark (or intergluon) distances, we performed a calculation with a cut imposed on ρ in (30). For this purpose, it is convenient to introduce a Heaviside step function in the relevant integrand explicitly:

$$d^2\rho \longrightarrow d^2\rho\theta(r_{\text{cut}} - \rho). \tag{36}$$

In our calculations, we set $r_{\text{cut}} = 0.2$ fm. The results of this calculation are displayed in Fig. 7; we denote by $\sigma(\gamma_\perp^*(Q^2)p \longrightarrow \rho_\perp^0 p)_{\rho < r_{\text{cut}}}$ the cross section calculated with the above cut. We see that the selection of small interquark (or intergluon) distances with increasing Q^2 proceeds rather slowly at the initial stage; only for $Q^2 > 100$ GeV^2 do the cross sections calculated with and without the cut approach each other:

$$\frac{\sigma(\gamma_\perp^*(Q^2)p \longrightarrow \rho_\perp^0 p)}{\sigma(\gamma_\perp^*(Q^2)p \longrightarrow \rho_\perp^0 p)_{\rho < r_{\text{cut}}}} - 1 \leq 20\%. \tag{37}$$

Pomeron exchange is operative at large values of W^2/Q^2—the results of our calculations show that the condition in (37) holds for $W^2/Q^2 \geq 10^7$ (see Fig. 7).

The amplitude for version **B** is determined by expressions (32) and (33). The results of the calculation within the two versions virtually coincide [Fig. 8 displays the $\gamma_\perp^*(Q^2)p \longrightarrow \rho_\perp^0 p$ cross section calculated for versions **A** and **B**].

5. CONCLUSION

At high Q^2 and W^2/Q^2, the process $\gamma_\perp^*(Q^2)p \longrightarrow \rho_\perp^0 p$ proceeds in the following way. The hard photon produces a quark–antiquark pair at small distances; the quarks transform into a vector meson, emitting gluons that also occur at small distances in the impact-parameter space and which form the gluon ladder of a hard perturbative QCD Pomeron (BFKL Pomeron). The gluons that form the Pomeron undergo evolution in the impact-parameter space and can transform into a soft Pomeron, provided that the gluon ladder is sufficiently long. Bearing in mind this possibility, we have performed two versions of the calculation, that in which this transformation occurs (**A**) and that which is free from it (**B**), but we have obtained virtually identical results.

The block featuring the production of a quark–antiquark pair depends on the photon and rho-meson wave functions. The photon wave function is determined quite reliably by the $\gamma^*(Q^2)p \longrightarrow \pi, \eta, \eta'$ transition form factors for $Q^2 \leq 20$ GeV^2 [8], but information about the high-energy part of the rho-meson wave function is less certain.

We have calculated the cross section for the reaction $\gamma_\perp^*(Q^2)p \longrightarrow \rho_\perp^0 p$ by invoking various assumptions about the behavior of the $\rho \longrightarrow q\bar{q}$ transition vertex at large $M_{q\bar{q}}^2$: specifically, we relied on the generalized vector-dominance model, where $G_\rho \sim M_{q\bar{q}}^{-2}$ [version (I)], as well as on models where G_ρ decreases faster (versions II and III).

The results indicate definitively that, at $Q^2 \sim 5$–50 GeV^2, the cross section for the production of a transverse rho meson is governed by a BFKL Pomeron at not very small (on the hadron scale) interquark distances of $\rho > 1/4R_{\text{had}}$, where $R_{\text{had}} \sim 0.6$–0.8 fm. The contribution from small distances of $\rho < 1/4R_{\text{had}}$ becomes dominant only at very large Q^2 ($Q^2 \geq 100$ GeV^2).

An immediate conclusion from this result is that, in hadron-electroproduction reactions, the genuine perturbative regime has not yet set it at $Q^2 \sim 5$–50 GeV^2. We do not think that this is surprising, because the situation in electroproduction processes is completely similar to the situation in form-factor physics, where nonperturbative contributions dominate at $Q^2 \sim 20$ GeV^2 and where the perturbative regime is fully established no sooner than Q^2 becomes greater than 100 GeV^2 [6–8]. In addition, we would like to emphasize that α_s corrections to the BFKL Pomeron remain sizable up to similar Q^2 values of 50–100 GeV^2 [15].

That a noticeable contribution from large ρ (of about the hadron size) survives up to $Q^2 \sim 100$ GeV^2 has an important implication for processes occurring in the interval $Q^2 \sim 10$–50 GeV^2 because, for such processes, this adds importance to the problem of matching the BFKL Pomeron with the contribution of the soft region. First of all, this means that it is necessary to take into account the effective mass of the soft gluon on the order of 800–1000 MeV [16].

REFERENCES

1. A. V. Efremov and A. V. Radyushkin, Phys. Lett. B **94**, 45 (1980).
2. S. J. Brodsky and G. P. Lepage, Phys. Rev. D **22**, 2157 (1980).
3. E. A. Kuraev, L. N. Lipatov, and V. S. Fadin, Zh. Éksp. Teor. Fiz. **71**, 840 (1976) [Sov. Phys. JETP **44**, 443 (1976)]; Ya. Ya. Balitsky and L. N. Lipatov, Yad. Fiz. **28**, 1597 (1978) [Sov. J. Nucl. Phys. **28**, 822 (1978)].
4. L. N. Lipatov, Zh. Éksp. Teor. Fiz. **90**, 1536 (1986) [Sov. Phys. JETP **63**, 904 (1986)].
5. V. L. Chernyak and A. V. Zhitnitsky, Phys. Rep. **112**, 173 (1984).
6. N. Isgur and C. Llewellin-Smith, Phys. Lett. B **217**, 535 (1989); Nucl. Phys. B **317**, 526 (1989).
7. V. V. Anisovich, D. I. Melikhov, and V. A. Nikonov, Phys. Rev. D **52**, 5295 (1995).
8. V. V. Anisovich, D. I. Melikhov, and V. A. Nikonov, Phys. Rev. D **55**, 2918 (1997).
9. N. N. Nikolaev and B. G. Zakharov, Z. Phys. C **49**, 607 (1991); C **53**, 331 (1992).
10. A. D. Martin, M. G. Ryskin, and T. Teubner, Phys. Rev. D **55**, 4329 (1997).
11. S. J. Brodsky *et al.*, Phys. Rev. D **50**, 3134 (1994); I. F. Ginzburg, D. Yu. Ivanov, and V. G. Serbo, hep-ph/9508309; I. F. Ginzburg and D. Yu. Ivanov, Phys. Rev. D **54**, 5523 (1996).
12. V. N. Gribov, L. N. Lipatov, and G. V. Frolov, Yad. Fiz. **13**, 588 (1971) [Sov. J. Nucl. Phys. **13**, 333 (1971)].
13. J. Bartels, L. N. Lipatov, J. Forshaw, *et al.*, Phys. Lett B **348**, 589 (1995).
14. J. Gayler, in *Proceedings of 28th International Conference on High Energy Physics*, Ed. by Z. Ajduk and K. Wroblewski (World Sci., Singapore, 1997), p. 608.
15. V. S. Fadin and L. N. Lipatov, Phys. Lett. B **429**, 127 (1998); V. S. Fadin, hep-ph/9807528; M. Ciafaloni and G. Camici, Phys. Lett. B **430**, 349 (1998).
16. G. Parisi and R. Petronzio, Phys. Lett. B **94**, 51 (1980); M. Consoli and J. H. Field, Phys. Rev. D **49**, 1293 (1994).

Translated by M. Kobrinsky

Physics of Atomic Nuclei, Vol. 63, No. 1, 2000, pp. 94–108. From Yadernaya Fizika, Vol. 63, No. 1, 2000, pp. 106–120.

ELEMENTARY PARTICLES AND FIELDS
Theory

Dynamics of Confinement and Chiral Symmetry Breaking in the Heavy–Light $q\bar{Q}$ System*

Yu. A. Simonov

Institute of Theoretical and Experimental Physics, Bol'shaya Cheremushkinskaya ul. 25, Moscow, 117259 Russia

Received May 12, 1999

Abstract—At large N_c, the gauge-invariant Green's function of the heavy–light $q\bar{Q}$ system satisfies a nonlinear nonlocal equation, which is studied in detail. Chiral-symmetry breaking reveals itself through the appearance of scalar confinement at large distances. Equations for partial waves are written explicitly with perturbative Coulomb interaction taken into account, and the structure of the interaction kernel is studied semiclassically.

1. INTRODUCTION

Chiral-symmetry breaking (CSB) is known to be realized spontaneously in QCD, a fact which is supported by phenomenology and lattice data. On the theoretical side, there is a theorem [1] proving CSB in QCD in the limit of large-N_c QCD.

An important property of CSB is that it disappears together with confinement at the critical temperature T_c, as was seen in numerous lattice studies [2]. As a consequence, both phenomena should be related in QCD, and, in particular, special care should be given to the gauge-invariant formulation of the problem, since otherwise confinement can be lost [3].

The simplest gauge-invariant formulation of the problem was considered recently in the example of the heavy–light quark–antiquark system [4, 5]. Here, the heavy antiquark can be viewed as a static fundamental source, not influenced by the dynamics of the light quark.

For the $Q\bar{Q}$ system, when both quarks are heavy (static), the situation is now understood. Assuming the presence in the QCD vacuum of the specific field correlation functions [3, 6], one obtains confinement for a static quark and antiquark, realized in the form of the string connecting two static quarks.

It is not clear beforehand what would happen if one uses the same field correlation functions for the system of light quark and heavy antiquark. Specifically, would one obtain linear confining interaction for the light quark, or would there appear another dynamics?

Therefore, the first task of the present paper is to prove that the light quark in the heavy–light system is subject to a linear confining potential entering the (nonlocal and nonlinear) Dirac equation. The second task is the study of CSB in the example of the heavy–light system.

The phenomenon of CSB can reveal itself in the heavy–light system in several ways. Firstly, the parity doubling in the spectrum should be lifted; secondly, the chiral condensate of light quarks is expected to be nonzero; and finally, the dynamics of a light quark should correspond to Lorentz scalar interaction, described by linear potential at large distances.

Recently the heavy–light system was considered in this formulation [4, 5], and equations for the quark Green's function have been written explicitly, having the form of a nonlinear and nonlocal equation of Dirac type. It was shown in [4, 5] that confining field correlation functions give rise to the mass operator, which in the limit of large N_c is proportional to the quark Green's function.

The complexity of the nonlinear equation precluded so far its explicit numerical solution, and the analysis in [4, 5] essentially exploited the approximate relativistic WKB method. In this way in [4, 5] the scalar confining interaction was demonstrated for the light quark at large distances, displaying CSB.

Another approach to the same equations was used in [5], and again a linear scalar potential for the light quark at large distance was found.

In the present paper, we reconsider the problem of the CSB in the heavy–light system, trying to improve the previous analysis in several points.

First of all, we study the nonlinear equations for partial waves and define properties of solutions.

Second, we analyze semiclassically the explicit form of the light-quark interaction, which is generally nonlocal, at all distances, and it is shown to reduce to local linear interaction asymptotically at large distances, in agreement with previous studies [5].

* This article was submitted by the author in English.

Third, the perturbative gluon exchange is taken into account, and the resulting equations for the Green's function and wave functions are written explicitly. The analysis made shows that the kernel in this case acquires in addition to a modified form of the scalar term also a vector part.

This article is organized as follows. In Section 2 we rederive the equations for the heavy–light Green's function in the limit of large N_c, keeping only the lowest (Gaussian) field correlation functions. As in [4], the limit of small vacuum correlation length T_g is used where possible, enabling one to write time-independent equations. In Section 3, the spherical spinor expansion is used, and nonlinear equations are written for the partial waves. The relativistic WKB form of solutions is discussed in Section 4, whereby also the WKB form of the kernel is obtained. Modifications due to the inclusion of perturbative gluons are discussed in Section 5. Discussion of the results, as well as prospects of the present study, is relegated to Section 6. Three appendices are devoted to the spherical spinors (Appendix 1), to the properties of the kernel (Appen-dix 2), and to modifications of the gauge contours (Appendix 3).

2. EQUATIONS FOR THE GREEN'S FUNCTION

We shall be working with the gauge-invariant heavy–light $q\bar{Q}$ Green's function. The $\bar{Q}$ Green's function $G_{\bar{Q}}(x, y)$ is

$$G_{\bar{Q}}(x, y) = \frac{i}{2}\delta^{(3)}(\mathbf{x}-\mathbf{y}) \times \{e^{-(h_4)M}\theta(h_4)(1+\gamma_4) + e^{(h_4)M}\theta(-h_4)(1-\gamma_4)\}\Phi, \quad (1)$$

where $h_4 = x_4 - y_4$ and the parallel transporter is along the straight line

$$\Phi(x, y) = P\exp\left(ig\int_y^x A_\mu dz_\mu\right) \quad (2)$$

and the points x and y should be sitting on the world line of $\bar{Q}$, which we choose to be the x_4 axis ($\mathbf{x} = \mathbf{y} = 0$).

Therefore the gauge-invariant object, which we shall call in this paper, as in [4], the gauge-invariant light-quark Green's function $S(w, z)$, is defined as follows:

$$S(w, z) = \mathrm{tr}_c(G_q(w, z)\Phi_C(z, x)\Phi(x, y)\Phi_{C'}(y, w)), \quad (3)$$

where $G_q(w, z)$ is the proper light-quark Green's function, and contours C and C' are arbitrary.

There is a class of gauges where Φ_C, $\Phi_{C'}$, and Φ in (3) are equal to unity. In [4], the so-called modified Fock–Schwinger gauge was used, and in [5] a more general gauge [7] was exploited. In these gauges, $S(w, z)$ and $G_q(w, z)$ coincide, while the vector potential is expressed through $F_{\mu\nu}$ as

$$A_\mu(x) = \int_C F_{\alpha\beta}(z)\frac{dz_\alpha(s, x)}{ds}\frac{dz_\beta(s, x)}{dx_\mu}ds, \quad (4)$$

where the contour C is described by $z_\mu(x, s)$ and $z_\mu(x, 0) = x_\mu$.

To account for the heavy-quark trajectory, one chooses the class of contours $\{C\}$ passing from an arbitrary point to the x_4 axis and going to $-\infty$ along it.

The partition function Z of the light quark in the Euclidean spacetime,

$$Z = \int DAD\Psi D\Psi^+ \exp\left\{g\int\Psi^+\hat{A}\Psi d^4x - \int\frac{1}{4}F_{\mu\nu}^2 d^4x + i\int\Psi^+(\hat{\partial}+m)\Psi d^4x\right\}, \quad (5)$$

can be written in terms of the effective quark Lagrangian

$$Z = \int D\Psi D\Psi^+ \exp(\mathscr{L}_{\mathrm{eff}}(\Psi^+, \Psi) + \mathscr{L}_0), \quad \mathscr{L}_0 = i\int\Psi^+(\hat{\partial}+m)\Psi d^4x, \quad (6)$$

where we have defined

$$\exp\mathscr{L}_{\mathrm{eff}} \equiv \left\langle \exp\int\Psi^+\hat{A}\Psi d^4x\right\rangle_A \equiv \frac{1}{N_0}\int DA\exp\left\{-\frac{1}{4}\int F_{\mu\nu}^2 d^4x + g\int\Psi^+\hat{A}\Psi d^4x\right\}. \quad (7)$$

Making use of the cluster-expansion theorem, one can write for $\mathscr{L}_{\mathrm{eff}}$ an infinite series

$$\mathscr{L}_{\mathrm{eff}} = \frac{g^2}{2}\int dx\int dy\Psi_a^+\gamma_\mu\Psi_b(x) \times\Psi_c^+\gamma_\nu\Psi_d(y)\langle A_\mu^{ab}(x)A_\nu^{cd}(y)\rangle + \ldots, \quad (8)$$

where a, b, c, and d are color fundamental indices.

Using the gauge (4) one can express a factor $\langle AA\rangle$ through the field correlation function $\langle FF\rangle$

$$\langle A_\mu^{ab}(x)A_{\mu'}^{cd}(y)\rangle = \frac{\delta_{ad}\delta_{bc}}{N_c^2}\int_x\Gamma_{\mu\beta}(u)du_\alpha \times\int_y\Gamma_{\mu'\beta'}(v)dv_\gamma\mathrm{tr}_c\langle F_{\alpha\beta}(u)F_{\gamma\beta'}(v)\rangle, \quad (9)$$

where $\Gamma_{\mu\beta}(u) \equiv du_\beta/dx_\mu$. In what follows we keep in (8) only the first term, neglecting all others. The reason for this is that the expansion in powers of A in the correlation function is actually a power expansion in small

parameter $\zeta = \bar{F}^2 T_g^4 \approx 0.1$, where T_g is gluon correlation length measured on the lattice [8], and the values $\bar{F}^2 = \bar{E}_x^2 = \frac{1}{12}\langle F_{\mu\nu}^2\rangle$ can be taken from the standard gluon condensate. Moreover, only connected correlation functions enter into $\mathscr{L}_{\text{eff}}$, and for them higher terms can be suppressed furthermore due to subtraction of disconnected parts. In agreement with this, quartic terms in A and higher order terms do not show up in the effects considered so far; e.g., the Casimir scaling law for static $Q\bar{Q}$ potentials is seen on the lattice, which is due to the lowest correlation function (9), and would be violated by higher correlation functions [3]. Also, the QCD string profile calculations [9] are in agreement with the dominance of the Gaussian correlation function (9). Moreover, higher order correlation functions have been considered in [4] and shown to give qualitatively the same effects as the Gaussian correlation function. Therefore, we shall confine ourselves to the form (8), (9), neglecting all higher terms in (8).

One can now use (8) to produce Dyson–Schwinger equations for the Green's function S.

The crucial point is the expression of the effective-mass operator $M(x, y)$, which in general contains all powers of g^n and all possible contractions in $(\mathscr{L}_{\text{eff}})^n$. However, in the limit of large N_c, the leading term is obtained by contracting two internal or two external Ψ and Ψ^+ operators, and the result can be written as

$$\mathscr{L}_{\text{eff}}^{\text{con}} = \int dx dy \Psi_a^+(x) iM(x, y)\Psi_a(y), \tag{10}$$

where it was defined

$$iM(x, y) = \gamma_\mu S(x, y)\gamma_\nu J_{\mu\nu}(x, y), \tag{11}$$

$$J_{\mu\nu}(x, y) = \int^x \Gamma du \int^y \Gamma dv (D(u, v) + \Delta^{(1)}(u, v)). \tag{12}$$

Here, we have used the standard definition [6]

$$\frac{1}{N_c}\text{tr}_c\langle F_{\mu\nu}(u)F_{\rho\sigma}(v)\rangle = (\delta_{\mu\rho}\delta_{\nu\sigma} - \delta_{\mu\sigma}\delta_{\nu\rho}) \times D(u - v) + \Delta^{(1)}_{\mu\nu,\,\rho\sigma}(u - v), \tag{13}$$

$$\Delta^{(1)}_{\mu\nu,\,\lambda\sigma}(x) = \frac{1}{2}\partial_\mu\{[(x_\lambda\delta_{\nu\sigma} - x_\sigma\delta_{\nu\lambda}) + \mu\nu \longleftrightarrow \lambda\sigma]D_1(x)\}. \tag{14}$$

Both D and D_1 are known from lattice measurements [8].

Insertion of the contracted form (10) in (6) leads to the nonlocal Dirac equation for S:

$$(-i\hat{\partial} - im)S(x, y) - i\int M(x, z)S(z, y)d^4z = \delta^{(4)}(x - y), \tag{15}$$

which, together with (11), defines S as a solution of the nonlinear equation. Equations (11) and (15) have been first derived in [4].[1)]

To proceed with the solution of the nonlinear nonlocal equation (15), we shall use several approximations.

First of all, we neglect the term $\Delta^{(1)}$ in (13) since it is a full derivative and does not give rise to string formation (area law in Wilson loop) [6]. Its contribution in the framework of equation (15) was discussed in the appendix of [4].

Second, we shall neglect the contribution of the spatial components of the kernel $J_{\mu\nu}$, since the latter are produced by the color-magnetic components of the field correlation function, while the string is primarily made of the color-electric field, and associated with J_{44}. This approximation can and will be lifted in the future study of spin effects associated with the string and CSB.

Finally, we assume for $D(u - v)$ the Gaussian form, $D(u) = D(0)\exp(-u^2/4T_g^2)$, since it allows one to proceed with analytic calculations. Since correlation functions contribute to the string under the integral, the use of the Gaussian form instead of a more realistic exponential [8] should not change our results essentially. With this in mind and using for simplicity the modified Fock–Schwinger gauge [11], one obtains

$$iM(z, w) = J(z, w)\gamma_4 S(z, w)\gamma_4, \tag{16}$$

$$J(z, w) \equiv J_{44}(z, w) \equiv J(\mathbf{z}, \mathbf{w})e^{-(z_4 - w_4)^2/4T_g^2} = \mathbf{z}\cdot\mathbf{w}\, f(\mathbf{z}, \mathbf{w})D(0)e^{-(z_4 - w_4)^2/4T_g^2}, \tag{17}$$

$$f(\mathbf{z}, \mathbf{w}) = \int_0^1 ds \int_0^1 dt \exp\left(-\frac{(\mathbf{z}s - \mathbf{w}t)^2}{4T_g^2}\right). \tag{18}$$

As a next step, the gluon correlation length T_g, which is about 0.2 fm [8], can be exploited in (17) as a small parameter. To this end, one can make the Fourier transformation in the fourth components of coordinates z and v in (15) and (16) with the result

$$\left(ip_4 + \frac{\boldsymbol{\alpha}}{i}\frac{\partial}{\partial\mathbf{z}} + \beta m\right)S(p_4, \mathbf{z}, \mathbf{w}) + \beta\int M(p_4, \mathbf{z}, \mathbf{y})S(p_4, \mathbf{y}, \mathbf{w})d^3\mathbf{y} = i\beta\delta^{(3)}(\mathbf{z} - \mathbf{w}), \tag{19}$$

$$iM(p_4, \mathbf{z}, \mathbf{w}) = 2T_g\sqrt{\pi}\int\frac{dp_4'}{2\pi}e^{-(p_4 - p_4')^2T_g^2}J(\mathbf{z}, \mathbf{w}) \times \beta S(p_4', \mathbf{z}, \mathbf{w})\beta, \tag{20}$$

[1)] An independent study in [10] resulted in equations similar to (11) and (15), but where S in (11) was replaced by the free Green's function S_0. Thus defined $M_0(x, y) = -i\gamma_\mu S_0(x, y)\gamma_\nu J_{\mu\nu}$ does not produce CSB and may be applicable only for heavy mass m.

where $\beta \equiv \gamma_4$.

The eigenfunctions Ψ_n can be found in a standard way, now depending on p_4 as a parameter

$$\left(\frac{\boldsymbol{\alpha}}{i}\frac{\partial}{\partial \mathbf{z}} + \beta m\right)\Psi_n(\mathbf{z}, p_4) + \beta\int M(p_4, \mathbf{z}, \mathbf{w})\Psi_n(\mathbf{w}, p_4)d\mathbf{w} = \varepsilon_n(p_4)\Psi_n(\mathbf{z}, p_4) \tag{21}$$

with the completeness and orthogonality conditions

$$\sum_n \Psi_n(\mathbf{z}, p_4)\Psi_n^+(\mathbf{w}, p_4) = \delta^{(3)}(\mathbf{z}-\mathbf{w}), \tag{22}$$

$$\int \Psi_n^+(\mathbf{z}, p_4)\Psi_m(\mathbf{z}, p_4)d^3\mathbf{z} = \delta_{nm}. \tag{23}$$

The Green's function is expressed as

$$S(p_4, \mathbf{z}, \mathbf{w}) = \sum_n \frac{\Psi_n(\mathbf{z}, p_4)\Psi_n^+(\mathbf{w}, p_4)}{p_4 - i\varepsilon_n}\beta. \tag{24}$$

Now, one can notice that p_4 enters only as a spectral parameter in (19), and it appears in M (20) multiplied by T_g in the exponent.

Therefore, in the limit $T_g \longrightarrow 0$, the kernel M does not depend on p_4, as is seen from (20), and hence, $\Psi_n(\mathbf{z}, p_4)$ is also independent of p_4. The integration with respect to p_4' can be performed in (20). This yields

$$\int \frac{dp_4'}{2\pi}\frac{e^{-(p_4-p_4')^2T_g^2}}{p_4' - i\varepsilon_n} = \frac{i}{2}\mathrm{sgn}\varepsilon_n(1 + O(p_4T_g)). \tag{25}$$

Hence, in the limit $p_4T_g \longrightarrow 0$, one can represent M as

$$M(p_4, \mathbf{z}, \mathbf{w}) \longrightarrow M(\mathbf{z}, \mathbf{w}) = T_g\sqrt{\pi}D(0)\mathbf{z}\cdot\mathbf{w}\, f(\mathbf{z}, \mathbf{w})\beta\Lambda(\mathbf{z}, \mathbf{w}), \tag{26}$$

where the 4×4 matrix Λ is

$$\Lambda(\mathbf{z}, \mathbf{w}) = \sum_n \Psi_n(\mathbf{z})\mathrm{sgn}\varepsilon_n\Psi_n^+(\mathbf{w}), \tag{27}$$

and we have omitted the p_4 dependence in $\Psi_n(\mathbf{z}, p_4)$, assuming the limit $p_4T_g \longrightarrow 0$.

3. PARTIAL WAVE EXPANSION OF (15) AND (16)

One can expand in (21) both solution $\Psi_n(\mathbf{w})$ and the kernel $M(\mathbf{z}, \mathbf{w})$ in spherical spinors as it is done for a relativistic electron wave function in the field of a static source [12]

$$\Psi_n(\mathbf{r}) = \frac{1}{r}\sum_{jlM}\begin{pmatrix} G_n(r)\Omega_{jlM} \\ iF_n(r)\Omega_{jl'M}\end{pmatrix}. \tag{28}$$

We use here standard notation [12], $l' = 2j - l$ and

$$\Omega^\mu_{jlM} = G^{jM}_{LM-\mu,\frac{1}{2}\mu}Y_{l,M-\mu}, \quad \mu = \pm\frac{1}{2}; \tag{29}$$

accordingly, the 4×4 matrix Λ (and M) can be written in terms of the box structure

$$\Lambda = \begin{pmatrix} \Lambda_{11} & \Lambda_{12} \\ \Lambda_{21} & \Lambda_{22}\end{pmatrix}, \tag{30}$$

and each of Λ_{ik} is a 2×2 matrix,

$$\Lambda_{ik}^{\mu\mu'}, \mu, \mu' = \pm\frac{1}{2}.$$

To obtain equations for G_n and F_n, we substitute in (21) the form (28) and multiply from the left by $\Omega^*_{jlM}(\mathbf{z})$ and $\Omega^*_{jl'M}(\mathbf{z})$ and perform integration with respect to $d\omega(\mathbf{z}) \equiv d\cos\theta_z d\varphi_z$.

We list in Appendix 1 some useful formulas mostly taken from [12], for the convenience of the reader, and here we quote only the final result

$$\frac{dF_\nu}{dr} - \frac{\kappa}{r}F_\nu + (\varepsilon_\nu - m)G_\nu - \int\langle\nu|M_{11}|\nu'\rangle\frac{r}{w}G_{\nu'}(w)w^2dw - i\int\langle\nu|M_{12}|\nu'\rangle\frac{r}{w}F_{\nu'}(w)w^2dw = 0, \tag{31}$$

$$\frac{dG_\nu}{dr} + \frac{\kappa}{r}G_\nu - (\varepsilon_\nu + m)F_\nu - \int\langle\nu|M_{22}|\nu'\rangle\frac{r}{w}F_{\nu'}(w)w^2dw + i\int\langle\nu|M_{21}|\nu'\rangle\frac{r}{w}G_{\nu'}(w)w^2dw = 0. \tag{32}$$

Here, $\nu = njlM$, $\nu' = nj'l'M'$, and

$$\langle\nu|M_{11}|\nu'\rangle = \int\Omega^{*\mu}_{jlM}(\mathbf{r})M_{11}^{\mu\mu'}(\mathbf{r}, \mathbf{w})\Omega^{\mu'}_{j'l'M'}(\mathbf{w})d\omega(\mathbf{r})d\omega(\mathbf{w}). \tag{33}$$

For M_{21}, M_{12}, and M_{22}, one should replace l and l' or both, respectively, by $2j - l$ and $2j' - l'$.

Finally, we quote the explicit expansions for M,

$$M_{ik}^{\mu\mu'} = \sqrt{\pi}T_gD(0)\mathbf{z}\cdot\mathbf{w}\, f(\mathbf{z}, \mathbf{w})(-1)^{i+1}\Lambda_{ik}^{\mu\mu'}(\mathbf{z}, \mathbf{w}), \tag{34}$$

where

$$zw\Lambda_{ik}^{\mu\mu'}(\mathbf{z}, \mathbf{w}) = \sum_{njlM}\mathrm{sgn}\varepsilon_n\begin{pmatrix} G_\mu G^*_{\mu'} & -iG_\mu F^*_{\mu'} \\ iF_\mu G^*_{\mu'} & F_\mu F^*_{\mu'}\end{pmatrix} \tag{35}$$

and we defined

$$G_\mu \equiv G_n(z)\Omega^\mu_{jlM}(\hat{z}), \quad G^*_{\mu'} \equiv G^*_n(w)\Omega^{*\mu'}_{jlM}(\hat{w}),$$

$$F_\mu \equiv F_n(z)\Omega^\mu_{jl'M}(\hat{z}), \quad F^*_{\mu'} \equiv F^*_n(w)\Omega^{*\mu'}_{jl'M}(\hat{w}), \qquad (36)$$

$$l' = 2j - l.$$

Equations (31) and (32) together with definitions (35) and (36) are invariant under transformation [13]

$$\varepsilon_n \longleftrightarrow -\varepsilon_n, \quad \kappa \longleftrightarrow -\kappa, \quad G_n \longleftrightarrow F_n. \qquad (37)$$

From (34)–(36), one can notice that under this transformation M_{ik} change as

$$M_{11} \longleftrightarrow +M_{22}, \quad M_{12} \longleftrightarrow -M_{21}. \qquad (38)$$

The invariance under transformations (37) and (38) is the same as that of a Dirac equation with scalar potential [see (A.15) and (A.16)].

Using (37), one can rewrite (35) as a sum over only positive values ε_n, denoted as $n > 0$ (it is proven in [13] that there are no states with $\varepsilon_n = 0$ for scalar interaction),

$$zw\Lambda^{\mu\mu'}_{11} = \sum_{j,l,M,n>0} (G_\mu G^*_{\mu'} - F_\mu F^*_{\mu'}), \qquad (39)$$

$$\Lambda^{\mu\mu'}_{22} = -\Lambda^{\mu\mu'}_{11},$$

$$zw\Lambda^{\mu\mu'}_{12} = -i \sum_{j,l,M,n>0} (G_\mu F^*_{\mu'} - F_\mu G^*_{\mu'}), \qquad (40)$$

$$\Lambda^{\mu\mu'}_{21} = \Lambda^{\mu\mu'}_{12}.$$

To proceed further, one can expand $\Lambda^{\mu\mu'}_{ik}$ as follows:

$$\Lambda^{\mu\mu'}_{ik}(\mathbf{z}, \mathbf{w}) = a_{ik}\delta_{\mu\mu'} + \mathbf{b}_{ik} \cdot \boldsymbol{\sigma}_{\mu\mu'}, \qquad (41)$$

where

$$a_{ik} = \frac{1}{2}\mathrm{tr}_\mu \Lambda^{\mu\mu}_{ik}, \quad \mathbf{b}_{ik} = \frac{1}{2}\mathrm{tr}_\mu(\Lambda^{\mu\mu'}_{ik}\boldsymbol{\sigma}^{\mu'\mu}), \qquad (42)$$

so that, e.g.,

$$M^{\mu\mu'}_{11}(\mathbf{z}, \mathbf{w}) = \sqrt{\pi}T_g D(0)\mathbf{z} \cdot \mathbf{w} f(\mathbf{z}, \mathbf{w}) \times (a_{11}\delta_{\mu\mu'} + \mathbf{b}_{11} \cdot \boldsymbol{\sigma}_{\mu\mu'}) \equiv m^{(0)}_{11}\delta_{\mu\mu'} + \mathbf{m}_{11} \cdot \boldsymbol{\sigma}_{\mu\mu'}, \qquad (43)$$

$$M^{\mu\mu'}_{22} = M^{\mu\mu'}_{11}, \quad M^{\mu\mu'}_{21} = -M^{\mu\mu'}_{12}. \qquad (44)$$

Insertion of the term $m^{(0)}_{11}$ in (33) yields

$$\langle jlM|M_{11}|jlM'\rangle \longrightarrow \int \Omega^{*\mu}_{jlM}(\mathbf{r}) m^{(0)}_{11}(\mathbf{r}, \mathbf{w})\Omega^\mu_{jlM'}(\mathbf{w}) d\omega(\mathbf{r}) d\omega(\mathbf{w}) = \delta_{MM'}\frac{1}{2j+1}\sum_M \int \Omega^{*\mu}_{jlM}(\mathbf{r})\Omega^\mu_{jlM}(\mathbf{w}) \times m^{(0)}_{11}(\mathbf{r}, \mathbf{w}) d\omega(\mathbf{r}) d\omega(\mathbf{w}). \qquad (45)$$

Taking into account (see Appendix 1)

$$\sum_{M,\mu} \Omega^{*\mu}_{jlM}(\mathbf{r})\Omega^\mu_{jlM}(\mathbf{w}) = \frac{2j+1}{4\pi}P_l(\cos\theta_{rw}), \qquad (46)$$

we have

$$\langle jlM|M_{11}|jlM'\rangle = \delta_{MM'}\int m^{(0)}_{11}(\mathbf{r}, \mathbf{w})P_l(\cos\theta_{rw}) d\omega_{rw}, \qquad (47)$$

$$m^{(0)}_{11} = \sqrt{\pi}T_g D(0)\mathbf{z} \cdot \mathbf{w} f(\mathbf{z}, \mathbf{w}) \times \frac{1}{2zw}\sum_{\mu,j,l,M,n>0} (G_\mu G^*_\mu - F_\mu F^*_\mu), \qquad (48)$$

or, using (46), one can rewrite (48) as

$$m^{(0)}_{11} = \sqrt{\pi}T_g D(0)\mathbf{z} \cdot \mathbf{w} f(\mathbf{z}, \mathbf{w})\frac{1}{2zw}\sum_{j,l,n\geq 0}\frac{2j+1}{4\pi} \times \left\{P_l(\cos\theta_{zw})G_n(z)G^*_n(w) - P_{l'}(\cos\theta_{zw})F_n(z)F^*_n(w)\right\}, \qquad (49)$$

$$l' = 2j - l.$$

In a similar way, using (A.27), one can express $\mathbf{m}_{11}$ as follows:

$$\mathbf{m}_{11} = \sqrt{\pi}T_g D(0)\mathbf{z} \cdot \mathbf{w} f(\mathbf{z}, \mathbf{w})\frac{1}{2zw}\sum_{jl}\left(-\frac{\mathrm{sgn}\kappa}{2\pi}\right) \times \left\{\mathbf{L}_z P_l(\cos\theta_{zw})G_n(z)G^*_n(w) + \mathbf{L}_z P_{l'}(\cos\theta_{zw})F_n(z)F^*_n(w)\right\}, \qquad (50)$$

where we have used (A.28) in the last term.

Insertion in (33) of the term $\mathbf{m}_{11} \cdot \boldsymbol{\sigma}$ yields

$$\langle jlM|\mathbf{m}_{11} \cdot \boldsymbol{\sigma}|jlM'\rangle = \sum_{\mu\mu'}\int \Omega^{*\mu}_{jlM}(\mathbf{r}) \times \mathbf{m}_{11}(\mathbf{r}, \mathbf{w}) \cdot \boldsymbol{\sigma}^{\mu\mu'}\Omega^{\mu'}_{jlM'}(\mathbf{w}) d\omega(\mathbf{r}) d\omega(\mathbf{w}). \qquad (51)$$

Setting $M = M'$ as in (45) and performing summation over M, one has

$$\sum_M \frac{\langle jlM|\mathbf{m}_{11} \cdot \boldsymbol{\sigma}|jlM\rangle}{2j+1} = -\frac{\mathrm{sgn}\kappa}{(2j+1) \cdot 2\pi} \times \int d\omega(\mathbf{r}) d\omega(\mathbf{w}) \mathbf{m}_{11}(\mathbf{r}, \mathbf{w}) \cdot \mathbf{L} P_l(\cos\theta_{rw}). \qquad (52)$$

Equations (47) and (52), together with (49) and (50), yield all necessary information about the kernel $M_{11} = M_{22}$ in terms of usual Legendre polynomials.

Let us now address the nondiagonal term M_{12}, which can be written as in (43)

$$M_{12}^{\mu\mu'} = m_{12}^{(0)}\delta_{\mu\mu'} + \mathbf{m}_{12}\cdot\boldsymbol{\sigma}_{\mu\mu'}. \tag{53}$$

The matrix element entering equations (31) is

$$\langle jlM|M_{12}|j\tilde{l}'M'\rangle = \int \Omega_{jlM}^{*\mu}(\mathbf{r})M_{12}^{\mu\mu'}(\mathbf{r},\mathbf{w}) \times \Omega_{j\tilde{l}'M'}^{\mu'}(\mathbf{w})d\omega(\mathbf{r})d\omega(\mathbf{w}) \tag{54}$$

with $\tilde{l}' = 2j - l' = l$.

Putting in (54) $M' = M$ and summing over M as before, one obtains from $m_{12}^{(0)}$ the sum of the same form as the first sum in (A.26), which vanishes, and the only nonzero contribution comes from $\mathbf{m}_{12}$,

$$\sum_M \frac{\langle jlM|M_{12}|j\tilde{l}M\rangle}{2j+1} = -\int\frac{d\omega_r d\omega_w}{4\pi}\left\{\mathbf{m}_{12}\cdot\mathbf{n}_r P_l(\cos\theta_{rw}) + i\frac{2\,\mathrm{sgn}\,\kappa}{2j+1}\mathbf{m}_{12}\cdot[\mathbf{n}_r\times\mathbf{L}_r]P_l(\cos\theta_{rw})\right\}. \tag{55}$$

The vector function $\mathbf{m}_{12}(\mathbf{r},\mathbf{w})$ can now be written in the form similar to $\mathbf{m}_{11}$, equation (50),

$$\mathbf{m}_{12} = (-i)\sqrt{\pi}T_g D(0)\mathbf{z}\cdot\mathbf{w}\,f(\mathbf{z},\mathbf{w})\frac{1}{2zw} \times \sum_{j,l,n>0}[G_n(z)F_n^*(w)\mathbf{J}_{jl}(\mathbf{z},\mathbf{w}) - G_n^*(w)F_n(z)\mathbf{J}_{jl}^*(\mathbf{w},\mathbf{z})], \tag{56}$$

where $\mathbf{J}_{jl}$ is given in (A.30).

4. THE RELATIVISTIC WKB APPROXIMATION

The equations to be solved, (31) and (32), involve the nonlocal kernels $\langle\nu|M_{ik}(\mathbf{r},\mathbf{w})|\nu'\rangle$ which can be reduced to the angular integral (47), (52), and (55) of a function, having a general structure [cf. equations (49) and (52)]

$$m_{ik}(\mathbf{z},\mathbf{w}) = \mathrm{const}\cdot\mathbf{z}\cdot\mathbf{w}\,f(\mathbf{z},\mathbf{w})\Lambda_{ik}(\mathbf{z},\mathbf{w}). \tag{57}$$

We are interested in the behavior of $m_{ik}(\mathbf{z},\mathbf{w})$ at both small and large values of $\mathbf{z}$ and $\mathbf{w}$. Now, since the kernel Λ_{ik} consists of an infinite series of solutions (it is actually a spectral representation of the propagator), one may expect that solutions G_n and F_n with large n (and also large j, l) might be important, especially at large $\mathbf{z}$ and $\mathbf{w}$. To check this, in [4], the relativistic WKB method [14] was used to create $\tilde{G}_n$ and $\tilde{F}_n$ for some chosen scalar local potential $\tilde{V}(r) = \sigma r$ in the framework of the local Dirac equation. It was shown there that the resulting $\tilde{\Lambda}(\mathbf{z},\mathbf{w})$ at large distances behaves as a smeared δ function:

$$\tilde{\Lambda}(\mathbf{z},\mathbf{w}) \sim \tilde{\delta}(1-\cos\theta_{zw})\tilde{\delta}(|\mathbf{z}|-|\mathbf{w}|). \tag{58}$$

Insertion of $\tilde{\Lambda}$ in (57) produces immediately the scalar quasilocal linear potential $M(r) \approx \sigma r$ at large distances with the same string tension σ. In this way, the choice of the potential $\tilde{V}$ is proved a posteriori, at least at large distances.

It is a purpose of the present paper to make the semiclassical analysis more quantitative and, particularly, to find the behavior of the kernel $M(r, w)$ at both large and small distances.

Moreover, it is our purpose to check in the next publication the stability of the result, using for the lowest states G_n and F_n the solutions of (31) and (32) calculated with the kernel $\tilde{\Lambda}(z, w)$ improved gradually by the insertion of the lowest states found self-consistently rather than the WKB approximants, $\tilde{G}_n$ and $\tilde{F}_n$.

We expect that the highest states are given by the WKB approximants $\tilde{G}_n$ and $\tilde{F}_n$ reliably, and they are the lowest states which can be influenced by the local WKB approximation most of all; also, nonlocality can distort mostly the lowest states and not at large distances.

According to [4, 14], the WKB solution $\tilde{V} = \sigma r$ can be written separately in 3 regions:

$$\begin{aligned}&\text{region I: } 0 \le r \le r_-,\\ &\text{region II: } r_- \le r \le r_+,\\ &\text{region III: } r \ge r_+,\end{aligned} \tag{59}$$

where

$$r_\pm^2 = \frac{\varepsilon^2 \pm \sqrt{\varepsilon^4 - 4\sigma^2\kappa^2}}{2\sigma^2}. \tag{60}$$

The WKB solution in region II (most important to find the kernel $\tilde{\Lambda}(r, w)$) was written in [4] as

$$\tilde{G}_n^{\mathrm{II}} = C_1\sqrt{\frac{m+\sigma r+\varepsilon}{p(r)}}\sin\theta_1, \tag{61}$$

$$\tilde{F}_n^{\mathrm{II}} = C_1\,\mathrm{sgn}\,\kappa\sqrt{\frac{\varepsilon_n - m - \sigma r}{p(r)}}\sin\theta_2, \tag{62}$$

$$p(r) = \sqrt{\varepsilon_n^2 - \frac{\kappa^2}{r^2} - (m+\sigma r)^2}, \tag{63}$$

while θ_1 and θ_2 are defined as

$$\theta_1(r) = \int_{r_-}^{r}\left(p + \frac{\kappa w}{pr'}\right)dr' + \frac{\pi}{4}, \tag{64}$$

$$\theta_2(r) = \int_{r_-}^{r}\left(p + \frac{\kappa\tilde{w}}{pr'}\right)dr' + \frac{\pi}{4}, \quad (65)$$

$$w(r) = -\frac{1}{2r} - \frac{1}{2}\frac{\sigma}{m + \sigma r + \varepsilon_n}, \quad (66)$$

$$\tilde{w}(r) = \frac{1}{2r} - \frac{1}{2}\frac{\sigma}{m + \sigma r + \varepsilon_n}. \quad (67)$$

The semiclassical eigenvalues ε_n are defined from the quantization condition [14]

$$\int_{r_-}^{r_+}\left(p + \frac{\kappa w}{pr}\right)dr = \pi\left(n + \frac{1}{2}\right), \quad n = 0, 1, \ldots, \quad (68)$$

which gives approximately

$$\varepsilon_n^2 = 4\sigma\left(n + \frac{j+1}{2} + \frac{1 + \operatorname{sgn}\kappa}{4} + O\left(\frac{\kappa\sigma}{2\pi\varepsilon_n^2}\right)\right). \quad (69)$$

For large l and n, when $\sin\theta_i(r)$ oscillates quickly, one can find the normalization constant C_1 from the condition

$$C_1^{-2} = \varepsilon_n\int_{r_-}^{r_+}\frac{dr}{p(r)}, \quad C_1^2(n, l) = \frac{2\sigma}{\varepsilon_n\pi}. \quad (70)$$

Let us now consider region I. Using the standard matching condition [14], one obtains

$$\tilde{G}_n^{\mathrm{I}} = \frac{C_1\sqrt{m + \sigma r + \varepsilon_n}}{2\sqrt{|p(r)|}}\exp\left(-\int_r^{r_-}\left|p + \frac{\kappa w}{r'p}\right|dr'\right), \quad (71)$$

$$\tilde{F}_n^{\mathrm{I}} = \frac{C_1\sqrt{\varepsilon_n - m - \sigma r}}{2\sqrt{|p(r)|}}\operatorname{sgn}\kappa\exp\left(-\int_r^{r_-}\left|p + \frac{\kappa\tilde{w}}{r'p}\right|dr'\right). \quad (72)$$

It is important that behavior of the WKB solutions near $r = 0$ is given correctly by (71) and (72), namely [13]

$$\tilde{G}_n^{\mathrm{I}} \simeq A_n r^{|\kappa|}, \quad \tilde{F}_n^{\mathrm{I}} \simeq B_n r^{|\kappa|}, \quad (73)$$

where $\kappa = -1$ for $\tilde{G}_n^{\mathrm{I}}$ and $\kappa = +1$ for $\tilde{F}_n^{\mathrm{I}}$. The solution in region III can be written as (for $\kappa < 0$)

$$\tilde{\psi}_n = \begin{pmatrix}\tilde{G}_n^{\mathrm{III}}\\ \tilde{F}_n^{\mathrm{III}}\end{pmatrix} = C_3\frac{1}{\sqrt{Q|p|}} \times \exp\left\{-\int_{r_+}^{r}\left(|p(r')| - \frac{w(r')|\kappa|}{|p|r'}\right)dr'\right\}\begin{pmatrix}m + \sigma r + \varepsilon\\ -Q\end{pmatrix}, \quad (74)$$

where $Q = |p(r)| - \kappa/r$, and for $\kappa > 0$,

$$\tilde{\psi}_n = \begin{pmatrix}\tilde{G}_n^{\mathrm{III}}\\ \tilde{F}_n^{\mathrm{III}}\end{pmatrix} = C_3'\frac{1}{\sqrt{Q|p|}} \times \exp\left\{-\int_{r_+}^{r}\left(|p(r')| + \frac{|\kappa|\tilde{w}}{|p|r'}\right)dr'\right\}\begin{pmatrix}-Q'\\ m + \sigma r - \varepsilon_n\end{pmatrix}, \quad (75)$$

$$Q' = |p(r)| + \frac{\kappa}{r}. \quad (76)$$

Let us now consider the sum in (19) and replace it by the semiclassical solutions $\tilde{G}_n$ and $\tilde{F}_n$

$$\tilde{\Lambda}_{11}^{(0)} \equiv \sum_{\bar{j}, \bar{l}, n>0}\frac{2\bar{j}+1}{2xy \times 4\pi} \times\left\{\tilde{G}_n(x)\tilde{G}_n^*(y)P_{\bar{l}}(\cos\theta) - \tilde{F}_n(x)\tilde{F}_n^*(y)P_{\bar{l}'}(\cos\theta)\right\} \quad (77)$$

$$= \frac{1}{2xy}\sum_{\bar{j}, \bar{l}, n>0}\frac{2\bar{j}+1}{4\pi}C_1^2 \times\{N_1(x)N_1(y)P_{\bar{l}}(\cos\theta)\sin\theta_1(x)\sin\theta_1(y) - N_2(x)N_2(y)P_{\bar{l}'}(\cos\theta)\sin\theta_2(x)\sin\theta_2(y)\},$$

where θ_1 and θ_2 are given in (64) and (65), while N_1 and N_2 are, respectively,

$$N_1 x = \sqrt{\frac{m + \sigma x + \varepsilon_n}{p(x)}}, \quad N_2(x) = \sqrt{\frac{\varepsilon_n - m - \sigma x}{p(x)}}. \quad (78)$$

We shall now show that, at x and y such that $|x - y| \ll x, y$, we are able to calculate the sum (77) analytically. We shall use the method described in [4], but modify it to take the dependence on κ explicitly, not assuming it to be small as compared to n, as was done in [4].

One can write for $y < x$

$$\sin\theta_1(x)\sin\theta_1(y) = \frac{1}{2}\cos\int_y^x\left(p(r') + \frac{\kappa w(r')}{p(r')r'}\right)dr' - \frac{1}{2}\cos(\theta_1(x) + \theta_1(y)). \quad (79)$$

The last term in (79) quickly oscillates for excited states from term to term; therefore, its contribution to the sum (77) can be neglected.

For large x and y, the term $\kappa w/p(r')r'$ can be neglected as compared to $p(r')$, and we obtain approximately

$$\sin\theta_i(x)\sin\theta_i(y) \approx \frac{1}{2}\cos[p(x^*)(x - y)], \quad x^* \sim \frac{x+y}{2} \sim x. \quad (80)$$

One can go over from the summation over n to the integration with respect to $d\varepsilon$ according to (69)

$$\sum_{n\geq 0} = \int_{\varepsilon_{\min}} \frac{\varepsilon d\varepsilon}{2\sigma}. \tag{81}$$

After that, let us make another change of variables from ε to τ, coupled by

$$\varepsilon = \tau\sqrt{\frac{\kappa^2}{x^2} + \sigma^2 x^2}, \quad p(x) = \sqrt{\frac{\kappa^2}{x^2} + \sigma^2 x^2}\sqrt{\tau^2 - 1}. \tag{82}$$

We note that the semiclassically allowed region $p(x) \geq 0$ corresponds to $\tau \geq 1$ and (77) assumes the form

$$\tilde{\Lambda}_{11}^{(0)} \equiv \sum_{\bar{j}} \frac{(2\bar{j}+1)\sigma x P_l(\cos\theta)}{4\pi \times 2xy\pi}$$
$$\times \int_1^\infty \frac{d\tau}{\sqrt{\tau^2-1}} \cos\left(\sqrt{\frac{\kappa^2}{x^2} + \sigma^2 x^2}|x-y|\sqrt{\tau^2-1}\right) \tag{83}$$
$$= \frac{\sigma}{2\pi y}\sum_{\bar{j}} \frac{2\bar{j}+1}{4\pi} P_l(\cos\theta) K_0(a),$$

where

$$a = |x-y|\sqrt{\frac{\kappa^2}{x^2} + \sigma^2 x^2}, \tag{84}$$

and K_0 is a Macdonald function.

One can consider large x, satisfying the condition $\kappa_{\max}^2/x^2 \ll \sigma^2 x^2$. Then, the sum over $\bar{j}$ decouples in (83), and one has, as in [4],

$$\sum (2\bar{j}+1) P_l(\cos\theta)$$
$$\cong 2\sum_l (2l+1) P_l(\cos\theta) = 2 \times 4\delta(1-\cos\theta), \tag{85}$$

where the factor 2 comes from two possibilities $j = l \pm 1/2$ for each l. Finally, one has, as in [4],

$$\tilde{\Lambda}_{11}^{(0)} = \frac{\sigma}{\pi^2 y}\delta(1-\cos\theta) K_0(\sigma x|x-y|), \quad x \sim y. \tag{86}$$

The accuracy of the δ function in (86) or its smearing, is bounded by the condition

$$\Delta\theta\kappa_{\max} \gtrsim 1, \quad \Delta\theta \gtrsim 1/\sigma x^2. \tag{87}$$

Therefore, for smaller x, the δ function in (86) becomes "softer." This property may be seen from (83), which can be rewritten as

$$\tilde{\Lambda}_{11}^{(0)} = \frac{2\sigma}{8\pi^2 y}\int_0^\infty 2j dj J_0\left(\left(j+\frac{1}{2}\right)\theta\right)$$
$$\times K_0\left(|x-y|\sqrt{\frac{(j+1/2)^2}{x^2} + \sigma^2 x^2}\right) \tag{88}$$
$$= \frac{\sigma^2 x^3 K_1(\sigma\sqrt{x}\sqrt{|x-y|^2 + \theta^2 x^2})}{2\pi^2 y\sqrt{|x-y|^2 + \theta^2 x^2}}.$$

We also note that $\tilde{\Lambda}_{11}^{(0)}$ (86) and (88) is the normalized smeared δ function, namely (note that $\int \delta(1-\cos\theta) d\cos\theta = 1/2$),

$$\int_0^\infty \tilde{\Lambda}_{11}^{(0)}(x,y) d^3 y = 1. \tag{89}$$

We now consider the kernel $m_{11}^{(0)}$ (49) to find it in the semiclassical (and local) approximation, $\tilde{m}_{11}^{(0)}$. From (34), we then obtain

$$\tilde{m}_{11}^{(0)} = \sqrt{\pi} T_g D(0) \mathbf{z}\cdot\mathbf{w} f(\mathbf{z},\mathbf{w}) \tilde{\Lambda}_{11}^{(0)}. \tag{90}$$

Using the properties of $f(\mathbf{z}, \mathbf{w})$, defined in Appendix 2, one obtains

$$\tilde{m}_{11}^{(0)} \simeq \sigma \min(|\mathbf{z}|, |\mathbf{w}|) \tilde{\Lambda}_{11}^{(0)}. \tag{91}$$

This fact, together with the δ-function property of $\tilde{\Lambda}_{11}^{(0)}$, tells that at large z and w the kernel $\tilde{m}_{11}^{(0)}$ becomes a linear (almost) local confining interaction.

Taking into account the nonlocality in the angle θ, equation (88), one realizes that at small θ and small $|x-y|$ one can approximate (88) as

$$\tilde{\Lambda}_{11}^{(0)} \cong \frac{\sigma\sqrt{xy}}{2\pi^2} \frac{1}{(x-y)^2 + \theta^2 xy}. \tag{92}$$

Again using (88) and (90), we can now express the nonlocal kernel $\tilde{m}_{11}^{(0)}$ explicitly in terms of z, w, and the angle θ between vectors $\mathbf{z}$ and $\mathbf{w}$. The integral of $\tilde{m}_{11}^{(0)}$ with the ground-state eigenfunction Ψ_{jl}, $j = 1/2$, $l = 0$, displays the influence of nonlocality on the resulting effective potential.

We turn now to the vector part of the kernel $\mathbf{m}_{11}$ (50), which enters into the equations as a matrix element of $\mathbf{m}_{11}\cdot\boldsymbol{\sigma}$, equation (52).

One can proceed here as in the case of $\Lambda_{11}^{(0)}$, namely one has the following chain of equalities

$$\begin{aligned}
\mathbf{\Lambda}_{11}(x,y) &\equiv \frac{1}{2xy}\sum_{j,l,n>0}\mathbf{L}\left(-\frac{\mathrm{sgn}\kappa(j,l)}{2\pi}\right)\\
&\times\left\{P_l(\cos\theta)G_n(x)G_n^*(y)-P_{l'}(\cos\theta)F_n(x)F_n^*(y)\right\}\\
&= -\frac{\sigma\mathbf{L}}{4\pi y}\sum_j\left(P_{j+\frac12}(\cos\theta)-P_{j-\frac12}(\cos\theta)\right)\\
&\times K_0\left(|x-y|\sqrt{\frac{(j+1/2)^2}{x^2}+\sigma^2x^2}\right) = -\frac{\sigma\mathbf{L}}{4\pi y}\frac{|x-y|}{x^2}\\
&\times\int_0^\infty t\,dt\frac{K_1(|x-y|\sqrt{t^2/x^2+\sigma^2x^2})J_0(t\theta)}{\sqrt{t^2/x^2+\sigma^2x^2}}\\
&= -\frac{\sigma\mathbf{L}}{4\pi y}K_0\left(\sigma x^2\sqrt{\theta^2+\left(\frac{x-y}{x}\right)^2}\right),
\end{aligned}\tag{93}$$

where K_1 and J_0 are Macdonald and Bessel functions, respectively. Inserting this form in (50) and symmetrizing in x and y (since $|x-y|\ll x, y$), one finally obtains

$$\mathbf{m}_{11} = -\frac{\sigma^2\mathbf{x}\cdot\mathbf{y}}{4\pi\sqrt{xy}}\frac{f(\mathbf{x},\mathbf{y})}{2\sqrt{\pi}T_g}\mathbf{L}K_0\left(\sigma xy\sqrt{\theta^2+\frac{(x-y)^2}{xy}}\right). \tag{94}$$

Note that in (94) the function K_0 effectively separates forward direction, $\theta\ll 1$, and therefore at large x, y it can be understood as a smeared δ function, with the normalization

$$C\int d^3yK_0\left(\sigma xy\sqrt{\theta^2+\frac{(x-y)^2}{xy}}\right)\sigma^3(xy)^{3/2} = 1. \tag{95}$$

Therefore $\mathbf{m}_{11}$ can be rewritten as

$$\mathbf{m}_{11}\approx -\frac{\mathbf{x}\cdot\mathbf{y}\,f(\mathbf{x},\mathbf{y})}{\sigma(xy)^2T_g}\mathbf{L}\tilde{\delta}^{(3)}(\mathbf{y}-\mathbf{x}). \tag{96}$$

Hence, $\mathbf{m}_{11}$ yields a correction $O(1/x)$ since $|\mathbf{L}|\sim\partial/\partial\theta$ and $\theta^{-1}\sim\sigma xy$.

Now, we consider the last remaining piece in the kernel $\mathbf{m}_{12}$, defined in (55) and (56).

Denoting

$$\begin{aligned}
\mathbf{\Lambda}_{12}\equiv\frac{1}{2zw}\sum_{j,l,n>0}&[G_n(z)F_n^*(w)\mathbf{J}_{jl}(\mathbf{z},\mathbf{w})\\
&-G_n^*(w)F_n(z)\mathbf{J}_{jl}(\mathbf{w},\mathbf{z})]
\end{aligned}\tag{97}$$

and using (A.30) as well as the fact that vectors $\mathbf{z}$ and $\mathbf{w}$ almost coincide (as can be checked a posteriori), one can write

$$\mathbf{\Lambda}_{12} = -\mathbf{n}_z\Lambda_{12}^{(0)}-i(\mathbf{n}_z\times\mathbf{L}_z)\Lambda_{12}^{(1)}(\mathbf{z},\mathbf{w}), \tag{98}$$

where we have denoted

$$\Lambda_{12}^{(0)} = \frac{1}{2zw}\times\sum_{j,l,n>0}\frac{2j+1}{4\pi}P_l(\cos\theta_{zw})(G_n(z)F_n^*(w)-G_n^*(w)F_n(z)), \tag{99}$$

$$\Lambda_{12}^{(1)}(\mathbf{z},\mathbf{w}) = \frac{1}{2zw}\times\sum_{j,l,n>0}\frac{\mathrm{sgn}\kappa}{2\pi}P_l(\cos\theta_{zw})(G_n(z)F_n^*(w)-G_n^*(w)F_n(z)). \tag{100}$$

As before, we are mostly interested in region II, which provides the dominant contribution to the wave function and to the Green's function (i.e., to the kernel of the equations, in the approximation where one replaces the exact Green's function by the WKB one).

Using WKB formulas (59)–(65), one can represent $\Lambda_{12}^{(0,1)}$ (in the region $|z-w|\ll z, w$) as

$$\begin{aligned}
\Lambda_{12}^{(0)}(\mathbf{z},\mathbf{w}) &= \frac{1}{2zw}\sum_{j,l,n>0}\frac{2j+1}{4\pi}P_l(\cos\theta)\frac{2\sigma}{\pi\varepsilon_n}\frac{\mathrm{sgn}\kappa}{\sqrt{p(z)p(w)}}\\
&\times\{\sqrt{(\varepsilon+\sigma z)(\varepsilon-\sigma w)}\sin\theta_1(z)\sin\theta_2(w)-(z\longleftrightarrow w)\},
\end{aligned}\tag{101}$$

where θ_1 and θ_2 are defined in (64) and (65).

We neglect as before the quickly oscillating term, $\cos(\theta_1+\theta_2)$, while, for the difference, one can write, e.g., for $z>w$,

$$\begin{aligned}
\theta_1(z)-\theta_2(w) &= \int_w^z\left[p(r')-\frac{\kappa\sigma}{2(\sigma r'+\varepsilon)p(r')r'}\right]dr'\\
&-\frac{\kappa}{2}\left[\int_{r_-}^z\frac{dr'}{pr'^2}+\int_{r_-}^w\frac{dr'}{pr'^2}\right]\equiv\bar{\theta}(z,w)-\mathrm{sgn}\kappa\,\bar{\vartheta}(z,w),
\end{aligned}\tag{102}$$

where $\bar{\theta}(z,w)=-\bar{\theta}(w,z)$ and $\vartheta(z,w)=\vartheta(w,z)$,

$$\bar{\theta}(z,w) = \int_w^z\left[p(r')-\frac{\kappa\sigma}{2(\sigma r'+\varepsilon)p(r')r'}\right]dr', \tag{103}$$

$$\vartheta(z,w) = \frac{1}{2}|\kappa|\left[\int_{r_-}^z\frac{dr'}{pr'^2}+\int_{r_-}^w\frac{dr'}{pr'^2}\right]\approx\frac{\pi}{2}|\kappa|. \tag{104}$$

The summation over n can be done as in (81)–(83); then, for large z and w and fixed l and κ, one obtains

$$\varphi(z, w) \equiv \sum_n (G_n(z)F_n^*(w) - G_n^*(w)F_n(z)) = \frac{\sigma\sqrt{wz}}{\pi}\mathrm{sgn}\kappa \sin\frac{\kappa\pi}{2}K_1(a)\mathrm{sgn}(z-w), \quad (105)$$

where

$$a = \sigma\sqrt{xy}|x-y|,$$

and

$$\mathbf{m}_{12} = (-i)\sqrt{\pi}T_g D(0)\frac{\mathbf{z}\cdot\mathbf{w}}{2zw} f(\mathbf{z},\mathbf{w})\sum_{j,l} P_l(\cos\theta) \times \frac{2j+1}{4\pi}\left\{-\mathbf{n}_z\varphi(z, w) - i[\mathbf{n}_z\times\mathbf{L}_z]\frac{2\mathrm{sgn}\kappa}{2j+1}\varphi(z, w)\right\}. \quad (106)$$

One can estimate that $\int\varphi(z, w)\Psi_n(w)zwdw$ grows at most as z at large z; hence, $\mathbf{m}_{12}$ does not grow at all.

5. INCLUSION OF PERTURBATIVE GLUON EXCHANGES

In the preceding sections, gluon fields have been represented by the correlation function $D(x)$, which yields the contribution of nonperturbative configurations responsible for confinement. In this section, we generalize the treatment to include perturbative gluon fields and, first of all, perturbative gluon exchanges between light and heavy quark. To this end, we write the total gluon configuration as a sum [15, 16]

$$A_\mu(x) = B_\mu(x) + a_\mu(x), \quad (107)$$

where B_μ denotes the nonperturbative part used before, and $a_\mu(x)$ denotes the perturbative part. As in [16], we can use the 't Hooft identity to integrate in the partition function independently with respect to $B_\mu(x)$ and $a_\mu(x)$,

$$Z = \frac{1}{N}\int\exp\{-S_0(A) + g\int\psi^+\hat{A}\psi dx\}DAD\psi D\psi^+ = \frac{1}{N'}\int DB\eta(B)\exp\{g\int\psi^+\hat{B}\psi dx\} \times\int DaD\psi D\psi^+\exp\{g\int\psi^+ a\psi dx - S_0(B+a)\}, \quad (108)$$

where

$$S_0 = \int dx\left[\frac{1}{4}F_{\mu\nu}^2 - i\psi^+(\hat{\partial}+m)\psi\right],$$

and $\eta(B)$ is an (arbitrary) weight of integration with respect to B_μ.

Expansion of $S_0(B+a)$ in powers of a_μ provides the basis for the perturbative series in the background of vacuum nonperturbative fields B_μ. We shall not pursue this line in what follows, referring the reader to the papers [16, 17], where this background perturbation theory was used, and here we only concentrate on color Coulomb interaction due to gluon exchanges between light and heavy quark. As was argued in [15], this Coulomb interaction is not modified at small distances by the nonperturbative background when the system interacts for a large time T. In our case, we are interested in small-distance modifications of interaction, when the influence of the nonperturbative background on the perturbative exchanges can be neglected anyhow.

As in Section 2, we are interested in the heavy–light Green's function $G_{q\bar{Q}}$, where from the heavy antiquark one can retain only the contribution of the parallel transporter. Inserting in (5) the remnant of the $\bar{Q}$ Green's function, the term $\Phi(B+a)$ defined in (2), one can factorize due to (108) averaging over B_μ and A_μ, with the final result

$$Z = \int D\psi D\psi^+\exp(\mathscr{L}_{\mathrm{eff}} + \mathscr{L}_0 + \mathscr{L}_c). \quad (109)$$

Here, $\mathscr{L}_{\mathrm{eff}}$ and $\mathscr{L}_0$ are the same as in (8) with substitution $A_\mu \longrightarrow B_\mu$, and $\mathscr{L}_c$ is obtained as follows:

$$\langle\exp\{g\int dx\psi^+(x)\hat{a}(x)\psi(x) + ig\int dz_4 a_4(z_4)\}\rangle_a = \exp\{ig^2\int dx\psi^+\gamma_4\psi(x)\int dz_4\langle a_4(x)a_4(z)\rangle\}. \quad (110)$$

Using the same arguments as in [17, 18], one can write $\mathscr{L}_c$ as follows:

$$\mathscr{L}_c = g\int dx\psi^+(x)\hat{A}^{(c)}(x)\psi(x), \quad (111)$$

where we have defined

$$A_\mu^{(c)}(x) = -ig\int dz_4\langle a_4(x)a_4(z_4)\rangle = \delta_{\mu 4}\frac{(-i)gC_2}{4\pi|\mathbf{x}|}. \quad (112)$$

Note that we have neglected all interference terms, mixing B_μ and a_μ.

The presence of $\mathscr{L}_c$ in (109) does not influence the derivation of basic equations (11) and (15); the only difference is that equation (15) assumes the form

$$(-i\hat{\partial} - g\hat{A}^{(c)}(x) - im)S(x, y) - i\int M(x, z)S(z, y)d^4z = \delta^{(4)}(x-y). \quad (113)$$

Equation (11) does not change, and the kernel $J_{\mu\nu}(x, y)$ contains as before only nonperturbative contributions. Note, however, that $S(x, y)$ in $M(x, y)$ in (11) now contains also perturbative gluon exchanges, and this is a new type of interference of perturbative and NP terms, which appears irrespectively of our neglect of this interference within the averaging procedure over B_μ and a_μ. In other words, another class of diagrams is responsible for this interference.

Correspondingly, in the static equations (19), one should replace

$$\beta m \longrightarrow \beta m - C_2\alpha_s/|\mathbf{z}|. \tag{114}$$

Equations for partial waves (31) and (32) are modified due to the presence of the color Coulomb potential $V(r)$ in a simple way; since

$$V(r) = -C_2\alpha_s/r \tag{115}$$

is local and is a Lorentz vector, it always appears in the combination $\varepsilon_n - V(r)$. Hence, we have, instead of (31) and (32),

$$\frac{dF_\nu}{dr} - \frac{\kappa}{r}F_\nu + (\varepsilon_\nu - V(r) - m)G_\nu - \hat{M}_{11}G - i\hat{M}_{12}F = 0, \tag{116}$$

$$\frac{dG_\nu}{dr} + \frac{\kappa}{r}G_\nu - (\varepsilon_\nu - V(r) + m)F_\nu - \hat{M}_{22}F + i\hat{M}_{21}G = 0, \tag{117}$$

where we have denoted

$$\hat{M}_{ik}\begin{pmatrix}G\\F\end{pmatrix} \equiv \int \langle \nu|M_{ik}|\nu'\rangle \begin{pmatrix}G_{\nu'}(w)\\F_{\nu'}(w)\end{pmatrix} rwdw. \tag{118}$$

Here, M_{ik} is defined as in (34), and the matrix Λ_{ik} in (35) involves the sum over all states, including positive and negative ε_n. There in Section 3, we have exploited the symmetry (37). However, equations (116) and (117) are invariant under another transformation, namely

$$\varepsilon_n \longleftrightarrow -\varepsilon_n,\ V(r) \longleftrightarrow -V(r),\ \kappa \longleftrightarrow \kappa,\ G_n \longleftrightarrow F_n. \tag{119}$$

Now, the sum over negative ε_n can be expressed through the corresponding sum over positive ε_n with exchange $G_n \longleftrightarrow F_n$ as before, but also with the inversion of sign of Coulomb interaction; i.e., Coulomb attraction for positive ε_n is replaced by Coulomb repulsion for negative ε_n.

In what follows, we shall denote wave functions of the positive energy states with repulsive Coulomb with a tilde: $\tilde{G}_\nu$ and $\tilde{F}_\nu$.

With the aid of (35), the matrix $\beta\Lambda_{ik}$ can then be written as a sum over only positive ε_n as follows:

$$zw\beta\Lambda_{ik}^{\mu\mu'} = \sum_{j,\,l,\,M,\,n>0} \begin{pmatrix} G_\mu G^*_{\mu'} - \tilde{F}_\mu \tilde{F}^*_{\mu'} & -i(G_\mu F^*_{\mu'} - \tilde{F}_\mu \tilde{G}^*_{\mu'}) \\ -i(F_\mu G^*_{\mu'} - \tilde{G}_\mu \tilde{F}^*_{\mu'}) & \tilde{G}_\mu \tilde{G}^*_{\mu'} - F_\mu F^*_{\mu'} \end{pmatrix}. \tag{120}$$

Since $\beta\Lambda$ is exactly the combination which enters into the mass matrix (34), one can list in (120) scalar and vector (proportional to β) parts:

$$\hat{M} = M_s \cdot \hat{1} + M_v \cdot \beta + \Delta M, \tag{121}$$

where ΔM contains spin-dependent terms, which can be considered as in Section 3, while M_s and M_v are

$$M_{s,\,v} = C \sum_{j,\,l,\,M,\,\mu,\,n>0} \left[G_\mu G^*_\mu - \tilde{F}_\mu \tilde{F}^*_\mu \pm \left(\tilde{G}_\mu \tilde{G}^*_\mu - F_\mu F^*_\mu \right) \right], \tag{122}$$

where

$$C = \frac{1}{4}\sqrt{\pi} T_g D(0) \frac{\mathbf{z}\cdot\mathbf{w}}{zw} f(\mathbf{z}, \mathbf{w}). \tag{123}$$

From (122), it is clear that the vector part M_v is only due to the presence of Coulomb interaction and vanishes when it can be neglected.

Corrections at large distances due to $V(r)$ can be treated again by the relativistic WKB, and a rough estimate of M_v at large r is

$$\frac{M_v}{M_s} \sim \frac{\alpha_s}{\sigma r^2} \tag{124}$$

and, hence, can be neglected at large enough r.

6. CONCLUSION

The purpose of the paper is twofold: first, to write down explicit one-dimensional equations for the partial waves of the heavy–light $q\bar{Q}$ system, which takes into account effects of confinement and chiral-symmetry breaking, and, second, to give the WKB analysis of solutions.

The first task is done in equations (31) and (32) for partial waves F_n and G_n, where the kernels are expressed through the F_n and G_n in (49), (50), and (56). In these equations, all remaining angular integrations are in terms of Legendre polynomials. Nonlinearity of equations is essential for the spontaneous chiral-symmetry breaking, since both the QCD string and the chiral condensate occur due to the nonlinear structure; namely, as shown in [4], the solutions sum up in Λ_{ik} to a smeared δ function, and the latter "focuses" the string, making a linear potential out of the kernel J_{44}. The same kernel $\Lambda_{11}^{\mu\mu}$ gives rise to the nonzero chiral condensate, so both confinement and CSB appear simultaneously as a kind of feedback effect.

The numerical calculations clearly demonstrating these phenomena are now in progress and will be published elsewhere.

The second task of the paper is fulfilled in Section 4, where the WKB method is used to derive expressions for the kernel Λ_{ik} and m_{ik}. The corresponding formulas are given in (83), (88), (93), (96), (98), and (106).

These results display two main features of the kernel M, (i) the scalar part $M_{11} \sim m_{11}^{(0)}$ is dominating and linearly growing at large distances, while M_{12} and $\mathbf{m}_{11}$ are

subleading, and (ii) all parts of the kernel are quasilocal at large distances, which simplifies considerably dynamics of the light quark.

We plan to check all these w properties in future numerical calculations.

ACKNOWLEDGMENTS

I am grateful to J.A. Tjon for numerous detailed discussions on all points of this paper. A large part of the paper was written during my stay at the Institute for Theoretical Physics at Utrecht University. It is a pleasure to thank all authorities involved and especially J.A. Tjon and G. 't Hooft for kind hospitality.

This work was supported by the Russian Foundation for Basic Research (project nos. 97-02-16404, 97-02-17491, and 96-15-96740).

APPENDIX 1

Some Useful Formulas with Spherical Spinors

Orthonormality condition

$$\int \Omega^{*\mu}_{jlM}\Omega^{\mu}_{j'l'M'}d\omega = \delta_{jj'}\delta_{MM'}\delta_{ll'}, \tag{A.1}$$

$$\Omega_{jlM} = \begin{pmatrix}\Omega^{\mu=1/2}_{jlM}\\ \Omega^{\mu=-1/2}_{jlM}\end{pmatrix}, \quad \Omega^{\mu}_{jlM} = C^{jM}_{lM-\mu,\frac{1}{2}\mu}Y_{lM-\mu}. \tag{A.2}$$

The Clebsch–Gordan coefficients $C^{j\mu}_{lm-\mu,\frac{1}{2}\mu}$

μ \ j	$l+\frac{1}{2}$	$l-\frac{1}{2}$
$\frac{1}{2}$	$\sqrt{\frac{l+M+\frac{1}{2}}{2l+1}}$	$-\sqrt{\frac{l-M+\frac{1}{2}}{2l+1}}$
$-\frac{1}{2}$	$\sqrt{\frac{l-M+\frac{1}{2}}{2l+1}}$	$\sqrt{\frac{l+M+\frac{1}{2}}{2l+1}}$

(A. 3)

Relations between $\Omega_{jlM}(\mathbf{n})$ and $\Omega_{jl'M}(\mathbf{n})$, where

$$l' = 2j - l = \begin{cases} l+1, & j = l+\frac{1}{2}\\ l-1, & j = l-\frac{1}{2},\end{cases}$$

$$(\boldsymbol{\sigma}\cdot\mathbf{n})\Omega_{jlM}(\mathbf{n}) = -\Omega_{jl'M}(\mathbf{n}), \tag{A.4}$$

$$|\Omega_{jlM}|^2 = |\Omega_{jl'M}|^2 = \frac{1}{4\pi}\sum_n a_{2n}P_{2n}(\cos\theta), \tag{A.5}$$

$$a_{2n} = (-1)^{2n-1-M}\frac{(2l+1)(2j+1)}{4\pi} \times C^{2n0}_{l0l0}C^{2n0}_{j-M,jM}W\left(ll_{jj};\,2n\frac{1}{2}\right).$$

Separation of variables in the central field. For a Hamiltonian containing scalar potential $U(r)$ and vector potential $V(r)$,

$$H = \boldsymbol{\alpha}\cdot\mathbf{p} + \beta m + V(r) + \beta U(r), \tag{A.6}$$

$$\Psi_{jlM} = \begin{pmatrix} g(r)\Omega_{jlM}\\ i f(r)\Omega_{jl'M}\end{pmatrix}, \quad H\Psi = \varepsilon\Psi, \tag{A.7}$$

$$\boldsymbol{\sigma}\cdot\mathbf{p}\chi = (\varepsilon + V - m - U)\varphi, \quad \varphi = g(r)\Omega_{jlM}, \tag{A.8}$$

$$\boldsymbol{\sigma}\cdot\mathbf{p}\varphi = (\varepsilon + V + m + U)\chi, \quad \chi = if(r)\Omega_{jl'M}. \tag{A.9}$$

Since

$$\boldsymbol{\sigma}\cdot\mathbf{p}\varphi = -i\frac{dg}{dr}(\boldsymbol{\sigma}\cdot\mathbf{n})\Omega_{jlM} + g\boldsymbol{\sigma}\cdot\mathbf{p}\Omega_{jlM}, \tag{A.10}$$

one obtains by means of (A.4)

$$\begin{aligned} -(\boldsymbol{\sigma}\cdot\mathbf{p})\Omega_{jlM} &= (\boldsymbol{\sigma}\cdot\mathbf{p})(\boldsymbol{\sigma}\cdot\mathbf{n})\Omega_{jl'M}\\ &= (\mathbf{p}\cdot\mathbf{n} + i[\mathbf{p}\times\mathbf{n}]\cdot\boldsymbol{\sigma})\Omega_{jl'M}\\ &= -i\left(\frac{2}{r} + \frac{1}{r}\mathbf{L}\cdot\boldsymbol{\sigma}\right)\Omega_{jl'M},\\ \mathbf{L} &= \mathbf{r}\times\mathbf{p}.\end{aligned} \tag{A.11}$$

But

$$\mathbf{L}\cdot\boldsymbol{\sigma}\Omega_{jl'M} = \left(j(j+1) - l'(l'+1) - \frac{3}{4}\right)\Omega_{jl'M}. \tag{A.12}$$

Introducing

$$\kappa = \mp\left(j+\frac{1}{2}\right) = \begin{cases} -l+1, & j = l+\frac{1}{2}\\ l, & j = l-\frac{1}{2},\end{cases}$$

one obtains

$$\boldsymbol{\sigma}\cdot\mathbf{p}\varphi = +i\Omega_{jl'M}\left(\frac{dg}{dr} + \frac{\kappa+1}{r}g\right), \tag{A.13}$$

$$\boldsymbol{\sigma}\cdot\mathbf{p}\chi = -\Omega_{jlM}\left(\frac{df}{dr} - \frac{\kappa-1}{r}f\right) \tag{A.14}$$

and, finally, equations for $g(r)$ and $f(r)$,

$$\frac{d(rg)}{dr} + \frac{\kappa}{r}(rg) - (\varepsilon + m + V + U)(rf) = 0, \tag{A.15}$$

$$\frac{d}{dr}(rf) - \frac{\kappa}{r}(rf) + (\varepsilon + V - m - U)(rg) = 0. \tag{A.16}$$

The above equations (31) and (32) can be obtained if one takes scalar potential $U \equiv M$ and $V = 0$.

Some additional formulas are useful. From (A.11) and (A.12), one has

$$\mathbf{L}\cdot\boldsymbol{\sigma}\Omega_{jlM} = -(1+\kappa)\Omega_{jlM}, \tag{A.17}$$

$$\boldsymbol{\sigma}\cdot\mathbf{p}\Omega_{jlM} = i\frac{1+\kappa}{r}\Omega_{jl'M}, \quad l' = 2j-l, \tag{A.18}$$

$$\boldsymbol{\sigma}\cdot\mathbf{p}\Omega_{jl'M} = i\frac{1-\kappa}{r}\Omega_{jlM}, \tag{A.19}$$

$$\mathbf{L}^2\Omega_{jlM} = l(l+1)\Omega_{jlM} = \kappa(\kappa+1)\Omega_{jlM}. \tag{A.20}$$

To derive (46), one first must fix $m = M - \mu$ and sum up over μ:

$$\sum_{M\mu}\Omega^{\mu *}_{jlM}(\mathbf{r})\Omega^{\mu}_{jlM}(\mathbf{w}) = \sum_m\sum_\mu\left(C^{jm+\mu}_{lm\frac{1}{2}\mu}\right)^2 Y^*_{lm}(\hat r)Y_{lm}(\hat w), \tag{A.21}$$

where $\hat r$ and $\hat w$ are unit vectors. Substituting $C^{jM}_{lm\frac{1}{2}\mu}$ from (A.3), one has

$$(\text{A. 21}) = \frac{2j+1}{2l+1}\sum_m Y^*_{lm}Y_{lm} = \frac{2j+1}{4\pi}P_l(\cos\theta_{rw}). \tag{A.22}$$

A more complicated structure occurs in $\mathbf{m}_{ik}$, namely,

$$\mathbf{I}_{jl}(\mathbf{w},\mathbf{r}) \equiv \sum_{\mu M}\Omega^{*\mu'}_{jlM}(\mathbf{w})\boldsymbol{\sigma}^{\mu'\mu}\Omega^{\mu}_{jlM}(\mathbf{r}). \tag{A.23}$$

To do this, one can write

$$\boldsymbol{\sigma}\Omega_{jlM}(r) = c_1\mathbf{n}\Omega_{jl'M} + c_2\mathbf{p}\Omega_{jl'M} + c_3\mathbf{L}\Omega_{jlM}; \tag{A.24}$$

multiplying (A.24) by $\mathbf{n}$, one gets (from A.4) $c_1 = -1$. Multiplying by $\mathbf{p}$ and using

$$\mathbf{p}^2\Omega_{jlM} = \frac{\kappa(\kappa+1)}{r^2}\Omega_{jlM}, \tag{A.25}$$

one obtains $c_2 = ir/\kappa$, and multiplying by $\mathbf{L}$, one has $c_3 = -1/\kappa$.

Now (A.23) can be rewritten as

$$\mathbf{I}_{jl} = (c_1\mathbf{n} + c_2\mathbf{p})\sum_{\mu M}\Omega^{*\mu}_{jlM}(\mathbf{w})\Omega^{\mu}_{jl'M}(\mathbf{r}) + c_3\mathbf{L}_r\sum_{\mu M}\Omega^{*\mu}_{jlM}\Omega^{\mu}_{jlM}. \tag{A.26}$$

The first sum in (A.26) vanishes when one uses explicit values from (A.3), while the last sum was done in (A.22); hence,

$$\mathbf{I}_{jl} = \frac{2j+1}{4\pi}\left(-\frac{1}{\kappa}\right)\mathbf{L}_r P_l(\cos\theta_{rw}) = -\frac{\operatorname{sgn}\kappa}{2\pi}\mathbf{L}_r P_l(\cos\theta_{rw}). \tag{A.27}$$

We also note that, if one denotes $\kappa = \kappa(j, l)$ then

$$\kappa' = \kappa(j, l' = 2j - l) = -\kappa. \tag{A.28}$$

For M_{12}, one needs the sum of another form ($l' = 2j - l$),

$$\mathbf{J}_{jl} = \sum_{\mu M}\Omega^{*\mu}_{jlM}(\mathbf{w})\boldsymbol{\sigma}_{\mu\mu'}\Omega^{\mu'}_{jl'M}(\mathbf{r}) = -\sum_{\mu M}\Omega^{*\mu}_{jlM}(\mathbf{w})(\boldsymbol{\sigma}(\boldsymbol{\sigma}\cdot\mathbf{n}))_{\mu\mu'}\Omega^{\mu'}_{jlM}(\mathbf{r}) \tag{A.29}$$

$$= -\mathbf{n}\sum_{\mu M}\Omega^{*\mu}_{jlM}(\mathbf{w})\Omega^{\mu}_{jlM}(\mathbf{r}) + i[\mathbf{n}\times\mathbf{I}_{jl}].$$

Substituting (A.21) and (A.27), one gets

$$\mathbf{J}_{jl}(\text{A. 29}) = -\frac{\mathbf{n}_r(2j+1)}{4\pi}P_l(\cos\theta_{rw}) - i\frac{\operatorname{sgn}\kappa}{2\pi}[\mathbf{n}\times\mathbf{L}_r]P_l(\cos\theta_{rw}). \tag{A.30}$$

APPENDIX 2

Properties of the Kernel $f(\mathbf{x}, \mathbf{y})$ (18)

Introducing dimensionless variables $\hat z$ and $\hat w$,

$$\hat z = \frac{\mathbf{z}}{2T_g}, \quad \hat w = \frac{\mathbf{w}}{2T_g},$$

one has

$$f(\hat z, \hat w) = \int_0^1 ds\int_0^1 dt e^{-(\hat z s - \hat w t)^2}. \tag{A.31}$$

It is easy to obtain the expansion at small $\hat z$ and $\hat w$

$$f(\hat z, \hat w) \approx 1 - \frac{\hat z^2}{3} - \frac{\hat w^2}{3} + \frac{\hat z\times\hat w}{2} + O(z^3, w^3). \tag{A.32}$$

At large $\hat z$ and $\hat w$, the asymptotic expression for f depends on the direction. For $\cos\theta_{zw} = 1$, $|\hat z| \gg 1$ and $|\hat w| \gg 1$, one gets

$$f(\hat z, \hat w) = \frac{\sqrt{\pi}}{\max(|\hat z|, |\hat w|)}; \tag{A.33}$$

for $\cos\theta_{zw} = -1$, $|\hat z| \gg 1$, and $|\hat w| \gg 1$, one has

$$f(\hat z, \hat w) = \frac{1}{2|\hat z||\hat w|}; \tag{A.34}$$

and for $\cos\theta_{zw} = 0$, $|\hat{z}| \gg 1$, and $|\hat{w}| \gg 1$, the result is

$$f(\hat{z}, \hat{w}) = \frac{\pi}{4(|\hat{z}||\hat{w}|)}. \quad \text{(A.35)}$$

The approximate expression describing asymptotic behavior (A.33)–(A.35) within better than 10% accuracy and satisfying $f(0, 0) = 1$ is

$$\mathbf{z} \longrightarrow \frac{\mathbf{z}}{2T_g}, \quad \mathbf{w} \longrightarrow \frac{\mathbf{w}}{2T_g},$$

$$\tilde{f}(z, w)$$

$$= \begin{cases} \left[1 + \frac{4}{\sqrt{\pi}}\sqrt{\mathbf{z}^2 - \mathrm{sgn}(\mathbf{z}\cdot\mathbf{w})\frac{(\mathbf{z}\cdot\mathbf{w})^2}{w^2}}\right]^{-1}\left[1 + \frac{w}{\sqrt{\pi}}\right]^{-1}, \\ z \le w \\ \mathbf{z} \longleftrightarrow \mathbf{w}, \quad w \le z. \end{cases} \quad \text{(A.36)}$$

APPENDIX 3

Equations for a Modified Contour

Since the QCD partition function (5) does not depend on the choice of the contour in (4), one can introduce in (5) additional integration with respect to the space of contours $D\mu(C)$, where the measure is normalized. Whereas the total $\mathscr{L}_{\mathrm{eff}}$ (8) does not depend on C, each term of cluster expansion in (8) does, and the integration $D\mu(C)$ serves to optimize the contour. In the case of heavy quarks, one effectively gets the Wilson loop as $\exp\mathscr{L}_{\mathrm{eff}}$ (see, e.g., in [3]), and the optimization of contours leads to the surface of minimal area inside the Wilson loop.

Here, we choose a modified set of contours for $\mathscr{L}_{\mathrm{eff}}$ (8) having in mind to find the sensitivity of our results to the form of contours. In the case when new contours yield lower eigenvalues, this new choice is an optimization procedure, discussed above.

Choice of contours: for every pair of points x, y in (8), one defines the contours $z_\mu(\alpha, s; x(y))$ and $z_\mu(\beta, t; y(x))$, each consisting of two cuts of straight lines; e.g., $z_\mu(\alpha, s; x(y))$ from $(\mathbf{x}, x_4)$ to $\left(\frac{\mathbf{x}+\mathbf{y}}{2}, x_4\right)$ and from $\left(\frac{\mathbf{x}+\mathbf{y}}{2}, x_4\right)$ to $(\mathbf{0}, x_4)$; $z_\mu(\beta, t; y(x))$ from $(\mathbf{y}, y_4)$ to $\left(\frac{\mathbf{x}+\mathbf{y}}{2}, y_4\right)$ and from $\left(\frac{\mathbf{x}+\mathbf{y}}{2}, y_4\right)$ to $(\mathbf{0}, y_4)$.

The vector potentials can be computed according to (4). The result is

$$A_4(x) = \frac{x_i + y_i}{2}\int_0^1 d\alpha F_{i4}\left(\alpha\frac{x_i + y_i}{2}, x_4\right) + \frac{x_i - y_i}{2}\int_0^1 ds F_{i4}\left(x_i s + \frac{x_i + y_i}{2}(1-s), x_4\right), \quad \text{(A.37)}$$

$$A_4(y) = \frac{x_i + y_i}{2}\int_0^1 d\beta F_{i4}\left(\beta\frac{x_i + y_i}{2}, y_4\right) + \frac{y_i - x_i}{2}\int_0^1 dt F_{i4}\left(y_i t + \frac{x_i + y_i}{2}(1-t), y_4\right). \quad \text{(A.38)}$$

The function J_{44} in (17) now becomes

$$J_{44}(x, y) = \langle A_4(x)A_4(y)\rangle = D(0)\exp[-(x_4 - y_4)^2/4T_g^2]\left\{\left(\frac{\mathbf{x}+\mathbf{y}}{2}\right)^2\tilde{f}_-\left(\frac{\mathbf{x}+\mathbf{y}}{2}\right) + \frac{\mathbf{x}^2 - \mathbf{y}^2}{4}\left(f\left(\frac{\mathbf{x}+\mathbf{y}}{2}, -\frac{\mathbf{x}-\mathbf{y}}{2}\right) - f\left(\frac{\mathbf{x}+\mathbf{y}}{2}, \frac{\mathbf{x}-\mathbf{y}}{2}\right)\right) - \left(\frac{\mathbf{x}-\mathbf{y}}{2}\right)^2\tilde{f}_+\left(\frac{\mathbf{x}-\mathbf{y}}{2}\right)\right\}, \quad \text{(A.39)}$$

where we have defined

$$\tilde{f}_\mp(\mathbf{u}) = \int_0^1 d\alpha\int_0^1 d\beta\exp\left(-\frac{\mathbf{u}^2}{4T_g^2}(\alpha \mp \beta)^2\right), \quad \text{(A.40)}$$

and $f(\mathbf{x}, \mathbf{y})$ is defined in (18).

One can see in (A.39) that the term with $\tilde{f}_+$ is asymptotically $O(x^0, y^0)$, whereas the first three terms are $O(|\mathbf{x}|, |\mathbf{y}|)$. Therefore, one can find an approximate form for J_{44}, similar to (A.36). One obtains

$$J_{44}(x, y) = D(0)\exp\left[-\frac{(x_4 - y_4)^2}{4T_g^2}\right] \times \frac{(\mathbf{x}+\mathbf{y})^2}{4}\left[1 + \frac{|\mathbf{x}+\mathbf{y}|}{4T_g\sqrt{\pi}} + C\frac{|\mathbf{x}^2 - \mathbf{y}^2|}{4T_g^2}\right]^{-1}, \quad \text{(A.41)}$$

where $C \approx 1$.

For $|\mathbf{x}| \approx |\mathbf{y}| \gg T_g$ and $\cos\theta(x, y) \approx 1$, one finds from (A.41) that

$$J_{44}(x, y) \cong D(0)\exp\left[-\frac{(x_4 - y_4)^2}{4T_g^2}\right]\sqrt{\pi}|\mathbf{x}| \times 2T_g. \quad \text{(A.42)}$$

This asymptotic expression coincides with that of (17), giving the confirmation of the contour independence of our basic results.

REFERENCES

1. S. Coleman and E. Witten, Phys. Rev. Lett. **45**, 100 (1980).
2. J. Cleymans, R. V. Gavai, and E. Suhonen, Phys. Rep. **130**, 21 (1986); F. Karsch, in *QCD: 20 Years Later*, Ed. by P. M. Zerwas and H. A. Kastrup (World Sci., Singapore, 1993).
3. Yu. A. Simonov, Usp. Fiz. Nauk **166**, 337 (1966) [Phys. Usp. **39**, 313 (1996)].
4. Yu. A. Simonov, Yad. Fiz. **60**, 2252 (1997) [Phys. At. Nucl. **60**, 2069 (1997)]; hep-ph/9704301.
5. Yu. A. Simonov, Few-Body Syst. **24**, 45 (1998).
6. H. G. Dosh, Phys. Lett. B **190**, 177 (1987); H. G. Dosh and Yu. A. Simonov, Phys. Lett. B **205**, 339 (1988).
7. V. I. Shevchenko and Yu. A. Simonov, Phys. Lett. B **437**, 149 (1998); hep-th/9802134.
8. M. Campostrini, A. Di Giacomo, and G. Muassardo, Z. Phys. C **25**, 173 (1984); A. Di Giacomo and H. Panagopoulos, Phys. Lett. B **285**, 133 (1992); A. Di Giacomo, E. Meggiolaro, and H. Panagopoulos, Nucl. Phys. B **483**, 371 (1997); M. D'Elia, A. Di Giacomo, and E. Meggiolaro, Phys. Lett. **408**, 315 (1997).
9. L. Del Debbio, A. Di Giacomo, and Yu. A. Simonov, Phys. Lett. **332**, 111 (1994).
10. N. Brambilla and A. Vairo, Phys. Lett. B **407**, 167 (1997).
11. I. I. Balitsky, Nucl. Phys. B **254**, 166 (1985).
12. A. I. Akhiezer and V. B. Berestetskiĭ, 3rd ed., *Quantum Electrodynamics* (Nauka, Moscow, 1969; Wiley, New York, 1965).
13. V. D. Mur, V. S. Popov, Yu. A. Simonov, *et al.*, Zh. Éksp. Teor. Fiz. **105**, 3 (1994) [JETP **78**, 1 (1994)].
14. V. S. Popov, P. V. Voskresensky, V. L. Eletsky, *et al.*, Zh. Éksp. Teor. Fiz. **76**, 431 (1979) [Sov. Phys. JETP **49**, 218 (1979)]; V. D. Mur and V. S. Popov, Yad. Fiz. **28**, 837 (1978) [Sov. J. Nucl. Phys. **28**, 429 (1978)].
15. Yu. A. Simonov, Yad. Fiz. **58** 113 (1995) [Phys. At. Nucl. **58**, 107 (1995)].
16. Yu. A. Simonov, *Lecture Notes in Physics* (Springer–Verlag, 1996), Vol. 479, p. 139.
17. Yu. A. Simonov, S. Titard, and F. J. Yndurain, Phys. Lett. B **354**, 435 (1995).
18. Yu. A. Simonov, and J. A. Tjon, Ann. Phys. (N.Y) **228**, 1 (1993).